Influence of surface roughness on burner characteristics and combustion performance of AM combustors

Ianos Psomoglou

A thesis submitted in partial fulfilment of the requirements for the Degree of:

Doctor of Philosophy

Cardiff University

School of Engineering

Gas Turbine Research Centre

January 2023

Executive Summary

The transformation of the fossil fuel-based energy sector to a resilient, secure, and environmentally friendly equivalent, could potentially be achieved through the utilisation of “green” hydrogen-based energy. Although the introduction of pure, or blended hydrogen fuels to the power generation sector is associated with serious operability issues, novel manufacturing methods including Additive Manufacturing (AM) could assist in addressing such issues and facilitate the transformation of the power generation industry. Apart from the environmental, operational, and economic benefits afforded through AM, the latter is capable of delivering “manufacturable” surface roughness, enhancing the production efficiency of components and potentially improving gas turbine performance. This thesis aims to gain an understanding, through CFD and empirical investigations, of the impact of surface roughness on aerodynamics, combustion performance and emissions of a generic AM combustor characteristic of practical burners utilising conventional methane, pure hydrogen and an energy balanced mixture of methane and hydrogen.

Parametric combustion studies of the selected fuel types are conducted in a new generic swirl burner under atmospheric pressure and elevated temperature conditions, relevant to practical burner designs. A system comprising of several diagnostic tools has been developed and operated to accommodate the empirical investigation of surface roughness and deliver the relevant research objectives. Additionally, a computational study of the impact of surface roughness on the resultant aerodynamic flow field has also been designed and implemented. The effectiveness of the employed computational method was supported by the experimental results. The analysis of the empirical and computational findings of the present thesis, aims to build upon the existing knowledge concerning the influence of surface roughness on burner characteristics and combustion phenomena, informing gas turbine manufacturers on potential advantages and economic incentives of AM burners. With increasing surface roughness, the flame location is shifted towards the centreline of the burner, due to the alteration of the aerodynamic flow field. This observation is further supported computationally. The trend is consistent under any fuel type studied and did not influence the NO_x emissions or the burner stability envelopes.

Acknowledgements

For giving me the opportunity to do a PhD, for all the guidance and the support throughout this programme, I would like to thank Prof. Phil Bowen. For all the discussions, the thoughtful input, and the feedback, I would like to thank Dr. Andrew Crayford. For the continuous support, encouragement, and effort, I would like to thank Dr. Burak Gotkepe. These people offered me invaluable support and assistance, whilst helping me excel in my studies. I would not have been able to succeed without them.

For trusting me and giving me the opportunity to participate in research events, I would like to thank Dr. Jon Runyon. For helping with my experimental campaigns, I would like to thank Mr. Steve Morris, Mr. Jack Thomas, and Dr. Anthony Giles.

For motivating and inspiring me, I would like to thank all the people sharing my office.

Ultimately, I would like to thank my family and my best friends who kept believing, trusting, and supporting me in any possible way.

To all the above, Thank You.

Published & Presented work

Ianos Psomoglou, Jon Runyon, Andrew Crayford, Daniel Pugh, Phil Bowen, Richard Marsh, Anthony Giles, Steve Morris, Burak Goktepe: *Current and Future Topics in Additive Manufacture for Gas Turbine Combustion.* 47th TOTeM Technical Meeting on "Additive manufacturing for combustion applications", Paris, France, 5th February 2020.

Jon Runyon, **Ianos Psomoglou**, Recep Kahraman, Andrew Jones: *Additive Manufacture and the Gas Turbine Combustor: Challenges and Opportunities To Enable Low-Carbon Fuel Flexibility*. Gas turbines in a carbon-neutral society 10th International Gas Turbine Conference. 1–17 (2021).

Lee Weller, Anthony Giles, Priyav Shah, **Ianos Psomoglou**, Francesca De Domenico, Steve Morris, Philip Bowen, Ben Williams, Simone Hochgreb: *Spatial Temperature and Water Molar Concentration Measurements Using Thermal and Electrostrictive Ligs During Operation of a Swirl Burner at Pressure.* Turbomachinery Technical Conference & Exposition (GT 2023) – Accepted

Rashed Mohsen ALajmi, Mohammed Shaghdari, **Ianos Psomoglou**, Burak Goktepe, Phil Bowen: *Isothermal Investigation to Predict the Effect of Surface Roughness on Additive Layer Manufacturing Swirl Burner.* – Under development

Contents

List of Figures

List of Tables

Nomenclature

δ – boundary-layer thickness (m)

δ_v – viscous sublayer thickness (m)

δ_{99} – exact solution to boundary-layer thickness by Blasius (m)

δ_1 – boundary-layer displacement thickness (m)

δ_l – flame thickness (m)

ε – turbulent dissipation rate (m^2/s^3)

$\varepsilon_{2\text{-}layer}$ – turbulent dissipation rate for the two-layer modification (m^2/s^3)

ε^+ – dimensionless turbulent dissipation rate

E – log offset

θ – swirl vane angle

κ – von Karman constant

λ – pipe friction factor (Darcy's friction factor)

λ_c – thermal conductivity [W/(m·K)]

λ_w – wavelength (nm)

μ – (dynamic) viscosity (Pa·s)

μ_t – turbulent (dynamic) viscosity (Pa·s)

ν – kinematic viscosity (m^2/s)

ρ – density (kg/m^3)

ρ_u – unburnt density (kg/m^3)

δ_k - Prandtl number for k

δ_ε - Prandtl number for ε

τ – shear stress (N)

$\bar{\tau}$ – mean shear stress (N)

τ_{chem} – chemical timescale (s)

τ_{flow} – flow timescale (s)

τ_w – wall shear stress (N)

φ – equivalence ratio

χ – Reynolds-Averaged Navier-Stokes parameter

$\bar{\chi}$ – **mean Reynolds-Averaged Navier-Stokes parameter**

χ' – **fluctuating Reynolds-Averaged Navier-Stokes parameter**

ω – **specific turbulent dissipation rate (1/s)**

ω_k – **angular velocity (rad/s)**

$\overline{\Omega_{ij}}$ – **mean rate-of-rotation tensor (1/s)**

b – **breadth (m)**

d – **diameter (m)**

D – **total friction drag**

D_a – **Damköhler number**

D_h – **hydraulic diameter (m)**

D_{cf} – **constrictive flow diameter (m)**

$D_{i,j}$ – **binary mass diffusion coefficient**

D_T – **thermal diffusivity (m^2/s)**

c_D – **drag coefficient**

c_f – **skin friction coefficient**

c_L – **lift coefficient**

C_p – **specific heat capacity (J/kg·K)**

f' – **roughness function in the wall function treatment**

f_i – **examined parameter in GCI**

F – **force (N)**

F_s – **safety factor**

G_k – **production of turbulent kinetic energy (m^2/s^2)**

G_b – **production of turbulent kinetic energy due to buoyancy (m^2/s^2)**

h – **distance parallel to plates (m)**

k – **turbulent kinetic energy (m^2/s^2)**

k_s – **equivalent sand-grain roughness (m)**

k_{sand} – **sand-grain roughness (m)**

k^+_s – **roughness Reynolds Number**

k^+_{smooth} – **smooth (lower) limit of roughness regime**

k^+_{rough} – **rough (upper) limit of roughness regime**

l – length of plate (m)

L – integral length scale (m)

Le – Lewis number

$NO_{x,\,dry}$ – NO_x corrected for exhaust H_2O concentration (ppmV)

$NO_{x,\,dry15\%O2}$ – NO_x corrected for exhaust H_2O concentration and 15% excess O_2 (ppmV)

$NO_{x,\,wet}$ – uncorrected (hot, wet) measured NO_x (ppmV)

$O_{2,\,meas}$ – measured exhaust O_2 concentration (% vol)

$O_{2,\,ref}$ – reference exhaust O_2 concentration for emissions correction (% vol)

P – pressure (Pa)

ΔP – pressure drop (Pa)

Pr – Prandlt number

r_k – ratio of two consecutive grid refinements

R – characteristic radius (m)

R_a – arithmetic mean deviation (m)

R_p – maximum peak height (m)

R_q – standard deviation of roughness peaks (m)

R_v – maximum valley depth (m)

R_z – maximum peak to valley height (m)

Re – Reynolds number

Re_δ – Reynolds number formed with the viscous length scale and boundary-layer thickness

Re_x – Reynolds number formed with the length of flat plate

$Re_{x,\,crit}$ – critical Reynolds number for boundary layer transition

S – characteristic surface of a body

S_{ij} – strain rate (1/s)

S_L – laminar burning velocity (m/s)

S_N – Swirl number

S_T – turbulent flame speed (m/s)

t – time (s)

T – temperature (K)

T_{ad} – adiabatic flame temperature (K)

T_I – turbulence intensity (%)

T_L – turbulent length scale (m)

u – velocity (m/s)

U_b – mean flow velocity (m/s)

u_m – average velocity across the radius of a pipe (m/s)

u' – instantaneous axial velocity (m/s)

u^* – friction velocity (m/s)

u^+ – dimensionless velocity in wall function equation

U – relevant velocity length scale (m/s)

U_∞ – free stream velocity (m/s)

U^+ – dimensionless velocity in log-law equation

ΔU^+ – roughness function

v' – instantaneous tangential velocity (m/s)

x_{crit} – critical length for boundary layer transition (m)

X_{H2} – volume fraction of H_2

$\bar{w}$ – tangential mean velocity (m/s)

y – wall distance (m)

y^+ – dimensionless wall distance (viscous length distance)

Y_{H20} – mole fraction of water

Y_M – contribution of the fluctuating dilatation

Acronyms

AFT – Adiabatic Flame Temperature

AFR – Air Fuel Ratio

AM – Additive Manufacturing

APG – Adverse Pressure Gradient

APGSB – Atmospheric Pressure Generic Swirl Burner

CFD – Computational Fluid Dynamics

CIVB – Combustion Induced Vortex Breakdown

CMF – Coriolis Mass Flow

CRZ – Centra Recirculation Zone

DEM – Discrete Element Method

DNS – Direct Numerical Simulation

DLN – Dry Low NO_x

EGR – Exhaust Gas Recirculation

EU – European Union

FCV – Flow Control Valves

GCI – Grid Convergence Index

GT – Gas Turbine

GTRC – Gas Turbine Research Centre

HPGSB – High Pressure Generic Swirl Burner

HPOC – High Pressure Optical Chamber

ID – Internal Diameter

LBO – Lean Blow-Off

LBV – Laminar Burning Velocity

LDA – Laser Doppler Anemometry

LDV – Laser Doppler Velocimetry

LES – Large Eddy Simulation

LIF – Laser Induced Fluorescence

MGT – Micro Gas Turbine

OEM – Original Equipment Manufacturer

ORZ – Outer Recirculation Zone

PBF – Power Bed Fusion

PIV – Particle Image Velocimetry

PLIF – Planar Laser Induced Fluorescence

PM – Particulate Matter

POF – Positive Outwards Flow

PtG – Power-to-Gas

PVC – Precessing Vortex Core

RANS – Reynolds-Averaged Navier-Stokes

RES – Renewable Energy Sources

RMS – Root Mean Squared

RQL – Rich-Quench-Lean

SA – Spalart-Allmaras

SB – Swirler Base

SC – Swirler Curved

SCL – Swirler Curved Length

SFL – Swirler Flat Length

SLM – Selective Laser Melting

TFP – Technical Flashback Point

TRL – Technology Readiness Level

TS – Tollmien-Schlichting

UK – United Kingdom

US – United States

VSD – Variable Speed Drive

Abbreviations

CL – Chemiluminescence

CLD – Chemiluminescence Detector

F/A – Fuel air ratio

F/O – Fuel oxidiser ratio

GHG – Greenhouse gases

LPM – Lean premixed

St.Dev. – Standard deviation

STP – Standard Temperature and Pressure

TC – Thermocouple

UV – Ultraviolet

Chapter 1. Introduction

1.1 Energy mix – Energy trilemma

Energy is essential for all living beings and most aspects of life, continuously transforming from one form to another. Access to energy is a basic human need and a fundamental requirement for maintaining a healthy society, which continuously advances. Historically, energy needs were covered through the utilisation of coal and traditional biomass [1]. For the last 100 years, the global primary energy consumption has increased by more than a factor of 10, as shown in Figure 1.1-1. In 2019, approximately 84% of the global total energy demand (electricity, transportation and heat) was met through fossil fuels, including coal (≈27%), oil (≈33%) and gas (≈24%), whilst low carbon and renewable sources form the rest of the energy mix [1]. Specifically for electricity, roughly 60% is generated world-wide through fossil fuel combustion, though the share of low-carbon technologies in the energy mix steadily increases, with nuclear and hydropower being the major contributors (Figure 1.1-2).

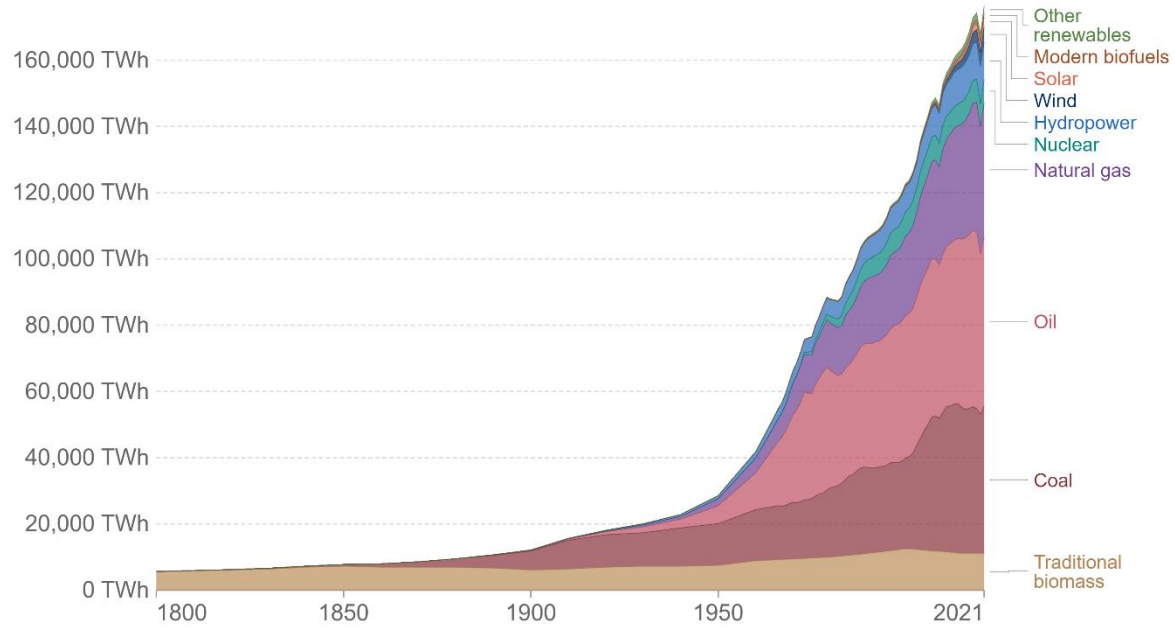

Figure 1.1-1 *Timeline of global primary energy consumption. Graphic from:* [1]*. Data from:* [2, 3].

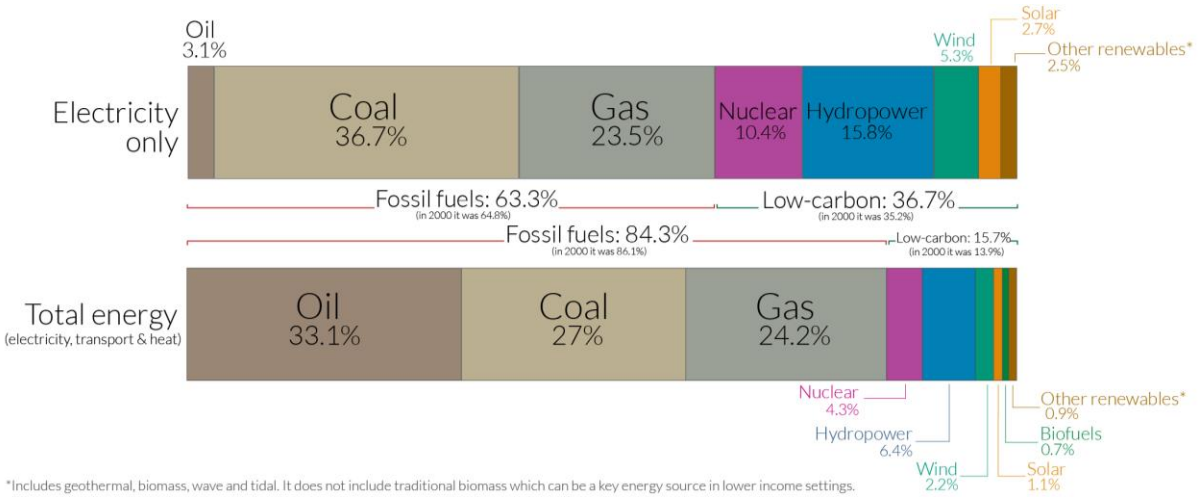

Figure 1.1-2 *Total and electricity only energy mix. Graphic from:* [1]*. Data from:* [2, 3].

However, the process known as combustion of fossil fuels typically emits local air pollutants, most prominently carbon monoxide (CO), nitrogen dioxide (NO_2), sulfur dioxide (SO_2), ozone (O_3), particulate matter (PM) and air toxics [4]. These polluting emissions have become of serious public concern due to their harmful consequences on the ecosystem [5] and in particular, local air quality. Approximately 90% of air pollutant are generated from the combustion of fossil fuels [6]. Moreover, the products of the combustion process of hydrocarbon-based fuels involve greenhouse gases (GHG), such as carbon dioxide (CO_2), methane (CH_4), water vapor (H_2O) and nitrous oxides (N_2O). Augmented concentrations of such gases in the atmosphere have been found to significantly contribute to global warming and, consequently to climate change [7]. The share of the CO_2 emissions resulting from fossil fuel combustion and industrial processes, in the total global GHG emissions mix, increased by 78% in the period of 1970-2010 [8], whilst in 2020 the total percentage of CO_2 in the GHG mix was approximately 79% [7].

To avert the catastrophic consequences of climate change [9], while mitigating pollutant emissions, several legislative developments have been put in place with a view to reducing the environmental impact associated with meeting energy demand. The gas turbine power generation industry, being an established prime consumer of gas and a major provider of electrical energy, has been continuously challenged to develop highly efficient fuel flexible systems of reduced environmental impact, accommodating low/zero carbon fuels while maintaining security of supply and delivering affordable energy [5]. These challenges are encompassed to what is widely

referred to as *Energy Trilemma*, a term that is frequently found in the energy industry literature. As shown in Figure 1.1-2, the energy trilemma describes the achieving of a balance between energy security, social impact and environmental considerations. Balancing these three pillars is the key to achieve a stable transition towards a resilient, decarbonised, energy sector and hence economy.

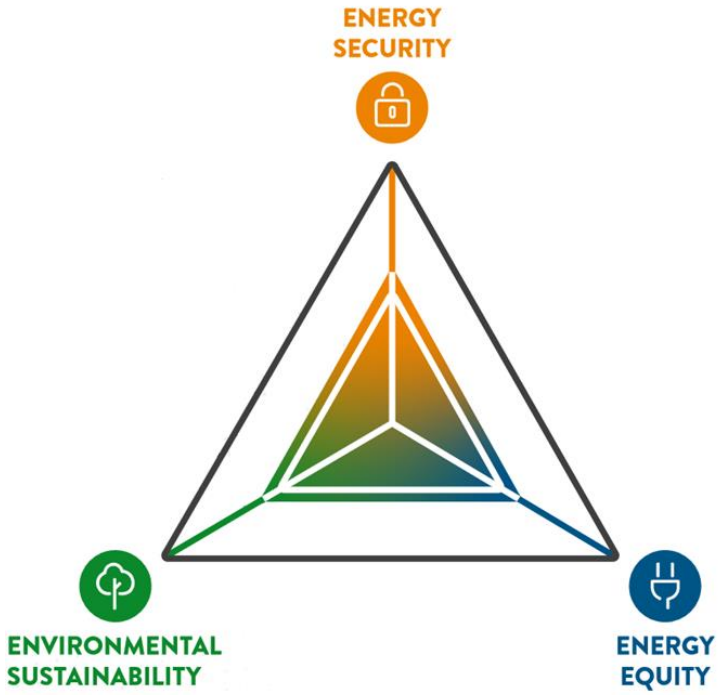

Figure 1.1-3 *Energy Trilemma visualisation. Graphic from:* [10].

Energy security is associated with the reliability and resilience of energy delivery systems, to cover the energy needs of society, providing security of supply without intermittent phenomena. *Energy Equity* relates to the affordable and abundant access to energy by the members of society, whilst, an energy system characterised by highly positive environmental performance, utilising renewable fuels of minimised environmental impact, describes the tenet of *Environmental sustainability* [11]. However, the identification and implementation of the appropriate synergistic strategy satisfying the requirements set by the energy trilemma, is particularly challenging [12].

1.2 Hydrogen (H_2) energy – Opportunities & Challenges

As the transformation of the fossil fuel-based energy sector to a renewable-energy sources (RES) equivalent poses serious risks associated to grid stability and security of supply, the utilisation of hydrogen (H_2) based energy and its chemical derivatives emerges as a suitable driving force for overcoming the three, often

opposing, challenges encompassing the energy trilemma concept. This energy-sector transformation approach relies upon the fundamental conditions that hydrogen is generated via low-carbon technologies, such as electrolysis, utilising the excess electrical power generated by RES. Therefore, the hydrogen produced can either be stored to serve as an energy storage medium or can be directly used as a final energy carrier. Additionally, hydrogen can be transformed to synthesis gas (syngas), methane (CH_4) or other chemicals, including ammonia (NH_3), as well as to electricity through the reverse process of electrolysis. This concept of "green" hydrogen production being used for power generation or storage purposes, thus balancing the energy market, is widely referred to as *power-to-gas* (PtG) (Figure 1.2-1) [13, 14]. Through interlinking several energy sectors via power-to-heat and power-to-mobility, using either electricity or hydrogen-derivatives as an end fuel, the decarbonisation of the three main energy sectors (electricity, transportation and heat) can be achieved in parallel, while ensuring enhanced fuel flexibility, security of supply and minimum environmental impact [15].

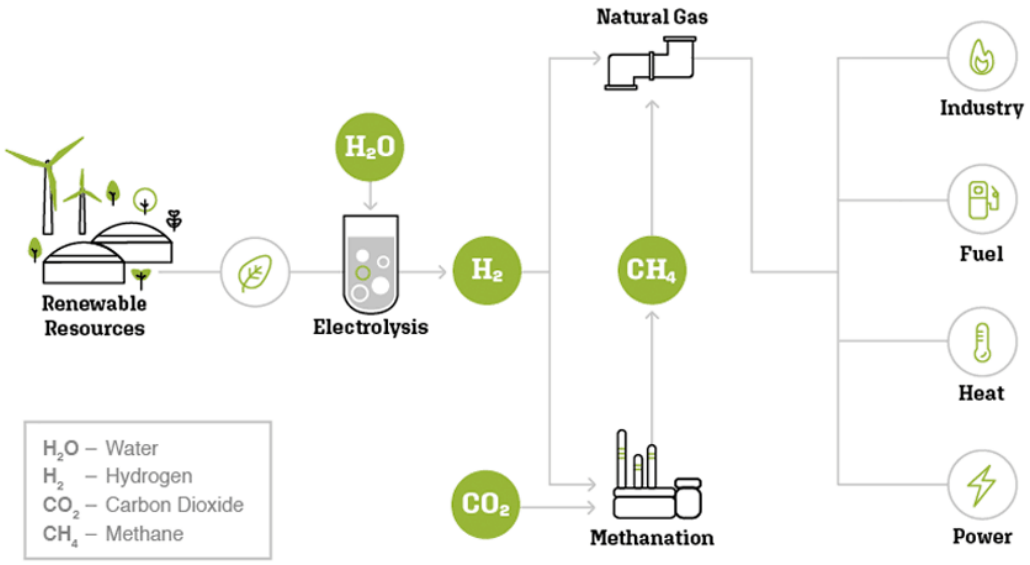

Figure 1.2-1 *Simplified schematic of the Power-to-Gas concept. Graphic:* [16].

However, there are serious challenges associated with the large-scale penetration of hydrogen in the power generation sector as the dominant energy contributor. These challenges are identified in all aspects of hydrogen production and utilisation chain. Primarily, only 4% of hydrogen is produced renewably from electrolysis ("green" hydrogen), whilst the rest of it, is produced from fossil fuels ("grey" and "blue" hydrogen), consuming annually, 6% and 2% of natural gas and coal

reserves, respectively [15, 17]. Moreover, the storage and transportation of hydrogen, which largely associates with hydrogen compression, still defines a serious issue preventing its widespread adoption. Current research focuses on advanced materials of enhanced thermal properties to avoid composite degradation during the compression process and to reduce total weight of the carrier cylinders. Additionally, solid and underground hydrogen storage concepts have been developed, while liquid hydrogen storage has also been achieved, though, it is associated with increased cost due to the reduced overall process efficiency [13, 18]. Although, 80% of hydrogen is consumed to produce NH_3, owing to a lot of small-scale pilot projects demonstrating the use of hydrogen for transport, heating and power generation purposes, the utilisation of hydrogen as a final energy carrier is expected to grow in the future [15, 17, 18] with positive signals particularly from the UK and Europe. Specifically Germany has the largest share of these projects, with more than 100 PtG demonstration and research programmes, 32% of which relate to hydrogen or methane blending into natural gas [14].

Apart from the difficulties related to the production, storage and transportation chain of H_2, particularly in the field of industrial, power generation gas turbines, there are important challenges that have to be addressed to enable the widespread integration of pure H_2 and H_2-blends in the power generation energy mix. To achieve the transition to H_2-based energy systems, highly fuel-flexible gas turbines (GTs) are desirable to efficiently operate on blends of hydrogen (or their derivatives) and natural gas. The introduction of hydrogen changes significantly the combustion properties of H_2-blends compared to natural gas [19]. In particular, hydrogen enrichment in natural gas mixtures results in significantly higher flame speeds, reduced ignition delay time and extended lean flammability limits [20]. Although this allows gas turbines to operate under leaner equivalence ratios, it also increases the risk of autoignition and flame flashback, which is a serious safety concern which has to be managed. Additionally, with increasing hydrogen concentration in the mixture, the thermo-acoustic behaviour of the combustor differs significantly, whilst due to the higher burning rates, heat release is faster and the flame temperature is higher resulting in potentially higher NO_x levels and reduced component lifetime due to the enhanced thermal load [19, 20].

Although for GTs operating steam-diluted diffusion flames, 100% H_2 combustion is achievable, further research must be undertaken to develop fuel-flexible

lean premixed combustors that can operate from 100% natural gas to 100% H_2, within acceptable emissions levels, by 2030 [19]. Currently, the limits for H_2 concentration accommodated in the mixture varies for different OEMs. Siemen's new GT systems can burn up to 30%$_{vol}H_2$, while SOLAR turbines latest combustion system is promoted to run on mixtures of 5-25%$_{vol}H_2$. Few OEMs, such as ANSALDO ENERGIA and General Electrics (GE) have achieved premixed H_2 combustion for a wide allowable range of H_2 variation in the mixture of 15-60%$_{vol}H_2$ [19].

In this regard, novel manufacturing techniques such as *Additive Manufacturing* (*AM*) is potentially capable of addressing challenges related to fuel flexible H_2 GT combustors. Recent work by the National Academies of Science, Engineering and Medicine (2020) [21], have declared AM and combustion as high-priority research areas to achieve pure H_2 combustion, while ensuring safe, reliable and environmentally friendly operation.

1.3 Additive Manufacturing (AM) for fuel-flexible power generation

Additive Manufacturing (*AM*), also referred as *Additive Layer Manufacturing* (*ALM*) or 3D printing, has increasingly emerged as a revolutionary technology for several applications related to industrial and biomedical sectors [22]. This innovative manufacturing technique aid the fabrication of enhanced structures of complexed geometry that would be impossible to build through traditional subtractive manufacturing methods. There are several advantages that deem AM superior compared to conventional manufacturing techniques. These include multiple component integration, rapid prototyping and freedom of design, reduced lead-time and minimisation of waste material, as well as highly precise multifunctional components with novel internal structures [22]. Recently the total number of EU AM related projects have increased from approximately 50 to over 400 in Horizon 2020. Subsequently, the research output concerning AM have augmented by an order of magnitude in the last 5 years, whilst original equipment manufacturers (OEMs) predict even higher development of AM in the manufacturing industry [23].

Particularly for the gas turbine (GT) manufacturing industry, metal AM utilising power bed fusion (PBF) technology via selective laser melting (SLM) is vastly preferred over other AM technologies for new product development and fabrication as well as for repair of in-service equipment [23]. The establishment of AM methods to

the energy sector is expected to significantly increase the use of renewable, low-carbon fuel (H_2, NH_3 and biofuels), whilst addressing issues linked to material properties, such as low melting points, and combustion inefficiencies, including unburnt fuel, flashback and combustion instabilities. Ultimately, AM is anticipated to assist in transitioning from fossil-fuel based combustion, while reducing CO_2 and NO_x emissions and improving combustion performance [19, 21]. Market leading industrial and micro-gas turbine OEMs, already invest and examine the use of AM for the manufacturing of critical GT components, including burners (Figure 1.3-1 A), guide vanes, turbine blades, nozzles (Figure 1.3-1 C) and swirlers (Figure 1.3-1 D). Characteristic examples are the AM fabricated fuel nozzle tip, manufactured by GE Additive (part of General Electric – GE), that is already commercially available and used in the LEAP jet engine developed by CFM international [24], and the micromixer shown in Figure 1.3-1 B, which is used in GE's dry low NO_x (DLN) combustor (DLN 2.6e), achieving 50%$_{vol}H_2$ operation [25].

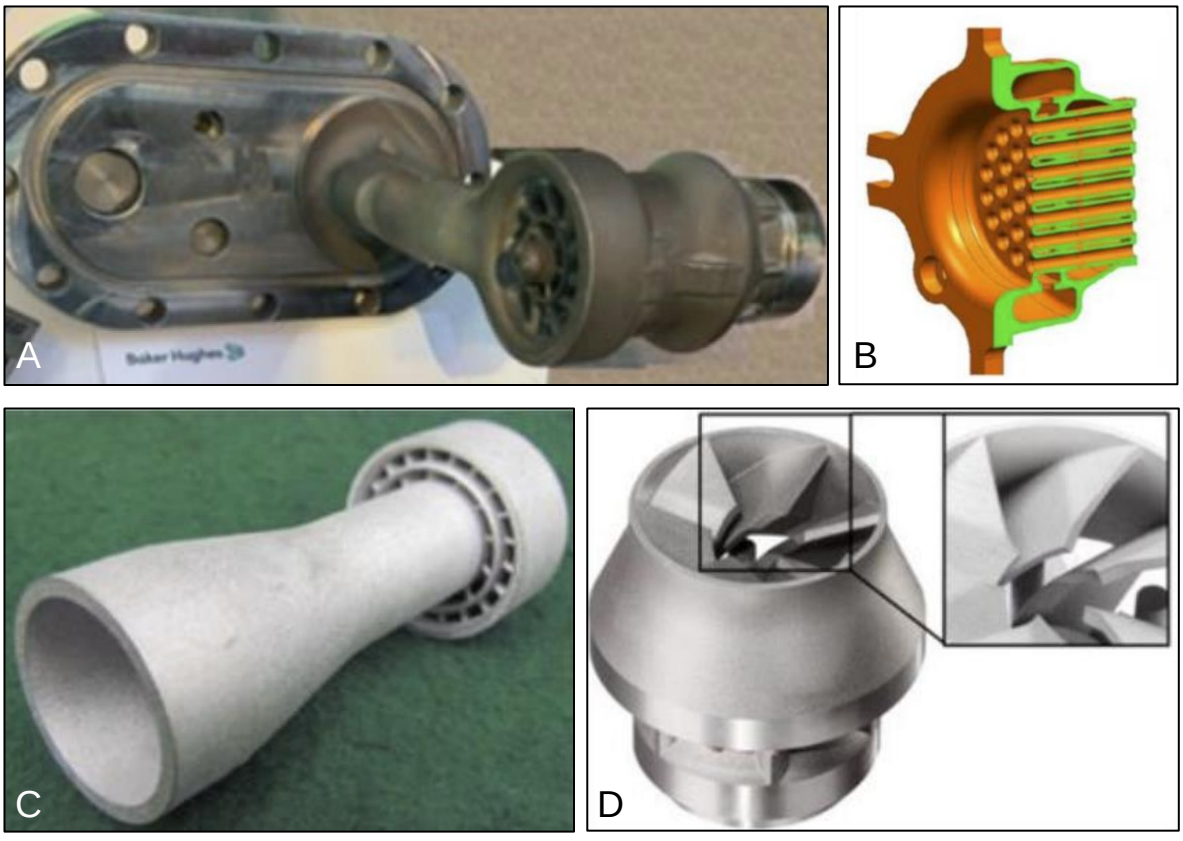

Figure 1.3-1 *(A) fuel burner from Baker Hughes, Source:* [26]*. (B) micromixer for high-H_2 combustors from GE, Source:* [27]*. (C) fuel nozzle from Solar, Source:* [26]*. (D) swirler from Siemens, Source:* [28]*.*

For gas turbine swirlers of increased geometrical complexity, AM is regarded as a suitable candidate to promote their development. The scale of these components is appropriate for AM fabrication, enabling enhanced and optimised design for improved cooling performance, low pressure drop and improved mixing [29]. Fundamental combustion research, which has been facilitated due to the increased access to AM machines, has already proven the potential of AM on enhancing combustion performance. In a recent study conducted by Giuliani et al. [30], three axial swirlers were manufactured through AM techniques out of Inconel 718, emphasising the impact of significant parameters such as building direction. The AM swirler showed significant advantages in the lean blow-off performance of the burner, due to the novel single S-vane design (Figure 1.3-2 A). Moreover, a driver of this current research study, Runyon et al. [29], quantified the surface roughness of two AM radial/tangential swirlers, one of which had be post-processed to result in reduced surface roughness height. Subsequently, the effect of surface roughness on axial velocity, NO_x emissions and flame positions, was evaluated for methane (CH_4) turbulent flames under ambient pressure and elevated inlet temperature, reporting improved NO_x performance of the AM swirler of highest surface roughness (Figure 1.3-2 B).

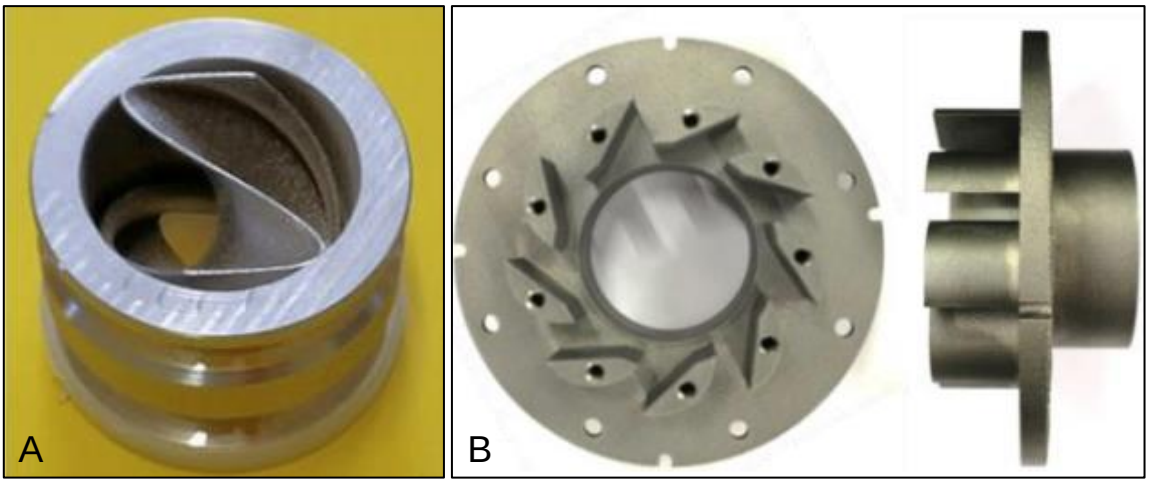

Figure 1.3-2 *(A) AM swirler for combustion research, Source:* [30]*. (B) AM swirler used in combustion research at the GTRC, Source:* [29].

Amongst other advantages offered by AM, the latter facilitates the fabrication of gas turbine components of specific, predefined surface roughness, based on the selected building parameters prior to printing stage. Since rough surfaces can significantly influence the operation and the efficiency of gas turbines, the investigation of surface finish, as a function of building orientation and surface roughness, is a

currently active research area [31, 32]. Delivering “manufacturable” surface roughness might be of interest for GT OEMs, as in this way the need and cost for post-processing of critical GT components is minimised. The impact of surface roughness on gas turbines is briefly discussed in the following Section 1.4.

1.4 Surface roughness for gas turbines (GTs)

Surface roughness directly affects the performance, and hence, the efficiency of gas turbine systems. The influence of surface roughness on flow parameters, such velocity, and flow structures like boundary layers, has been studied for more than 100 years, with the first studies of Darcy [33] and Fanning [34] conducted in 1857 and 1882, respectively. Recently, the influence of surface roughness on turbomachinery flows has gained great attention due to the continuous need for improvements on gas turbine performance [35]. A thorough review on surface roughness effects on gas turbines is provided by Bons [36]. A brief discussion of the most common issues associated with surface roughness is described as follows.

Both the rotor and the stator blades of a gas turbine have a specific surface finish that usually results from post-manufacturing processes. Usually, this surface finish is altered due to the addition of thermal barrier coating for enhanced thermal resistance [37]. Moreover, during the lifetime of the component, its surface finish unevenly increases due to the degradation of its surface. Several factors might result in blades degradation, including low quality fuels, internal oil leaks and inadequate maintenance. Furthermore, erosion and corrosion, as well as particulate deposition (Figure 1.4-1) may also result in changing the surface roughness of the blades [38, 39]. Consequently, important design parameters such as the shape and the effective length of the blades are affected, changing the incident and discharge angles, and limiting the aerodynamic turning. As erosion takes place, the thermal coating of the blades fails, exposing a region of the blades to excessive gas temperatures. Consequently, the flow properties of both the compressor and the turbine blade cascade are deteriorated, promoting efficiency losses and enthalpy drop [39].

Figure 1.4-1 *Deposition of first stage vanes of utility gas turbine after approximately 8000 hours of service. Firing temperature 1150^{o}C. Source:* [36].

However, apart from the aforementioned issues that reduce the performance of GTs, several experimental studies have shown that roughness features manufactured intentionally can potentially improve the efficiency of GTs' components by enhancing their aerodynamic and heat transfer performance [40–43]. Similar to the dimpled surface on golf balls, biomimetic structures, such as sharkskin denticles have found to reduce aerodynamic drag while improving heat transfer, due to turbulent mixing promoted near the wall [44–46]. Apart from swirlers, nozzles and turbine blades, these concepts are increasingly incorporated into mini/microchannel and conventional heat exchanger designs, forming a strongly active area of research [47–49].

Concerning the recent rapid development in the manufacturing industry, novel fabrication techniques such as AM, can deliver "manufacturable roughness" enabling the integration of a certain, predefined roughness profile, as a building parameter during the printing stage. Due to the freedom of design that is offered, customised on-demand designs of roughness elements can be introduced, whilst due to high spatial resolution provided by the AM machines, the shape of such elements is accurately and precisely controlled. Additionally, due to advantages related to the multiple component integration, internal microchannels can be built providing advanced cooling features for nozzles, turbine blades and swirlers, hence forming multifunctional components of advanced surface finish. These structures would be impossible to be built using conventional manufactured techniques. Through this advanced manufacturing method, the need and cost of post-processing activities can be

minimised, reducing further the lead-time and the production chain and cost of gas turbine parts. Additionally, in some cases, aerodynamic and heat transfer enhancements can also be achieved [30, 48, 50–52].

Consequently, surface roughness can be crucial for the overall efficiency of gas turbines, as it can affect them both positively and negatively. Currently, there is a critical gap between the measured surface roughness and the net drop in efficiency, as the formulas that are used for the design and evaluation of surface roughness performance are based on empirical observation and assumption such as the concept of *equivalent sand-grain roughness* (further discussed in Section 4.2.2). Hence, the development of predictive models and the acquisition of accurate data are major considerations for modelers and experimentalists, respectively [36]. Moreover, the interaction between surface roughness and combustion specific phenomena has generally been neglected [53]. Although the influence of surface roughness on boundary layer and heat transfer has been vastly investigated, only a limited number of studies exist on the impact of surface roughness on specific combustion phenomena [29, 45, 46, 53, 54]. As AM is increasingly employed for the design and fabrication of critical gas turbine components, the impact of surface roughness on combustion, the necessity for post-processing the components and the associated cost, should be investigated further from the scope of innovative surface finishes [29, 55].

Other than experimental studies, computational fluid dynamics (CFD) methods can be employed for the investigation of the influence of surface roughness on specific combustion phenomena and gas turbine performance. However, as described in the following Section, the incorporation of roughness elements in computational investigations as a design parameter constitutes a novel modelling challenge [56].

1.5 Computational fluid dynamics (CFD) as a design tool for AM parts

Computational fluid dynamics (CFD) codes are greatly concerned with investigating the surface roughness interaction with flow and heat transfer [57, 58]. There are several methodologies that can be utilised, from modelling the effect of surface roughness through Reynolds Averaged Navier-Stokes (RANS) [31, 42, 59–63] to solving the underlying system of non-linear equations over a wide range of time and length scales through computationally expensive Large Eddy Simulation (LES)

[64–66] or resolving all the scales prevailed in the flow via Direct Numerical Simulation (DNS) [67–69]. The exponential advancements in computational capabilities have enabled detailed investigation of the interaction of turbulent structures with realistic surface roughness, enabling a fundamental investigation of such phenomena. These studies require the 3D spatial representation of surface roughness structures, to accurately characterise their effect [48]. However, as the practicality of a CFD simulation relies on several factors including geometry, Reynolds number, and most importantly, computational resources, the fundamental numerical investigation of surface roughness is limited to small regions of the flow field and simplified computational domains [48, 56].

Hence, most CFD simulations concerning surface roughness effects focus on rectangular sections [31, 59, 60, 62] and microchannels [70–73] of simplified geometry and to lesser extent, to mini-channels [48, 73]. The integration of surface roughness to the full 3D geometry of burners without resulting in unrealistically expensive computational requirements have received currently little attention. However, with the rapid emergence of AM as a design tool, the incorporation of surface roughness as a design parameter in the predevelopment stage of a product has become a real possibility [56].

To facilitate the realisation of this exciting opportunity, low fidelity, computationally inexpensive methodologies that effectively capture the influence of surface roughness, require development. These numerical methods can be utilised to promote the synergy (or more controversially, competition) between CFD and AM, in the context of gas turbine development, enhancing concepts such as rapid prototyping and rapid experimental validation. The combination of numerical and experimental investigations has already been applied in biomedical sectors [74]. Additionally, the introduction of such product development methodologies may have a significant impact on cost reduction of critical gas turbine components, as the duration of product development stage can be decreased by rapid prototyping, whilst expensive testing campaign can be averted through the utilisation of efficient, but computationally inexpensive, CFD models.

Currently, computationally inexpensive methodologies for modelling the effect of surface roughness on flow parameters include the use of *wall functions*, which have

been previously applied in flow evolving complex geometries, including swirl flow [61]. However, the incorporation of *wall functions* to full 3D burner geometries for the evaluation of surface roughness on the burner-resulted aerodynamic flow field, to the best knowledge of the author, has not been previously undertaken.

1.6 Summary – Motivation for current study

Today, the global primary energy consumption is still heavily dominated by fossil fuels, whilst 60% of electricity globally is generated by hydrocarbon fuel-based combustion processes. The need for transitioning from a fossil fuel-based energy system to a renewable energy, equivalent one is essential. However, to commonly achieve resilient, affordable, and environmentally friendly energy, and thus satisfying the three pillars of Energy Trilemma, is a challenging task. For the transformation of the energy system, an increasingly appealing option is the utilisation of hydrogen (H_2) energy through the Power-to-Gas concept. However, there are significant challenges that must be addressed, not only with respect to transportation and storage, but also related to the efficient and ecologically friendly combustion of H_2-based energy via gas turbine (GT) technology.

The recent emergence of innovative manufacturing techniques, such as Additive Manufacturing (AM) may assist in addressing challenges related to H_2 penetration to the power generation sector, providing ultimately the appropriate infrastructure for highly fuel-flexible gas turbines operating safely, efficiently, affordably, reliably, and environmentally friendly on a variety of fuels ranging from 100% natural gas to 100%H_2. Apart from several unique advantages delivered by AM including, waste material minimisation, freedom of design, multiple component integration and multifactional structures of advanced mechanical properties, AM components can be built with pre-defined, “manufacturable” surface roughness. In this way, the need and cost for post-processing activities is minimised, whilst in some cases, advanced aerodynamic and heat transfer performance can additionally be achieved.

Surface roughness is an important parameter for gas turbine system, as it critically affects their operation. Although extensive research has been conducted with respect to the impact of surface roughness on aerodynamic and heat transfer performance, the impact of surface roughness on specific combustion phenomena has been neglected generally. With the introduction of AM and the opportunity to

predetermine the surface finish for critical gas turbine components, the need for the further appraisal of AM burners of specific surface roughness is amplified. Apart from experimental investigations, CFD-based numerical studies can be used to gain advanced knowledge on combustion performance and to serve as a powerful design tool for AM-fabricated gas turbine components. However, to be widely utilised by gas turbine OEMs, resulting in reduced product-development cost, low-fidelity CFD models should be sufficiently efficient to capture the effect of surface roughness with low computational requirements.

1.6.1 Aim, objectives, and structure of the PhD thesis

Being motivated by the aforementioned challenges and opportunities in the power generation industry, as well as a recent Cardiff/Renishaw patent application, the aim of the present PhD programme is:

To gain an understanding, through CFD and parametric empirical investigations, of the impact of surface roughness on aerodynamics, combustion performance and emissions of a generic AM combustor characteristic of practical burners utilising conventional methane, pure hydrogen and an energy balanced mixture of methane and hydrogen across a range of equivalence ratios.

Consequently, the objectives of the PhD programme are:

1. To design and undertake a computationally inexpensive, isothermal CFD study, appraising the predictive capability of the RANS Realizable k-epsilon (k-ε) model with respect to predicting dominant surface roughness effects.
2. To empirically observe, quantify and appraise the influence of surface roughness effects of two additively manufactured (AM) swirlers together with a conventionally manufactured one, on the lean premixed (LPM) combustion performance and burner characteristics (burner stability envelope, NO_x emissions, and exhaust thermocouple temperatures) of a generic swirl burner operating under conditions relevant to practical burner designs and utilising traditional (CH_4) fuel.
3. As for objective 2 above, but for low-carbon (CH_4/H_2) and zero-carbon (H_2) fuels.

The structure of the PhD thesis is presented as follows:

Chapter 1 introduces the scope of the present PhD thesis. Chapter 2 presents the relevant theoretical background and literature review concerning fundamental concepts and surface roughness effects on both reacting and non-reacting flows, as well as the opportunities and challenges of additive manufacturing (AM), with respect to gas turbine (GT) systems. In Chapter 3 and Chapter 4, the experimental and computational methods are described, respectively. Chapter 5 concerns the evaluation of the predictive capabilities of the computational scheme employed for capturing the effect of surface roughness. Chapter 6 and Chapter 7 regard the empirical investigation of the influence of surface roughness on burner characteristic for the conventional (CH_4) and alternative (CH_4/H_2 and H_2) fuels, respectively. Chapter 8 summarises the most important conclusions of this thesis, and points to future research to successfully assess the potential of this exciting technology applied in the energy sector.

Chapter 2. Theoretical Background & Literature review

2.1 Wall-bounded flows

In combustion systems such as gas turbines, the chemical reactions occur in a flowing medium. Consequently, the knowledge of the fluid mechanics is necessary to successfully comprehend the combustion phenomena [6].

2.1.1 Fundamental concepts

2.1.1.1 *Viscous flow*

Gas turbine applications are greatly concerned with wall-bounded, also known as internal, flows. Traditionally, the theoretical investigation of such flows was assuming the working fluid to be ideal, i.e., a fluid that is inviscid and incompressible. For the case of inviscid fluid, there are no tangential forces (shear stresses) acting between the fluid layers, and only normal (pressure) forces are applied. Although, the theoretical models for ideal fluids were producing satisfactory representation of real fluids in certain cases (i.e., when describing inviscid or almost inviscid fluid such as water), the models were collapsing when the drag of a body had to be calculated. In real fluids, tangential (friction) forces are also present, in addition to normal forces. Those tangential (or friction) forces of real fluids act not only in between the adjacent layers of the fluid but also between the fluid and its boundaries or walls. This property of the real fluids is called the *viscosity of the fluid.* The presence of shear stresses satisfies the *no-slip condition* of the fluid at the wall, meaning that the particles of the fluid stick to the wall, and thus, their velocity is zero. This is the main difference between real and ideal flows. Water and air are usually treated as ideal flow since their viscosity is very low, and hence, minimum shear stresses exist. However, the no-slip condition is valid even for low viscosity fluid and the violation of such condition often creates serious discrepancies in the laws of motion and the resulted aerodynamic drag [57].

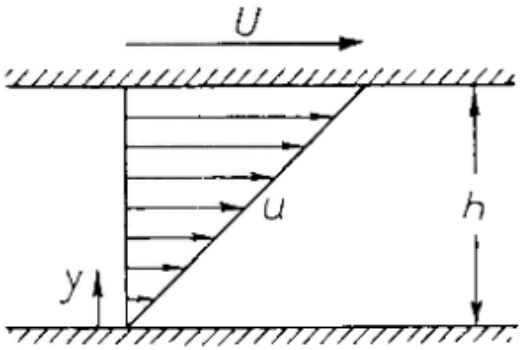

Figure 2.1.1.1-1 *Velocity distribution of a viscous fluid between two parallel flat walls (Couette flow). Source:* [57].

Assuming Couette flow of a Newtonian fluid (Figure 2.1.1.1-1), at constant pressure and temperature, where h is the distance of the parallel plates, the linear distribution of velocity can be plotted in the form of:

$$u(y) = \frac{y}{h}U \qquad (2.1)$$

A tangential force on the direction of motion must act to maintain the steady-state movement of the upper plate. This force, which is called shear stress (τ) is proportional to $\partial u/\partial y$. The constant of proportionality is a physical property of the fluid, strongly dependent on the temperature of the fluid and it is called *viscosity* (μ). Hence, the elementary law of friction or *Newton's law of friction* is defined as:

$$\tau = \mu \frac{\partial u}{\partial y} \qquad (2.2)$$

This equation is valid for Newtonian fluid, in which the relationship between shear stress and velocity gradient is linear. Following from Equation 2.2, the S.I. units for viscosity are:

$$[\mu] = \frac{\mathrm{kg}}{\mathrm{m\ s}} = \frac{\mathrm{N\ s}}{\mathrm{m}^2} = \mathrm{Pa\ s} \qquad (2.3)$$

Since viscosity is a variable in the momentum transport equation, it falls into the category of the transport properties of the fluid. It is a function of predominantly temperature and secondarily pressure; an increase in temperature increases the viscosity of gases whereas it decreases the viscosity of liquids. Dividing the viscosity of a fluid by its density, the *kinematic viscosity* (ν) is derived:

$$\nu = \frac{\mu}{\rho} \qquad [\nu] = \frac{\mathrm{m}^2}{\mathrm{s}} \qquad (2.4)$$

2.1.1.2 *Reynolds number & flow regimes*

Being able to evaluate if two flows with the same flow direction, passing from two geometrically similar bodies, are mechanically similar (their boundaries and streamline profiles are geometrically similar) is of paramount importance since it allows a comparison of their properties. This evaluation is quite complicated if there are two different fluids that are moving in different velocities and passing through different bodies of various sizes. As Hermann Schlichting [57] states, such flows are mechanically similar if *"the forces acting on volume elements situated in similar positions are in the same ratio to each other".* There are three different types of forces that generally act on a volume element, namely, friction forces (proportional to the viscosity μ), inertial forces (proportional to density ϱ) and pressure and volume forces (gravitational forces). Excluding the gravitational forces and taking into consideration Schlichting's statement, the ratio of friction forces to inertia forces must be equal for the similarly positioned volume elements of the two flows. For a flow moving in the x direction under steady-state condition, this ratio is equal to:

$$\frac{inertial\ force}{friction\ force} = \frac{\varrho u\, \partial u/\partial x}{\mu\, \partial^2 u/\, \partial y^2} = constant \qquad (2.5)$$

Considering that the velocity at any point of the flow is proportional to the free stream velocity U_∞, the velocity gradients $\partial u/\partial x$ and $\partial^2 u/\, \partial y^2$ are proportional to U_∞/d and U_∞/d^2 respectively. Thus, equation (2.6) can be written as:

$$\frac{\varrho u\, \partial u/\partial x}{\mu\, \partial^2 u/\, \partial y^2} \sim \frac{\varrho U_\infty^2/d}{\mu U_\infty/d^2} = \frac{\varrho U_\infty d}{\mu} = \frac{U_\infty d}{\nu} \qquad (2.6)$$

where *d* is the diameter of the body that the flow passes over. Therefore, if this ratio is equal for both flows, then the flows are regarded as mechanically similar. This ratio is first discovered by Reynolds (1883) and it is called *Reynolds number (Re)* [75].

Reynolds number similarity can also be derived by dimensionless analysis of the relevant physical quantities. In the case of flows passing a body, the corresponding important quantities are the free stream velocity U_∞, the diameter of the body d, the

density of the fluid ρ and the viscosity μ. To find the correct combination of quantities that yields a dimensionless number, the following equation is assumed:

$$V^{\alpha} d^{\beta} \rho^{\gamma} \mu^{\delta} = K^0 L^0 T^0 \quad (2.7)$$

where K, L and T represents force, length and time respectively. Replacing the characteristic quantities with their corresponding dimensions, Equation 2.7 can be also written:

$$V^{\alpha} d^{\beta} \rho^{\gamma} \mu^{\delta} = \left(\frac{L}{T}\right)^{a} L^{\beta} \left(\frac{KT^2}{L^4}\right)^{\gamma} \left(\frac{KT}{L^2}\right)^{\delta} = K^0 L^0 T^0 \quad (2.8)$$

Assigning to any of the four variables the value of 1, reduces the number of both equations and variables to three and thus, the system can be solved. The only possible solution of the latter yields $\beta = 1$, $\gamma = 1$ and $\delta = -1$, thus:

$$Re = \frac{\varrho U_{\infty} d}{\mu} \quad (2.9)$$

Dimensionless analysis can also be applied for the examination of force and velocity field of flows with geometrically similar boundaries and different Reynolds number. When two systems are mechanically similar, (geometrical similarity is satisfied and Reynolds number is equal for the two systems), the dimensionless velocity u/U_{∞} (where U_{∞} is the free stream velocity) and dimensionless stresses $p/(\rho U^2_{\infty})$, $\tau/(\rho U^2_{\infty})$ (where ρU^2_{∞} equals to twice the stagnation pressure), are only dependent on the dimensionless spatial coordinates x/d, y/d, z/d. However, if the Reynolds number of such systems is not matching and thus, they are solely geometrically similar, the dimensionless stresses and velocity are also a function of U_{∞}, d, ρ, μ. In principle, physical laws are independent of system of unit and thus, the above dimensionless quantities must be only dependent on a dimensionless combination of U_{∞}, d, ρ, μ. As it has been proved above, the Re is the only dimensionless combination. Therefore, in the case of geometrical similar systems of different Reynolds number, the dimensionless quantities of velocity and stresses are only a function of the dimensionless spatial coordinates and Reynolds number.

Excluding the gravitational forces, the total force exerted on a body, due to a fluid flow that passes over it, is equal to the summation of shear stresses and normal pressure forces. The dimensionless form of the total force F can be expressed as

$F/(d^2\rho U^2_\infty)$. Substituting d for S, which is the characteristic surface of the body, derives the dimensionless coefficient for total force, that is $F/(S\rho U^2_\infty)$. The latter coefficient corresponds to the integral of $p/(\rho U^2_\infty)$ and $\tau/(\rho U^2_\infty)$ over the surface S of the body. Following the previous consideration for geometrical similarity systems, the total force coefficient can be solely dependent on the dimensionless combination of U^2_∞, d, ρ, μ, which is the Reynolds number. Therefore, *lift* and *drag* coefficients C_L and C_D have been developed representing the component of the resulting force perpendicular and parallel to the free stream direction, respectively.

$$C_D = \frac{\mathrm{D}}{\frac{\rho}{2} U_\infty^2 S} \qquad (2.10) \qquad\qquad C_L = \frac{\mathrm{L}}{\frac{\rho}{2} U_\infty^2 S} \qquad (2.11)$$

These coefficients are solely a function of Reynolds number, when the flow is geometrically similar, enabling a much easier experimental evaluation of the performance of gas turbine components based on Reynolds number similarity. Thus, instead of replicating and matching all the characteristic quantities from two different experiments that would result in a huge volume of experimental data, a single variable, Reynolds number, can be used to compare the data.

Regarding internal flows, which are widely present in gas turbines, the dimensionless pipe friction factor (λ) is of great importance. Assuming a flow that passes through a circular pipe, where x – direction is the streamwise direction, the pressure gradient $\partial p/\partial x$ affects the dimensionless pipe friction factor (λ).

$$\lambda = -\frac{d}{\frac{\rho}{2} u_m^2} \frac{\partial p}{\partial x} \qquad (2.12)$$

In the above equation, d, ρ, u_m, corresponds to diameter of the pipe, density, and average velocity across the radius of the pipe, respectively. When the internal surface of the pipe is smooth, the pipe friction is a solely a function of Re. Schlichting plotted λ against Re for several measurements derived from various experiments and operating

conditions. As it is depicted in Figure 2.1.1.2-1, there is a critical point where the relationship of Re and pipe friction, λ, obviously changes.

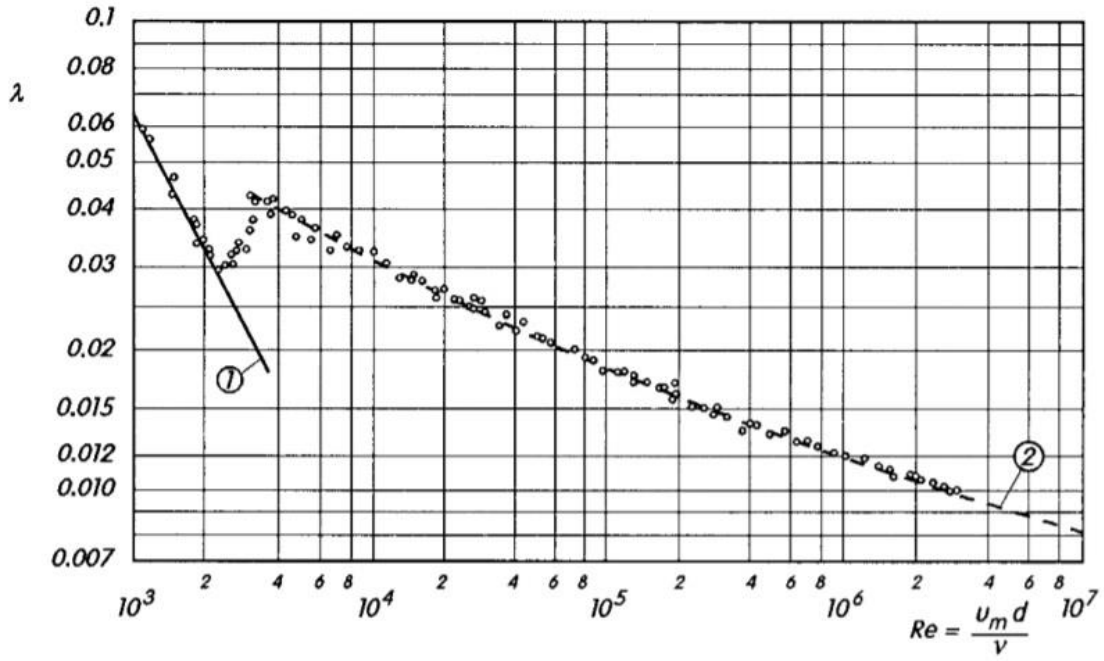

Figure 2.1.1.2-1 *Pipe friction factor for smooth pipes, dependent on the Reynolds. Source:* [57].

At this critical point *($Re_{crit} = 2300$)*, the pipe friction factor rises sharply as Re increases. A further increase in *Re* results in a deficit in λ but with a different slope compared to the previous decrease. This phenomenon is explained by Reynolds and his *coloured filament experiment.* In brief, it is stated that at Reynolds Number below the critical point, where the free stream velocity of the flow is low, a layered flow is generated called *laminar.* As velocity increases and Re exceeds the critical value, the flow starts transitioning and the flow profile changes significantly as it is represented by irregular transverse motions. This regime is called *turbulent* [57].

Turbulent flows are characterised by vortex structures of different size and frequency, which interact with each other. Larger structures, which are affected by the main flow, break up to smaller ones that rotate at higher frequency. Due to the aerodynamic nature of such flow, small and large structures interact with each other, exchanging energy and traveling through the flow, affecting the mixing length. Larger vortices with higher kinetic energy are described by the integral length scale, while the Taylor scale describes the size of the eddies in the inertial subrange, which contain the highest amount of kinetic energy. Additionally, the Kolmogorov microscale are the smallest turbulent vortices. The level of turbulence significantly affects the

performance of the gas turbine by influencing the stability of boundary and shear layers [58] .

Usually, the flow inside a gas turbine is of high velocity and low viscosity, as air, water or other low viscosity fluids are often used. This combination of high velocity and low viscosity results in high Reynolds number turbulent flow. Thus, the asymptotic behaviour of dimensionless coefficients, when Reynolds number tends to infinity, is of paramount importance for the flow field to be accurately described. Regarding the latter, the limiting case when $Re = \infty$, implies that the viscosity effects are vanished and therefore, the flow behaves as the ideal fluid flow case. With respect to the dimensionless pipe friction factor, as it is depicted in Figure 2.1.1.2-1, $\lambda \to 0$, when $Re \to \infty$. Additionally, based on Nikuradse's measurements [76], the velocity distribution in smooth pipes as a function of Reynolds number, seems to flatten as Reynolds number increases (Figure 2.1.1.2-2)

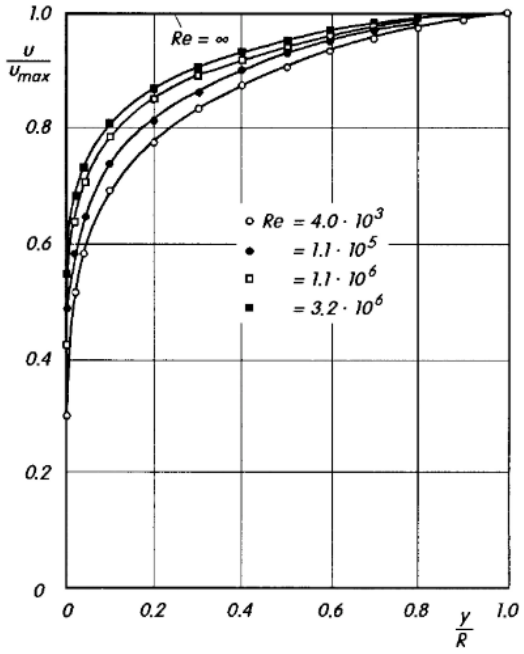

Figure 2.1.1.2-2 *Velocity distribution in a smooth pipe at different Reynolds Number. Source:* [76] *Graphic:* [57].

The limiting case of real flows should only marginally differ from the corresponding solution of inviscid flows, as real flows are concerned with very high but finite Reynolds numbers. In order for the viscosity effect to be included into the limiting cases and therefore, the no-slip condition to be satisfied at the wall, the *Boundary-layer Theory* has been developed and represent the traditional example of singular

perturbation method. Using Boundary-layer theory, the flow equations are modified to account for the viscosity of the fluid, while the inviscid limiting case represents the starting point of the solution.

2.1.2 Boundary Layer Theory

An extensive review of the boundary layer theory, including the overall structure and different characteristics of boundary layers, can be found in the *Boundary Layer Theory* textbook by Schlichting and Gersten [57]. This section aims to provide a summary of the fundamental relevant background information concerning the development and progression of laminar and most importantly, turbulent boundary layers on flat plates, airfoils and pipes, as well as their structure and important characteristic quantities.

As explained in the previous section, numerous technical applications are concerned with low viscosity working fluids of high velocity that results in high Reynolds numbers. Although the limiting solution $Re = \infty$ is a good approximation, the no-slip condition at the wall is violated, since inviscid flow is assumed and therefore the velocity at the wall is not zero but finite. However, by taking viscosity effects into consideration, the previously violated condition of no-slip is now satisfied, as velocity is transitioning from the limiting's solution finite value near the wall to the value of zero directly at the wall. This transition takes place in a thin layer near the wall, which Prandtl denoted as the *boundary layer* or *frictional layer*. Therefore, the concept of a boundary layer entails that the flow at high Reynolds number can be unequally split into two different regions; the bulk of the flow region where viscosity has a negligible effect and the flow is expressed through the inviscid limiting solution and the second, very thin region near the wall, where viscosity effects are dominant and must be taken into consideration. The former region is called the outer inviscid region, while the latter is named *boundary layer*, or *transitional layer* [77].

2.1.2.1 *Boundary layer over flat plate*

As laminar and turbulent flow can coexist inside the boundary layer, the following description of boundary layers commences discussing the characteristics of laminar boundary layers before it concludes with the fundamental characteristics of the turbulent boundary layer. In Figure 2.1.2.1-1, the velocity distribution and consequently, the formation of laminar boundary layer over a flat plate at zero

incidence angle, is shown. Although Figure 2.1.2.1-1 is out of scale, especially in the trailing edge of the plate, it presents a simplified and reasonable schematic of the overall shape of laminar boundary layers. As free stream velocity, U_∞ approaches perpendicularly and flows over the leading edge of the flat plate, the particles in the near wall (flat plate) region are slowing down due to the presence of the wall. This retardation in velocity becomes greater as the fluid flows along the length of the plate (x-axis), since increasingly more fluid particles are affected by the friction forces. Hence, it can be assumed that the thickness, δ, of the layer that encompasses the slow-moving particles increases monotonically with the length of the plate (x-axis). The concept of boundary layer thickness $\delta(x)$ has been artificially introduced and corresponds to the distance from the wall to the point where the velocity reaches a finite percentage, usually 99%, of the free stream velocity U_∞. Especially in laminar boundary layer the transition between boundary-layer flow and outer flow is a continuous event, and thus, a precise location cannot be estimated explicitly. However, the boundary layer thickness concept is widely used in practise due to its importance in boundary layer modelling [57].

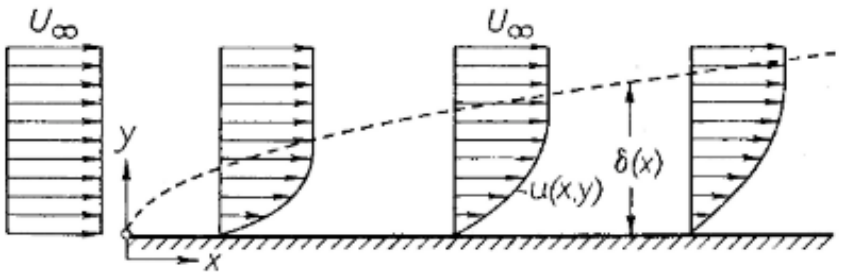

Figure 2.1.2.1-1 *Boundary layer at a flat plate at zero incidence (schematic). Source:* [57].

The thickness $\delta(x)$ of the laminar boundary layer over a flat plate can be easily estimated by assuming that at the corresponding location, the friction and inertial forces are in equilibrium. As shown in Section 2.1.1, the inertial force per unit volume is equal to $\rho u\, \partial u/\partial x$, whilst for a flat plate of length x and free stream velocity (U_∞), $\partial u/\partial x \sim U_\infty/x$. Similarly, the friction force per unit volume in laminar flows is $\partial \tau/\partial y = \mu \partial^2 u/\partial y$. Since the velocity gradient perpendicular to the wall $\partial u/\partial y$ is of the order of magnitude U_∞/δ, the friction force per unit volume $\partial \tau \partial y \sim \mu U_\infty/\delta$. Thus,

$$\mu \frac{U_\infty}{\delta^2} \sim \frac{\rho U_\infty^2}{x} \qquad (2.13)$$

or,

$$\delta \sim \sqrt{\frac{\mu x}{\rho U_\infty}} = \sqrt{\frac{\nu x}{U_\infty}} \qquad (2.14)$$

where ν is the kinematic viscosity. The exact solution for *boundary-layer thickness* $\delta_{99}(x)$ for laminar boundary layer at zero incident angle, provided by Blasius [78], is:

$$\delta_{99}(x) = 5\sqrt{\frac{\nu x}{U_\infty}} \qquad (2.15)$$

Assuming that the flat plate is of length *l*, the dimensionless boundary-layer thickness can be obtained as:

$$\frac{\delta_{99}(x)}{l} = \frac{5}{\sqrt{Re}}\sqrt{\frac{x}{l}} \qquad (2.16)$$

where, $Re = U_\infty l/\nu$. It is therefore observed that as Re increases, the boundary-layer thickness decreases and for $Re = \infty$, the boundary-layer vanishes. Additionally, from Equation 2.16, it results that $\delta_{99}(x) \propto \sqrt{x}$. Since boundary-layer thickness is a conceptual measure of boundary layer, to quantify and compare the characteristics of the latter, the *displacement thickness* δ_1 (also referred as δ^*) is often used. It is defined as:

$$\delta_1(x) = \int_{y=0}^{\infty} \left(1 - \frac{u(y)}{U_\infty}\right) dy \qquad (2.17)$$

where, U_∞ is the velocity at the outer edge of the boundary layer, or *free stream velocity*, at the position x. The *displacement thickness* represents how far the streamlines of the outer flow are displaced by the boundary layer. For a flat place at zero incidence angle, δ_1 can be obtained as:

$$\frac{\delta_1(x)}{l} = \frac{1.721}{\sqrt{Re}}\sqrt{\frac{x}{l}} \qquad (2.18)$$

Thus, the displacement thickness in laminar flow, for a flat plate at zero incidence angle is around 1/3 of the boundary-layer thickness. As the boundary layer is the fluid region affected by viscous forces, the *wall shear stress* (τ_w) can be estimated using *Newton's law of friction* (described in Section 2.1.1). As stated above, $\partial u/\partial y \sim U_\infty/\delta$,

and $\tau_w(x) = \mu \partial u/\partial y$, thus, $\tau_w(x)/\mu \sim U_\infty/\delta$. By rearranging with respect to $\tau_w(x)$ and substituting for δ, the following equation 2.19 is formed.

$$\tau_w(x) \sim \mu U_\infty \sqrt{\frac{\rho U_\infty}{\mu x}} = \sqrt{\frac{\mu \rho U_\infty^3}{x}} \qquad (2.19)$$

It is observed that the wall shear stress $\tau_w(x)$ is proportional to $U^{3/2}_\infty$ and inverse proportional to $\sqrt{x}$ and δ. Hence, wall shear stress is a function that monotonically increases with U, while it monotonically decreases with x and boundary-layer thickness (δ). Utilizing the factor of proportionality, which can be found in [57], and dividing by $U^2_\infty \rho/2$, the *skin-friction coefficient* is defined:

$$c_f = \frac{\tau_w(x)}{\frac{\rho}{2} U_\infty^2} = \frac{0.664}{\sqrt{Re}} \sqrt{\frac{x}{l}} \qquad (2.20)$$

Finally, by integrating $\tau_w(x)$ over the total length l of a plate with breadth b, the total friction drag D can be estimated:

$$D = b \int_0^l \tau_w(x) dx \qquad (2.21)$$

whereas, by using Equation 2.22, the *friction drag coefficient* defined in Section 2.1.1, can be rewritten as:

$$C_D = \frac{D}{\frac{\rho}{2} U_\infty^2 \cdot b \cdot l} = \frac{1.328}{\sqrt{Re}} \qquad (2.22)$$

As the flow progresses from the leading edge of the flat plate further downstream, the boundary layer gradually transitions from laminar to turbulent. Therefore, there is a certain length at which this transition occurs. This phenomenon becomes apparent by a significant increase in the boundary-layer thickness and in the wall shear stress. Although the transition region is of finite length, the assumption that the transition happens abruptly at a specific point, is often used for simplicity [57]. As shown in Figures 2.1.1-1 and 2.1.1-2, there is a critical Reynolds number at which this transition takes place. For flat plates at zero incident angle (Figure 2.1.2.1-1), the critical Reynolds number corresponds to $Re_{x\,crit} = 5 \cdot 10^5$. Therefore, the critical distance

(x_{crit}) at which the transition is expected to take place can be found by the critical Reynolds number $Re_{x\,crit}$, which is formed as:

$$Re_{x\,crit} = \left(\frac{U_\infty x}{\nu}\right)_{crit} \qquad (2.23)$$

The value of $Re_{x\,crit}$ is majorly influenced by the level of perturbations that the outer flow is subjected to. Thus, the critical value varies between $3x10^5$ to $3x10^6$ for strongly perturbed and smooth flows, respectively. The thickness of the turbulent boundary layer (δ) for a flat plate at zero incident angle increases along the length of the flat plate, as $\delta \sim x/\ln x$, for large x [57]. Conversely, for a given x, boundary-layer thickness slowly reduces with increasing Reynolds number, as $\delta/x \sim 1/\ln(Re)$. As for the laminar boundary layer case, the skin-friction coefficient and total drag coefficient can also be approximated for the turbulent boundary layers case:

$$c_f = 2\left[\frac{\kappa}{\ln Re_x} G(lnRe_x)\right]^2 \qquad (2.24)$$

$$c_D = 2\left[\frac{\kappa}{\ln Re} G(lnRe)\right]^2 \qquad (2.25)$$

The function $G(\ln Re_x)$ is only weakly depended on $\ln Re_x$ and has a limiting solution of 1 for $\ln Re_x \to \infty$. In the range of interest $10^5 < Re_x < 10^6$, $G \approx 1.5$. For the total drag coefficient, the G function is slightly modified as in this case, Re is formed with the total length of the plate. Concerning the quantity κ, it is universal fundamental constant, called the *von Karman constant* and it is equal to 0.41. From Equation 2.24 and 2.25, it can be concluded that both the skin-friction coefficient and the drag coefficient, are inverse proportional to $\ln^2(Re)$, and thus reducing with increasing Reynolds number. The analytical derivations resulting in the above scaling relationship can be found in [57].

As previously stated, the laminar boundary layer is defined as the region of the flow field that is affected by viscosity, while the flow outside the laminar boundary layer is regarded inviscid. In contrast, the turbulent boundary layer is defined as the region where the flow is turbulent and characterised by random fluctuating motion, whilst the outer flow (outside the turbulent boundary layer) is characterised by relatively reduced turbulence intensity. Since inside the turbulent boundary layer “apparent” friction forces occur [57], due to the turbulent flow, the latter is also called a frictional layer.

The most important characteristic of the frictional or turbulent boundary layer is that the effect of viscosity is restricted to a layer directly in contact to the wall, which is much thinner than the rest of the boundary layer. This small layer is called *viscous sublayer* or *viscous wall layer*. Hence, the turbulent boundary layer is formed by a double layered structure. The larger part is the turbulent or frictional boundary layer, where “apparent” friction forces are dominant, due to the turbulent motions, and it is unaffected by viscosity, whilst in the very thin viscous sublayer, the “true” friction forces prevail due to the dominant role of viscosity. In Figure 2.1.2.1-2, a schematic of the boundary layer development over a flat plate at zero incident angle is presented, showing the laminar, transition and turbulent boundary layer region, while indicating the various components constituting the turbulent boundary layer. The *viscous*, *buffer* and *overlap sublayers* are frequently referred in the literature as *inner layers* of the turbulent boundary layer, while and *turbulent (or friction) layer* is referred as *outer layer* of the turbulent boundary layer [57]. These concepts are further discussed in Chapter 4.

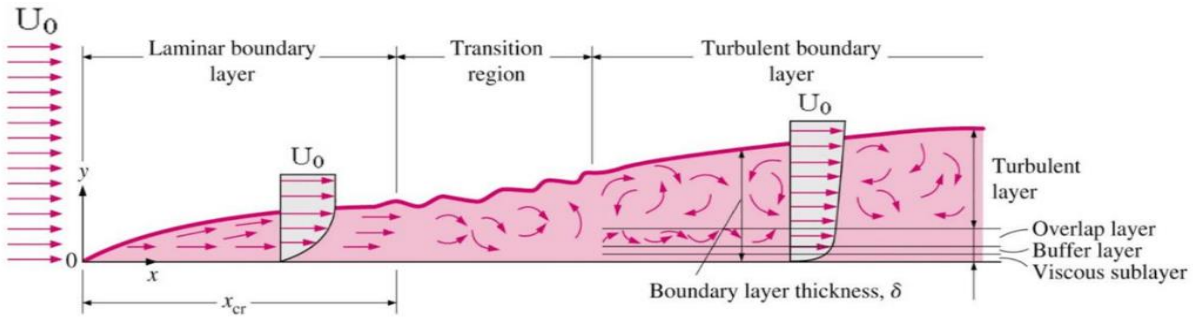

Figure 2.1.2.1-2 *Laminar-turbulent transition over a flat plate (schematic). Graphic:* [79].

Similar to the laminar boundary layer case, although the transition between viscous and turbulent layer is continuous, for practical reason, the concept of the viscous sublayer thickness is frequently used, where:

$$\frac{\delta_v}{x} = \frac{50}{Re_x\sqrt{\frac{c_f}{2}}} \qquad (2.26)$$

where, c_f is given by Equation 2.24. From Equation 2.26 it can be concluded that the thickness of the viscous sublayer increases slowly with the distance from the leading edge of the flat plate, as the relationship is of the form $\delta_v \sim \ln x$. On the contrary, at a given x, δ_v decreases with increasing Reynolds number as $\delta_v \sim \ln Re_x / Re_x$. Finally, the

ratio of viscous sublayer thickness to total boundary layer thickness can be estimated as:

$$\frac{\delta_v}{\delta} = 680\frac{\ln^2 Re_x}{Re_x} \qquad (2.27)$$

From Equation 2.27, it is shown that as Reynolds number increases the ratio of the frictional layer thickness to the viscous sublayer thickness increases too.

2.1.2.2 *Fully developed turbulent pipe flow*

Although the fully developed turbulent pipe flow (Figure 2.1.2.2-1) is not a typical case of boundary layer flow, similar to the turbulent boundary layer, it consists of a double layer structure with a turbulent core and a viscous sublayer. With increasing Reynolds number, the thickness of the viscous sublayer decreases, and consequently, the final limiting solution corresponds to a flow of homogeneous velocity. Thus, the fully developed turbulent pipe flow can be handled using methods of boundary layer theory.

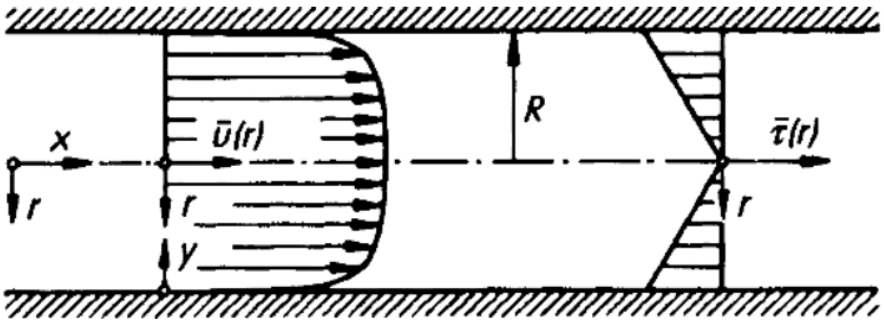

Figure 2.1.2.2-1 *Turbulent pipe flow. Distribution $\bar{u}(r)$ and $\bar{\tau}(r)$, u is the velocity component in the r direction. Source:* [57].

Already from Section 2.1.1, the concept of pipe friction factor has been presented. Utilising Equations 2.12 and 2.20, it can be shown that $c_f = \lambda/4$. Thus, the pipe friction factor can be also rewritten as:

$$\lambda = \frac{4\bar{\tau}_w}{\frac{\rho}{2}u_m^2} \qquad (2.28)$$

Additionally, as proven in [57], for the case of a smooth wall, the pipe friction factor can be related to Reynolds number as follows:

$$\lambda = 8\left[\frac{K}{\ln Re}G(lnRe)\right]^2 \qquad (2.29)$$

Again, $G(\ln Re)$ monotonically decreases with increasing Re, with $G(\ln Re) \to 1$, for $Re \to \infty$. In the range of interest $2300 < R < 10^7$, $G = 1.35$. Similar to the analysis conducted for the turbulent boundary layer over the flat plate of zero incident angle, the *viscous sublayer thickness* for the case of the fully developed turbulent pipe flow can be approximately determined as a function of Re, as described in [57]:

$$\frac{\delta_v}{d} = 122 \frac{lnRe}{ReG(\ln Re)} \qquad (2.30)$$

The above equation agrees with the previous statement that $\delta_v \to 0$, for $Re \to \infty$.

2.1.2.3 *Boundary layer on an airfoil*

The nature of boundary layer development over an airfoil is of particular interest in aerospace and gas turbine applications. In contrast to flat plates at zero incidence and circular pipes, where the limiting solution resulting to simple flows of constant pressure gradient, for airfoils, additional pressure forces occur owning to their geometry. In Figure 2.1.2.3-1, a schematic of the development of the boundary layer over an airfoil, in which the dimensions in the trailing edge are enlarged for clarity, is presented. From this Figure it is apparent that similar to case of the flat plate, near the leading edge of the airfoil the boundary layer remains laminar before developing to turbulent at a certain distance x_{crit}, where the transition takes place. However, for the case of the airfoil, the geometry of the body give rise to a pressure distribution on the outer flow, which is then imposed onto the boundary layer, so that at every x position, the pressure perpendicular to the wall is constant. Hence, for a given position, the pressure at the wall is equal to the pressure of the outer edge of the boundary layer. Inconsistencies in the pressure distribution between the wall and the outer edge pressure can arise from pressure gradient perpendicular to the main flow direction, due to strong streamline curvature. However, since the boundary layer is much thinner at high Reynolds number, than the curvature radius of the airfoil, this phenomenon does not occur [57]. Subsequently, as indicated in Figure 2.1.2.3-1, the pressure distribution is only a function of x.

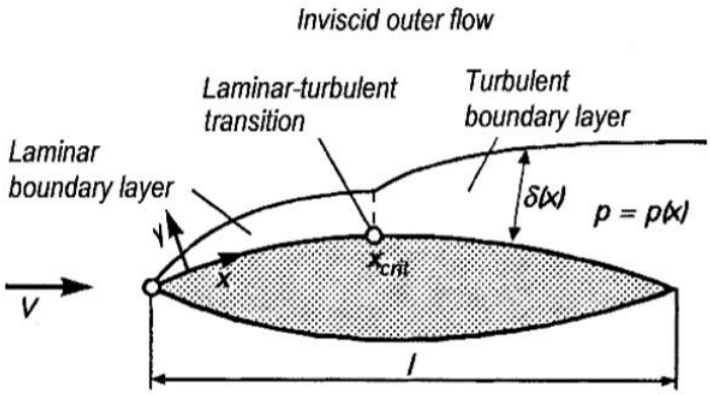

Figure 2.1.2.3-1 *Development of the boundary layer at an airfoil. Source:* [57].

The remarks discussed for the case of flat plate at zero incidence boundary layer are also valid in the airfoil case. Thus, at the laminar region, the wall shear stress decreases, whilst boundary-layer thickness increases as the fluid moves downstream. At the transition point a significant increase in wall shear stress and boundary-layer thickness occurs. As the turbulent boundary layer further develops downstream, the boundary-layer thickness continues to increase whilst the wall shear stress gradually reduces before it attains its constant fully developed value. The Reynolds number in this case is formed with the free stream velocity U_∞ and the characteristic length of the airfoil *l*, thus, the thickness of the boundary layer tends to zero for Re→∞. The critical length at which transition occurs is dictated by the imposed pressure distribution. A significant increase in pressure near the trailing edge of the airfoil can lead to the fundamental phenomenon of separation [57].

2.1.2.4 *Boundary layer separation*

Considering a symmetric flow past a circular bluff body, as shown in Figure 2.1.2.4-1 A, the flow field can be split into the inviscid outer flow and the friction boundary layer. At the leading edge of the blunt body (point D), the stagnation point is formed, and the pressure is high. The particles of the outer flow are accelerated from D to E and the pressure drops. Subsequently, for E to F, the particles are decelerated, and the pressure rises again. Thus, there is a constant conversion of pressure to kinetic energy (from D to E), which is then transformed back to pressure (from E to F). The particles restricted in the frictional layer also follow the same energy transformation pattern, as the same pressure distribution of the outer flow is also imposed to them. However, due to the augmented friction within the friction layer,

particles particularly close to the wall have lost excessive energy. Consequently, their kinetic energy is not enough to reach the high-pressure point F. Thus, these particles come to a momentarily stop before being pushed backwards into motion, dictated by the outer pressure distribution. This phenomenon results in a vortices-filled region at the back of the blunt body, as shown in Figure 2.1.2.4-1 B. This vortices-filled region is characterised by low pressure and is responsible for the production of *form drag* [57].

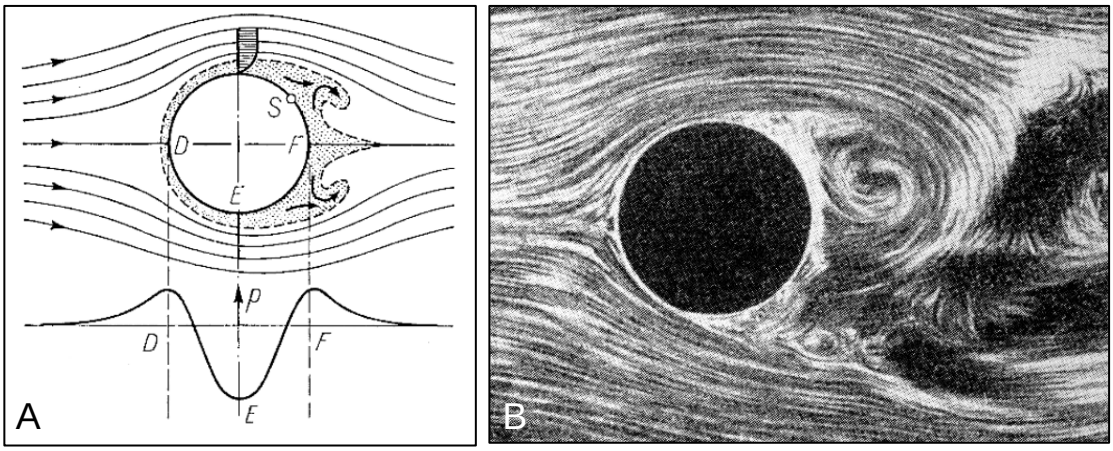

Figure 2.1.2.4-1 *(A) Separation of the boundary layer and vortex formation at a circular cylinder (schematic). S = separation point. Source:* [57]. *(B) Snapshot of the completely separated flow behind a circular cylinder. Source:* [57].

Consequently, the *total pressure drop* (or *total drag*) of a fluid past a body, is a function of both the *friction drag* and the *form drag* (also called *pressure drag*). While the former is associated with the energy loss due to friction, the latter is linked to the energy loss due to separation. Consequently, if flow separation is limited, due to streamlining or other separation prevention measures, most of the pressure drop stems from only the friction drag. Both the pressure distribution along the wall and the friction forces, govern the separation phenomenon, which is often appraised on the basis of the *drag coefficient* (C_D). The risk of separation is significantly greater for large pressure increase, especially at the trailing edge of blunt bodies. At the position when separation occurs (Figure 2.1.2.4-2), the velocity gradient perpendicular to the wall vanished, and thus, the wall shear stress is equal to zero ($\tau_w=0$). Due to the presence of backflow in the near wall vicinity, boundary layer thickens as its mass is displaced further away from the wall [57]. Therefore, the position of separation can only be estimated by exact calculation of Equation 2.31, as follows:

$$\tau_w = \mu \left(\frac{\partial u}{\partial y}\right)_w = 0 \qquad (separation) \qquad (2.31)$$

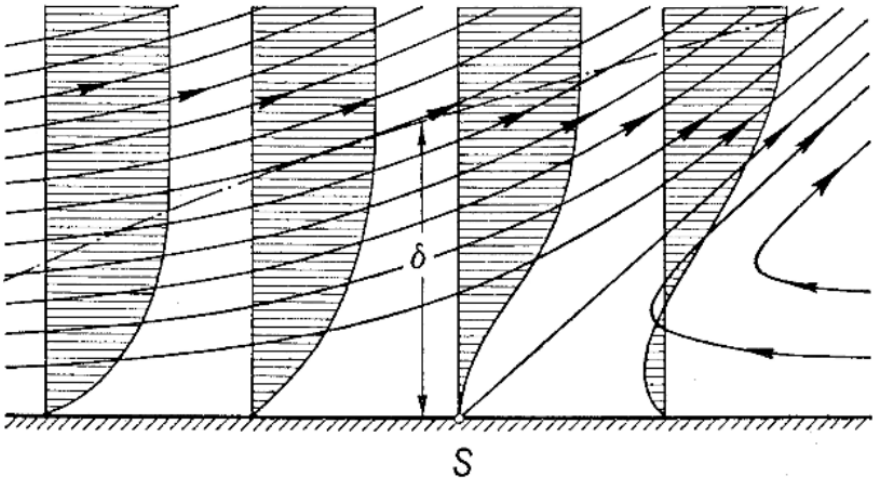

Figure 2.1.2.4-2 *Boundary-layer flow close to the separation point (schematic). S = separation point. Source:* [57].

This separation mechanism is also observed in channels of sudden expansion, also referred as diffusers, when the expansion ratio is large, and thus, the great increase in pressure forces the boundary layer to separate from both walls. Furthermore, the state of the boundary layer can affect separation and the resultant drag coefficient. For turbulent boundary layers, due to the enhanced turbulent mixing, the particles restrained in the inner boundary layer region are energized by the outer layer. Thus, the separation point is displaced further downstream, resulting in a narrower low-pressure area as the trailing edge of the body, which consequently reduces form drag [57].

Several strategies have been developed to prevent boundary layer separation and to reduce the resultant form drag, particularly by the automotive and aerospace sector. These strategies include shape optimisation and angle-of-attack modifications to enhance the streamline of the flow over automotives and airfoils, respectively [57]. Moreover, as it will be discussed in Section 2.2, surface roughness also plays a significant role in separation prevention and form drag reduction. Surface roughness can significantly influence separation performance by inducing earlier boundary layer transition (from laminar to turbulent), thus reducing form drag [80, 81]. Additionally, since it affects the resultant wall friction, several surface roughness biomimetic

structures have been developed to reduce the resultant wall shear stress and, thus, to enhance aerodynamic performance [53, 82, 83].

2.2 Surface roughness effects on fluid flows

Surface roughness is an important parameter in the field of fluid mechanics, as it often interacts with boundary layer, modifying its characteristics and influencing the performance of the process. An in-depth review of the effects and experimental findings of surface roughness effects on turbulent boundary layers is provided by Jiménez [84]. Surface roughness is usually determined by the manufacturing or post-processing stage of the component development chain. However, factors such as component degradation (wear), due to prolonged operation, and mechanisms including erosion and corrosion, as well as deposits from the combustion process, often result in non-uniform surface roughness patterns of increased length-scale [36, 55, 62]. When surface roughness height increases above a critical value (often referred to as *admissible roughness*), which is determined from the respective flow field, it interacts with boundary layer, influencing the momentum and heat transfer mechanisms [36]. It is therefore important to describe and categorise the effects of surface roughness on boundary layers. In general, these effects are associated with increased pressure drop, modified boundary layer transition and decreased form drag due to separation reduction. Additionally, other effects include the induction of secondary flows and the enhancement of heat transfer, which however, are out of the scope of the present study.

2.2.1 Pressure Drop

For internal flows, such as channel and pipe flows, the overall pressure drop is mainly due to the presence of surface roughness elements, which result in skin friction. Phenomenologically, the resultant skin friction is the cumulative effect of blockage and form drag induced by each individual roughness element, presuming that each one of them act as a bluff body [55]. However, the term *form drag* is mainly associated with the additional pressure drop due to flow separation at the trailing edge of larger bluff bodies [57]. Therefore, this concept is discussed in Section 2.2.2 along with flow separation. In this section, the discussion is restricted to wall-bounded flows where the total pressure drop stems only from the resultant skin friction.

The first studies of pressure drop in pipes and friction losses in boundary layer flows due to surface roughness, took place before 1900 with Darcy in 1857 studying the effect of various surface roughness on pipe flows [33] and Fanning in 1882 proposing relationships for pressure dop in water pipes, taking also into account the effect of surface roughness [34]. Their pioneering work forms the first investigations of surface roughness in relation to wall bounded turbulent flows and have led to a great volume of experimental, computational and theoretical work. Subsequently, Nikuradse's contributions is of great significance, since in his study [76], he investigated the impact of surface roughness on pressure drop, for a wide range of Reynolds numbers and pipe diameters. To do so, he covered the inner wall of the pipes with uniform sized sand-grain roughness. He found that although an increase in surface roughness had an insignificant influence on laminar flows, it significantly affected turbulent flows by increasing the skin friction, and thus, the resultant pressure drop. Additionally, he identified three distinct roughness regimes and determined their limits.

Nikuradse's categorisation was based on both the relative roughness, which was defined as the ratio of sand-grain roughness to pipe radius, and the Reynolds number. Thus, using what later was termed as *roughness Reynolds number (*$k^+_s = u^* \cdot k_{sand}/\nu$, where u^* is the friction velocity, k_{sand} is the sand-grain roughness and ν is the kinematic viscosity*)*, he identified the smooth or *hydraulically smooth*, the transition or *transitionally rough* and the rough or *fully rough*, regions. For the first region *(hydraulically smooth)*, he found that since the height of the roughness elements was much smaller than the thickness of the viscous sublayer, surface roughness had no effect on pressure drop and the latter was solely a function of Reynolds number. Thus, the resistance friction factor could be estimated as:

$$\lambda = \frac{64}{Re} \qquad (2.32)$$

For the second roughness regime *(transitionally rough)*, both Reynolds number and relative roughness contributed to the total pressure drop and the thickness of the viscous sublayer was of similar size to the average roughness projection. Individual roughness projections extended through the viscous sublayer and generated vortices that produced additional losses. As the Reynolds number increased further and the thickness of the viscous sublayer reduced, an additional number of projections

extended through the viscous sublayer, amplifying further the resistance. This resistance increased with increasing Reynolds number or roughness height. Finally, in the third regime *(fully rough)*, the vast majority of the roughness projection extended above the viscous sublayer. In this range the resistance due to surface roughness is independent of Reynolds number and only a function of roughness height. This is observed in the Moody's diagram by the flattening of the curves for high Reynolds number. The utilisation of *roughness Reynolds number* and Nikuradse's roughness regimes are still of paramount importance for the modelling of surface roughness, as it will be shown and discussed further in Chapter 4.

Similar to Nikuradse, Colebrook [85] studied experimentally the effect of surface roughness on the flow friction factor in pipes of various diameter, deriving the famous Colebrook equation (Equation 2.33). This equation was later used by Moody [86] to plot the friction factor *(λ)* against the Reynolds number, for several relative roughness values, generating the well-known *Moody diagram* (Figure 2.2.1-1). It is noted that Moody derived the relative roughness values using the *equivalent sand-grain roughness* (k_S), a concept first introduced by Schlichting aiming to provide a universal surface roughness categorisation. Since the idea of *equivalent sand-grain roughness* is extensively used for the modelling of surface roughness, it is further discussed in Section 4.2.2. As the estimate of the friction factor via Colebrook equation is based on an iterative procedure, non-iterative empirical correlations have also been suggested, such as the one proposed by Gregory and McEnery [87], providing good approximations. A new correlation for the calculation of the total frictional drag has also been introduced by Flack and Schultz for rough pipes, using data comprising several surface roughness types and roughness elements [88].

$$\frac{1}{\lambda} = -2\log\left(\frac{\frac{k_s}{D_h}}{3.7} + \frac{2.51}{Re \cdot \lambda}\right) \qquad (2.33)$$

where, λ is *Darcy's friction factor* and D_h is the hydraulic diameter of the pipe or the channel.

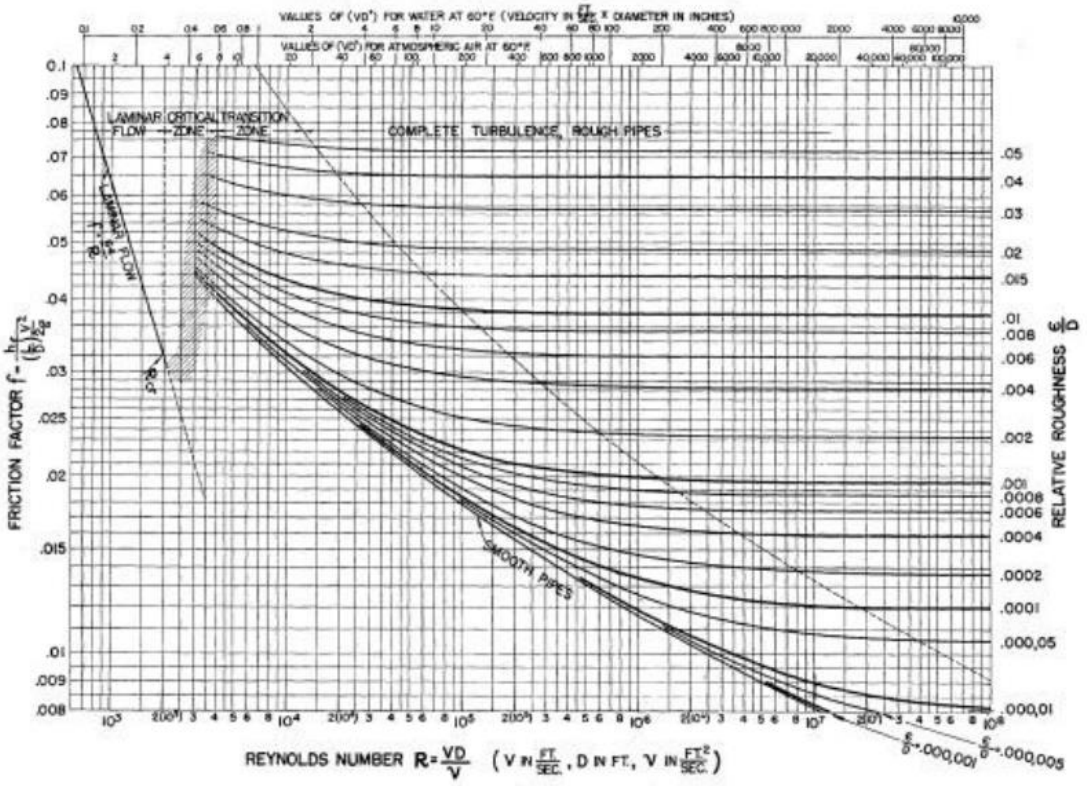

Figure 2.2.1-1 *Moody diagram. Source:* [86] *Graphic:* [89].

Several improvements of the Moody diagram have been proposed with a view to overcoming shortcomings related to the overestimation of friction factors, for some specific cases, and the limited relative roughness range covered [90]. Taylor et al. [91] produced a revised version of Moody diagram, extending the relative roughness range plotted, while providing correlation for micro and mini channels. Especially for these types of channels, of which the hydraulic diameter is less than 3 mm, the effect of surface roughness seems to be amplified, as reported by several researchers, especially under laminar flow conditions. This is attributed to the increased dissipation due to the roughness elements, which results in pressure drop [92]. Finally, Kandlikar et al. [93], argued that apart from increased skin-friction, surface roughness restricts the flow in microchannels, contributing additionally to pressure drop. He proposed the *constricted flow diameter* (D_{cf}) term, as defined in Equation 2.34, which could then be used in Reynolds number and friction factor calculation, replacing the previous hydraulic diameter (D_h).

$$D_{cf} = D_h - 2k \qquad (2.34)$$

2.2.2 Transition and separation

The influence of surface roughness on boundary layer transition and flow separation is of great significance as it vastly affects the performance of gas turbines, and particularly of turbine and compressor blades. Erosion, corrosion, and particle deposition, can significantly alter the surface finish of gas turbine blades, inducing instabilities and promote the boundary layer transition [94]. Additionally, they may result in flow separation, a phenomenon that contributed significantly to form drag, and thus, pressure drop, as discusses in Section 2.1.2.4.

For an attached boundary layer developing over a hydraulically smooth surface with a low level of free stream turbulence intensity (less than 0.5%), natural laminar-turbulent transition occurs [95]. This mode of transition is initiated by the *primary instability*, generated by exponentially growing 2D waves, denoted as Tollmien-Schlichting (TS) waves. A *secondary instability* follows, induced by 3D streamwise and spanwise vortices that leads to the final transition stage, referred as the *breakdown* stage. At this stage, the large-scale generated vortices cascade into smaller structures eventually resulting in fully turbulent flow [57]. However, if higher levels of free stream turbulence intensity (more than 1%) are present in the outer flow [96], or the roughness height is higher than the admissible roughness height [81], the transition from laminar to turbulent boundary layer occurs faster, since the *primary instability* is bypassed due to the increased level of disturbances that destabilise the flow earlier.

This mode of transition is frequently referred as *bypassed transition* or *surface roughness induced transition.* Bypassed transition comprises three main regions. The first region is the buffeted laminar boundary layer region, where amplified shear stress results to elongated streaks in the streamwise velocity fluctuations. This is followed by the intermittent, turbulent spot formation region, where the local perturbations destabilise the flow by generating instabilities that form turbulent spots. Subsequently, the last region is the fully turbulent boundary layer where the fully formed turbulent spots dominate the main turbulent region. Durbin [97], Jacobs [96] and Wei et al. [98, 99] extensively studied both numerically and empirically the processes related to this kind of transition, developing numerical models accounting for these mechanisms. The practical impact of surface roughness induced transition is the upstream displacement of the *transition point* onset. The level of this displacement relies on the rate of

disturbances, since higher levels of turbulence intensity or surface roughness impose larger disturbances resulting in faster transition.

Maintaining a constant roughness height, the transition point progresses upstream with increasing Reynolds number, reducing the aerodynamic performance of the turbine blade cascade [100]. Under such conditions, a further increase in roughness height, results in roughly double pressure drop. Conversely, under lower Reynolds number and low free stream turbulences conditions, surface roughness seems to have an advantageous effect on aerodynamic performance [101]. This phenomenon was also reported by Bons [36], reporting a “specific region” of roughness benefit at low Reynolds number, thus demonstrating the potential for enhanced aerodynamic and heat transfer performance via the use of specific surface roughness patterns.

These observations can be attributed to the combined effects of surface roughness, laminar-turbulent transition, and flow separation under adverse pressure gradients (APG). At relatively low Reynolds number when the flow is primarily laminar, surface roughness displaces the separation point further downstream by inducing earlier laminar-turbulent transition. This phenomenon reduces the separation at the trailing edge, and consequently, decreases the resultant form drag, improving the aerodynamic performance of the body. However, at fully turbulent boundary layers, the addition of roughness has the opposite effect, resulting in earlier separation and drop in aerodynamic performance, due to the augmented momentum deficit induced by the roughness elements [66].

Hence, the position of roughness in relation to the boundary layer progressions, significantly affects the aerodynamic performance, as shown by Song and Jeong [80], who empirically observed the transition of an attached boundary layer over a rough flat plate. At the early transition region, where the flow was still primarily laminar, surface roughness had no effect on momentum deficit. At the intermediate transition region, which initiated earlier for higher surface roughness, surface roughness had a positive impact, since it reduced Reynolds stresses and accelerated the breakdown of turbulent spots into small-scale turbulent eddies. Consequently, the turbulent energy and momentum deficit were reduced. However, at the late transition region, where the transitional boundary layer is similar to a fully turbulent one, the effect of surface

roughness had a negative impact, since it increased boundary layer mixing, and therefore, the thickness of the boundary layer and the momentum deficit, reducing the aerodynamic performance of the surface. As demonstrated both empirically and numerically by Durbin et al. [102], since the thickness and the momentum deficit of a turbulent boundary layer are increased due to surface roughness, the turbulent boundary layer is more susceptible to separation under adverse pressure gradient. Thus, the aerodynamic performance of the surface is further reduced.

2.3 Reactive flows

2.3.1 Fundamental concepts

This section outlines some fundamental combustion parameters related to the present study. The concepts of s*toichiometry* and *equivalence ratio (φ)* are described, together with their influence of *burning velocity* and *adiabatic flame temperature (AFT),* for which a short review is provided.

The combustion intensity between a fuel and an oxidiser relies on the relative concentration of the reactants. Combustion intensity is close to highest when the relative concentrations are chemically correct, and thus, the reactants are totally consumed in the reaction. Under this condition, stoichiometric combustion is achieved [6]. The fuel-oxidiser ratio (F/O) is used to measure the relative concentration of the reactants in a mixture, and it is defined as the ratio of the mass of the fuel to the mass of the oxidiser. If air is used as oxidiser, the fuel-air (F/A) ratio can also be defined. The reciprocal form of this ratio (air-fuel ratio or AFR) is often used too.

The fundamental combustion parameter referred as equivalence ratio (φ) demonstrates the divergence of mixture's concentration from stoichiometry and it is defined as [6]:

$$\varphi = \frac{(F/O)}{(F/O)_{st}}, \qquad (2.35)$$

The subscript "st" stands for stoichiometric condition. The numerator of the fraction designates the actual fuel-oxidiser ratio. Hence, for $\varphi < 1$, the actual oxidiser concentration in the mixture is higher than the stoichiometric one and corresponds to fuel-lean combustion, whilst, for $\varphi > 1$, the mixture corresponds to fuel-rich combustion. The practical importance of equivalence ratio is highlighted by its influence on *adiabatic flame temperature (AFT)* and *laminar burning velocity (LBV).*

Concerning the *adiabatic flame temperature (AFT),* it is one of the most important quantities in combustion studies as it determines the rate of chemical reactions. Although the flame temperature can be measured experimentally, the *adiabatic flame temperature* is usually calculated with respect to combustion conditions, as it represents the net energy released by the chemical reaction, assuming no heat losses. As in reality there are always heat losses due to radiation and convection heat transfer mechanisms, the adiabatic flame temperature is rarely achieved in practise [5]. As shown in the Figure 2.3.1-1, where the AFT, T_{ad}, is plotted as a function of equivalence ratio for a variety of fuel-air mixtures under STP conditions, it is slightly above stoichiometric conditions were AFT peaks, while it steadily decreases under leaner or richer conditions [6]. Equivalence ratio is the most influential parameter on AFT, though, other factors such as inlet temperature of the premix and pressure also affect AFT [5, 6, 103, 104].

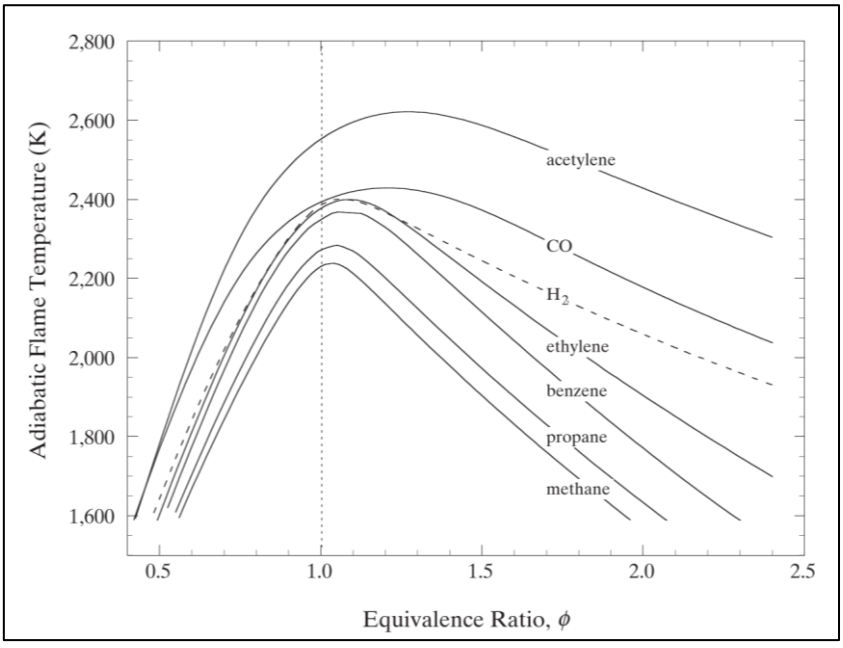

Figure 2.3.1-1 *Adiabatic flame temperature, T_{ad}, as a function of fuel equivalence ratio (φ), for a variety of fuel-air mixtures at STP. Source:* [6].

Regarding the *laminar burning velocity (LBV)*, also referred as *burning velocity* or *adiabatic laminar burning velocity*, it is a fundamental physiochemical property of the combustible mixture, defined as the velocity at which a plane flame front propagates in a direction normal to its surface through the adjoining unburnt gas [5, 105]. It is often referred to as *fundamental flame speed*, describing the laminar burning velocity under standard temperature and pressure conditions. LBV is a key

combustion parameter, of increased practical importance, as it is widely used for modelling and validation of turbulent and kinetic models, respectively, as well as for the characterization of the fundamental combustion properties and chemistry of fuels [106]. It is categorized as laminar or turbulent burning velocity, depending on the state of the wave that it propagates through a gaseous flammable mixture. Heat and mass transfer, as well as chemical kinetics of a flame can have an impact on the propagating plane combustion wave [5]. The equivalence ratio as well as fuel composition, significantly impact the laminar burning velocity, as shown in Figure 2.3.1-2, where the experimentally measured LBVs *(u_l)* for CH_4 and various CH_4/H_2 blends are plotted as a function of equivalence ratio (φ) [107]. It is also shown that the laminar burning velocity of the flame increases with increasing hydrogen concentration in the premixture.

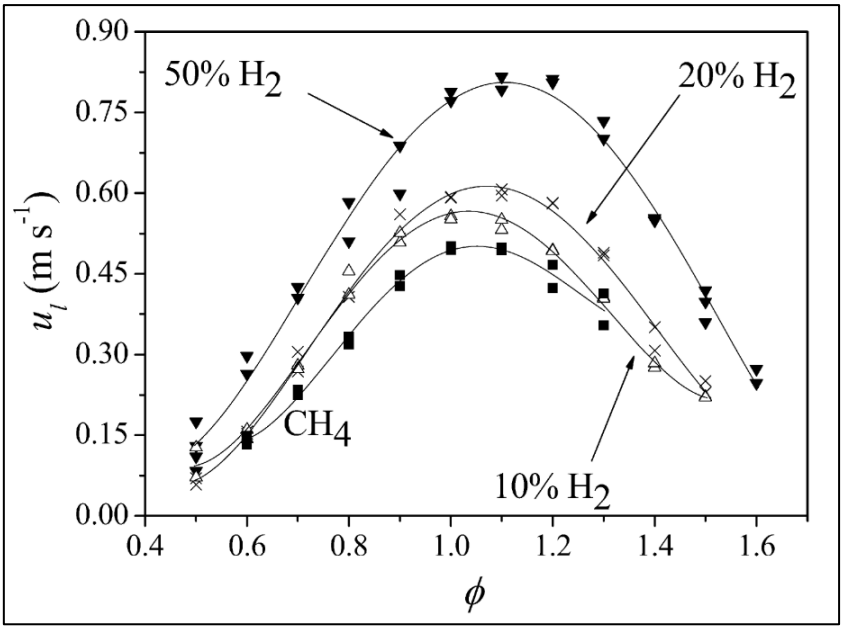

Figure 2.3.1-2 *Measured unstretched laminar burning velocity (LBV) against equivalence ratio for CH_4 and CH_4-H_2 blends. Source:* [107].

Additionally, the burning velocity of a flame is influenced by the temperature of the flame through radiation, by local gas properties such as diffusion and viscosity, as well as by the effect of pressure and inlet temperature as shown in Figure 2.3.1-3, where the LBV is plotted for several pressure and inlet temperature conditions of propane-air mixtures [108].

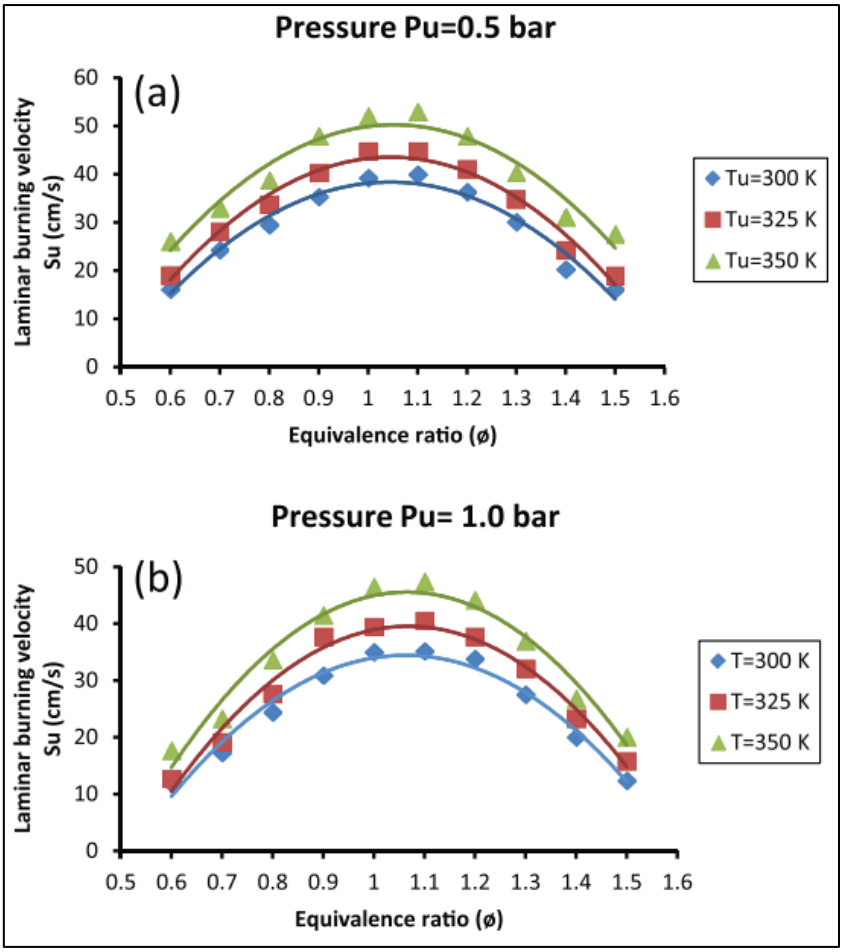

Figure 2.3.1-3 *Effect of equivalence ratio (φ) on laminar burning velocity at fixed pressure for different initial temperature. Source:* [108].

Apart from gas properties (e.g., diffusion, viscosity) determined by the flow composition and the flow parameters (pressure, temperature), the flow regime also significantly affects the burning velocity. Turbulence are well known for increasing substantially the burning rate of a flame, as indicated in following Figure 2.3.1-4, where average turbulent burning rates are plotted against equivalence ratio for CH_4 and CH_4/H_2 air mixtures at various compositions. Comparing those values to the analogous ones from Figure 2.3.1-2, it can be shown that turbulent burning rates have increased up to 5 times [107].

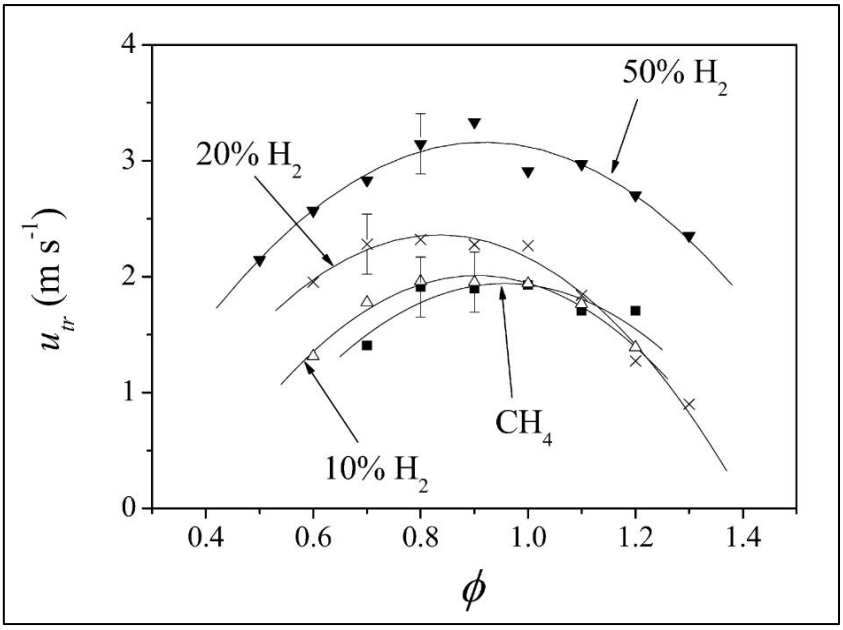

Figure 2.3.1-4 *Average turbulent burning rates plotted against equivalence ratio (φ) for various fuel compositions. Source:* [107].

A notable contributor to turbulent burning velocity modelling development was Damköhler, he was one of the first to attribute the increased burning rate to the effect of turbulence in wrinkling the flame front, which increase the specific flame area and thus the reactants were consuming faster [109]. For large-scale turbulence, he proposed:

$$S_T = S_L + u' \qquad (2.36)$$

where S_T is turbulent flame speed, S_L is the laminar burning velocity and u' is root-mean-squared (RMS) value of fluctuating velocity. Subsequently, several more theories based on the wrinkled-flame approach came up [5]. Schelkin's [110] approach resulted to the following relationship:

$$S_T = S_L \left[1 + B\left(\frac{u'}{S_L}\right)^2\right]^{0.5} \qquad (2.37)$$

where B is a constant of the order of unity. At high velocities, Equation 2.36 and Equation 2.37 become:

$$S_T = u' \qquad (2.38)$$

Ballal and Lefebvre [111] conducted experiments investigating the impact of turbulence intensity and turbulent length scale on burning velocity. They found out that

at low turbulence conditions ($u'<2S_L$) the flame maintains a smooth laminar appearance and burning rate is higher due to turbulences that wrinkle the flame, hence increasing the flame area, as first proposed by Damköhler [109]. The relationship of turbulent to laminar flame speed is given by:

$$\left(\frac{S_T}{S_L}\right)^2 = 1 + 0.03\left(\frac{u'L}{S_L\delta_L}\right)^2 \qquad (2.39)$$

where, L is the integral length scale, which represents the size of the eddies and δ_L is the flame thickness.

Finally, at very high turbulence levels, the flame is not wrinkled anymore as the turbulent eddies are extremely small. However, higher burning rates are achieved due to the very large total surface of flame area, which is created by the interaction of abundant small eddies and combustion products that are encircled within the latter. Under these conditions, the assumption of continuous, coherent flame surface is invalid, as the combustion zone is more relevant to a thick matrix of burned gases, infused by pockets of unburned eddies. In this case the ratio of turbulent to laminar flame speed is given by:

$$\frac{S_T}{S_L} = 0.5\frac{u'\delta_L}{S_L\eta} \qquad (2.40)$$

The propagation of the combustion wave is also impacted by the *flame stretch,* which is a measure of the change in flame area due to its motion and its underlying hydrodynamic stretch. Consequently, flame stretch is dependent upon the curvature of the flame surface and its hydrodynamic strain. Additionally, the thermo-diffusive properties of the mixture influence the *flame stretch* and consequently the burning velocity [6, 112]. The dimensionless parameter Lewis number defines the ratio of thermal to mass diffusivity and it is expressed as:

$$Le_i = \frac{\lambda_c}{C_p\rho_u D_{i,j}} = \frac{D_T}{D_{i,j}} \qquad (2.41)$$

where, λ represents thermal conductivity, ρ_u unburnt density of the mixture, C_p specific heat, whilst their combination results in D_T, which is the thermal diffusivity; $D_{i,j}$ represents the binary mass diffusion coefficient. Le is slightly affected on temperature as thermal and mass diffusivity present similar dependencies on temperature, whilst

both are inversely proportional to pressure, thus Le is independent of pressure [113]. Combustion intensity, stability and propagation, as well as extinction characteristics of stretched flames are significantly affected by imbalance of thermal and mass diffusivity of a mixture, known as, non-equidiffusivity $(Le \neq 1)$. When $Le < 1$, the flame is unconditionally unstable as mass diffusion is predominant. In contrast, for $Le > 1$, the flame stabilizes through diffusion. In general, the flame temperature and therefore, the burning velocity of stretched flame reduces with positive stretch if $Le > 1$. Equally, the opposite holds true for $Le < 1$, meaning that flame temperature and burning velocity increases with positive stretch [6].

2.3.2 Lean premixed (LPM) combustion

Lean premixed (LPM) combustion has gained a lot of attention in the last decades and has become the power generation standard in many applications, due to its superior performance compared to traditionally preferred diffusion combustion [114]. As modern energy legislations and polices required cleaner combustion systems of reduced pollutants, LPM became an attractive candidate to facilitate the transition to alternative fuels of cleaner and lower exhaust emissions. Burning under lean conditions involves several advantages such lower CO levels, high thermal efficiency, minimised knock (especially in reciprocating engines), reduced heat transfer and higher compression ratios [115]. However, the most significant characteristic of LPM is arguably the reduction of NO_x emissions. This is attributed to the excess air concentration in the mixture, which lower the flame temperature and thus the formation of NO_x emissions, since the latter is majorly dependent on temperature, as known from the Zeldovich mechanisms [5, 116]. However, LPM combustion is also associated with challenges, especially regarding flame stability. Due to operating near the lean blow-off (LBO) (also referred as lean blow-out) limit, the flame is prone to several instabilities, such as unsteady flame stabilization or thermoacoustic instability, whilst there is even the risk for complete blow-off [117].

To overcome the challenges associated with LPM combustion, while reducing further the carbon footprint of the power generation sector and the consumption of non-renewable fuels, the use of Hydrogen (H_2) as enrichment for hydrocarbon fuels is very much promoted. Hydrogen is the most abundant element on earth, though only 1% exists in the form of molecular H_2. Currently the majority of commercially available H_2 is produced through steam methane reforming from natural gas, however, there is

a variety of widely available production techniques, which can operate through renewable electricity, with the popular one to be the process of electrolysis [13, 20]. Hydrogen enrichment significantly improves the stability of LPM combustion of methane (CH_4), which is characterised by low ignitability and low flame speed [118], as it increases the total chemical reaction rate [119] and the burning velocity of the flame [107, 120]. Due to the high diffusivity, laminar burning velocity and combustibility of hydrogen, the lean flammability limit of the mixture is extended, enabling stable operation, and shifting the LBO limit towards leaner equivalence ratios [116, 117, 121–123]. Thus, the increase in flame temperature is offset by burning under leaner equivalence ratio, whilst the NO_x and CO emissions are significantly reduced. Additionally, due to the thermo-diffusive properties of hydrogen $(Le \approx 0.3)$ [124], its addition to CH_4 under lean conditions, results in increased stretched flame speed, which increases with increased stretch rate. As the resultant Le is less than 1, CH_4 reactivity and oxidation is promoted due to the dominant mass diffusivity of the fuel towards the oxidiser, improving the stability performance [107, 124].

Several experimental studies have been conducted concerning H_2 enrichment on CH_4-air flames, focusing on swirl stability, flame structure and emissions [116, 117, 122, 123, 125–127], as well as fundamental flame measurements [107, 120, 128]. Those studies were carried out with volumetric H_2 addition up to 50%. Less available studies exist for higher H_2 concentration mixtures, up to 80%$_{vol}$ H_2 [115, 124, 129, 130] and 100%H_2 [131–133]. The significance of those three regimes (50%, 80% and 100%) has been pointed out by Tang et al. [20], who utilised data provided by Hu et al. [133] and Di Sarli et al. [134], to show that the rate of increase in laminar burning velocity of CH_4/H_2-air flames can generally be categorised into those three regimes. As shown in Figure 2.3.2-1, the first regime ($X_{H2} \leq \approx 50\%_{vol}$) is characterised by gradually slow increase of LBV, indicating that the oxidation process is dominated by the CH_4. Increasing the H_2 concentration in the mixture and approaching the second regime ($\approx 50\%_{vol} \leq X_{H2} \leq \approx 80\%_{vol}$), the rate of increase in LBV with increasing H_2 concentrations is higher, whereas, in the third regime ($\approx 80\%_{vol} \leq X_{H2}$), small reduction in CH_4 concentration have a significant impact on LBV of mixture [20]. The increase in LBV with H_2 addition is linked to the promoted chemical kinetics due to the augmented concentrations of H, O, and OH radicals in the reaction zone [119].

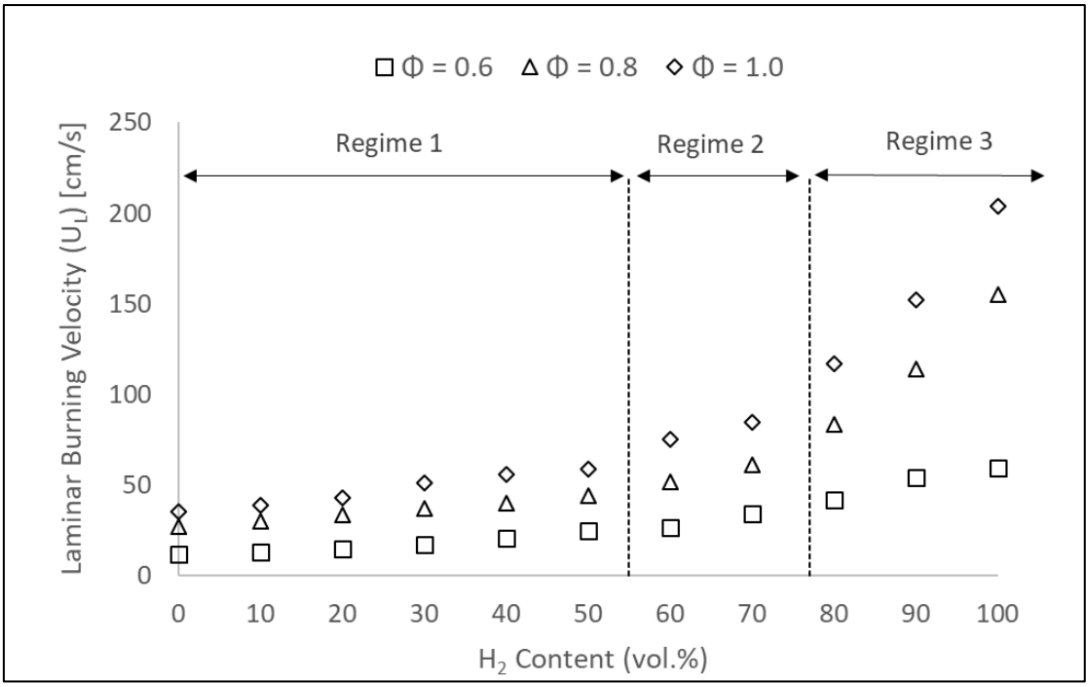

Figure 2.3.2-1 *Laminar Burning Velocity of H_2/CH_4-air mixtures as function of H_2 addition (vol.%) φ=0.6, 0.8, 1.0; Data source:* [133]*, Figure source:* [135].

2.3.3 Emissions

Several polluting emissions are produced as by-product during gas turbine applications. Such pollutants include nitrogen oxides, sulfur oxides, soot, and carbon dioxide (CO_2) as well as unburnt intermediate species, including carbon monoxide (CO), formaldehyde and unburnt hydrocarbons [6].

Oxides of nitrogen include nitric oxide (NO) and nitrogen dioxide (NO_2), which are generally referred to as NO_x, and nitrous oxide (N_2O). The nitrogen atom required for their formation is derived either from the molecular nitrogen in the oxidising gas, which is usually air, or from the fuel composition. [6] NO_x emissions are of particular interest in the present study, as they directly contribute to atmospheric pollution, such as photochemical smog, whilst enhancing the greenhouse effect by ozone depletion [136]. Additionally, gas turbine performance is often characterised with respect to NO_x since modern energy policies and legislations require minimization of polluting emissions and compliance with the respective regulations. Most of nitric oxide (NO) produced in combustion afterwards oxidises to nitrogen dioxide (NO_2). For this reason, NO and NO_2 are presented as total and referred to as NO_x. NO emissions can be formed by four different mechanisms, namely, *thermal NO, nitrous oxide mechanism*, *prompt NO* and *fuel NO* [5].

Concerning the *thermal NO*, it is formed by the endothermic oxidation of atmospheric nitrogen in high-temperature flame areas and in the post flame gases and it is very much dependent on temperature. NO formation increases exponentially with temperature, whilst it undergoes a steep reduction as temperatures reduce, especially at normal combustors residence times of 5 ms. Its formation is generally regarded negligible below 1,800 K. Additionally, NO is weakly dependent on the availability of O_2. The dependency on temperature, oxygen and residence time constitutes that NO is therefore affected by equivalence ratio as indicated in Figure 2.3.3-1 A. Although in fuel-rich side of stoichiometry the flame temperature is higher, the oxygen is preferably consumed by the fuel, and thus, NO is slightly lower compared to fuel-lean conditions. The influence of inlet air temperature on NO is also expressed in Figure 2.3.3-1 B [5, 6]. The thermal NO mechanism consists of three reactions known as the Zeldovich mechanism:

$$N_2 + O \rightarrow NO + N \qquad (N1)$$

$$O_2 + N \rightarrow NO + O \qquad (N2)$$

$$N + OH \rightarrow NO + H \qquad (N3)$$

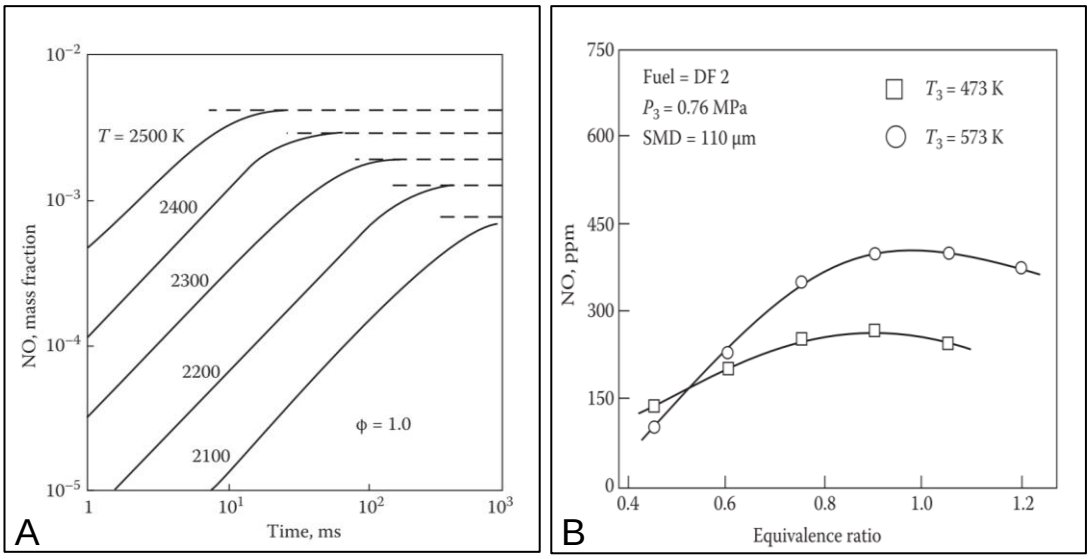

Figure 2.3.3-1 *(A) NO_x formation as a function of time and temperature for P = 1 MPa, Source:* [5]*. (B) Influence of inlet air temperature on NO_x formation, Source:* [5].

Regarding the *prompt NO* mechanism, it is related to the NO presence very early in the flame region. According to Nicol et al. [137], the initiating reaction is:

$$N_2 + CH = HCN + N \qquad (N4)$$

Under LPM combustion the HCN oxidises to NO through the sequence of HCN → CN → NCO → NO. Thus, the formation of prompt NO is dependent on the formation of HCN molecules and N atoms. Similarly, the f*uel NO* mechanism, which is related to the fuel-bound nitrogen usually found in aromatics or polyaromatics, is also dependent on the reaction sequence of HCN, since the nitrogen-based species that evolve through fuel-bond nitrogen oxidation are majorly HCN and to a lesser extend NH_3. [6]. For LPM combustion of H_2 and CH_4, fuel NO emissions are expected to be minimal. Finally, NO formation through the *nitrous oxide (N_2O)* pathway follows the sequence:

$$N_2 + O + M \rightarrow N_2O + M \qquad (N5)$$

$$N_2O + O \rightarrow NO + NO \qquad (N5)$$

During LPM operation close to lean blow-off (LBO) limit with low flame temperatures (lower than 1,800K), the production of thermal NO is limited, thus prompt and N_2O pathways become the dominant NO contributors [5, 6, 137].

The influence of pressure in the production of oxides of nitrogen (NO_x) is of paramount importance as higher working pressures are very much attractive for meeting the energy demand under lower fuel consumption. Moreover, as testing under elevated pressures incurs increased cost, while posing some remarkable challenges, it is preferable to conduct the relevant testing under atmospheric conditions and to extrapolate the results obtained to higher pressure levels. Therefore, the scale of NO_x with pressure is of increased significance. However, the experimental results obtained by several combustor types are contradicting, varying from no effect conclusions to quite major increase in NO_x with pressure [5]. For conventional combustion the general scaling law of NO_x with pressure is of the form of $NO_x \propto P^n$, where $0.5 < n < 0.8$. For natural gas, specifically, Maughan et al. [138] found that *n* increases with higher exhaust gas temperature. This was attributed to the fact that at low temperatures, the NO formation is dominated by the N_2O and prompt mechanism, which are independent of pressure. As temperature rises, thermal NO_x pathway becomes the dominant mechanism. Since the latter exhibits a square-root dependency on pressure, overall

NO_x formation becomes pressure dependent at high temperatures. As shown in Figure 3.2.2-3, for methane-air flames, NO_x is independent of pressure below $\varphi \approx 0.7$. However, an increase in flame temperature triggered by an increase in equivalence ratio leads the majority of NO_x emissions to be produced through the thermal pathway and therefore, to an increased dependency on the pressure factor. Conversely, recent modeling [139, 140] and experimental [141] studies conclude on significant pressure dependency on prompt NO_x, even under fuel-lean conditions.

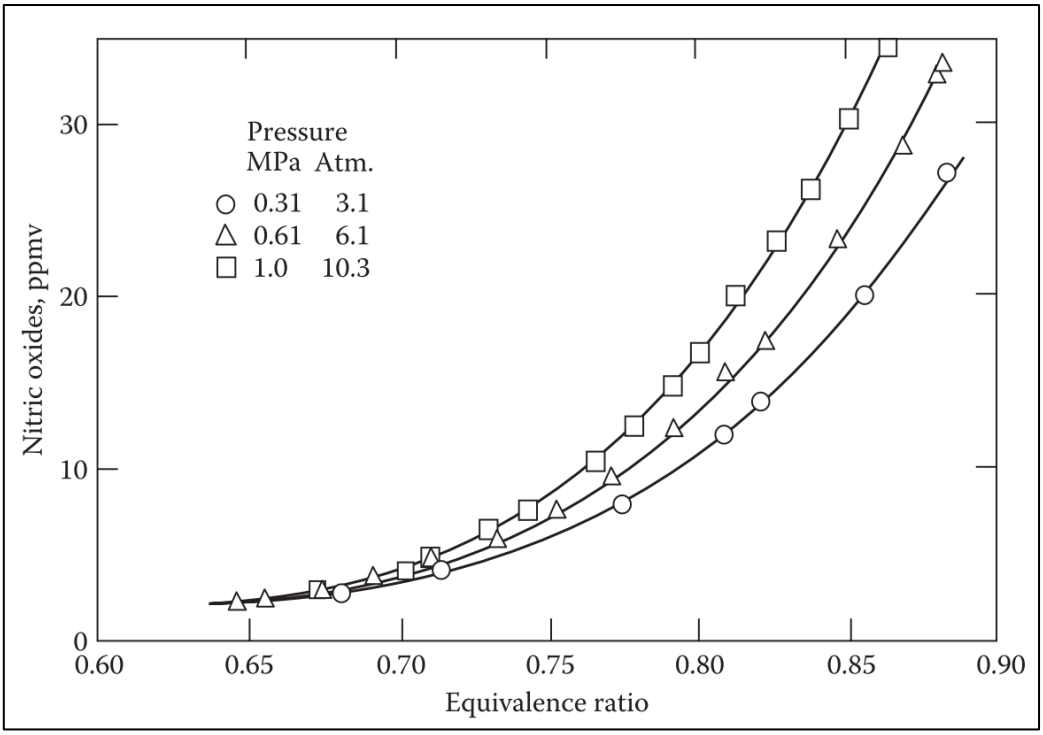

Figure 2.3.3-2 *Data illustrating the effect of pressure on NO_x formation. Source:* [5].

Several experimental and numerical studies portrayed the effect of H_2 addition on NO_x formation. The experimental comparison of several burner combusting CH_4/H_2-air mixtures showed that the burner type has a significant effect on resultant NO_x in relation to H_2 addition [127]. Coppens at al. [142, 143], found that at very lean equivalence ratios H_2 addition has no effect on NO_x, whilst under fuel-rich conditions NO_x tend to reduce due to the reduction in prompt NO_x species. Hu et al. [133] also reported this trend when numerically studied H_2-air mixtures. Lantz et al. [129], showed that under constant AFT, H_2 enrichment in natural gas results in ≈50% more NO_x emissions, compared to baseline natural gas results, due to local flame hot-spots and reduced mixing in reaction zone. This was also supported by numerical analysis [144], where DNS simulation of H_2 enriched CH_4 (up to 30%) at $\varphi = 0.52$ was

undertaken. They found that NO_x was increased by 50% per unit heat release due to higher temperatures. While flame stability was enhanced overall, Griebel et al. [145] showed that H_2 addition to CH_4 (up to 20%$_{vol}$) can potentially reduce NO emissions by 35% due to the shifting of LBO towards leaner equivalence ratios. For constant $\varphi < 0.4$, H_2 enrichment had negligible influence on NO, while for higher equivalence ratios the additional OH available due to H_2, promoted NO production. These finding are consistent with the work of Tuncer at al. [122] and de Persis [141]. Wang et al. [146] numerically supported this observation and found very little effect on NO_x with H_2 addition (up to 40%), whilst Zahedi and Yousefi [147] numerically showed that NO tends to increase with higher H_2 concentrations at elevated pressures. Finally, Guo et al. [148], numerically simulated CH_4/H_2-air combustion in a counterflow burner, with H_2 concentration up to 60%, under atmospheric conditions and φ ranging from 0.4 to 0.7. They reported that NO increase with H_2 addition when φ was kept constant.

2.3.4 Swirl flame stability

Flames can be stabilised within a flow field through the utilisation of several stability mechanisms including bluff bodies, diffusers that generate sudden flow expansion, piloted flames, opposed jets and swirling flows [5]. In this way, the balance between the flame speed and the flow velocity is maintained and the flame remains virtually stable. The flame stabilisation approach that is employed in the present study encompasses the concepts of recessed bluff body, sudden expansion, and most dominantly swirling flow. Swirl-stabilised combustion is widely used in a variety of burners, including power generation burners, refinery and process burners, as well as in numerous applications related to internal combustion engines and gas turbine combustors [149]. Specifically with respect to gas turbines applications, most gas turbines systems utilise swirl injectors that produce central toroidal recirculation zones (CRZs) to stabilise the flame [150]. This characteristic feature of swirling flow is of paramount importance, as through the formation of a CRZ, both heat and chemically active species are recirculated to the root of the flame. Therefore, the flame is anchored at a low velocity region where flow and the turbulent flame velocity can be balanced. Through the formation of a central toroidal recirculation zone, flame stability is significantly enhanced [149]. A schematic diagram of processing leading to CRZ formation is presented in Figure 2.3.4-1.

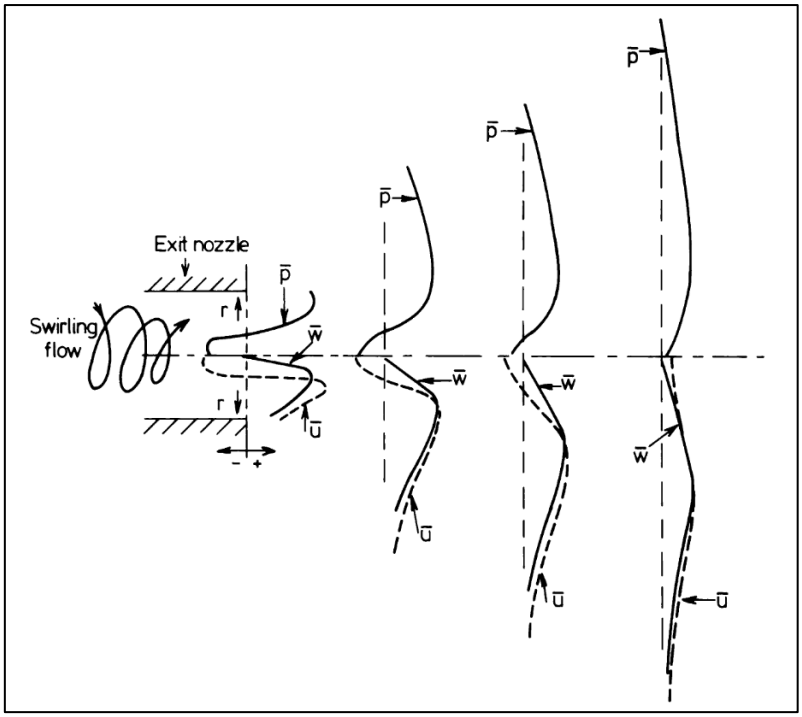

Figure 2.3.4-1 *Schematic diagram of processing leading to CRZ formation. Source:* [149].

The combination of axial $(\bar{u})$ and tangential $(\bar{w})$ velocities in swirling flow generates a centrifugal pressure gradient and an adverse pressure gradient near the centre axis of symmetry. As the swirl flow exits the nozzle and expands into the combustion chamber, the decayed profiles of axial and tangential velocities cause a reduction in the radial distribution of centrifugal pressure gradient as the flow travels downstream. Consequently, this generates a negative axial pressure gradient, which induces reverse flow and the formation of CRZ. Hence, the latter is very much dependent on the decay of swirl velocity as the flow expands at the exit of the nozzle [149]. Apart from the formation of CRZ, another important advantage of the swirl-stabilised combustion is the increased rate of entrainment of fuel and ambient air which mixing faster close to the edge of the nozzle and on the boundaries of CRZ. Additionally, as the flame is aerodynamically anchored, flame impingement on the burner is minimised, allowing extended burner lifetime of reduced maintenance [151].

The most widely used factor that is used to characterise the intensity of the swirling flow is the swirl number (S_N). It is defined as the ratio of the axial flux of the tangential momentum to the product of the axial momentum flux and the characteristic radius, as presented in Equation 2.42.

$$S_N = \frac{\int_0^R \bar{u}\bar{w}r^2 dr}{R \times \int_0^R \bar{u}^2 r dr} \qquad (2.42)$$

where $(\bar{u})$ is the axial and $(\bar{w})$ is the tangential (or azimuthal) velocity and R is the characteristic radius [150, 151]. Experimental testing has proved that S_N is a major similarity criterion in swirling flows, which is always considered for burner development. For instance, CRZ is only generated for $S_N > 0.6$. The swirl number should be calculated based on experimental measurements of the velocity and pressure field, however, as this is not always possible, it can also be calculated from the geometry of most swirlers, assuming that the two velocity components are uniform and that the vanes are very thin. Thus, S_N can be approximated by:

$$S_N = \frac{2}{3}\tan\theta \qquad (2.43)$$

where, θ is the swirler vane angle [150].

The resultant flow field of a common gas turbine swirl injector is characterised by three main structures, namely, vortex breakdown-induced CRZ downstream of the nozzle exit, precessing vortex layer around the CRZ and shear layers forming from the outer to the inner annulus [150], as presented in Figure 2.3.4-2. The vortex breakdown region, which is usually developed downstream of the nozzle exit, is the most important phenomenon as it anchors the flame. It is characterised by internal stagnation points and reversed flow. The axisymmetric bubble is the most common vortex breakdown structure in LPM gas turbine combustion; however, other structures might also exist such as spiral and double helix ones [150, 152]. Concerning the precessing vortex core (PVC), it is a 3D unsteady vortex asymmetric flow structure that often manifests itself in turbulent swirl combustion. The PVC is formed when a central vortex core starts to rotate around the axis of symmetry at a constant frequency. This frequency is dependent on the swirl number and combustion chamber geometry, while it scales linearly with flowrate. Although PVC might enhance combustion efficiency by improving mixing and turbulence intensity, it can also result in undesirable phenomena such as flame flashback or blow-off and due possible resonant coupling with low-frequency acoustic oscillations [150]. Finally, as the flow expands downstream of the nozzle exit, strong shear layers are generated due to the velocity gradient between the fast-moving region and the ambient flow field. Thus, in-

between the outwards propagating and the reverse flow, shear layers are generated offering enhanced mixing between fuel and oxidiser. Moreover, the sudden expansion of the flow generates low pressure outer recirculation zones (ORZ) that also act as flame stabilisers [150].

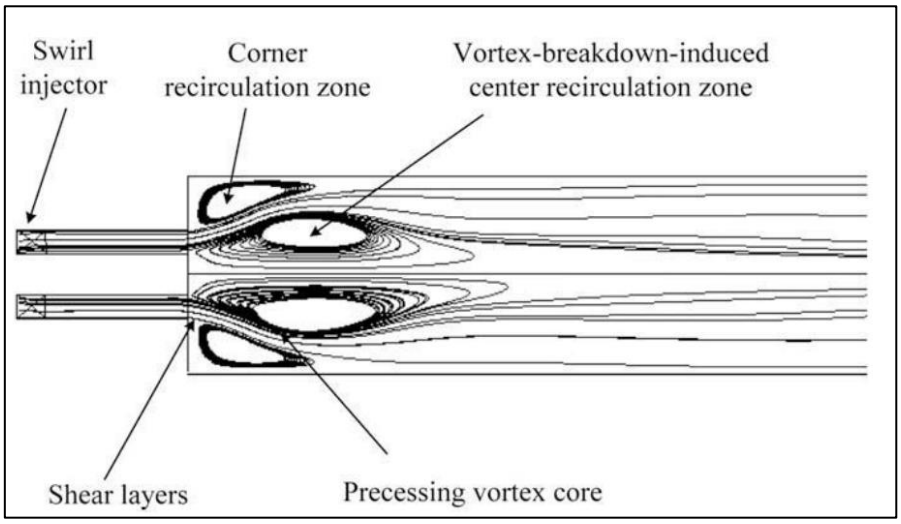

Figure 2.3.4-2 *Flow structures of a typical gas turbine combustor with a coaxial injector. Source:* [150].

As shown in figure 2.3.4-3, swirlers are generally categorised into radial or axial swirler, based on the orientation of their vanes with respect to the flow direction. The radial distributions of axial, radial and tangential (azimuthal) velocity components are presented in Figure 2.3.4-4 for a double axial swirler at counterrotating vane configurations (left) and a tangential one with converged nozzle (right), respectively. Both figures present a comparison between experimentally obtained velocity profiles (through LDV) and computationally derived ones (through LES).

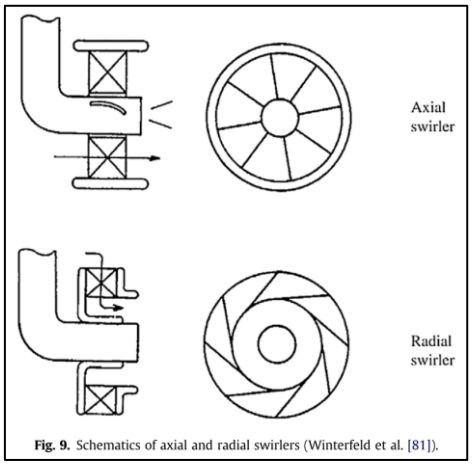

Figure 2.3.4-3 *Schematic of axial and radial swirlers. Source:* [150].

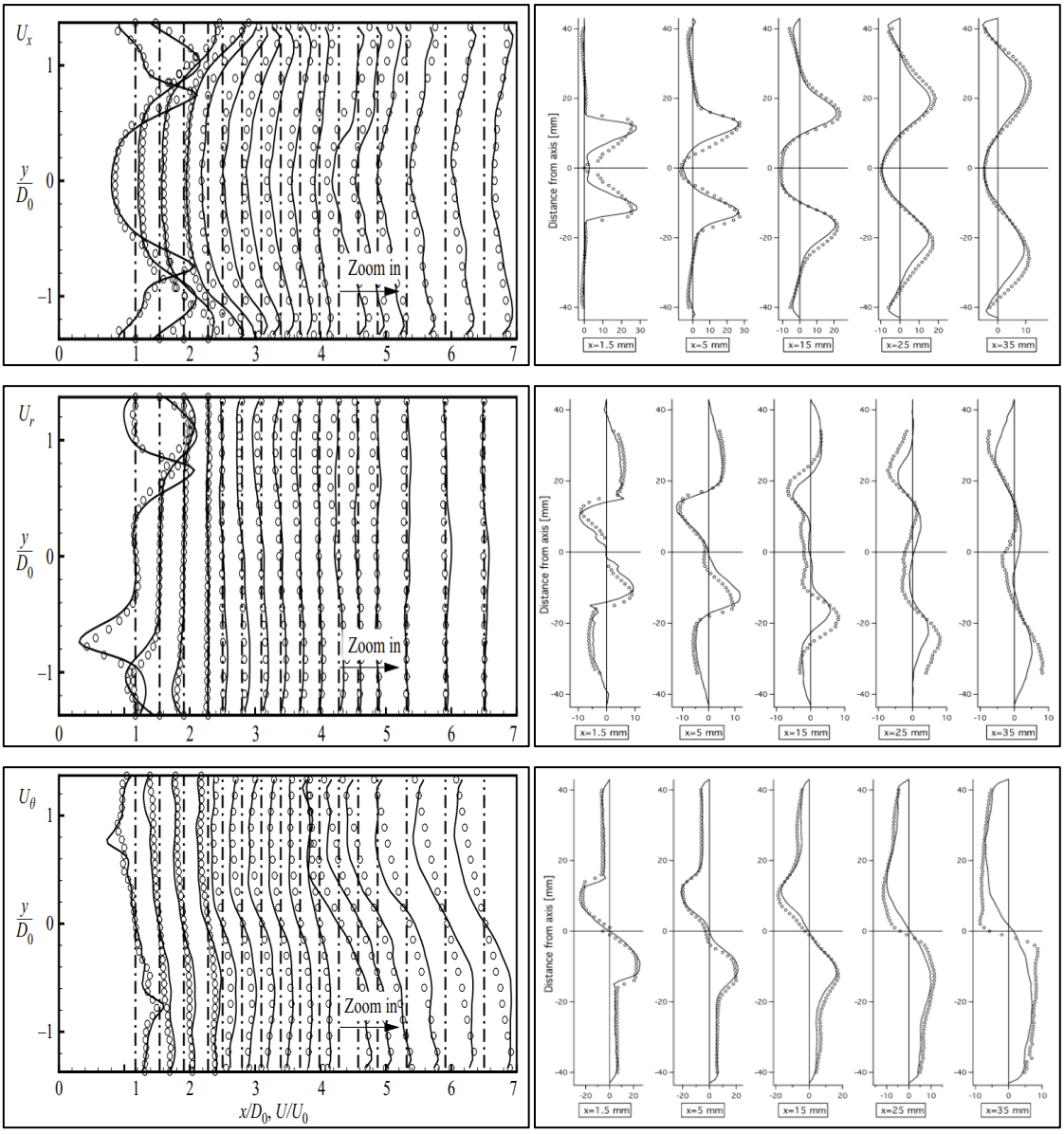

Figure 2.3.4-4 *Radial distributions of normalized mean velocity components in axial, radial and azimuthal directions at various axial locations. Lines: LES simulations, circles: LDV measurements. Data: on the left by* [153]*, on the right by:* [154].

The resultant radial distribution of the three velocity components for axial and the radial swirler present noticeable similarities. Apart from the swirler decay, which is evident as the swirling flow progresses downstream, a symmetrical flow with respect to the x-axis is also observed both for the case of the radial and the axial swirler. For the results related to the radial swirler, the LES computational simulation predicts perfectly symmetrical profile for all velocity vectors. However, the experimental LDV results report small discrepancy, with respect to the symmetry, close to the burner exit (x=5mm). Roux et al. [154], attributed this characteristic to the difficulty of producing a perfectly symmetrical flow though LDV measurements at the vicinity of the burner exit.

Similar inconsistencies were noted by the Wang et al. [153], particularly near the burner exit, though their corresponding LES simulations presented almost complete symmetry.

Concerning the hydrogen addition to methane, numerous studies available in the literature note the advantageous characteristics of H_2 with respect to improving flame stability and extending the lean flammability limits compared to pure CH_4. However, it is also pointed out that under swirl-stabilised LPM combustion, a variety of undesired phenomena might arise, such as unsteady flame stabilisation and thermoacoustic instabilities [117, 130, 131, 155, 156]. Additionally, operating near the LBO limit increases the risk of complete blow-off. Although H_2 enriched in CH_4 flames shifts the LBO in leaner equivalence ratios, the burner stability envelope is narrower [117, 155]. Additionally, due to high diffusivity, increased burning velocities and enhanced combustibility, H_2/CH_4 mixtures are more susceptible to flashback under relatively lean conditions [121, 122, 131]. Hence, as H_2 addition CH_4 flames increases the propensity of LBO and flashback to occur under LPM swirl-stabilised combustion, it is essential to provide some important insight of those phenomena.

2.3.5 Instabilities

There are several critical operability issues that can often seriously jeopardise the safe, reliable and stable operation of a combustor. The four most critical problems relate to *autoignition*, *thermoacoustic instabilities* (also referred as *combustion instabilities* or *combustion dynamics*), *lean blow-off* (*LBO*) and flashback and are all majorly influenced by the fuel properties [157]. The current Section only concerns the last two of the four listed issues, as lean blow-off (LBO) and flashback usually characterise the static limits of stable operation of a given burner. Designing a successful, safe and reliable burner requires the consideration of such phenomena, with a view to minimising their propensity.

2.3.5.1 *Lean blow-off (LBO)*

Modern gas turbine systems are designed to operate under lean premixed (LPM) combustion conditions to benefit for pollutant emissions reduction. However, as operating very close to the *lean blow-off (LBO)* stability limit is characterised by low AFT and reduced combustion efficiency, combustion under such conditions is prone to potentially high amplitude, low frequency pressure fluctuations that can manifest

within the combustor as localised and periodic flame extinction and reignition events (Figure 2.3.5-1 A) [158]. The *lean blow-off (LBO)*, also known as *blow-out* refers to the phenomenon, in which the flame detaches from the stabilisation location and is physically extinct (Figure 2.3.5-1 B). As LBO can potentially disrupt the stable operation of the system through imposing a lengthy and often costly system shut down, purge cycle and restart, LBO is frequently characterised as a “static stability” limit of the combustor [157].

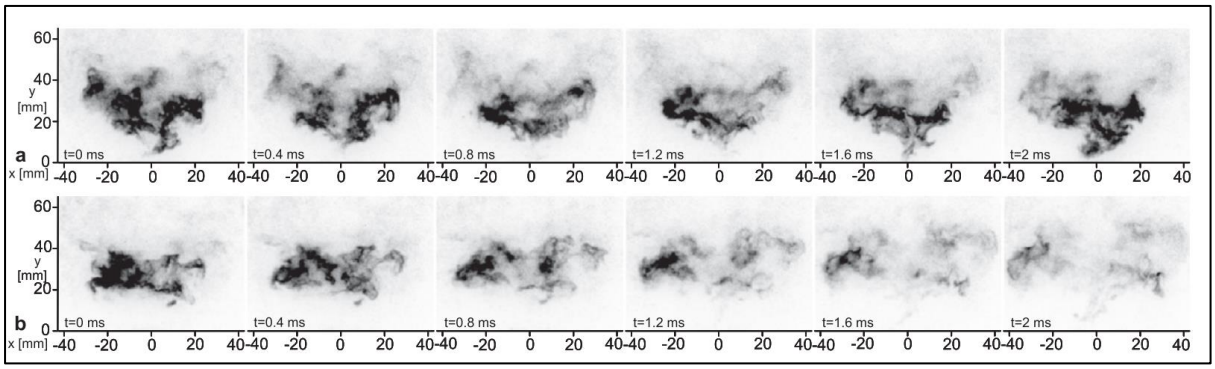

Figure 2.3.5.1-1 *Time series of OH* chemiluminescence (a) Extinction and re-ignition of flame root. (b) Ultimate blow-off Source:* [159].

The LBO situation arises from increasing chemical timescales, τ_{chem}, and decreasing flow timescales, τ_{flow}, under lean conditions (φ<1) [158]. The ratio of flow to chemical timescales as defined earlier by the *Damköhler* number ($Da = \tau_{flow}/\tau_{chem}$) which is extensively used in the field of chemical engineering. The above remark regarding the onset of the LBO phenomenon, led Radhakrishnan et al. [160], to propose a dimensionless *Damköhler* number relationship describing the critical condition, under which LBO initiates. This relationship, which is shown in Equation 2.44, recently applied in premixed turbulent CH_4-air swirling flames under atmospheric conditions [161]. This relationship postulates that extinction will occur when the required time for a flame to propagate from one Kolmogorov-scale vortex to a neighbouring one exceeds the lifetime of the large eddies of the turbulence [161]. Whilst the complete derivation of the relationship can be found elsewhere [161], the final form of the extinction criterion in can be formulated as:

$$\frac{1}{Da} = \left[\left(\frac{C_1}{C_2}\frac{15}{A}\right)\left(\frac{U_b}{d}\right)\left(\frac{v}{S_L^2}\right)\right]^{\frac{1}{2}} > C_3 \qquad (2.44)$$

where, the mean flow velocity (U_b) and lance diameter (d) define the reciprocal of flow timescale (τ_{flow}), the kinematic viscosity (ν) and the laminar burning velocity (S^2_L) form the chemical timescale (τ_{chem}), and C_1, C_2 and C_3, are constants.

Low frequency LBO instabilities have been identified in both laboratory burners [162–164] and industrial gas turbine systems [150, 165] operating near the LBO limit. Usually, the LBO instabilities are investigated using chemiluminescence (CL) photography and pressure transducers, whilst several other non-intrusive diagnostics, such as PIV and PLIF have been utilised too [158, 162, 163, 166]. Muruganandam et al. [158], carried out optical and acoustic measurements, to report the noticeable increase in the energy content of the low frequency spectrum (10-200Hz) near the LBO at $\varphi = 0.75$, in an atmospheric swirl combustor. Stöhr et al. using high-speed CL, PIV and PLIF, studied the onset of LBO for partially premixed CH_4 swirling flames near $\varphi = 0.55$. He found that the flame was characterised by extinction and reignition events that altered its anchoring position [159]. Kariuki et al., also showed that the stabilisation position of the flame transitioned from the outwards expanding shear layer to the central recirculation zone near LBO, using simultaneous OH and CH_2O PLIF [166].

As described in Section 2.3.2, with increasing H_2 concentration in CH_4/H_2 blends, due to the high diffusivity, reactivity and laminar burning velocity of hydrogen, the lean flammability limit of the mixture is extended, and thus, the LBO limit is shifted towards leaner equivalence ratios [116, 117, 121, 122]. This offers the potential to offset the increase in AFT, due to the hydrogen addition, and to ultimately result in reduced emissions. Experimental studies conducted under preheated, pressurised conditions showed the greater influence of H_2 addition on shifting the LBO towards leaner equivalence ratios, compared to an increase in pressure [130, 167].

2.3.5.2 *Flashback*

Flashback is a unique feature of premixed flames, which enables the flame front to propagate from a stable location within the flow field, upstream towards the regions where fuel and oxidiser are mixing. For gas turbines that are designed to operate under lean premixed (LPM) combustion, these regions are frequently not appropriate for flame stabilisation since they are not designed to withstand high temperatures. Thus, flashback can severely damage important gas turbine

components, imposing serious safety risks. In contrast to the lean blow-off mechanism, flashback is characterised by increasing τ_{chem} and reducing τ_{flow} and takes place when the local flow speed is outbalanced by the burning velocity of the flame, thus resulting in increasing flame speed [168]. This situation might move the flame near or within the nozzle of the burner, which consequently will act as a preheater for the incoming reactants, increasing further their temperature, and thus, their burning velocity. After flashback has occurred, the rapid temperature rise on nozzle typically leads eventually to overheating and failure [157].

In gas turbine combustors, the flashback is assigned to four main mechanisms. The simplest of the mechanisms is the *core flow flashback*, which occurs when the local flow velocity reduced below the turbulent burning velocity in the core area [157]. The turbulent burning velocity, which is dependent on turbulent-flame interaction and chemical kinetics, plays a major role in core flow flashback propensity. Consequently, the fuel composition and turbulence structure are important parameters affecting this phenomenon [169]. Although, this situation is frequently avoided by imposing high axial bulk flow velocities, common stabilisation techniques, such as swirl, may lead to core flow flashback, as it reduces the axial component of the velocity, while increasing the turbulent flame speed due stretch effects resulting from flame-vortex interaction [170].

Furthermore, *boundary layer flashback* (*BLF*) is also observed in gas turbine systems when the freestream velocity is higher than the turbulent flame speed, and therefore, core flow flashback cannot take place. This flashback situation is initiated within the boundary layer, where flow velocity is reduced due to the wall imposed no-slip condition and the viscosity effects. Thus, within the velocity gradient normal to the wall, it is possible that flame speed outbalances local flow rate [169]. The *critical velocity gradient* concept [171] has been developed widely used to estimate the boundary layer flashback propensity. Boundary layer flashback mechanism has been extensively studied both empirically [172, 173] and numerically [173, 174], under laminar and turbulent flow conditions and with respect to different parameters such as geometrical burner configuration [175, 176], operating conditions [176] and recently, surface roughness [53]. As fuel composition influences boundary layer flashback propensity significantly, recent experimental and numerical work focuses on H_2-rich

flames, as the latter is particularly prone to flashback due to its thermo-diffusive properties [172, 173, 175–177].

The third flashback mechanisms that can potentially take place in gas turbine system is referred to as *combustion instability induced flashback.* As the name suggests, this mode of flashback is initiated by large amplitude fluctuations in the flow field, emerging from the interaction of thermoacoustic instabilities and flow structure [157]. Collectively, these phenomena impose pressure and velocity fluctuations that can momentarily stagnate the flame which then propagates upstream. Finally, flashback due to *combustion induced vortex breakdown* (*CIVB*) is the prevailing flashback mechanisms in swirling flows [169]. It relies upon the phenomenon of vortex breakdown, which is a unique characteristic of swirling flows. Vortex breakdown results from the interaction of swirling flow with heat release and it is majorly dependent on swirl number [178]. Above a critical swirl number $(S_N \approx 1)$, the mode of vortex breakdown is initiated, due to the increased tangential velocity component relative to the axial one [157]. Vortex breakdown leads to the formation of a central recirculation zone (CRZ) with a reverse flow region and a stagnation point located upstream of the CRZ. The location of the flame front relatively to the recirculation bubble significantly affects the propensity of CIVB. If the flame front is positioned downstream of the stagnation point, then the upstream propagation of the recirculation bubble is facilitated and the flame moves further upstream, leading to flashback [169].

Specifically for swirling combustion flows, the flashback performance of a burner relies upon its swirl number, whilst multiple flashback mechanisms might successively take place, creating challenges in identifying the prevailing mechanism [169]. Mayer et al., observed that based on burner geometry, either a boundary layer flashback (BLF) or a combination of CIVB followed by a BLF occurred. Baumgartner [176], using a tubular low-swirl burner identified the same combination of CIVB and BLF for H_2-air flames. Ebi [172], studying the BLF mechanism in an optical access mixing plenum with an axial swirler, found that BLF is initiated by large flame tongues, swirling in the bulk flow direction. Previous studies of CH_4 and CH_4/H_2 swirling flames, conducted in Cardiff University's GTRC, investigated the impact of confinement geometry [155, 156] and effect of swirl number [131] on flashback and LBO phenomena.

Of particular interest to the current review is the recent experimental works of Hatem et al. [45] and Al-fahham et al. [46, 53], who investigated the effects of surface microstructure on BLF and CIVB propensity. Roughness elements of scallop riblet geometry were applied to the inner wall of the nozzle of a generic radial/tangential swirler. The introduction of the scallop riblets induced enhanced mixing, thus reducing the size of the viscous sublayer through displacing the log-layer closer to the wall. Consequently, due to the alteration of flow structures, the performance of the burner against CIVB was improved when combined with central air-injection mode. However, it was found that using central air injection to improve the flashback performance against CIVB, might result in worsening the flashback resistance of BLF. Additionally, two sets of micro-meshes, 50 μm and 150 μm, were used and their resultant BLF flashback performance was compared. The woven wire geometry micro-meshes resulted in improved velocity gradient, thus, reduced BLF propensity, with the 150 μm one performing better than the 50 μm. The improved performance led to an extended burner stability envelope, whilst the optimum performance of the burner was reported under central air injection configuration.

2.4 Surface roughness effects on reactive flows

The effects of rough surfaces on non-reactive flows have been investigated and reviewed in the literature. Specifically for gas turbines, empirical roughness correlations are frequently employed for drag and heat transfer estimations since the impact of roughness on gas turbine performance has been studied over the past 60 years [36]. However, the influence of surface roughness on specific combustion phenomena, related to gas turbine operation, such as boundary layer flashback, has been generally overlooked, so very limited literature exists on this topic.

The investigations of Hatem et al. [45] and Al-fahham et al. [46, 53] as previously, constitute pioneering work on the effect of surface roughness on boundary layer flashback, demonstrating a novel way of improving the flashback performance of a burner without modifying its bulk geometric characteristics or its configuration. Moreover, Maeda et al. [54], investigated the influence of surface roughness on the detonation-to-deflagration transition of H_2-O_2 mixtures in a rectangular 12x10 mm^2 channel. Compared to a smooth surface, the addition of surface roughness increased flame acceleration and reduced the required time needed for detonation.

In addition, Runyon et al. [29], used two additively manufactured (AM) radial/tangential swirlers of different surface finish, together with a conventionally manufactured one of reduced surface finish, to empirically evaluate the impact of surface roughness on swirl flow boundary layers and turbulence, flame stability limits, and emissions of a 25 kW methane flame under ambient pressure and elevated inlet temperature. The experimental results showed a noticeable surface roughness effect on flow structures and flame position, whilst a reduction on NO_x emissions was reported for the roughest swirler.

As mentioned in Section 1.3, additive manufacturing (AM) has emerged as an important tool for the development of gas turbine combustor components. Apart from significant advantages over traditional subtractive techniques, such as multiple component integration, multifactional designs and reduction in material waste, lead time and cost, AM also offers the potential for pre-determined surface finish, integrated to component under its fabrication stage. This unique capability of AM process reduces the needs for post-processing, whilst allowing the incorporation of beneficial roughness features. Therefore, the influence of surface roughness, the need for and the economics of components post-processing, and the potential for novel surface textures, are all worthy of further study.

The important advantages that AM delivers to gas turbine components development, as well as the current technological challenges of AM technology, are reviewed in the following Section 2.5.

2.5 Additive Manufacturing (AM) & Gas turbine (GT) technology

Additive manufacturing has recently emerged as a novel manufacturing technique, covering a wide range of applications over different engineering disciplines. The global market for AM was valued at >$10B in 2019, whilst it is predicted to increase over $30B in 2024 [179, 180]. In Europe, more than 400 projects are related to AM in Horizon 2020 [181], whereas in the UK, currently active AM projects equalling over £180M [182]. Specifically for the gas turbine industry, European research programmes related to metal AM including the €5M OXIGEN [183] and €1M ASLAM [184] projects, focus on novel AM alloys for GTs and on AM for lean burn combustors, respectively, whilst original equipment manufacturer (OEMs) prefer AM for product development, on-engine parts, and repair of in-service components.

Concerning metal AM technologies available for the GT sector, the market is largely dominated by *power bed fusion* (*PBF*) by selective laser melting (SLM), which represents approximately 80% of metal AM installations worldwide. This technology, which is schematically shown in Figure 2.5-1, relates to the sequential application of a thin metal powder layer onto the component where it is melted via laser, before the cycle is repeated. PBF machines are characterised by high spatial printing resolution, improved process control, utilisation of innovative materials and enhanced freedom of design. The challenges of this type of AM technology are related to the combined control of several building parameters, limited building volume, and relatively slow building process [185].

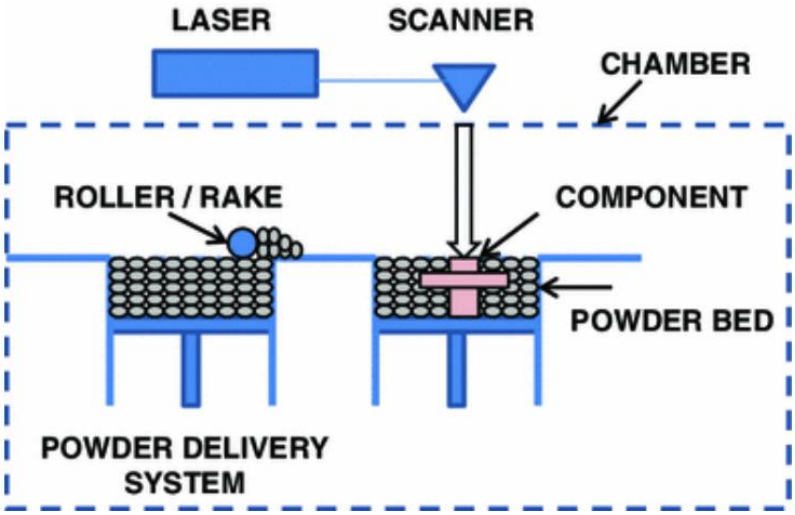

Figure 2.5-1 *Schematic of PBF via SLM. Source:* [185].

Several OEMs including Siemens, GE and Baker Hughes have reported an important increase in efficiency when utilising AM methods for the development of their components, due to reductions in product development and component validation related activities. Specifically, Siemens validated several cooling designs related to the SGT-4000F turbine blades, whilst significantly reducing the development time by more than 75% [28]. Due to similar reduction in development and testing timescales, GE/Baker Hughes reported overall saving of 50% [186]. In addition, GE aims to further accelerate the validation process of GT components by 50%, through the employment of artificial intelligence for optimisation of multifactional components, which then can be fabricated through AM rapid prototyping [187]. Consequently, the cost-competitiveness of AM is significantly improved compared to other fabrication methods, especially for prototyping of complex parts [21, 188], whilst additional cost

improvements can be achieved due to waste minimisation [22]. Apart from economic and environmental incentives, AM is expected to play a significant role in the development of the future fuel-flexible GT burners and components, addressing issues related to burner characteristics (flashback, combustion instabilities), with a view to achieving 100%H_2 combustion of reduced CO_2 and NO_x emissions [21].

In following Sections 2.5.1, 2.5.2 and 2.5.3, the current state-of-the-art in AM for GT combustion in relation to academic combustion research, micro gas turbine and industrial gas turbines, is presented, respectively.

2.5.1 AM for academic combustion research

The increasing development of metal AM industry has made SLM machined widely available to the academia. This new reality subsequently increased the academic research output related to AM methods. Supported by large investments, universities and research institutes address research challenges, whilst focusing on the low Technology Readiness Level (TRL) AM process equipment, optimisation, monitoring and modelling materials [189]. High TRL studies have also been demonstrated through the synergy of universities with industrial partners. Characteristic example is the development of the AM jet engine, by Monash University and SAFRAN [190] (Figure 2.5.1-1)

Figure 2.5.1-1 *AM jet engine from Monash University and SAFRAN. Source:* [191].

Although the academic research output related to AM has been greatly increased in the research years, specifically for GTs, the research enabled by AM related concepts, has fallen behind. As demonstrated in a recent study conducted by Runyon et al. [23], although the total number of publications related to AM increases by an order of magnitude every 5 years, the number of publications specifically related to GTs and GT combustion lags the general trend by 5 and 15 years, respectively. In

general, the academic research activity related to AM focuses on three main categories, including: (i) components that enable fundamental combustion studies, (ii) low TRL innovative combustion parts and (iii) high TRL prototype combustion components.

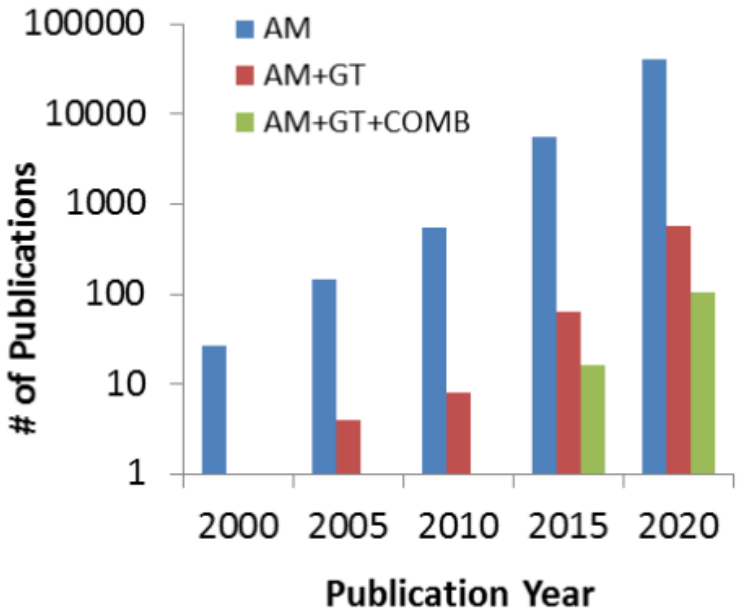

Figure 2.5.1-2 *Publications related to AM, GTs and combustion* [23].

Concerning the first category, the components developed through AM to enable fundamental combustion research are usually related to cooling and air nozzles. The air nozzle shown in Figure 2.5.1-3 A was produced by Boyette et al. [192] for turbulent syngas combustion. Rivera et al. [193], developed a cooling nozzle the design of which is presented in Figure 2.5.1-3 B, to facilitate laminar propane related combustion research. Additionally, an AM cooling nozzle (Figure 2.5.1-3 C), for the pressurised counterflow burner, was utilised in Cardiff University's GTRC experimental facilities with a view to enabling fundamental studies of flame speed and extinction behaviour. This cooling nozzle had been fabricated by Renishaw PLC via the RenAM 250 PBF machine.

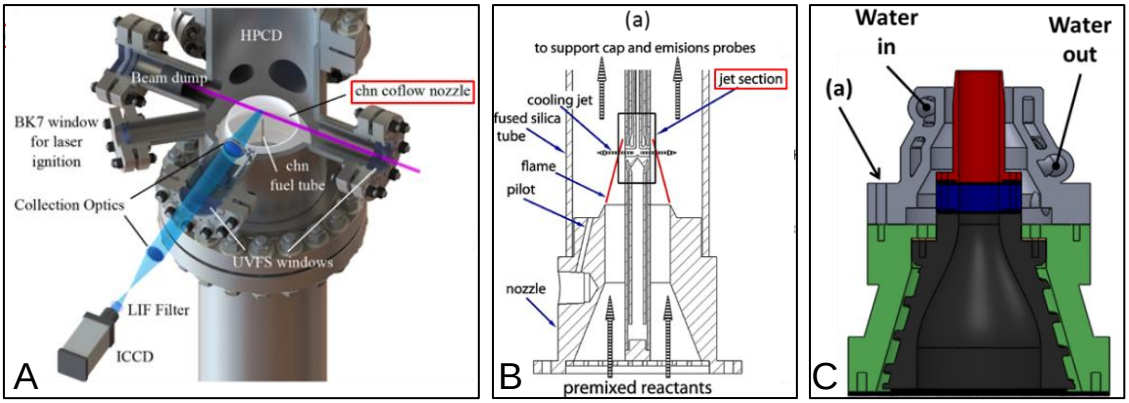

Figure 2.5.1-3 *(A)AM air nozzle, Source:* [192]*. (B) AM cooling nozzle, Source:* [193]*. (C) AM cooling nozzle.*

Exploiting the unique benefits of AM, including multiple component integration and enhanced design flexibility, low TRL GT parts are vastly developed. These critical GT parts mainly concern swirlers of innovative structure. As shown in Figure 2.5.1-4 A, a counter-rotating AM swirler was developed for the investigation of combustion instabilities [194], whilst the CeCOST conical swirler depicted in Figure 2.5.1-4 B was AM fabricated along with several other AM parts, such as a flow conditioner, a mixing tube, and a pilot flange, to assist the empirical investigation of gaseous fuels [195].

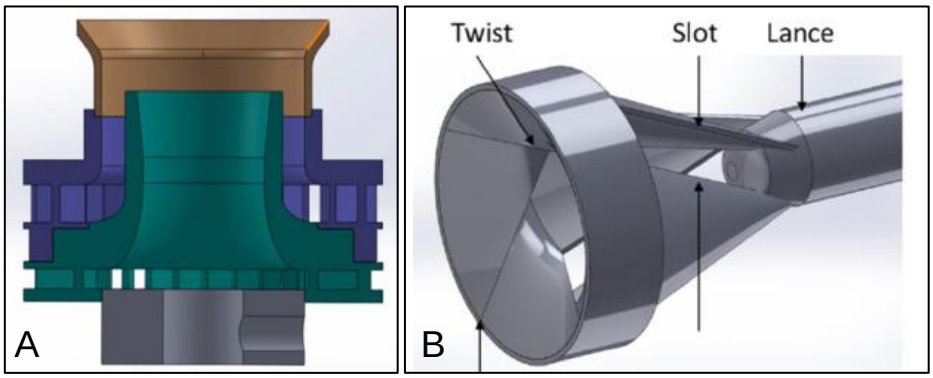

Figure 2.5.1-4 *(A) AM Counter-rotating radial swirler, Source:* [194]*. (B) AM CeCOST conical swirler, Source:* [195]*.*

With respect to the triple swirler, shown in Figure 2.5.1-5 A, it was developed upon the GE Twin Annular Premixed Swirl (TAPS) design to facilitate the study of the unsteady interactions of swirling flows. Through rapid prototyping, several versions of this swirler design were developed, with different swirl number in the outer swirler [196]. Giuliani et al. [30] developed a helicoid swirler (Figure 1.3-2 A), fabricated out of 718 Inconel, that resulted in improved LBO performance due to its innovative S-vane structure. He also identified surface finish as a potential issue. Crayford et al.

[197] also highlighted surface roughness as a potential area of future improvements, in relation to pre-filming airblast atomisers, used in rich-quench-lean (RQL) burner utilising liquid hydrocarbon fuels. The AM fabricated atomiser (Figure 2.5.1-5 B) demonstrated the concept of multiple component integration, since the fuel channels and the swirler was integrated in a single component. Additionally, the geometric features of the atomiser were sufficiently accurate to generate a uniform spray pattern. Moreover, Runyon et al. [29], evaluate the effect of surface roughness resulting from SLM technology on flame stability and NO_x emissions, using Inconel 625 swirlers (Figure 1.3-2 B). These AM radial-tangential swirlers were fabricated by HiETA Technologies Limited using a Renishaw RenAM 500Q machine. A reduction in NO_x emissions with increased surface roughness was highlighted.

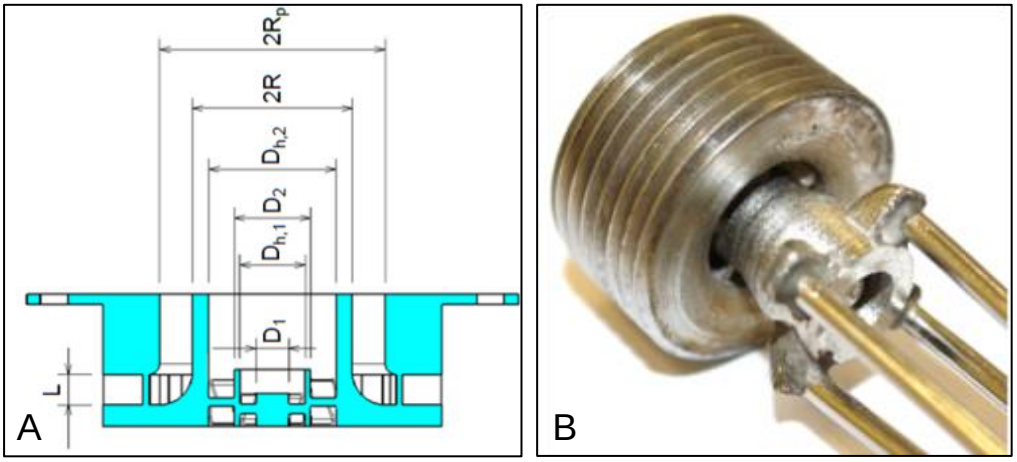

Figure 2.5.1-5 *(A) AM counter-rotating triple swirler, Source:* [196]*. (B) AM air-blast atomiser, Source:* [197]*.*

Apart from low TRL swirler developments for combustion performance and burner characteristics improvements, AM-based rapid prototyping is also preferred in academia for the fabrication of burners and components that enable the utilisation of low and zero carbon fuels. An et al. [198] developed a system comprising of an unconfined burner, a low-swirl injector nozzle and a flow conditioning plenum manufactured by AM, to study the flow/flame interaction for CH_4/H_2, emphasising the significance of rapid prototyping and accelerated tested, afforded by AM. Similarly, Fan et al. [199] developed an Inconel prototype multi-cluster burner, featuring a 0.3 mm diameter nozzle and an intricate manifold, for H_2, O_2, and H_2O combustion. In addition, the design of a fuel injector was optimised by the Southwest Research Institute, with a view to achieving complicated swirling and mixing geometry, for a 1 MW direct-fired combustor, which runs on a supercritical CO_2 power-cycle. The

injector is expected to be printed through AM machined, allowing easier design modifications and accelerated validation process [200].

With regard to high TRL AM components, other than the Monash University (Figure 2.5.1-1), Samara University have produced a complete full-scale GT combustion can (Figure 2.5.1-6 A), out of NiCoCr material, using an SLM 280HL machine that performed efficiently under realistic conditions [201]. Furthermore, the same university is expected to conduct tests related to an AM annular combustor (Figure 2.5.1-6 B) for a TA-8 GT, utilising biofuels [202]. Additional, currently active projects, involving the £1.4M UK Research and Innovation project [203], try to increase the synergy between AM and GTs, with a view to fabricating novel AM combustion parts for zero carbon H_2/NH_3 combustion.

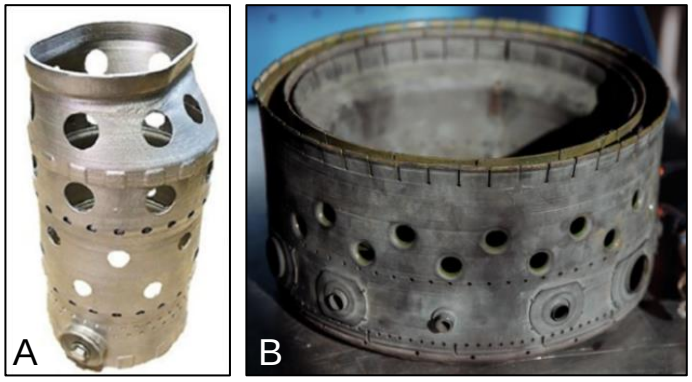

Figure 2.5.1-6 *(A) AM can combustor, Source:* [201]*. (B) AM Annular combustor, Source:* [202].

2.5.2 AM for low-carbon micro gas turbines (MGTs)

Micro gas turbines (MGTs), defined as GTs of low power output (less than 1MW), are regarded ideal for off-grid or distributed co-generation application due to their unique advantages including inexpensive maintenance, low levels of noise, and fuel-flexible combustion of reduced emissions [204]. Utilising a recuperated combustion unit, the inlet combustor air is preheated from the turbine exhaust through a high-temperature heat exchanger (HTHX). In this way, high cycle efficiencies and reduced fuel consumption are achieved [205, 206]. Several projects have demonstrated the feasibility of MGTs to run efficiently on low-carbon fuels such as biogas [207] and ammonia (NH_3) [208], whilst other on-going project aim for 100% H_2 combustion [209]. According to ETN MGT technology summary, the key future research areas for MGTs include fuel flexibility, emissions reduction, and AM of high-temperature materials [210].

Considering the characteristics of MGTs, such as compact size, high design complexity, and required material variety, AM through PBF is regarded as a suitable candidate to accommodate their development. Exploiting benefits including the fabrication of multifactional structures with increased design freedom and reduced production tooling cost [211], the fabrication of MGT combustors, porous structures and geometrically optimised HTHX can be realised through AM [185]. These benefits are translated into enhancements in MGT size, weight, production and assembly time and cost, as well as fuel flexibility and efficiency [22].

AM techniques are regarded particularly ideal for the fabrication of the recuperator unit, which roughly accounts for 25% of the MGT production cost [210]. For HTHX, such as recuperators, AM offers unique advantages offer conventionally manufacturing methods, as it enables the fabrication of complexed, optimised geometries from a variety of high-temperature materials available, such as Aluminium 6061, stainless steel, as well as alloys, including as Al-Si-10Mg and Inconel 718 and 625 [210]. Additionally, currently active research on ceramic-based powder has the potential to enhance further MGTs efficiency, due to improved resistance to thermal loads [212]. Several projects have demonstrated the performance benefits of AM HTHX over conventional manufactured ones, for waste heat recovery applications (Figure 2.5.2-1 A) [213], MGT recuperators (Figure 2.5.2-1 B) [210] of advanced heat transfer surfaces and compact size, and oil coolers, built as single components of 66% reduced weight and 50% reduced volume (Figure 2.5.2-1 C) [214].

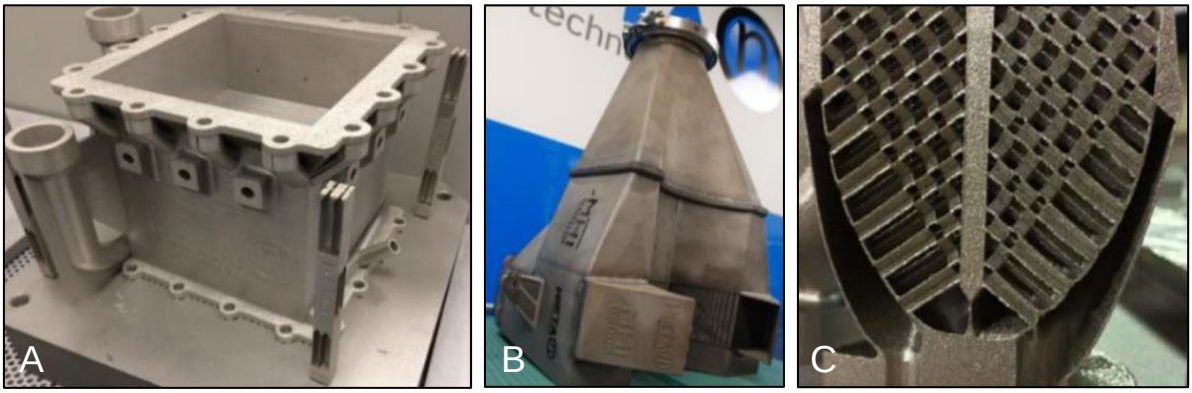

Figure 2.5.2-1 *(A) AM waste heat recovery HTHX, Source:* [213]. *(B) AM MGT recuperator, Source:* [210] *.(C) AM multi-furcating HTHX, Source:* [214].

Other examples of AM combustion components of enhanced performance include the combustion can fabricated by EOS (Figure 2.5.2-2 A) [215] resulting in

20% size reduction and the annular radial flow recuperator built by HiETA technologies, demonstrating an example of synergy between freedom of design, selected high-temperature material and internal porous passages for improved cooling performance (Figure 2.5.2-2 B) [216, 217]. Regarding liquid fuel-based combustion, an AM liquid fuel injector, which was integrated in a swirl-stabilised combustor showed improved burner stability and emissions characteristics, due to its complexed internal channels and heat transfer surfaces [218].

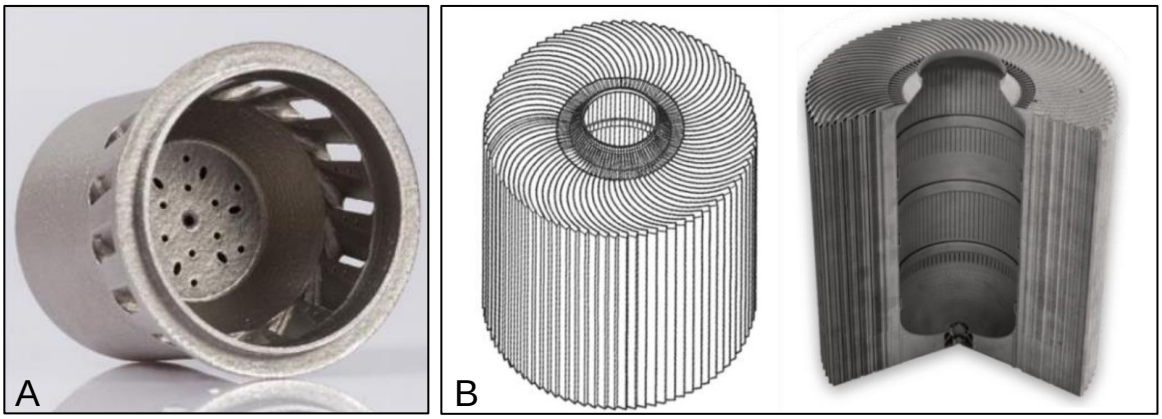

Figure 2.5.2-2 *(A) AM MGT combustion can (EOS), Source:* [215]*. (B) Combustor-Recuperator Design (HiETA Technologies), Source:* [216, 217]*.*

To take full advantage and to allow the further development and utilisation of AM techniques of MGTs, there are several challenges that must be addressed. Concerning the fabrication stage, the high initial AM machines costs, coupled with the expensive powder materials, inhibit the adoption of AM methods vastly. Furthermore, insufficient AM process repeatability may result in inferior mechanical properties that drop combustion performance. Particularly for injections and nozzles, inconsistencies in building quality may lead to clogging, higher pressure drop, combustion non-uniformities and instabilities as well as knock-on effects and local hot spots that reduce emission performance [22, 212]. Additionally, challenges related to the integration and sizing of MGT HTHX, as well as the effective distribution of outlet air in the combustion, must be overcome to improve further the efficiency of combustion process [219]. With respect to multiple component integration, issues related to differential material expansion have to be resolved to reduce operation risk.

To address the aforementioned challenges, the most important AM research needs, in relation to MGT development, were identified within published literature. For the AM processes, further research is required concerning the monitoring and control

of the building process, with a view to identifying building flaws and providing process feedback [220]. Moreover, to improve the competitiveness of AM processes and to reduce production time and cost, the geometric accuracy and the surface finish must be improved by optimising the building parameters. In addition, process modelling methods have to be further developed, allowing improved predictions of the resultant thermo-mechanical properties and surface finish. To gain advanced knowledge on surface roughness and emissivity, enabling design of combustion parts of improved aerodynamic and heat transfer design, CFD models capable of predicting the influence of manufacturable surface roughness on AM microchannels, are required. Finally, the interaction of different materials and the invention of new allows of better performance requires further attention [219].

2.5.3 AM for fuel-flexible industrial gas turbines (GTs)

With industrial GT OEMs aiming to provide fuel-flexible GT systems capable of efficiently operating from 100% CH_4 to 100% H_2, whilst generating allowable levels of emissions, significant research activities have to be undertaken. These systems must be able to adapt to low-carbon alternative fuels, such as NH_3, biomethane and liquid fuels combustion, which are expected to contribute to the future energy mix to assist meeting the energy demands. Under these circumstances, AM is expected to play an essential role in realising new designs and strategies [21, 210].

Acknowledging the operability issues associated with high-H_2 content fuels, including high flashback propensity and high flame temperatures resulting in augmented NO_x emissions, unique innovative strategies and designs must be developed and adopted by GT OEMs. The importance of AM is highlighted by considering the recent improvements on industrial GT systems, in terms of fuel-flexibility performance, that have been accomplished through AM methods. More than 30 different fuel-air swirl premixers and micromixers have been developed, fabricated, and characterised during the GE/US Department Energy project that was completed in 2015. This goal of this project, in which AM was extensively utilised, was the development of improved high-H_2/syngas combustion systems. The AM micromixer presented in Figure 1.3-1 B made it to production and is now part of the GE's dry low NO_x combustor (DLN 2.6e), enabling 50% H_2 operation [25, 27]. Operation with increased H_2 content premixtures had also been achieved by several other leading OEMs, including Siemens (up to 50% H_2 and 100% in wet-diffusion state) [221],

Ansaldo (up to 70% H_2 and 100% with decreased firing temperature) [222] and Mitsubishi (up to 30% H_2). The latter is currently developing a multi-cluster combustor that is expected to facilitate 100% H_2 (Figure 2.5.3-1 A) [223] whilst Kawasaki and RWTH Aachen University advanced a micromixer concept for H_2 utilisation (Figure 2.5.3-1 B) [224].

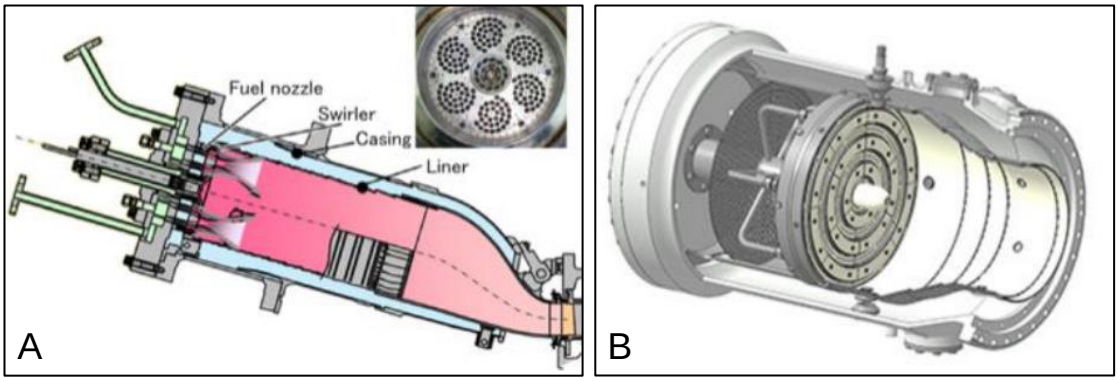

Figure 2.5.3-1 *(A) Multi-Cluster Combustor (Mitsubishi), Source:* [223]*. (B) Micromix Combustor (Kawasaki), Source:* [224].

Due to the important benefits that AM affords to GT system for improved fuel flexibility, numerous large-scale investments have been made by OEMs with concern to AM technologies. For instance, GE spent $1.4B to acquire AM equipment suppliers [225], whilst Siemens have invested more than €30M in AM technologies for GT applications regarding design, retrofitting and repair [187]. MAN Diesel and Turbo [226] and Mitsubishi [227] have also invested in facilities, promoting the use of AM. In general, all industrial GT OEM leaders devote significant amounts of investments for researching and utilisation of AM technologies to produce novel components and to repair existing equipment, extending its lifetime [228]. Low TRL building variables including, laser power and hatch distance, also receive significant research interest [229], whilst methodologies for incorporation of AM resultant surface finish on CFD simulations, are also developing [56].

Several examples of AM products have demonstrated the feasibility of this manufacturing technique for the development of GT parts. These examples comprise the new fuel-air mixing nozzle (Figure 2.5.3-2 A), which is included in GE's HA-class GT, resulting in improved combustion efficiency and reliability, due to multiple components integration [230], and the AM swirler produced by GE/Baker Hughes (Figure 2.5.3-2 B) for operation related to oil and gas [231].

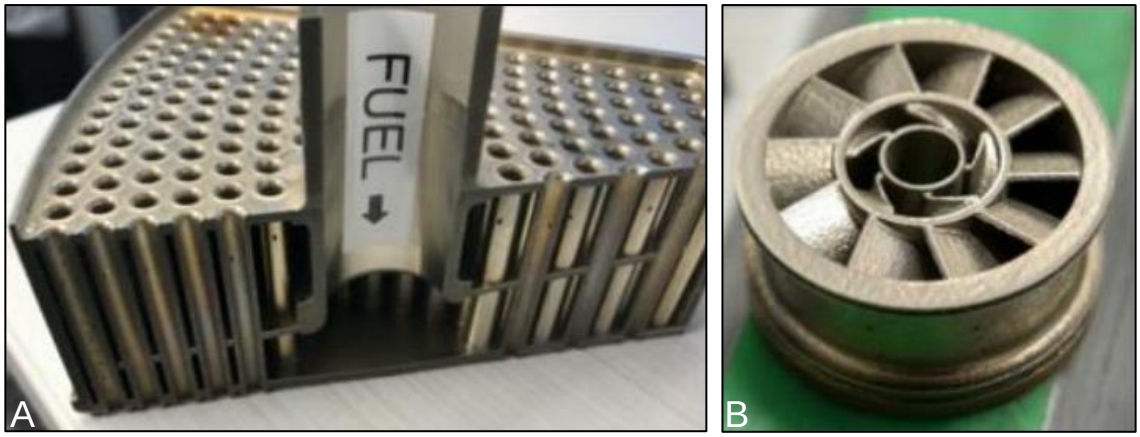

Figure 2.5.3-2 *AM Fuel/Air Mixer (GE), Source:* [230]*. (B) AM swirler (GE/Baker Hughes), Source:* [231]*.*

Siemens have also achieved to reduce the 13-piece third generation burner design (Figure 2.5.3-3 A), down to a single-part component (Figure 2.5.3-3 B), leading to 75% reduction in lead-time and 20% reduction in weight [232]. The SGT-A05 premixer (Figure 2.5.3-3 C) also constitutes an example of novel AM produced combustion component [233], while innovative designs have also been presented by Ansaldo, with the new sequential combustion system (Figure 2.5.3-3 D) [234]. Some of these examples have already proven their performance under realistic operation conditions of high H_2 content fuels. For instance, the burner shown in Figure 2.5.3-3 A recorded more than 8000 hours of operation in 2017, while it was expected to facilitate up to 60% H_2 combustion by 2021 [187, 235]. Additionally, GE has achieved retrofitting AM combustion parts, such as fuel injection lance and thermal dampers, to regulate low-frequency combustion instabilities, with a view to improving efficiency and power output, while reducing maintenance requirements [236, 237].

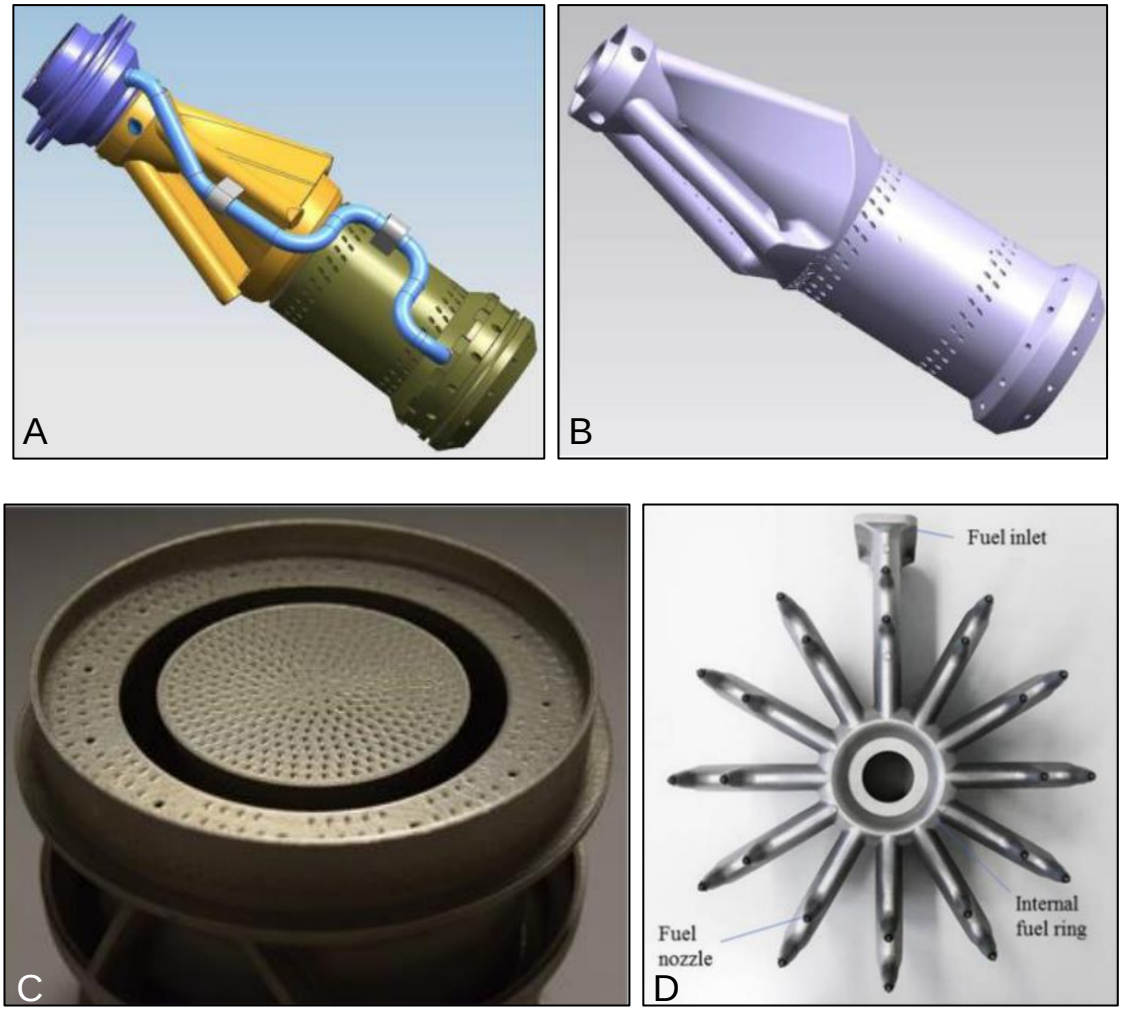

Figure 2.5.3-3 *(A) Traditional 3rd Generation Burner (Siemens). (B) AM 3rd Generation Burner (Siemens), Source:* [234]*. (C)SGT-A05 Premixer (Siemens), Source:* [233]*. (D) AM Center Body Burner (Ansaldo), Source:* [234].

However, as AM is a relatively newly introduced manufacturing method, there are still significant challenges associated with its implementation. With respect to the pre-fabrication stage, efficient and effective AM designs of GT components require multidisciplinary “out-of-the-box” thinking and advanced knowledge of both GT combustion phenomena and AM processes and materials. Subsequently, with respect to the printing stage, challenges that have to be overcome are related to repeatability and process optimisation through machine development, materials availability, as well as health and safety issues concerning powder handling, removal and machine maintenance. Specifically for H_2, critical challenges constitute cooling and mixing to minimise high temperatures and high NO_x emissions, respectively, whilst novel fuel-air mixing concepts have to be developed for NH_3 utilisation in RQL combustors.

Finally, the research requirements for further applicability of AM technology in the GT industry are identified, based on industry input, and categorised in relation to design, production, and implementation stages. Concerning the design stage of the process, upskilling of GT designs and university training emphasising on AM methodologies and materials have to be developed further. Equally, topology optimisation and machine learning designs tools require further investigation, with a view to optimising AM combustors in consideration to thermodynamic, aerodynamic and combustion phenomena. Concerning the production side of AM, powder materials for specific combustion applications and their cost optimisation, should be of particular research focus, to advance material utilisation and enhance combustion efficiency. With regard to the implementation of AM, research needs include the validation of new designs, repair strategies and retrofitting activities, and the in-parallel analysis of combustion products and material reliability.

2.6 Summary

The theoretical background, relevant to the aim and objectives of the present PhD programme, has been reviewed in this Chapter. Fundamental concepts such as the *viscous flow* (Section 2.1.1.1) and the *Reynolds number* (Section 2.1.1.2) have been derived and defined, whilst a review of the *boundary layer theory* (Section 2.1.2), summarising the most significant phenomena, was provided. This constitutes fundamental information, in order to understand the effects of surface roughness on fluid flows. Subsequently, a literature review of the effects of surface roughness on non-reacting and reacting flows, relevant to the experimental and numerical investigation, was presented. As published in the literature, surface roughness primarily increases skin-friction induced pressure drop. However, rough surfaces may also affect form drag related pressure drop by modifying the separation performance of bluff bodies and airfoils.

Parameters utilised in later Chapters to study and characterise reacting flows and combustion performance have been presented. An overview of established combustion phenomena, including LBO and flashback, and known empirical trends associated with traditional and alternative fuels, are summarised. Finally relevant research concerning AM developments and future trends of relevance to this study are outlined.

Chapter 3. Experimental facilities and methods

This Chapter describes the experimental facilities and methods developed and utilised for the empirical investigation of surface roughness. In Section 3.1, the experimental aim and the procedure of the test programme are presented. Section 3.2 introduces the relevant experimental GTRC facilities, as well as key test components and the various diagnostic tools utilised. Section 3.2.1 explains in some detail the newly manufactured atmospheric pressure generic swirl burner (APGSB) that accommodated the experimental investigation of the three swirlers. The three swirlers with differing surface roughness, together with their corresponding isothermal characterisation, are outlined in Sections 3.2.2 and 3.2.2.1, respectively. The air/fuel delivery system is described in Section 3.2.3, whilst, several basic and advanced diagnostic techniques utilised for this experimental campaign, including thermocouples, OH^* chemiluminescence photography and exhaust gas analysis, are specified in Section 3.2.4, 3.2.5 and 3.2.6, respectively.

3.1 Experimental aim & procedure

This experimental campaign was designed and successfully undertaken to help fulfil the overall aim and objectives of this study as laid out in Chapter 1. The objective of the empirical campaign was for the traditional as well as a low and zero carbon fuel, to observe, quantify and appraise the influence of surface roughness effects on the lean premixed (LPM) combustion performance of a generic swirl burner operating under atmospheric pressure and elevated inlet temperature (150±5 ^{o}C) conditions, relevant to practical burner designs. Two additively manufactured (AM) swirlers, together with one conventionally manufactured, were fabricated to assess the influence of surface roughness and burner characteristics on (i) the resultant burner stability envelope, (ii) NO_x emissions and (iii) exhaust thermocouple temperatures. For the two AM swirlers, denoted *AM-G* and *AM-R*, the average surface roughness height was measured using a traditional Taylor Hobson Form Talysurf Series 2 profilometer to be 5 µm and 9 µm, respectively, while for the conventionally manufactured one, referred as *Machined*, the respective average surface roughness height equated to 1 µm. These experimental rig components are described further in Section 3.2.2. As the impact of surface roughness on LPM combustion performance was appraised utilising both conventional and alternative, low-carbon fuels, the experimental study could in fact be split into two parts. The first concerns the experimental investigation of pure

methane (CH_4) combustion, whilst the second is related to pure hydrogen (H_2) and a methane/hydrogen blend ($23\%_{vol}CH_4/77\%_{vol}H_2$) representing a pure (zero-carbon) and a partially renewable (low-carbon) fuel, respectively. In this way, the experimental investigation related to CH_4 presents a benchmark dataset against the comparative appraisal of alternative fuels (H_2, CH_4/H_2). For both cases, the thermal power output was maintained at 25 kW. The selection of the CH_4/H_2 blend was based on the heating values of the two fuel components, so that each fuel contributed to ≈12.5 kW output. The three fuels were combusted with air under atmospheric conditions. The experimental procedure that was followed for each swirler and fuel case, is described below.

To appraise the effect of surface roughness on combustion performance, three swirlers of various surface roughness were successively characterised, under the same operating conditions, and their respective combustion-characteristic performance was evaluated and compared against each other. This evaluation included the identification of the burner stability envelopes and the collection of resultant NO_x and exhaust thermocouple temperatures, across the stable operating curves of each swirler and for each fuel type. To ensure safe and stable operation, the initial commissioning of the newly manufactured atmospheric pressure generic swirl burner (APGSB) took place within the facilities of GTRC, which has a mature safety system. At this stage, the light-up conditions for each fuel type were determined, and the effect of burner characteristics on combustion stability was observed. This activity was performed using the *Machined* swirler and the light-up conditions for 100% CH_4, $23\%_{vol}CH_4/77\%_{vol}H_2$ and 100% H_2, were measured as φ=0.66, φ=0.40 and φ=0.265, respectively. Moreover, some additional protective metallic plates were placed around the circumference of the burner's combustion chamber to regulate the heat loss to the surrounding environment. The final design of the atmospheric generic swirl burner, which was successfully commissioned during this programme, is further described in Section 3.2.1.

Having successfully completed the commissioning stage of the new burner, the experimental characterisation of the *Machined* swirler commenced, as it was already conveniently installed inside the burner. The first fuel tested was pure CH_4, followed by pure H_2 and CH_4/H_2 blend. The burner was ignited under the appropriate equivalence ratio (for the case of CH_4, $\varphi = 0.66$) and by gradually increasing the

atmospheric air flowrate, the corresponding LBO limits were identified. Subsequently, by gradually reducing the atmospheric air flowrate, the resultant flashback limit was also determined. In this way, the effect of surface roughness under high (LBO) and low (flashback) Reynolds numbers was observed. Particularly for the pure CH_4 case, the flame did not flashback under the current burner configuration and for the operating conditions deployed, since the burning velocity of the flame and the bulk flow velocity of the reactants, were balanced. Hence, the upper limit of the stable operating curve achieved during this programme was $\varphi = 1.05$, although richer equivalence ratios could have also been achieved. As the present experimental study was focusing on LPM combustion, richer equivalence ratios were out of the scope of the investigation.

Furthermore, to maintain a constant inlet plenum temperature of $150 \pm 5\ ^{o}C$, the air was preheated, via an external heater, before being mixed with the fuel at the inlet plenum section of the burner. In this way, the reactant premixture was maintained, within the inlet plenum, at a constant temperature of $150 \pm 5\ ^{o}C$. As the airflow rate was varying for each test point, the external heater temperature had to be adjusted accordingly to provide a constant inlet premixture temperature. Thus, after each equivalence ratio transition, adequate time had to be provided so that the temperatures were stabilised. A waiting period of a minimum of 5 minutes was employed to ensure that the inlet plenum temperature was under “steady-state” conditions, whilst the corresponding thermocouple was closely monitored to ensure that the temperature was within the acceptable range. Further description of the air and fuel delivery system is provided in Section 3.2.1.

For each investigated equivalence ratio of the burner stability envelope, the respective NO_x emissions were recorded using a water-cooled probe, while inlet plenum and exhaust temperatures were collected using single point measuring *K-type* thermocouples. The description and positions of the thermocouples and NO_x emissions related diagnostic tools are presented in Sections 3.2.4 and 3.2.6, respectively. Additionally, OH^* chemiluminescence measurements were conducted concurrently with the inlet plenum and exhaust temperatures measurements, to enable the combined analysis of the dataset generated. Several traditional diagnostic tools, including pressure transducers and *K-type* thermocouples were positioned around the burner for monitoring purposes. For all thermocouples, the recorded period for each test point was 60 seconds, with a frequency of 10 Hz, whilst for NO_x emissions

measurements, the sampling period was 60 seconds, with a frequency of 1 Hz. Concerning the OH^* chemiluminescence system, the camera frame rate was set at 4000 Hz, though only the first 2000 frames were used, thus the recording period corresponded to 0.5 seconds.

After the burner stability envelope had been identified for CH_4, and all the corresponding measurements had been recorded, the same procedure was repeated for pure H_2 and finally for the CH_4/H_2 blended mixture. Having completed the test matrix for all three fuel cases utilising the *Machined* swirler, a second experimental repeat of the same test matrix was undertaken. Hence, an estimation of the level of repeatability could be extracted. After completing the second experimental repeat, the *Machined* swirler was replaced by the *AM-R* one, and the same experimental procedure was followed strictly, with two experimental repeats being carried out. Finally, for the last swirler (*AM-G*) that was tested, due to laboratory constraints, only one experimental repeat was achieved for the CH_4 fuel case, and only one set of data was collected through the OH^* chemiluminescence data acquisition system for all the three types of fuel. Thus, at the corresponding OH^* chemiluminescence result plots, the absence of error-bars visualising the level of deviation between the two experimental repeats for the *AM-G* swirler, is noted (Figures 6.3-3, 7.2.2-3 and 7.3.2-3).

3.2 GTRC experimental facilities – test components & diagnostic tools

This section provides information concerning the GTRC experimental facilities related to the present investigation, including the various components, systems and diagnostics tools employed. Initially, the newly manufactured atmospheric pressure generic swirl burner (APGSB) that facilitated the experimental investigation, is described in Section 3.2.1. Following, in Section 3.2.2, the three swirlers of different surface roughness are outlined, whilst the previously acquired experimental results concerning their isothermal characterisation, are presented in Section 3.2.2.1. Furthermore, the fuel/air delivery system and the various thermocouples positioned around the system, are reported in Sections 3.2.3 and 3.2.4, respectively. Finally, in Sections 3.2.5 and 3.2.6, details of the OH^* chemiluminescence photography system and the exhaust gas analysis suite, are presented.

3.2.1 Atmospheric pressure generic swirl burner (APGSB)

To accommodate the experimental investigation of the three surface roughness swirlers, a new atmospheric pressure generic swirl burner (APGSB) was manufactured at Cardiff University, through conventional machining manufacturing techniques. The new burner, which was assembled in GTRC, was built with bulk geometric characteristics similar to the high-pressure generic swirl burner (Mk. II) (HPGSB-2), therefore enabling the comparison of the resultant measurements. In contrast to the HPGSB-2, the APGSB was utilised solely for atmospheric combustion and was positioned outside the high-pressure optical chamber (HPOC), which houses the HPGSB-2. Schematics of the cross-section and side view of the HPGSB-2, which shares the same geometric characteristics with APGSB, are presented in Figure 3.2.1-1(A) and 3.2.1-1(B), respectively. These figures are indicative of the various components that were assembled to form both HPGSB-2 and the newly manufactured APGSB. In-depth descriptions of HPGSB-2 and HPOC may be found elsewhere [238].

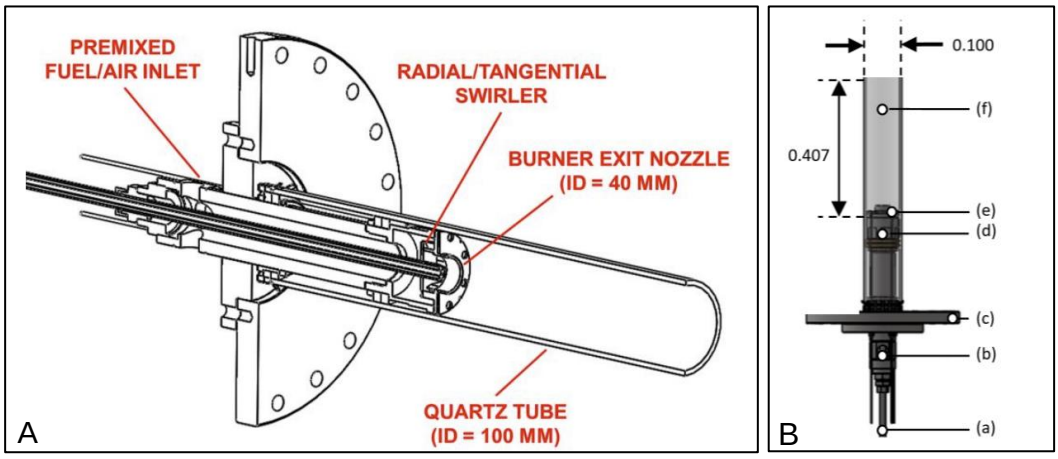

Figure 3.2.1-1 *(A): Cut-away schematic of HPGSB-2 with S_N=0.8 radial/tangential swirler installed (flow from left to right), (B): schematic of HPGSB-2 showing instrumentation and pilot lance (a), inlet plenum (b), HPOC connecting flange (c), mixing chamber (d), burner exit nozzle (e), and quartz confinement (f). Dimensions in meters. Source:* [238].

As for the HPGSB-2, the expansion ratio for the APGSB, calculated between the burner exit nozzle diameter (40 mm) and the inner diameter of the quartz tube (100 mm), was set at 2.5. The latter had a length of 0.407 m and acted as a confinement that directed the combustion products downstream, towards the exhaust gas sampling probe. For the current investigation, the burner was operated under fully premixed conditions, with a total premixing length of 0.7 m and a residence time of 20 ms at a bulk flow velocity of 30 m/s. The premix entered the system via two diametrically

opposed connections to the burner inlet plenum. Further details regarding the fuel/air delivering system are presented in Section 3.2.3. The burner also contained an 18 mm diameter instrumentation and pilot lance, which was inserted down the burner centreline and included seven 5 mm tubes used for instrumentation purposes, as shown in Figure 3.2.1-2. The central internal tube of the instrumentation and pilot lance can also be used for pilot fuel injection for future experimental investigations. Figure 3.2.1-2 shows that the face of the swirler within the combustion chamber is covered with a 3mm-thick ceramic coating for thermal protection. Three thermocouples are also indicated in the same figure, and were used for monitoring purposes. The complete set of thermocouples placed around the system is described in Section 3.2.4. Finally, as the burner is modular, its components can be replaced based on the investigation requirements. For the current investigation the three test swirlers were replaced successively. The geometric swirl number for all swirlers was kept constant at $S_N = 0.8$. In-depth descriptions of the three swirlers is provided in Section 3.2.2.

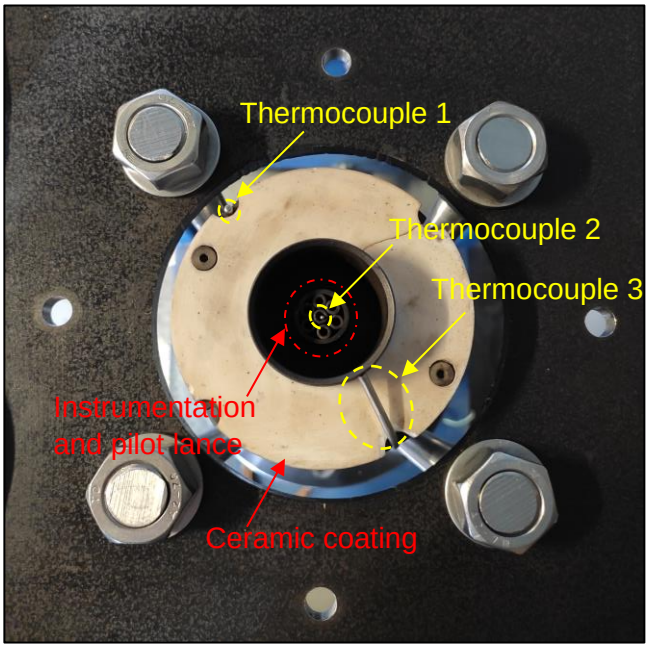

Figure 3.2.1-2 *Top view of the APGSB new burner, indicating the instrumentation and pilot lance, the ceramic coating, and the monitoring thermocouples.*

Although the APGSB has similar bulk geometric characteristics to HPGSB-2, it also includes some distinctive features that differentiate it from the latter. For instance, it is located outside the HPOC, hence, offering enhanced accessibility and observability, whilst its disassembly and maintenance is less complex. These were crucial operational improvements for the present experimental campaign which

required the successive testing of the three swirlers, and so the burner had to be disassembled frequently. Additionally, since it is located under one of the exhaust hoods of GTRC in vertical orientation, in contrast to HPGSB-2, which is located inside the HPOC housing under horizontal orientation, the heat loss performance of the APGSB is slightly improved, due to buoyancy force that is aligned with the flame orientation. It is also apparent that as the APGSB is positioned outside the HPOC, it can operate independently of the HPOC facility. As seen in Figure 3.2.1-2, the APGSB does not necessarily require the big *HPOC connecting flange* indicated in Figure 3.2.1-1, to operate, as it can be connected to the rig table using only the smaller flange. For future reference, it is noted that the *HPOC connecting flange* can readily be retrofitted to the APGSB, in case it must be operated inside the HPOC.

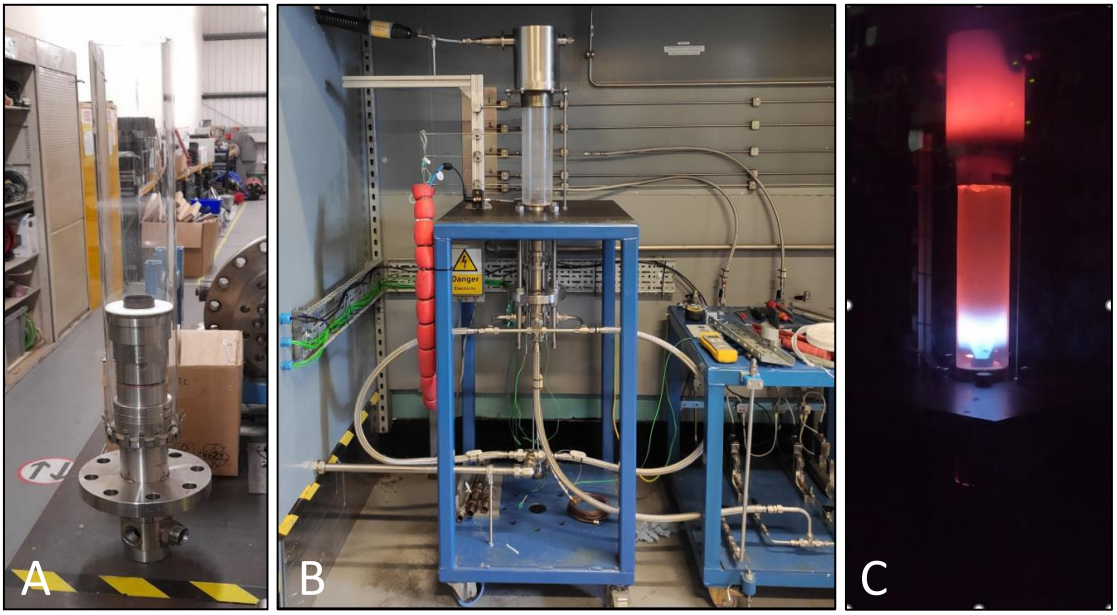

Figure 3.2.1-3 *(A): APGSB during assembly stage. (B): Assembled APGSB ready for commissioning. (C): APGSB during commissioning stage using pure* CH_4.

During the commissioning stage of the APGSB burner, excessive heat loss to the environment was noted, which could potentially risk the safe operation of the experimental facility by overheating the protective structures. This can be seen in Figure 3.2.3-3 (C), where during the commissioning stage the burner was glowing red. Thus, the test rig was slightly modified by the addition of metallic plates around the perimeter of the burner support structure, as indicated in Figure 3.2.1-4 (A). The plates were made from 0.9 mm thick Nimonic 80a alloy material, suitable for high temperature applications. Although this modification regulated the excessive heat loss to the environment, the optical access to the burner was reduced. As indicated in Figure

3.2.1-4 (B), a rectangular section was cut off the front metallic plate to enable the visual observation of the flame and to allow OH^* chemiluminescence measurements. It is worth noting that the same material was used for the construction of the sampling probe support structure, at the exhaust section of the burner, which can be seen in Figures 3.2.1-3 (B) and 3.2.1-4 (A).

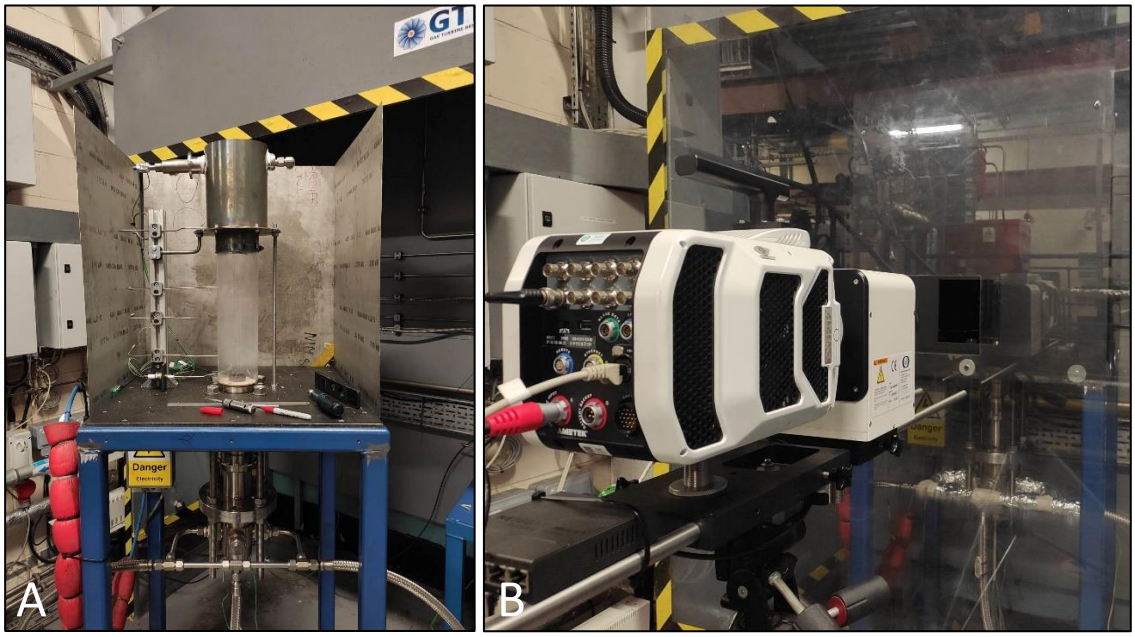

Figure 3.2.1-4 *(A) Modified test-rig with Nimonic 80a alloy plates added around it. (B) Final experimental set-up with the high-speed camera aligned in front of the APGSB burner.*

3.2.2 *AM-R*, *AM-G* and *Machined* swirlers

As explained in Section 3.1, the aim of the experimental investigation was to study empirically the influence of surface roughness on swirl-stabilised the lean premixed (LPM) combustion performance of conventional (CH_4) and alternative (H_2, CH_4/H_2) fuels. In this context, two additively manufactured (AM) swirlers, together with a conventionally manufactured one, all resulting in different surface roughness dimensions, were studied under atmospheric pressure and elevated temperature, via the newly atmospheric pressure generic swirl burner (APGSB) (Section 3.2.1). The two AM swirlers were fabricated as part of a previous experimental investigation undertaken by Runyon et al. [29] in Cardiff University's GTRC. As presented in [29], the bulk geometric characteristics of these three components were identical, resulting in a geometric swirl number of 0.8. The design of the AM swirlers *(AM-G, AM-R)* aimed to replicate the design of the *Machined* swirler, routinely deployed at GTRC which had been manufactured out of 304 stainless steel through conventional subtractive

methods, at Cardiff University. As its name implies, the *Machined* swirler, had undergone machining post-processing to reduce its surface roughness. This swirler is part of the 2nd generation high-pressure generic swirl burner (HPGSB-2), which has already been extensively characterised in terms of stable operating limits, fuel flexibility and emissions performance [238–241].

Concerning the two AM swirlers, *AM-R* and *AM-G* were manufactured by HiETA Technologies Limited in Bristol, England using a Renishaw RenAM 500Q power bed SLM, out of Inconel 625 powder. Both swirlers commonly underwent a post-build heat treatment to minimise residual stresses caused during the printing process, whilst only the *AM-G* swirler was additionally post-processed, since it was subjected to manual grit-blasting, to reduce its surface roughness further. The third swirler, namely *AM-R*, did not undergo any post-processing activity and thus resulted in the highest surface roughness [29]. The three swirlers are shown in Figure 3.2.2-1 from roughest to smoother (left to right). Their nozzle inner diameter and vane spacing were identical at 40 mm and 7.5 mm, respectively. Since their design was based on the geometric characteristic of the conventionally manufactured *Machined* swirler, the analytic design of the latter, and consequently the complete dimensions of these swirlers can be found in [238].

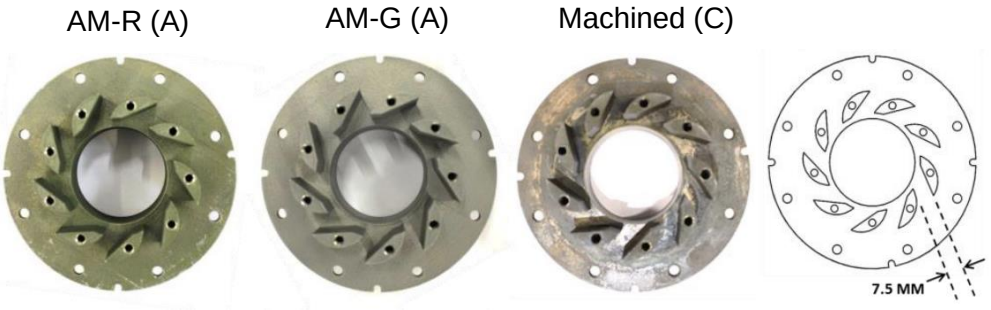

Figure 3.2.2-1 *AM swirler vanes, S_N=0.8, AM-R (A), AM-G (B), Machined (C). Source:* [29].

Regarding the physical properties of the materials utilised for their fabrication, the 304 stainless steel and Inconel 625 are characterised by similar properties. In terms of specific heat capacity, Inconel 625 results in ≈410 J/(kgK), whilst for 304 stainless steel the analogous property is equal to ≈500 J/(kg·K). Moreover, with respect to thermal conductivity, Inconel 625 and 304 stainless steel result in ≈9.8 W/(m·K) and ≈16.2 W/(m·K), respectively [242, 243]. This ensures that the three swirlers will have similar thermal behaviour under the assumed combustion conditions.

With regards to the quantification of surface roughness for the three swirlers, a Taylor Hobson Form Talysurf Series 2 profilometer was used to provide actual measurements of surface roughness over 5 selected regions for each swirler, as described in [29]. These characterised regions correspond to nozzle internal diameter *(ID)*, swirl base *(SB)*, swirl curve *(SC)*, swirl curve length *(SCL)* and swirl flat length *(SFL)*, as shown in Figure 3.2.2-2. Specifically for the nozzle internal diameter, nine measurements were conducted, for each swirler, at 40^{o} intervals. Further information about the measuring procedure can be found in [29].

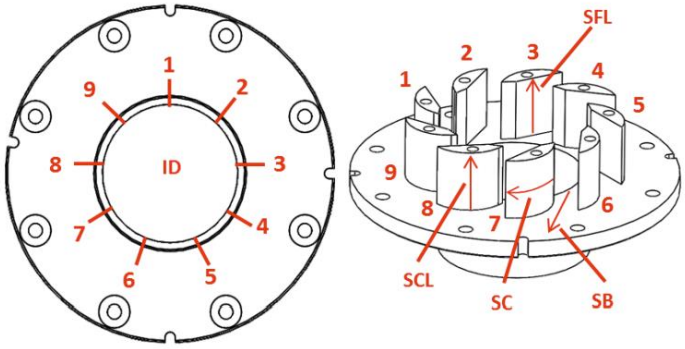

Figure 3.2.2-2 *Surface roughness measurement locations of AM and Machined swirlers. Source* [29].

The resultant measurements are listed in Table 3.2.2-1, where the arithmetic average surface roughness *(R_a)*, RMS surface roughness *(R_q)* and ten-point average surface roughness as a measure of 5 highest peaks and 5 lower valleys *(R_z)*, are listed. Excluding the base of the swirler, which resulted in substantially higher measured roughness, the arithmetic average surface roughness *(R_a)* of the *Machined* swirler (≈1.1 μm) was found ≈22% of that for the *AM-G* (≈5.1 μm) and ≈13% of that for the *AM-R* (≈8.5 μm). For easier comparison, the values of 1 μm, 5 μm and 9 μm are considered as the approximate averages of the *Machined, AM-G* and *AM-R* swirlers, respectively. It is worth noting that the surface roughness values of the *AM-R* swirler, are similar to the ones reported in the literature for “raw” AM parts of that did not undergo any post-processing activity [29].

Table 3.2.2-1 *Average surface roughness measurements for each generic swirler. Source* [29].

	Measurement location (‖ or ⊥, relative to ALM build direction)					
Swirler	**Measurement**	**Nozzle ID** (‖)	**Swirler Base** (⊥)	**Swirler Curve** (⊥)	**Swirler Curve Length** (‖)	**Swirler Flat** (‖)
AM-R	R_a (μm)	8.88	11.09	8.31	8.31	8.59
	R_q (μm)	10.97	14.92	10.29	10.14	10.64
	R_z (μm)	53.61	78.11	50.01	47.91	54.06
AM-G	R_a (μm)	5.48	8.12	5.13	4.73	4.92
	R_q (μm)	6.96	10.36	6.36	6.05	6.21
	R_z (μm)	35.5	49.57	31.15	31.06	33.54
Machined	R_a (μm)	1.39	1.76	0.67	0.97	1.26
	R_q (μm)	1.88	3.31	1.04	1.24	1.75
	R_z (μm)	8.96	11.21	4.27	6.12	9.07

Apart from the quantification of the surface roughness, the experimental study undertaken by Runyon et al. [29], aimed to characterise additionally the isothermal axial velocity profile of the three swirlers. Utilising the HPOC and the HPGSB-2 under unconfined configuration, isothermal 1D Laser Doppler Anemometry (LDA) measurements were undertaken, and the corresponding axial velocity profiles across the radial dimension of the three swirlers derived. Both the surface roughness quantification and the velocity characterisation are of paramount importance for the present computational investigation and modelling of surface roughness, presented in Chapter 5. The surface roughness measurements, listed in Table 3.2.2-1, were used to calculate the equivalent sand-grain roughness values, upon which the computational modelling of surface roughness in CFD was achieved. Subsequently, to evaluate the predictive performance of the CFD simulations, with respect to capturing the effect of surface roughness, the isothermal axial velocity profiles (presented in following Section 3.2.2.1) were compared against the computationally predicted ones.

3.2.2.1 *Isothermal axial velocity distributions*

The data collected from the 1D LDA measurements of the isothermal axial velocity distributions of the three various surface roughness swirlers, are plotted in Figure 3.2.2.1-1. These measurements took place under atmospheric pressure, whilst

the inlet air temperature and mass flowrate were kept constant at 300 ± 5 °C and 0.016 kg/s, respectively. This yielded a Reynolds number of ≈17,500 and a mean axial velocity, at the exit of the nozzle, of 20.7 m/s. These flow conditions were equivalent of lean premixed combustion at $\varphi = 0.55$. The measurements were conducted 5 mm above the exit of the nozzle, starting from the burner centreline *($x = 0$)* and moving radial towards the final position *($x = 30$ mm)*, with increments of 0.5 mm for $0.015 \text{ m} \leq x \leq 0.025$ m and 1 mm for the rest of the radial coordinates. From Figure 3.2.2.1-1, where the velocity distributions of *AM-R, AM-G* and *Machined* swirlers are plotted, it is evident that with increasing surface roughness, the positive outward flow (≈ 0.011 m $\leq x \leq \approx 0.030$ m) was shifted radially towards the centreline of the burner, whilst the peak axial velocities *(≈ 0.018 m $\leq x \leq \approx 0.020$ m)* decreased. The reduction in peak axial velocities was attributed to the increased pressure drop, owing to the higher surface roughness.

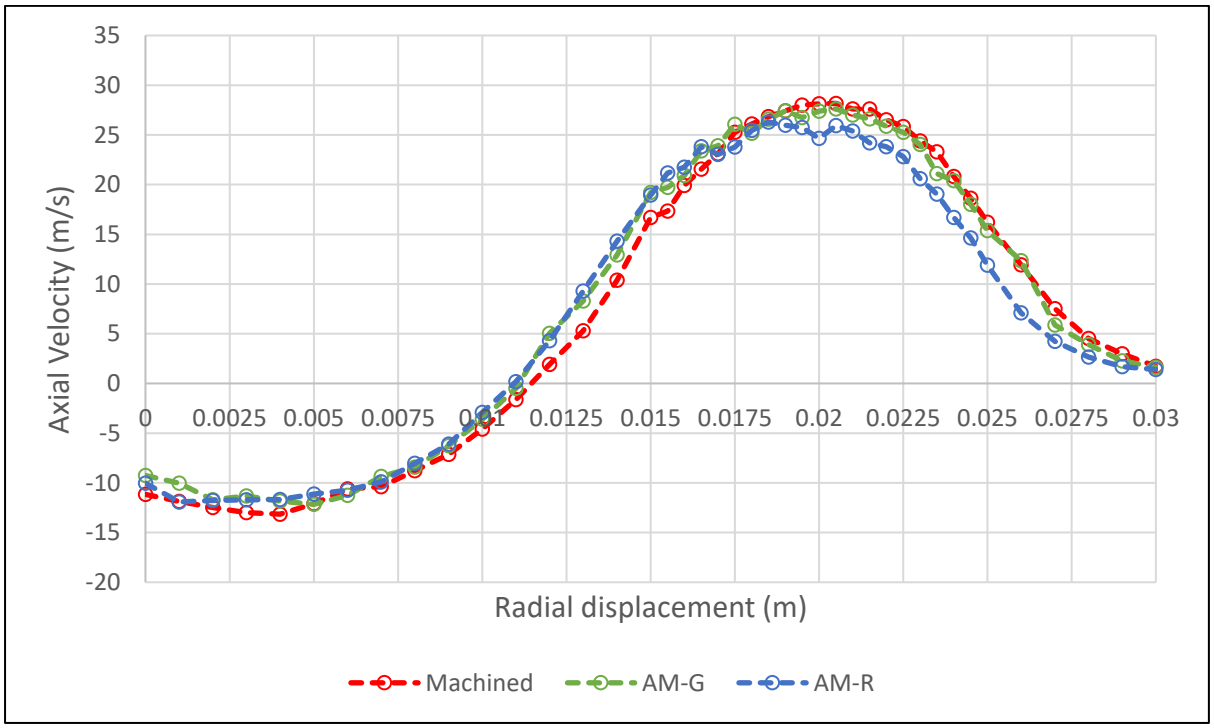

Figure 3.2.2.1-1 *1D LDA Isothermal axial velocity distribution across the radial dimension of Machined, AM-G and AM-R swirlers.*

As shown in several publications, for radial/tangential swirler burners, the flow field is symmetric with respect to its axis of rotation [152–154, 244]. Since for this study, the measurements were conducted across the radius of the swirler covering only half of the diameter, the symmetry of the flow cannot be verified. However, the results plotted in Figure 3.2.2.1-1, show that the axial velocities were increasing as

approaching the centreline of the burner. The geometry and configuration of HPGSB-2 did not justify an increasing axial velocity distribution towards the centreline of the burner. Since central injection was not used for this experimental programme, and the central bluff body was only utilised for instrumentation purposes, at the centreline position ($x = 0$), the axial velocities should had attained a maximum (negative) value due to the reverse flow of the central recirculation zone induced by the swirler.

Therefore, the increasing axial velocities from $x \approx 0.004\ \mathrm{m}$ to $x = 0$, indicates a small potential measurement error of a few millimetres. Taking into consideration the remarks above, the distributions of the axial velocity for the three swirlers were shifted equally radially towards the centreline of the burner ($x = 0$), so that the peak (negative) axial velocities were almost coincident with the axis of rotation (centreline, $x = 0$). As the LDA might result in small inconsistencies regarding the measured velocities, the mere examination of the peak (negative) axial velocity to determine the correct shifting of the velocity curves, might be insufficient. Thus, the appropriate shifting of velocity curves was majorly based on flow symmetry in the near vicinity of the centreline. As Roux et al. in [154] and Wang et al. in [153] point out, the production of perfectly symmetrical flow through LDA experimental measurements, especially in the region 5 mm downstream of the swirler burner nozzle, is “significantly challenging”. Therefore, to estimate the appropriate shifting of the velocity distribution, two separate cases were investigated, in which the velocity profiles were shifted 3 mm and 4 mm, accordingly. For each case, the percentage difference of the velocities in the range of $-0.003\ \mathrm{m} \leq x \leq 0.003\ \mathrm{m}$ with respect to the centreline velocity, was estimated. The results are plotted in Figures 3.2.2.1-2, 3.2.2.1-3 and 2.2.2.1-4 for the *Machined*, the *AM-G* and the *AM-R* swirlers, respectively.

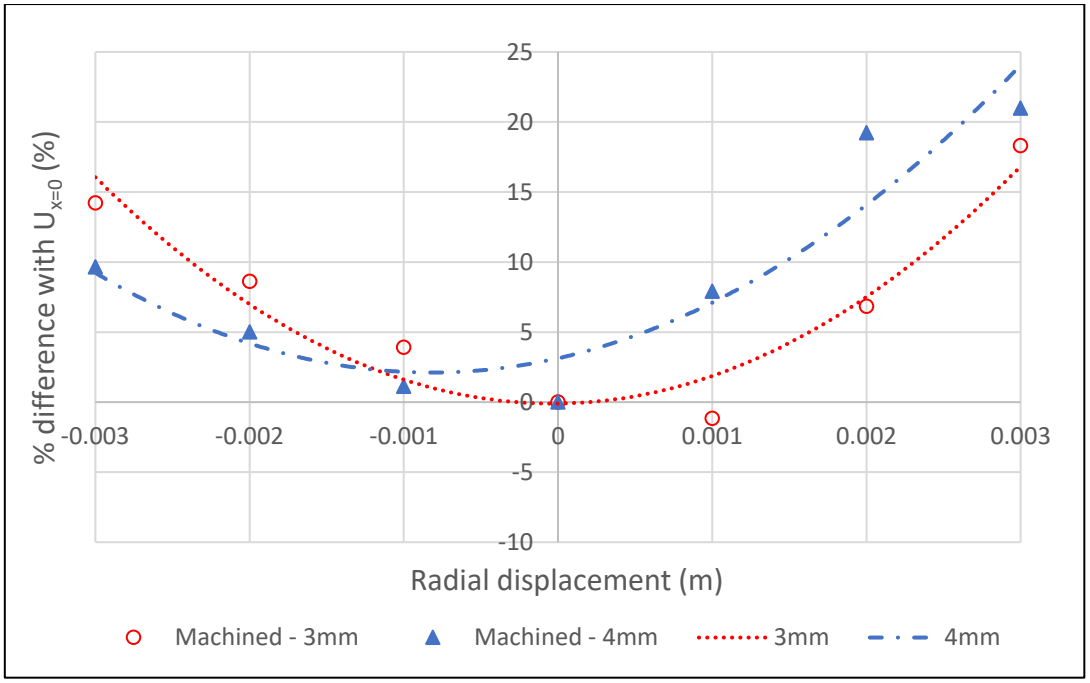

Figure 3.2.2.1-2 *Percentage difference between U_x (-0.003 m ≤ x ≤ 0.003 m) and $U_{x=0}$ of Machined swirler for 3 mm and 4 mm inwards radial shifting.*

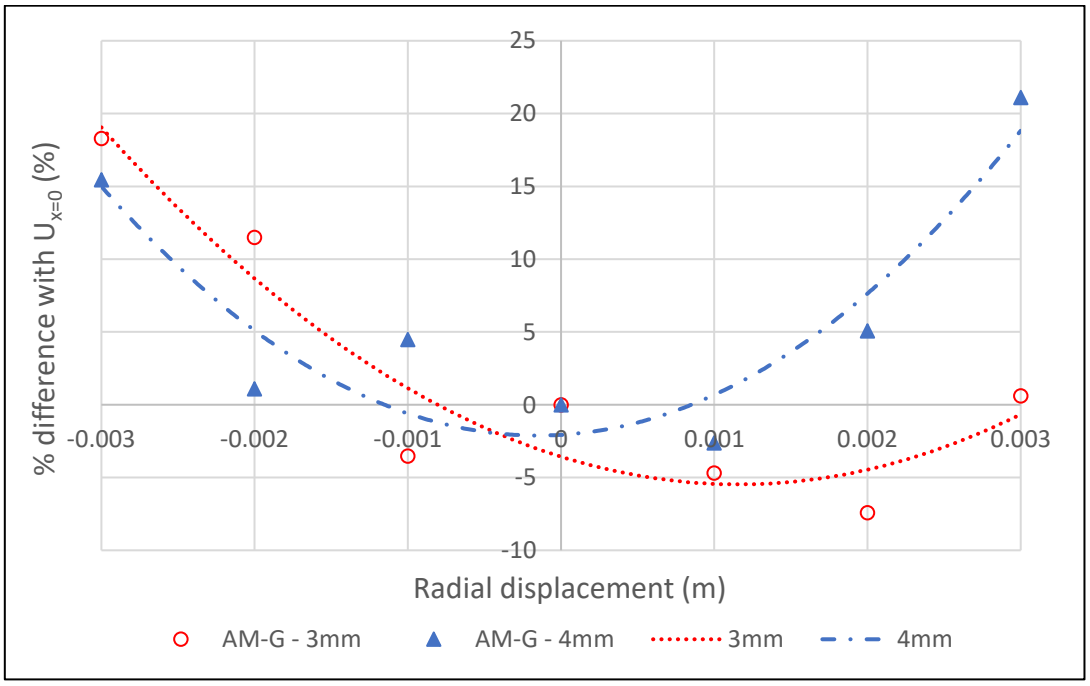

Figure 3.2.2.1-3 *Percentage difference between U_x (-0.003 m ≤ x ≤ 0.003 m) and $U_{x=0}$ of AM-G swirler for 3 mm and 4 mm inwards radial shifting.*

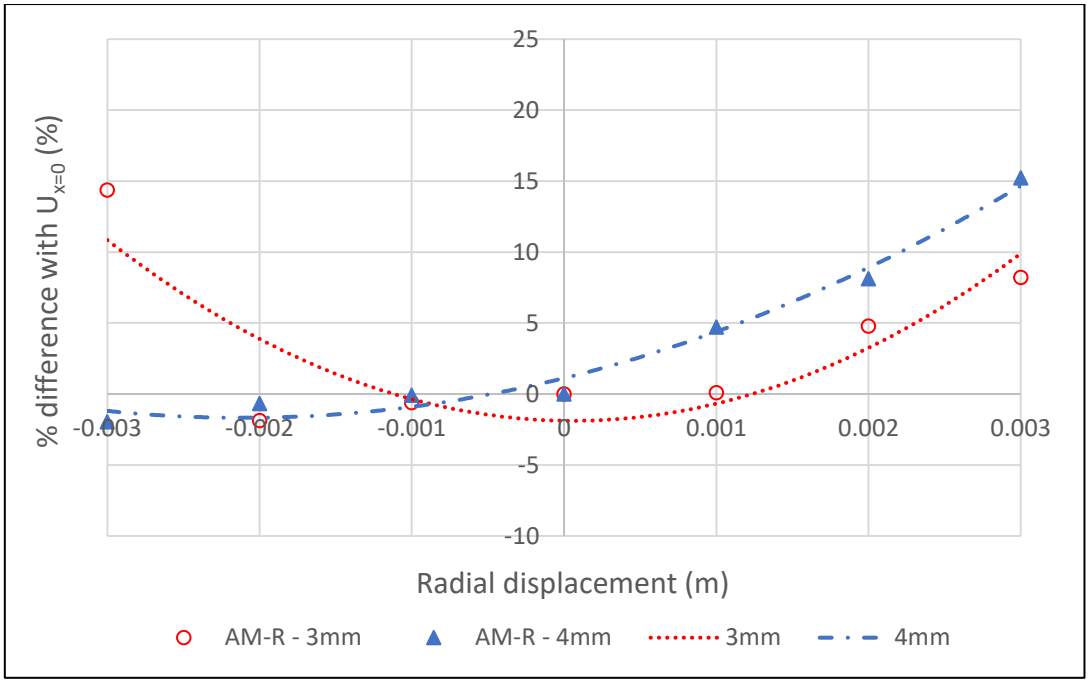

Figure 3.2.2.1-4 *Percentage difference between U_x (-0.003 m ≤ x ≤ 0.003 m) and $U_{x=0}$ of AM-R swirler for 3 mm and 4 mm inwards radial shifting.*

The percentage difference between the axial velocities U_x for $-0.003\ \mathrm{m} \leq x \leq 0.003\ \mathrm{m}$ and the centreline axial velocity *($U_{x=0}$)*, was plotted for the three swirler cases to estimate the appropriate radial shifting of the velocity curves. Since the estimation was mainly based on the swirling flow symmetry, a second order polynomial equation was fitted to the plotted points, as indicated in Figures 3.2.2.1-2, 3.2.2.1-3 and 3.2.2.1-4. Since the distribution of the points changed for either 3 mm or 4 mm radial shifting, the fitting of the second order polynomial equation to the corresponding distributions, was indicative of the level of symmetry with respect to the central axis. Since for the *Machined* (Figure 3.2.2.1-2) and the *AM-R* (Figure 3.2.2.1-4), the 3 mm shifting results in significantly enhanced symmetry, all velocity curves were shifted accordingly 3 mm. For the case of the *AM-G* (Figure 3.2.2.1-3), the 4 mm shifting resulted in better symmetry, however, since the axial velocity curves were equally shifted to maintain their relative difference, the latter was also shifted 3 mm. The shifted axial velocity profiles are presented in Figure 3.2.2.1-5, together with the respective unshifted ones. As it will be shown in Chapter 5, the computationally predicted isothermal velocity profiles are in very good agreement with the 3 mm shifted experimental isothermal axial velocity profiles of the three swirler cases.

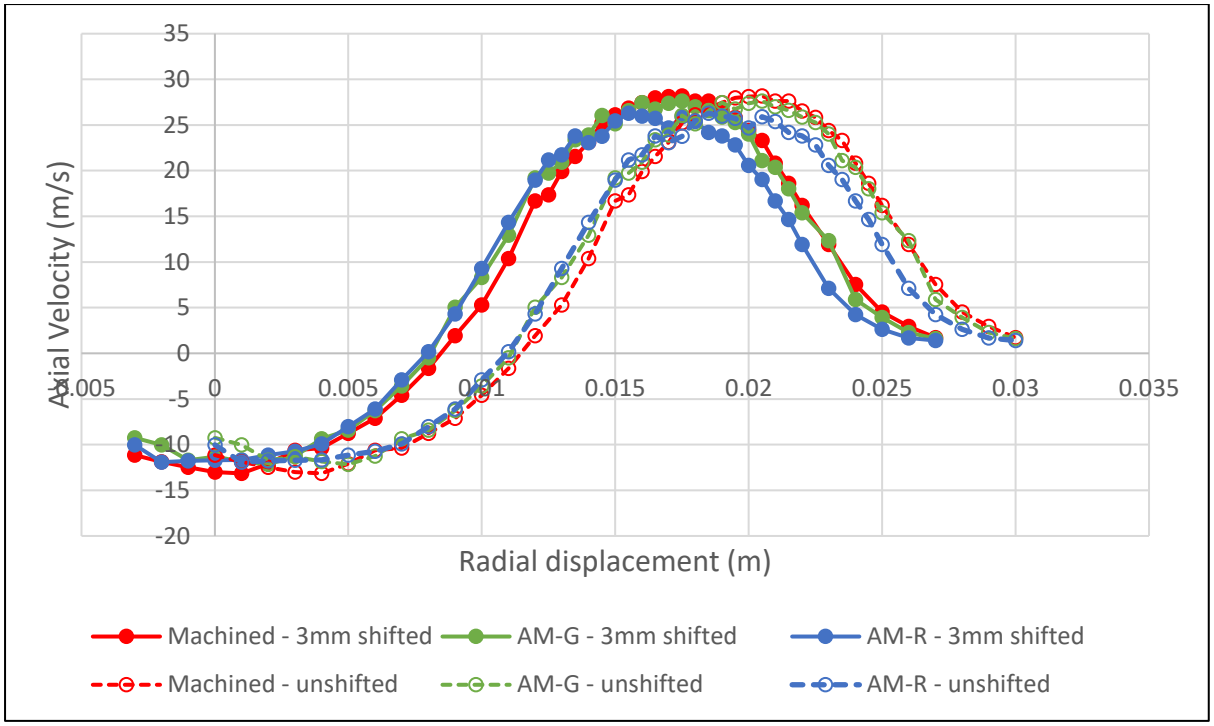

Figure 3.2.2.1-5 *Comparison between shifted and unshifted isothermal axial velocity distributions for Machined, AM-G and AM-R swirlers.*

3.2.3 Air and fuel delivery system

The air and fuel supply to the APGSB was achieved through a dedicated delivery system, designed for high repeatability and precise control over fuel and air flows. The system comprised of a variable speed drive (VSD) air compressor, air dryer, air preheater, flow control valves (FCV) and Coriolis mass flow (CMF) controllers, as indicated in the simplified schematic presented in Figure 3.2.3-1.

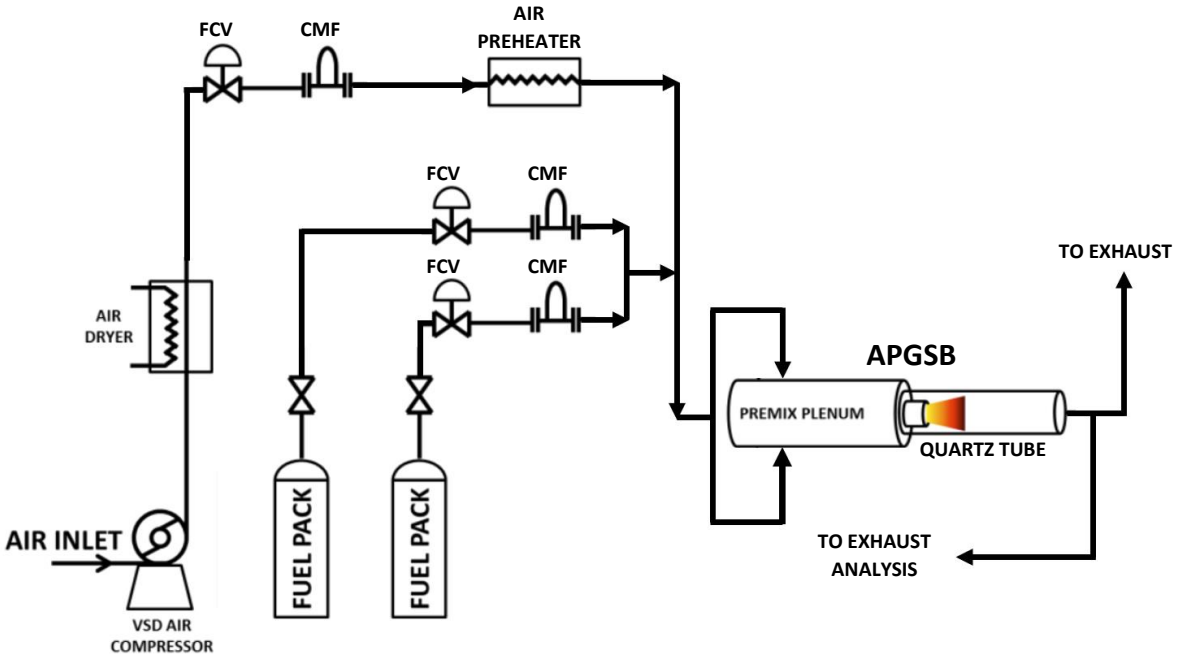

Figure 3.2.3-1 *Simplified schematic of the air and fuel delivery system for premixed and preheated operation of APGSB at GTRC. Reproduced by* [238].

Concerning the fuel delivery, Bronkhorst mini CORI-FLOW^{TM} M14V11l mass flow controllers were used, with an uncertainty of ±0.5% of flowrate, providing up to ≈8 g/s of fuel. Concerning the air delivery, an IN-FLOW F-203Al industrial style thermal mass flow controller was employed, with an uncertainty of ±0.5% of flowrate, supplying up to ≈25 g/s of air. For the limited cases where additional air was required, particularly for H_2 combustion, the latter was connected in parallel with a Bronkhorst mini CORI-FLOW^{TM} M14V11l mass flow controller. For all the mass flow controllers utilised, their uncertainty values were expected to be maintained constant, across the experimental range, as flows were typically above 10% of the nominal flow rate capacities. The fuel and air mass flow controllers were handled remotely through a computing system connected to the research facility network, in which the appropriate mass flowrate was input by the user.

Concerning the air supply chain, an Atlas Copco GA 45 variable speed drive (VSD) air compressor coupled with a Beko Drypoint DPRA960 air dryer were utilised to provide the required combustion air, and to lower its dew point. Followingly, the air was passing through the air preheater facility, before being mixed with the fuel. As shown in Figure 3.2.3-2, the preheated air (blue dotted line) was driven to the system through two flexible hoses, before being mixed with the incoming fuel (brown dotted line). Followingly, the premixture entered the system via two diametrically opposed

connections to the burner inlet plenum (yellow arrows). The fuel was supplied from multi-cylinder packs, stored in a remote onsite location.

Figure 3.2.3-2 *APGSB test rig during commissioning stage, indicating air (blue dotted line), fuel (brown dotted line) and mixture (yellow arrows) delivery paths.*

3.2.4 Thermocouples

To quantify the combustion performance of the three various surface roughness swirlers, while monitoring the system and ensuring safe and reliable operation, several *K-type* thermocouples were placed around the APGSB. As shown in Figures 3.2.4-1 (A) and (B), 8 thermocouples, referred as *"TC"*, were located around the combustion chamber of the burner.

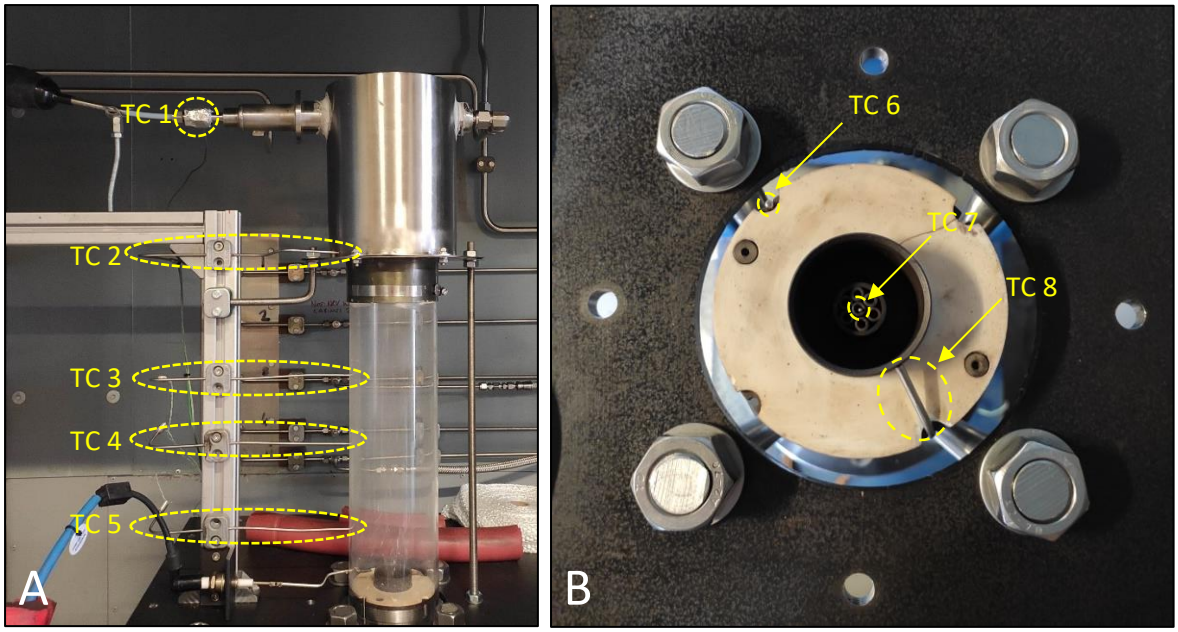

Figure 3.2.4-1 *(A) Front view of the APGSB showing the various thermocouples along its axial dimension. (B) Top view of the APGSB showing the various thermocouples placed around the swirler.*

An exposed junction thermocouple *(TC 1)* was placed around the water-cooled emissions probe to monitor the temperature of the latter. The rest of the thermocouples used were all covered in 310 stainless steel sheaths. These thermocouples were suitable for continuous exposure up to $+1100\ ^{o}\mathrm{C}$, with a maximum temperature rating of $\approx 1350\ ^{o}\mathrm{C}$. As shown in Figure 3.2.4-1 (A), *TC 2* was inserted inside the support structure of the sampling probe in order for the tip of the thermocouple to be located at the centreline of the burner. In this way, the exhaust thermocouple temperature measurements presented in Sections 6.3, 7.2.2 and 7.2.3, were collected. Additional three thermocouples, namely, *TC 3, TC 4* and *TC 5*, were placed along the axial dimension of the quartz glass confinement at fixed positions, as shown in Figure 3.2.4-1 (A). To achieve this, the quartz tube was drilled halfway through its thickness (≈1.5 mm) so that the thermocouples penetrated halfway through the glass wall (≈0.75 mm). Finally, as presented in Figure 3.2.4-1 (B) three thermocouples, *TC 6, TC 7* and *TC 8*, were located near the swirler, measuring the temperatures corresponding to burner face, pilot bluff body tip and burner nozzle outer diameter, respectively. Finally, an additional thermocouple (not shown in Figure 3.2.4-1) was placed in the centreline of the inlet plenum, to monitor and record the reactants inlet temperature.

The range of measuring uncertainty with respect to the K-*type* thermocouples that were used, was provided by the manufacturer equal to $\pm 2.2\ ^{o}\mathrm{C}$. The temperature

data was captured by a dedicated computer system connected to the National Instruments data acquisition system via the facility network. The data was logged with a frequency of 10 Hz, whilst the measured values were monitored in real time. In this way, useful data was provided with respect to the state of the combustion process. Through close, live monitoring of the thermocouples logged values, the identification of ignition, blow-off and flashback events, was enabled, whilst the assumed “steady-state” conditions, under which the measurements were undertaken, could be confirmed. In general, the placement of several thermocouples around the system ensured the safe and reliable operation of the burner, while providing fundamental information concerning the state, the performance and the level of repeatability of the combustion process.

3.2.5 Chemiluminescence (CL) measurements

Chemiluminescence measurements are part of the non-intrusive optical measuring techniques, which has gained significant attention over the past decades in the context of fundamental combustion studies both in academia and in the industry. As non-intrusive diagnostic tools do not physically interact with the investigated flow field, they provide a realistic, undisturbed view of the flow quantities of interest. The development of such equipment allows the close investigation of flame characteristics (position, shape, width, reaction zones and flame front) under both laminar and turbulent conditions [245]. Excellent analytic reviews of the use of non-intrusive diagnostic techniques, including LIF, PLIF and CL applications that enabled measurements in combustion environments, as well as fundamental investigations of combustion phenomena that led to the development of modern GTs, can be found in literature [246, 247]. In the industrial world, non-intrusive measurements are not only employed to gain advanced knowledge on fundamental concepts such as the influence of hydrogen enrichment on natural gas flame dynamics [248] or the complex processes of fuel/oxidant mixing [249], but also used to enable the optimisation and development of the future gas turbines [250].

The present experimental campaign focuses on the use of OH^* CL for enabling quantitative measurement of the fundamental flame characteristics (shape, location, size, relative heat release). As demonstrated in the literature, for laminar diffusive CH_4 flames, OH^* distribution is more representative of the flame structure, compared to CH^*, as the former covers a wider spectrum of the flame region whilst OH^* radicals are

located closer to flame front [251]. Whilst combining multiple optical, diagnostic techniques is very challenging and not considered essential to fulfil the goals of this thesis, it is suggested that future studies could add high-speed PIV for detailed flow field characterisation. This section is specifically concerned with the description of the method for capturing OH^* CL data together with relevant previous work from the literature.

Chemiluminescence (CL) measurements are concerned with the investigation of the electromagnetic radiation spectra emitted from electronically excited intermediates or products, due to a chemical reaction, such as oxidation [252]. The detection of OH^* through CL has been improved significantly in the last 70 years, reducing the required exposure time from 30 minutes [253] down to 10 μs [29]. Currently, the investigation of OH^* CL emissions can be achieved both numerically via the use of advanced chemical kinetics models [254], and experimentally to enable fundamental combustion research [255, 256] or to optimise industrial scale GTs [248, 257]. In figure 3.2.5-1, a typical chemiluminescence spectra of a premixed flame consisting of natural gas and air is presented, indicating the relationship between light intensity and equivalence ratio [258]. It may also be observed that radicals OH^*, CH^*, C_2^* and broadband CO_2^* are all contributing to the lean premixed combustion of natural gas-air flame, thus also to CL emissions.

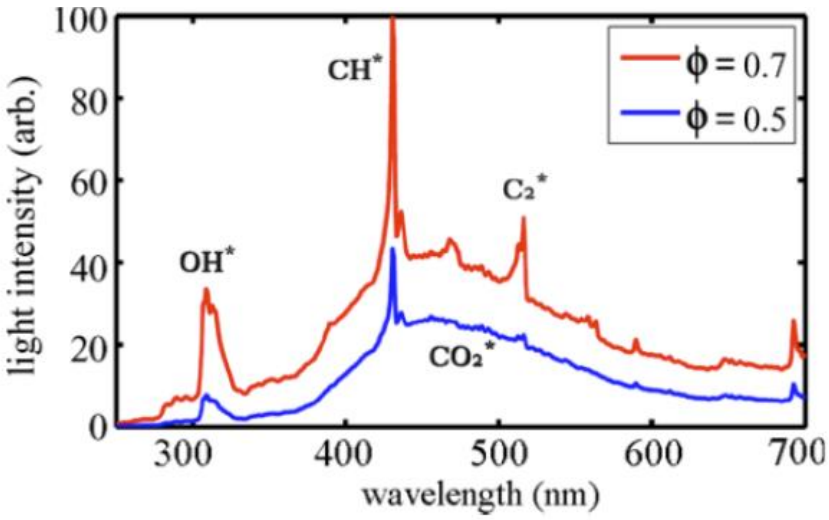

Figure 3.2.5-1 *Generic chemiluminescence spectra of natural gas/air flame at various φ. Source:* [258].

It is apparent in Figure 3.2.5-1 that OH^* CL peaks around $\lambda_w \approx 309$ nm, which corresponds to $A^2\Sigma \rightarrow X^2\Pi$ electronically excited to ground state energy level transition

[250]. To filter out the broadband light emissions from CO_2^*, while also capturing the spontaneous OH^* emissions, the use of a bandpass filter is required. In the case of OH^* CL measurements, the bandpass filter that corresponds to the peak wavelength of 309 nm must be integrated with the camera. The dominant chemical production reaction for the formation of OH^* are $CH+O_2 \leftrightarrow OH^*+CO$ [250, 254, 259] and $H+O+M \leftrightarrow OH^*+M$ [259].

The importance of the investigation of OH^* and CH^* emissions is highlighted by their contribution in the context of fundamental combustion research. Specifically, those studies are concerned with the investigation of flame structure [29, 239, 251, 260, 261], heat release [256, 262] and equivalence ratio [259, 263]. As it is presented in Figure 3.2.5-2, where the simplified reaction mechanisms for the oxidation of CH_4 is presented [264], OH^* and CH^* are formed from different reaction side-paths of the CH_4 oxidation process, and therefore there is no direct relationship between OH^* or CH^* chemiluminescence and the heat realise of the flame [256]. However, Haber [265] proved that the ratio of OH^*/CH^* ratio clearly characterises the air-fuel ratio of the reaction. Hence, estimating the air-fuel ratio using CL, heat release can be calculated from the second law of thermodynamics, taking into consideration the density of the air-fuel mixture, the heat capacity, the fluid velocity and the fluid temperature. This method has been widely used and developed previously to estimate equivalence ratio in a single point [259, 263, 266], as well as in 1D and 2D spatial resolution [256]. Furthermore, it should be pointed out that CL measurements have recently emerged to the validation process related to CFD numerical simulation activities. The line-of-sight measurements of CL is compared to 2D and 3D reconstruction of flame front to enable advances in modelling of boundary layer flashback phenomena [172] or characterisation of CRZ and heat release in swirling flows [267, 268], highly relevant to the objectives of this research.

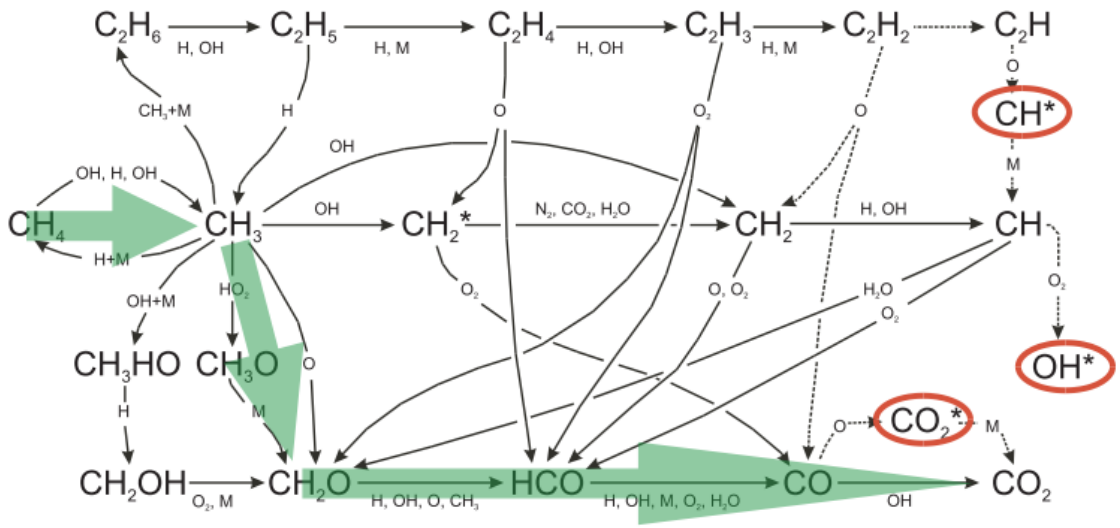

Figure 3.2.5-2 *Simplified mechanisms of CH_4 oxidation. Source:* [264].

The present experimental campaign utilises a newly manufactured improved version of the HPGSB-2 set-up, in vertical orientation, which operates under atmospheric pressure and elevated temperature. To be able to compare the present experimental results with previous data, the high-speed OH^* CL image capture system was set-up in accordance with previous experimental campaigns [29]. Specifically, the system is comprised of: a monochromatic high-speed camera (Vision Research Phantom v1212), with 72 Gb on-board memory and up to 12,000 frames/second at full resolution (1280 x 800) and bit depth of 12 bits, oriented 90º to the HPGSB-2; a high-speed image intensifier (Specialised Imaging Limited SIL40HG50) with UV-enhanced S20 photocathode, suitable for capturing up to 100,000 frames/second; a UV lens (Ricoh FL-GC7838-VGUV, f/16) and a 310 nm narrow bandpass filter. For this experimental campaign, the system was set at 4000 Hz, with the exposure time of the image intensifier at 10μm and the gain held constant for each fuel across all the investigated range of equivalence ratios. To capture the images, the system was triggered and controlled remotely from a dedicated computer system running the Vision Research PCC 2.8 and Specialised Imaging Limited SILControl2 software. For the calibration of the camera resolution a target image was located at the centre of the burner nozzle, providing the resolution of ≈3.46 pixels/mm. To reduce the recording time and so save space requirements, the camera resolution was set at a lower resolution of 544x648 pixels, in x and y coordinated respectively. Hence, the resulting field of view was ≈157 mm and ≈162 mm, in radial (x) and axial (y) direction.

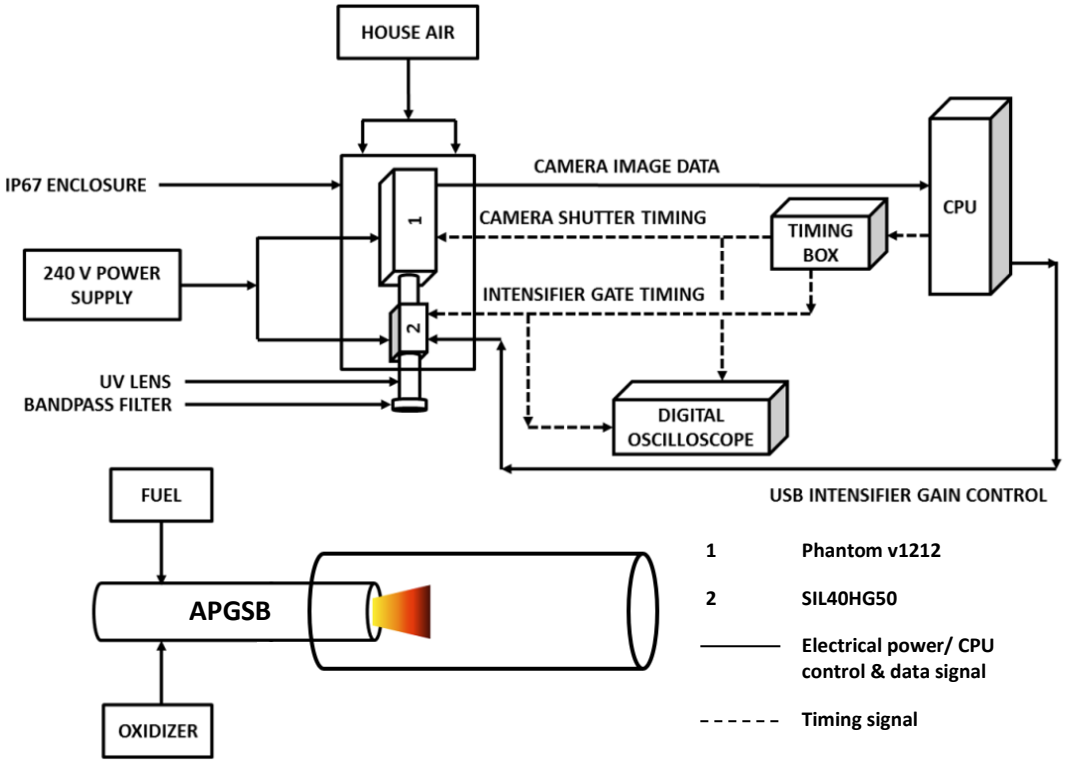

Figure 3.2.5-3 *Simplified schematic of the CL measuring system timing, image capture and utility setup at Cardiff University's GTRC, as used for measurements with the APGSB. Reproduced by* [238].

The chemiluminescence measuring system described above has been commissioned for the use of the generic swirl burner at Cardiff University's GTRC and has been extensively used in previously published work [29, 238–241, 260, 261, 269–271] to accommodate several experimental studies. A simplified schematic of the CL measuring system is shown in Figure 3.2.5-3. A detailed description of the specific components that were used under the commissioning process is presented and analysed in-depth in [238], comprising a parametric analysis of the influence of camera and intensifier parameters on CL results. For the HPGSB-2 configuration, flame characteristics measurements were conducted for CH_4-H_2 [239] and for CH_4 with Exhaust Gas Recirculation (EGR) combustion [261], while humidified high-CO syngas [240, 241] and diluted oxymethane [260] flame measurements have been also conducted using the HPGSB. The development of the CL facility also enabled experimental heat release distribution studies of pure CH_4 and high-CO syngas [269], NH_3 [270, 271] and biodiesel [272], which took place using the HPSGB.

One of the main issues regarding OH^* CL measurements is the line-of-sight integration. As CH_4-air flames are not generally optically dense, the radiated light is

not absorbed back into the flame. Therefore, the camera sensor captures all the intensities along the line-of-sight, including those at the front and at the back of the focal plane [256]. A solution to this problem is provided through deconvolution algorithms, which can be used to obtain the spatially resolved line-of-sight integrated signals [273]. Applying this former technique requires radial symmetry, thus for turbulent flames it is only valid for time/phase averaged measurements [256]. Due to the complexity and the highly variable structure of the turbulent premixed swirling flame that is analysed in the present study, only time averaged OH^* CL images are processed to provide symmetrical distribution in the radial direction. The description of the Abel inversion algorithm that was selected to accommodate the deconvolution of the time averaged signal is presented in the following sub-section 3.2.5.1

3.2.5.1 *OH^* chemiluminescence (CL) post-processing*

As it was described in the previous section 3.2.5, there are multiple ways of conducting the experimental measurements of OH^* CL, as well as numerous options for studying and presenting their outcomes. The reporting and use of time-averaged intensity values of the OH^* CL is commonly practised [241, 267, 274], where techniques such as the background intensity subtraction [263] and the implementation of various deconvolution algorithms, like the Abel transformation, are preferred [241, 251, 256, 263]. For the processing of the data that were collected during the present experimental study, several image processing techniques were combined, such as noise filtering using a 3x3 pixel median filter, background intensity subtraction and temporal averaging. These techniques were used along with a modified open-source MATLAB code developed by Killer [275], which is based on the Abel transformation method reported by Pretzel [276]. Thus, the OH^* CL images that were collected through the Vision Research PCC 2.8 software, were fed into the corresponding deconvolution algorithm, written in MATLAB, for the line-of-sight integrated signal to be spatially resolved.

The selected Abel inversion code is based upon a Fourier-series-like expansion, in which the radially distributed pixel intensity function is projected onto a theoretical 2D plane through cosine expansion. The number of cosine expansions that is used for the image reconstruction is a majorly influencing parameter for both computational time and intensity distribution filtering effects [276]. For the post-processing of the present results, five cosine expansions have been selected. As

explained earlier, the underlying assumption for the implementation of Abel deconvolution algorithm is the symmetry of the flame with respect to the central vertical axis. The use of quartz confinement (as described in Section 3.2.1) combined with the investigated radial-tangential swirler, gave rise to a conical shape flame in which the axial and tangential velocity are, in theory, symmetric about their central axis.

Thus, the swirling flame was expected to be symmetric about its rotating, vertical central axis. However, as shown in Figure 3.2.5.1-1 (A), where the spectrum distribution of a time averaged OH^* chemiluminescence image of CH_4 combustion under stoichiometric conditions is presented, a small variation in flame shape is observed, whilst the left side of the flame results in higher intensity values. The phenomenon of a theoretically symmetrical flame resulting in a time averaged OH^* CL image of an asymmetric flame, was also pointed out by Stopper et al. in [277], who attributed the observed visual asymmetry to the inhomogeneous opacity of the optical access, due to an asymmetric temperature distribution within the combustion chamber. However, the author did not provide qualitative evidence for this hypothesis.

This motivated the present study to examine if such hypothesis is valid, and to prove if, in fact, there is an optical medium related effect that increased the relative intensity at the left side of the flame, as presented in Figure 3.2.5.1-1 (A). Thus, the target image that was used for the calibration of the OH^* chemiluminescence measurements, and consequently, for the quantification of the flame dimensions in the present study, was investigated retrospectively. The spectrum distribution of the target image, which is presented in Figure 3.2.5.1-1 (B), reveals that the left side of the target is characterised by higher intensity values. Thus, it is sensible to conclude that the flame is in fact symmetric, as literature suggests [150, 152–154], though, due to an optical medium effect, it appears as if the left side of the image is of higher intensity.

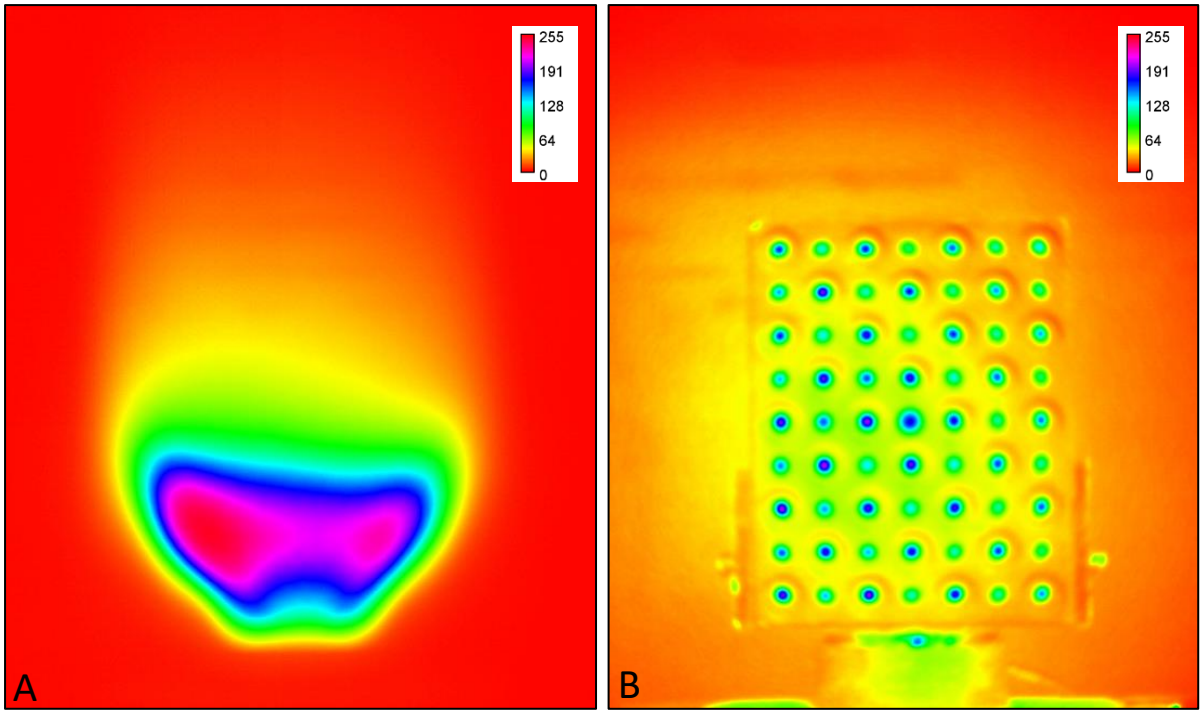

Figure 3.2.5.1-1 *(A) Spectrum distribution of time averaged OH^* chemiluminescence image for CH_4 stoichiometric combustion ($\varphi = 1.00$). (B) Spectrum distribution of calibration target.*

This effect was consistent for all OH^* chemiluminescence data acquired in the present study. Hence all the time averaged OH^* CL images resulted in higher intensity in the left side of the flame. In Figure 3.2.5.1-2 (A), where the time averaged OH^* CL image of CH_4 at $\varphi = 0.66$ is presented, the same effect is observed again. As the deconvoluted algorithm requires perfectly symmetrical flame input, the left side of the time-averaged image was cropped and fed into the corresponding algorithm, which performed the Abel operation. Then, the image was mirrored by its vertical central axis to provide the complete 2D Abel image. In the following Figure 3.2.5.1-2 (B) the Abel transformed image of CH_4 flame at $\varphi = 0.66$, is presented. This method, which is commonly used in the literature was preferred as the phenomenon was consistent across the whole set of results, whilst the current target image resolution did not allow any further appraisal of the optical medium related effect. In the future work, a new target image of improved resolution should be created, with a view to quantifying the influence of the optical medium related increase in image intensity and to calibrate the measuring system accordingly.

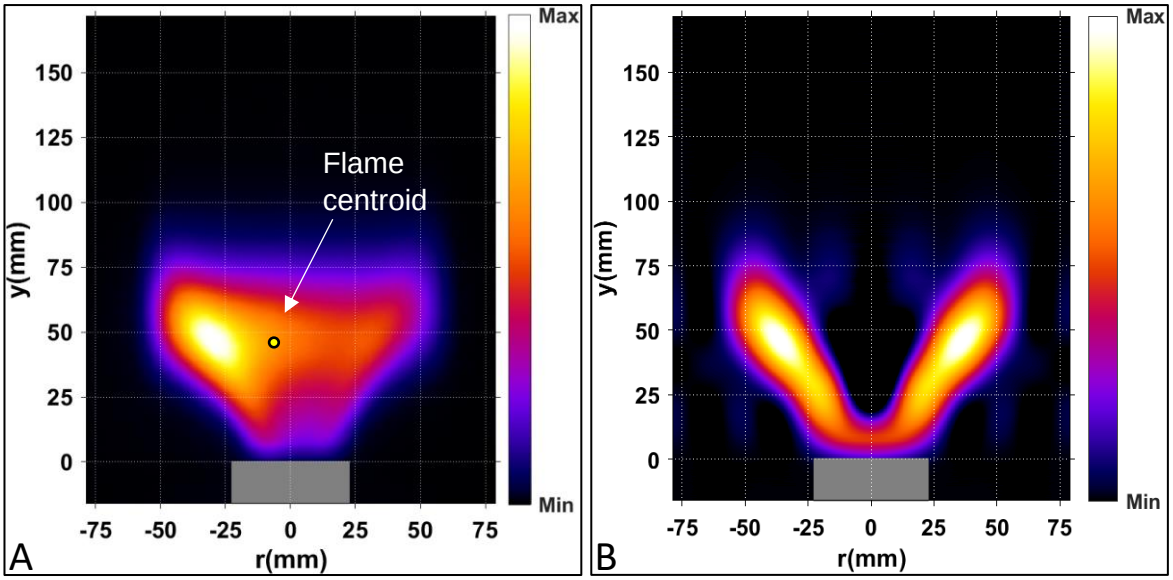

Figure 3.2.5.1-2 *(A) Time averaged OH^* chemiluminescence image for CH_4 combustion at φ=0.66. (B) Resultant Abel transformed image.*

Moreover, what is also apparent in the Figure 3.2.5.1-2 is the location of the "Weighted centroid" of the 2D image. The term "weighted" is used as the corresponding centroid represents the centre of a region based on both the shape of the flame and the spatial intensity distribution of the binarized image. The function for such calculation is provided through the open source "*regionprops"* group of functions through MATLAB software, which are widely used for measuring properties of image regions. The function returns the x and y coordinates of the weighted centroid, which can be plotted to quantify the stabilization location of the flame centroid.

Since both sides of the Abel resulted image are the same (as they are mirrored by the central vertical axis), for the following analysis that is conducted in the results chapters (Chapter 6 and Chapter 7) only the right side of the Abel image is considered. The "weighted centroid" is also included in the resulted cropped Abel images for visual examination of the flame centroid. In the following Figure 3.2.5.1-3, an example of such comparison between the *Machined* and the *AM-R* swirlers using the final cropped Abel images for the $\varphi = 0.66$ case is presented. In the presented image, the "weighted centroid" location and the distance from the latter to the centre of the burner are highlighted:

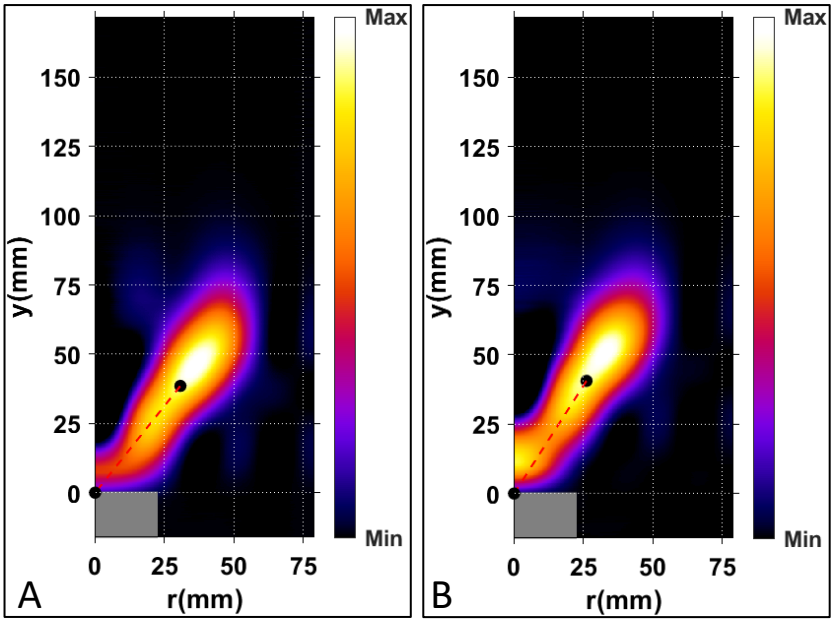

Figure 3.2.5.1-3 *Abel deconvoluted images of flame shape, indicating the location of the flame centroid, for the Machined (A) and AM-R (B) swirlers.*

3.2.6 Emissions Gas Analyser

The analysis of the exhaust gases was carried out using industry standard equipment provided by Signal Gas Analysers Ltd. Several experimental research studies have been conducted utilising the HPSGB-2 burner and the same gas analyser [29, 239, 240, 261]. For the current experimental campaign, a custom Nimonic 80a alloy structure was placed at the exit of the confinement, as described in Section 3.2.1 to support the exhaust gas sampling probe. Consequently, the probe was positioned within the metallic structure, at a fixed position, approximately 5 mm above the exit of the confinement quartz tube. The sampling probe, comprising 7 equally distanced holes, was water cooled via a chiller system, thus maintaining a constant temperature of $120\,^{o}C$. The metallic support structure (yellow dotted rectangular section), the water-cooling pipe network (blue & red dashed lines) and the sampling probe (green oval dotted section), are shown in Figure 3.2.6-1.

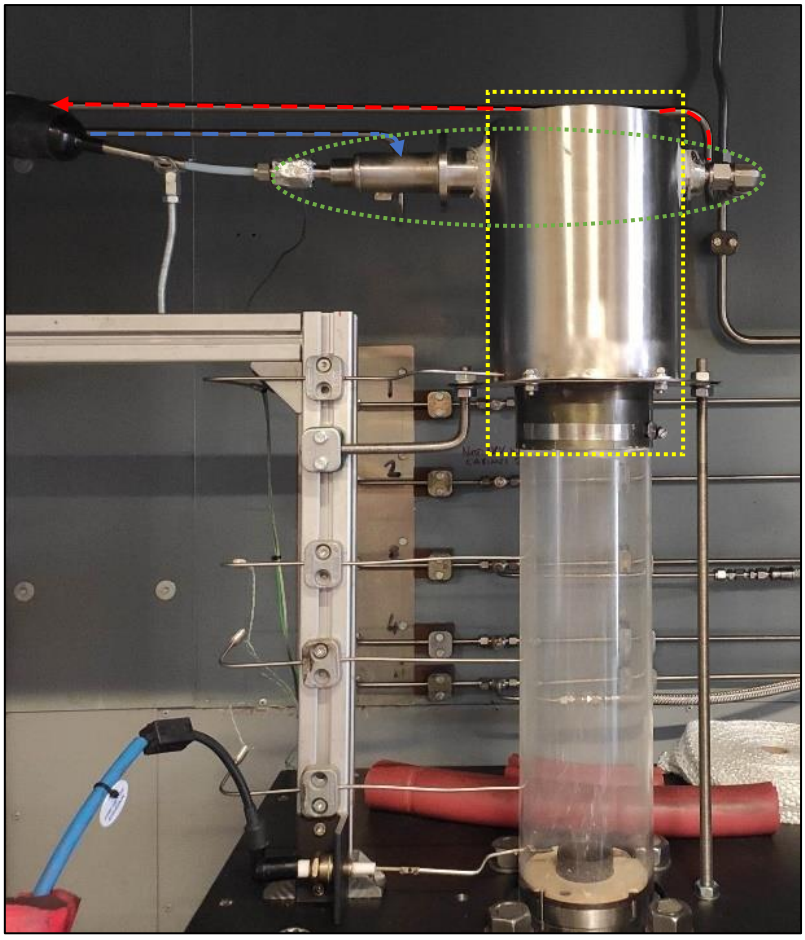

Figure 3.2.6-1 *Combustion and exhaust section of APGSB, indicating the metallic sampling probe support structure (yellow dotted rectangular section), the water-cooling pipe network (blue-red dashed lines) and the sampling probe (green dotted oval section).*

The temperature of the exhaust gas sample line, filter and distribution manifolds was kept constant at 160 ^{o}C, and the sample was delivered to the analyser setup via a heated pump. The NO_x emissions were monitored and recorded using a heated vacuum chemiluminescence analyser (Signal Instruments 4000VM) calibrated at the range of 0-100 ppmV. Their values were measured at hot and wet conditions ($NO_{x,\ wet}$) to minimise any losses related to condensed exhaust H_2O and corrected to the equivalent dry conditions ($NO_{x,\ dry}$), using Equation 3.1. To perform the conversion from wet to dry, the equilibrium water molar fraction (Y_{H2O}) was calculated from the corresponding equivalence ratio and cross examined with simple CHEMKIN simulations results. Finally, the emissions were normalised ($NO_{x,\ dry15\%O2}$) to a reference value of 15% O_2 ($O_{2,\ ref}$) concentration using Equation 3.2. The required O_2 ($O_{2,\ meas}$) measurements for the normalisation were performed using a paramagnetic analyser (Signal Instruments 9000MGA), which was calibrated in the range of 0-22.52 $\%_{vol}O_2$. Concerning the uncertainty of the measurement, it was calculated at ≈2 ppmV,

accounting for analyser specifications, linearization and accuracy in span gas specifications.

$$NO_{x,dry} = \frac{NO_{x,wet}}{1 - Y_{H20}} \qquad (3.1)$$

$$NO_{x,dry15\%O2} = NO_{x,dry} \times \left(\frac{20.9 - O_{2,ref}}{20.9 - O_{2,meas}} \right) \qquad (3.2)$$

3.3 Summary

The experimental aim and procedure, as well as the facilities required to undertake the experimental research programme, and hence, deliver the relevant research objectives, have been defined in this Chapter. Various pre and post processing techniques required for data optimisation, including the employed Abel-transformed 2D OH^* chemiluminescence image-processing, have been introduced and discussed. The final system comprises a new, optical, atmospheric generic swirl burner (APGSB) with swirlers of constant swirl number *($S_N = 0.8$)* but varying surface roughness, high-precision Coriolis mass-flow controllers, shielded *K-type* thermocouples, an inlet air preheater, a water-cooled probe for exhaust gas NOx measurements and a high-speed chemiluminescence photography suite. These systems are deployed to obtain data generated and analysed in Chapter 6 and 7.

Chapter 4. Numerical Methodologies

This Chapter describes the numerical methods and modelling techniques informing the computational investigation of surface roughness in the following Chapter 5. In Section 4.1, the fundamental concepts for the modelling of turbulent flows over smooth walls are presented. Subsequently, Section 4.2 explains the necessary concepts behind the modelling of turbulent flows over rough walls. The various roughness models accounting for roughness effects on turbulent flows are reviewed in Section 4.3. The description of the computational continua employed for the present CFD investigation is described in Section 4.4, whilst the most important conclusions are presented in Section 4.5.

4.1 Turbulent flows over smooth walls

A description of the fundamental quantities and laws that have been developed and are widely used for the numerical investigation and modelling of surface roughness effects, is provided in this section. The computational investigation, the results of which are presented in Chapter 5, was performed under isothermal conditions. Thus, this section focuses on the modelling methods related to isothermal flows, consequently, excluding temperature considerations.

4.1.1 Law of the wall

Although turbulences are chaotic in nature, the mean flow can be characterised by a standard group of expressions and laws, if assumed that the flow is at "equilibrium". As turbulent flows are time dependent, the term "equilibrium" is used to describe the state, in which boundary-layer thickness (δ) and friction velocity (u^*) ($u^* = \sqrt{\tau_w/\rho}$, where τ_w is the wall shear stress and ρ is the density) have attained an almost constant value (very slow variation in streamwise direction), and hence, can be handled as a "steady-state" flow. Those expressions must describe both the mean core flow and near-wall region, while satisfying the *zero-slope* and *no-slip* conditions at the edge of the boundary layer and the wall, respectively. Traditional asymptotic matching analysis can be used to derive the properties of the mean flow for both the smooth and the rough walls [57]. Based on asymptotic matching analysis, it is proposed that the boundary layer can be divided into an outer and an inner adjacent region, as described in Section 2.1.2. Each region is scaled with the corresponding relevant parameters, which are stratified in terms of wall distance (y) [278].

As proposed by Townsend [279], the inner layer, which is adjacent to the wall, is the “active” part of the turbulent flow, influenced by the local flow parameters and viscosity. The outer layer is the “inactive” part, and it is solely influenced by the wall geometry. The presence of the wall affects the formation of the inner region by splitting it into, the *viscous (laminar) sublayer*, the *buffer layer* and the *logarithmic layer*, as presented in Section 2.1.2. At the inner region, the viscous effects are dominant, and the scaling parameters are the *friction velocity* (u^*) and the *kinematic viscosity* (ν), from which the *viscous length scale* (ν/u^*) can be constructed. For the case of rough wall additional length scales are necessary to be included, such as the roughness height and the skewness. Based on the viscous length scale, the dimensionless *wall distance* or *viscous length distance* (y^+) ($y^+ = y\frac{u^*}{\nu}$), can be defined [84]. The dimensionless wall distance y^+ is used predominantly for the modelling of the turbulent boundary layer. In the context of CFD, it provides an estimation of the size of the viscous sublayer with respect to the size of the wall-adjacent cell [280]. For instance, a wall-adjacent cell with $y^+ = 30$ can be interpreted as that the distance from the wall to the centroid of the wall-adjacent cell is 30 times larger than the thickness of the viscous sublayer. Since the regions within the turbulent boundary layer are stratified in terms of wall distance (y), the dimensionless formulas, which express the scaling laws, are also dependent on the dimensionless wall distance (y^+). For the viscous (laminar) sublayer ($y^+ \leq \approx 5$), which is attached to the wall, the mean velocity is formulated as:

$$U^+ = y^+, \qquad (4.1)$$

where, U^+ is the dimensionless velocity defined as:

$$U^+ = \frac{U}{u^*}, \qquad (4.2)$$

and U is the relevant velocity scale [278].

At the outer layer, the relevant length scale becomes the boundary-layer thickness (δ). Subsequently, the Reynolds number can be formulated, based on the viscous length scale and the boundary-layer thickness ($Re_\delta = \delta\frac{u^*}{\nu}$). In this way, the level of scale separation between the inner and the out layer, can be determined [84]. When Re_δ is large enough, the overlap layer (logarithmic layer) above the buffer and the viscous (laminar) sublayer, survives. In this layer, y^+ is too large for the viscosity

to be relevant and y/δ is too small for δ to be the characteristic length scale. Consequently, the only available length scale is the wall distance (y). This leads to the logarithmic distribution, termed the *law of the wall* or *log-law*, which is dimensionally formed based on the dimensionless wall distance y^+, as follows [279]:

$$U^+ = \frac{1}{\kappa}\ln(y^+) + C, \qquad (4.3)$$

where, κ is the von Karman constant ($\kappa \approx 0.41$) and C is a model constant ($C \approx 5.1$). The logarithmic layer is a fully turbulent region of the turbulent boundary layer, in which the Reynolds stresses ($-\rho u'v'$) are significantly greater than the viscous stresses. In between the logarithmic layer and the viscous (laminar) sublayer, the buffer layer exists. In this region, which is characterised by augmented turbulent mixing, the viscous stresses are of the same magnitude to the Reynolds stresses. The logarithmic layer is also concerned with high turbulence intensity and enhanced mixing, though, to a lesser extent, as the velocity gradient is smaller, compared to the buffer layer.

As will be shown in Section 4.4.2, the *wall-function* approach, which is utilised in the present computational investigation, is based on the *law of the wall or log-law* (Equation 4.3). Consequently, for the modelling of the effects of surface roughness, the log-law is modified according to the *wall similarity hypothesis*, which is presented in the following Section 4.1.2. It is worth noting that the log-law is not applicable for $y^+ > 700$. In this region, the *law of the wake* can be used, which has been developed by Cole [281]. Moreover, since the log-law does not satisfy the no-slip conditions, and thus, cannot be applied at $y^+ \leq \approx 10$, Spalding [282], suggested an extended correlation that covers the whole inner layer of the turbulent boundary layer. Subsequently, Reichardt [283] proposed an equation for the mean velocity distribution of turbulent flows over pipes and channels that could be utilised from the wall to the core flow. The agreements between experimental and computationally predicted mean velocity profiles for zero and adverse pressure gradient turbulent boundary layers can be seen in Figure 4.1.1-1.

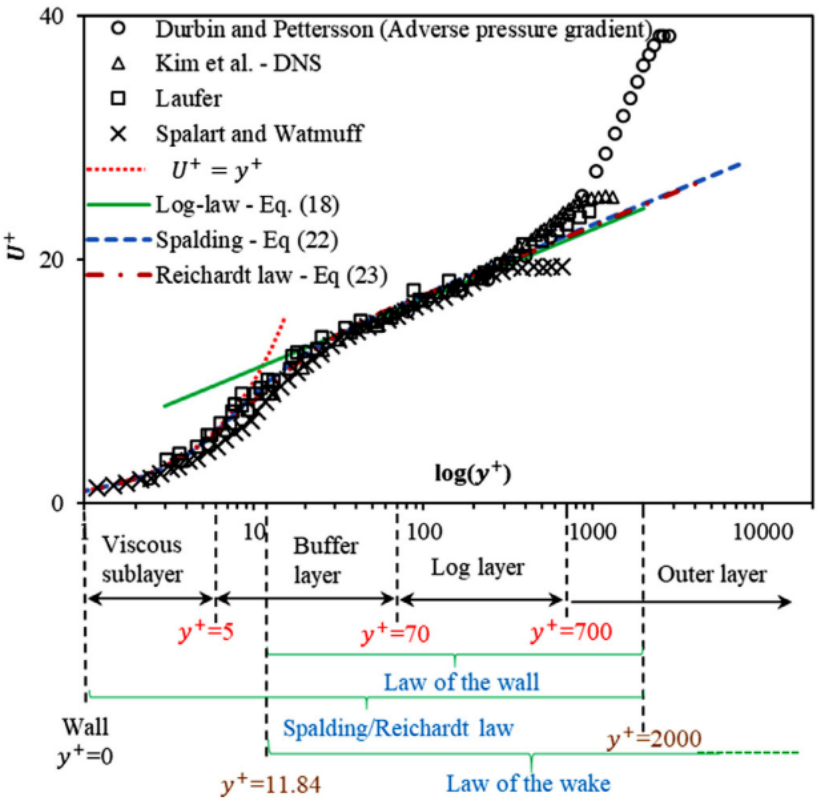

Figure 4.1.1-1 *Experimental and DNS mean velocity profile, for zero and adverse pressure gradient turbulent boundary layer flow. Sources:* [284–287] *Graph:* [55].

4.1.2 Wall similarity hypothesis

To effectively model the effect of surface roughness on turbulent flows, advanced knowledge of the flow structure in the inner and outer layer of the boundary layer is required. The engineering models developed assume surface roughness as small disturbances to the smooth wall boundary layer [278]. Thus, most turbulent models applied to rough walls form extensions of the smooth-wall turbulence models. Specifically, the flow over rough wall is modelled based on the *wall similarity hypothesis*, which is an extension to Townsend's *Reynolds number similarity hypothesis* [279].

Townsend's Reynolds number similarity hypothesis states that the structures of geometrically similar flows are very nearly similar for all Reynolds numbers which are large enough to allow fully turbulent flow conditions. Upon this hypothesis, the wall similarity hypothesis is built, stating that the wall roughness and viscosity are not affecting the region outside the viscous sublayer, apart from setting the velocity scale u^* and the boundary layer thickness δ. This implies that the ratio of turbulence stress to wall shear stress is universal outside the viscous sublayer [279]. Therefore, based

on the wall similarity hypothesis, the flow for both smooth and rough can be assumed to obey the *universal velocity defect law* in the logarithmic and outer layer of the turbulent boundary layer.

The wall similarity law (also referred as *universal velocity defect law*) has been supported by numerous experimental and computational investigations, for a variety of conditions and surface finishes. An extended list of such studies is provided by Kadivar et al. [55]. Flack and Schultz [288] reviewing their 15-year experimental investigation on turbulent boundary layers over rough walls, they reported that wall similarity hypothesis was valid for *all* their experiments. Furthermore, recent DNS numerical investigation have demonstrated the validity of wall similarity hypothesis for canonical flows [289, 290]. However, several researchers have also reported inconsistencies related to this hypothesis [291, 292]. These exceptions were related to alternations of the turbulence structures in the outer region of the boundary layer. Subsequently, Flack et al. [293] and Jimenez [84], attributed these disagreements to the small relative difference between the roughness height and boundary layer thickness. Specifically, for $\delta/k_s \leq 40$, it has been shown that surface roughness could potentially affect the outer layer of the turbulent boundary layer [291, 292]. However, the evidence is conflicting, since some researchers confirm the validity of the wall similarity hypothesis even for $\delta/k_s \leq 40$ [294], while others report perfect agreement for a wide range of relative differences (from $\delta/k_s = 100$ to $\delta/k_s = 16$) [288].

4.2 Turbulent flows over rough walls

As presented in Chapter 2, surface roughness influences turbulent flows significantly by increasing the skin-friction drag and by altering the laminar-turbulent transition of boundary layers. Consequently, the characteristics of surface roughness, in relation to the flow field structure significantly affects the performance of GTs. To be able to investigate, model and predict these effects, the characteristics of surface roughness must be quantified.

4.2.1 Roughness parameters

Surface finish also referred as *surface texture* or *surface morphology*, contains a series of geometrical inconsistencies that are randomly, or uniformly, developed over a smooth surface [55]. Raja et al. [295] categorised these irregularities, based on their frequency in *roughness* (high frequency), *waveness* (medium frequency), and *surface*

form (low frequency), which is no longer regarded surface finish and constitutes surface shape. To quantify the surface finish, which is often highly irregular, international standards, such as ASME Y14.36M and ISO 1302, have been developed adopting several statistical surface parameters [296]. These parameters can be calculated using either the profile of a sampling length (*R* parameters), or the area of a sampling section (*S* parameters). Subsequently, the amplitude parameters (*R* and *S*) can be quantified with a heightmap (Figure 4.2.1-1), in which the roughness profile is characterised based on the peak and valleys distribution. A list of the frequently used, amplitude parameters can be found elsewhere [55].

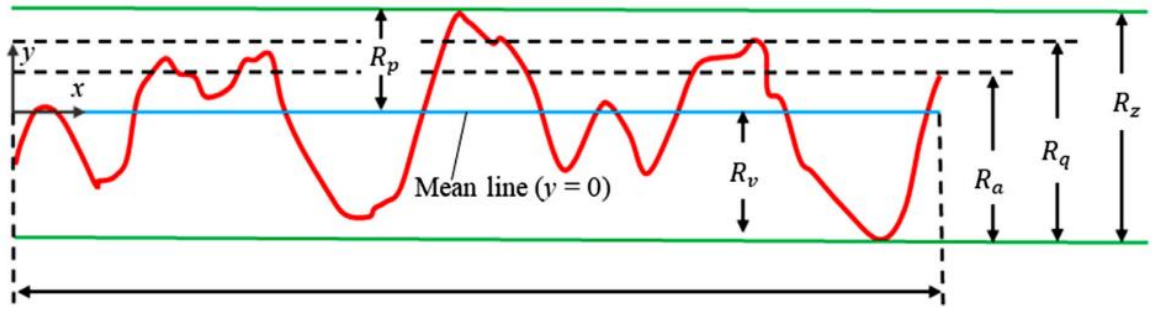

Figure 4.2.1-1 *Schematic representation of R_a, R_q, R_z, R_v and R_p parameters, Source:* [55].

The amplitude parameters shown in Figure 4.2.1-1, describe the surface roughness profile in a statistical manner. The R_a parameter represents the arithmetic mean deviation of the roughness profile from the surface. The R_q parameter defines the standard deviation of the roughness peaks profile from the surface, while the R_z parameter gives the maximum peak to valley height of the distribution. R_p and R_v parameters represent the maximum peak height and maximum depth, respectively, above the mean line within a simple sampling length [55]. As different surface roughness profiles might result to the same arithmetic average height, the mere consideration of the R_a parameter might be problematic. The R_q parameter is of greater physical importance, compared to R_a, whereas the R_z is more suitable to frequent high peaks or deep valleys.

4.2.2 Equivalent sand-grain roughness

As described in Section 4.11, the *law of the wall* is developed upon the assumption that in the near vicinity of the wall is dominated solely by viscous forces. This is only true for smooth surfaces, or for surface with roughness height smaller than the viscous sublayer thickness (*hydraulically smooth* surfaces). With surface

roughness extending through the viscous sublayer, additional friction forces occur, which must be taken into consideration [57]. Since surface roughness is often highly irregular, whilst there are several statistical parameters that can be used to describe its characteristics, the concept of *equivalent sand-grain roughness* (k_s) is widely employed in the literature to characterise the surface roughness and to model its effects using a simple, universal length scale [297]. Thus, the equivalent sand-grain roughness represents a roughness scale which reflects the influence of the surface finish on the flow.

The equivalent sand-grain roughness concept for describing the surface roughness was first introduced by Schlichting [298], who researched the effect of several roughness features and correlated the resulted skin friction losses to the actual *sand-grain roughness* that Nikuradse [76] used for his experiments. This concept was widely used for several scaling laws to provide prediction related to skin friction, heat transfer and boundary layer transition. Almost 50 years later, Coleman et al. [299], re-evaluated the correlation between Schlichting's skin friction coefficients and equivalent sand-grain roughness, using more accurate data and assumptions. Since then, several formulae for different roughness shapes and types have been proposed to correlate the actual measured surface roughness to the equivalent sand-grain one. A thorough review on the widely-used correlations is provided by Bons [36]. As shown in Figure 4.2.2-1, the equivalent sand-grain roughness (k_s) represents the equivalent height of a random and irregular roughness, which, in the *fully rough* regime, produces the same effects as the uniform sand-grain roughness that Nikuradse [76] used in his experiment. Based on the concept of equivalent sand-grain roughness the *roughness Reynolds number* (k^+_s) and *the roughness regimes* are defined. These concepts are discussed in the following section 4.2.3.

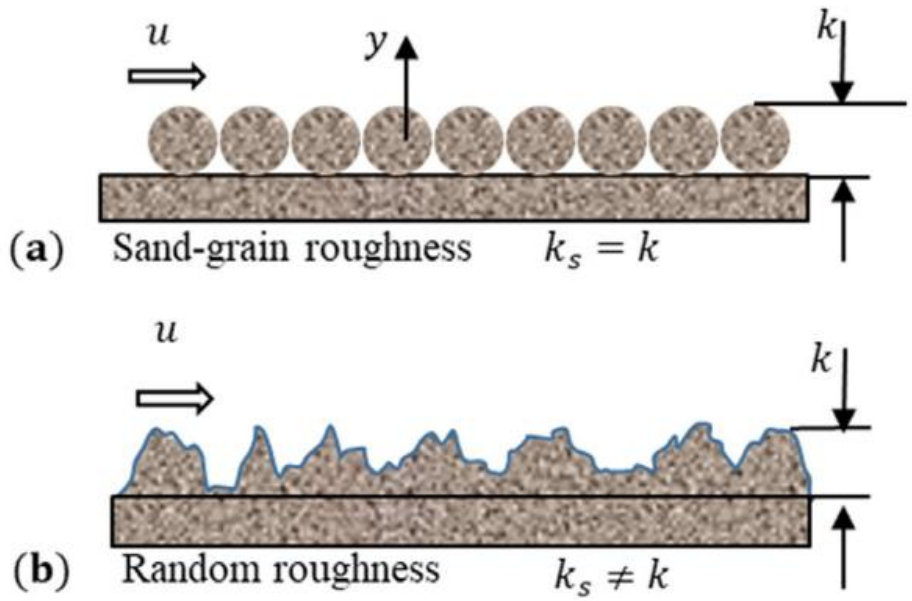

Figure 4.2.2-1 *Equivalent sand-grain roughness concept. Source:* [55].

For the computational investigation presented in Chapter 5, the equivalent sand-grain roughness was estimated by the algorithm that has been suggested by Adams et al. [297]. Subsequently, the real surface roughness measured using a *Taylor Hobson Form TalySurf Series 2 profilometer* was converted into the equivalent sand-grain roughness using Equation 4.4, where R_z corresponds to the peak-to-valley roughness parameter:

$$k_s = 0.978R_z, \qquad (4.4)$$

4.2.3 Roughness regimes

The *roughness Reynolds number* (k^+_s), or *roughness parameter* in the context of CFD methods (described in Section 4.4.2), which is defined in Equation 4.5, is extensively used to model the effect of surface roughness through modifying the log-law formula (Equation 4.3).

$$k_s^+ = \frac{k_s u^*}{\nu}, \qquad (4.5)$$

where, k_s is the equivalent sand-grain roughness, u^* is the friction velocity (defined in Section 4.1.1) and ν is the kinematic viscosity. This dimensionless number was first defined by Nikuradse [76], who examined the pressure drop of a turbulent flow in a sand-roughened pipe for different flow regimes and pointed out the various dependencies on *Reynolds number* (Re). Using the sand-grain roughness, instead of

the equivalent one, he categorised the influence of surface roughness on three distinct *roughness regimes*, whose limits (k^+_{smooth} *and* k^+_{rough}) were defined in terms of the roughness Reynolds number. Depending upon the roughness regime, the *roughness function* is modified, which subsequently alters the log-law, accordingly. The roughness function is further discussed in following Section 4.2.4. Based on Nikuradse [76], the three roughness regimes are defined as follows:

- *Hydraulically smooth* ($k^+_s \leq k^+_{smooth}$)*:* In this region, the roughness height is much smaller than the thickness of the viscous sublayer (Figure 4.2.3-1 A). Thus, all the roughness elements are embedded within the viscous sublayer, which is dominated by viscous forces. The skin-friction and drag coefficients are not modified and the surface can be regarded as smooth.
- *Transitionally rough* ($k^+_{smooth} \leq k^+_s \leq k^+_{rough}$)*:* In this case, the height of the roughness peaks is comparable to the thickness of the viscous sublayer (Figure 4.2.3-1 B). In this region, the effect of roughness is complex as both the Reynolds number and the surface roughness height affect the skin friction and drag coefficients. This region is dominated by both viscous and pressure forces, and it is characterised by reduced sublayer thickness, resulting in reduced wall damping effects.
- *Fully rough* ($k^+_s \geq k^+_{rough}$)*:* In this region, the vast majority of roughness elements extend through the viscous sublayer into the fully turbulent region (logarithmic region) of the turbulent boundary layer (Figure 4.2.3-1 C). The logarithmic profile is shifted downwards, towards the wall, due to the enhanced mixing caused by the roughness elements. Consequently, the viscous sublayer is destroyed. The pressure forces induced by the roughness elements significantly increase the friction drag, and hence, the wall shear stress, which, in this case is independent of the viscous forces. Thus, the pressure drop is independent of the molecular viscosity of the fluid and rely solely on the roughness height. In this case, the viscous sublayer is replaced by the *roughness sublayer*, which extends $\approx 3k_s$-$5k_s$ above the wall, as shown by Schultz and Flack [300] (Figure 4.2.3-1 D).

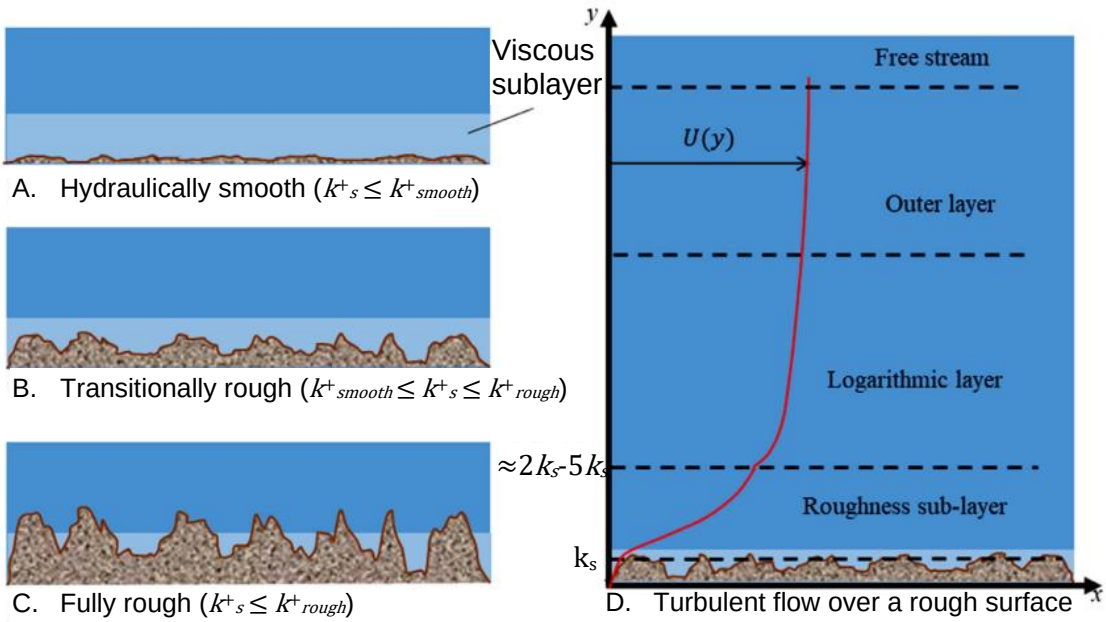

Figure 4.2.3-1 *Turbulent flow over rough wall. (A) Hydraulically smooth, (B) Transitionally rough, (C) Fully rough, (D) schematic of the velocity profile u(y) over roughness, indicating the roughness, logarithmic and outer layer. Source:* [55].

Since the roughness Reynolds number can be defined with different roughness length scales, the roughness regime limits can also be defined with different values, based on the employed roughness length scale. For equivalent sand-grain roughness, Cebeci and Bradshaw [301] found that $k^+_{smooth} = 2.25$ and $k^+_{rough} = 90$. In conclusion, to estimate the effect of a rough surface on mean flow quantities, the roughness Reynolds number is calculated, and hence, its roughness regime is determined. Subsequently, the log-law equation is modified accordingly, based on the roughness function, as described in the following Section 4.2.4.

4.2.4 Roughness function (ΔU^+)

The modelling of surface roughness effects on turbulence flows is achieved by extending the smooth-wall turbulence models to rough wall, based on the wall similarity hypothesis, as described in Section 4.1.2. The predominant effect of surface roughness in isothermal flows is the amplification of shear stresses and the enhancement of mass transfer to the wall, resulting in the alteration of the velocity profile near the wall [36]. As discussed in previous Section 4.2.3, the influence of surface roughness varies depending on the roughness regime, which is determined using the roughness Reynolds number. However, according to the wall similarity hypothesis, outside the viscous (laminar) sublayer, the turbulent boundary layer is

unaffected by wall roughness and viscosity, except for defining the relevant length scales (u^* and δ). For the fully rough case, where the viscous sublayer is replaced by the roughness sublayer, the effects of surface roughness is extended to $\approx 2k_s$-$5k_s$. Based on these observations, the models concerning the turbulent flows over rough wall have been developed.

In Figure 4.2.4-1 the mean velocity profiles, for the inner layer of the turbulent boundary layer, have been plotted for several surfaces. A similarity in the overlap and outer layer of the velocity distributions, is reported. This similarity implies that the effect of surface roughness should be limited to the viscous sublayer (for the smooth surface) and the roughness sublayer (for the rough surfaces), as the wall similarity hypothesis predicts. Additionally, it is apparent that the velocity profiles for the rough surfaces have been distinctively displaced downwards, compared to the smooth surface. Subsequently, this shifting of the mean velocity profile, also referred as *velocity deficit*, under the effect of surface roughness, is modelled through the *roughness function (ΔU⁺)*. This modelling approach was first introduced by Clauser [302], who identified that the mere effect of surface roughness, was the downwards shifting of the velocity profile in the logarithmic region, based on roughness Reynolds number. This modelling approach is vastly utilised since then for computational methods and it is also employed in the present numerical study.

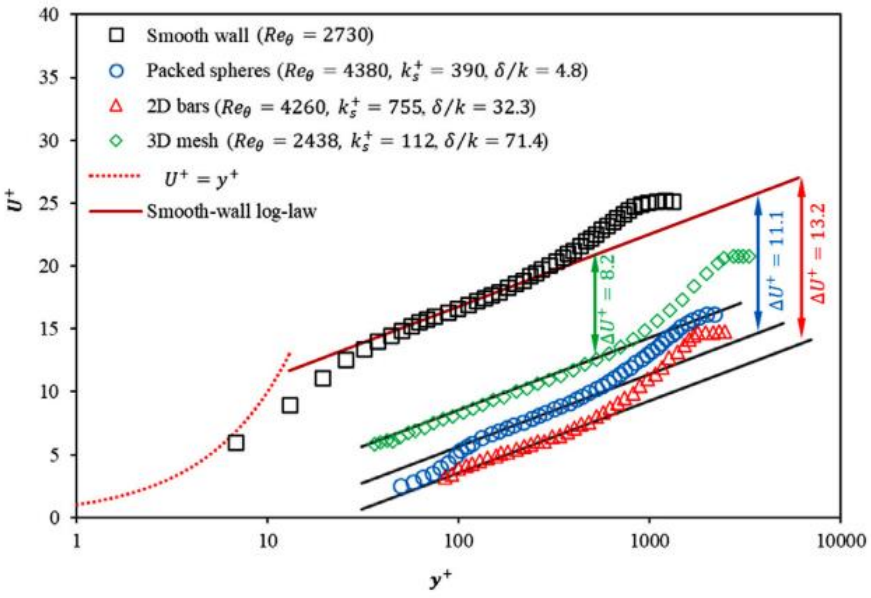

Figure 4.2.4-1 *Mean velocity profiles of experimental turbulent flows over 2D bars and 3D mesh. Downward shift (ΔU⁺) of the mean velocity profile below the smooth wall (velocity deficit) is illustrated for each rough surface. Source:* [285, 303, 304].

Clause [302] and Hama [305], in separate studies, introduced their roughness functions (Clause-Equation 4.6, Hama-Equation 4.7), and attributed the downward shifting of the mean velocity to the augmented momentum deficit due to the roughness elements. As shown in their corelations, the velocity deficit is proportional to $\ln k_s$ and independent of y^+. This modelling approach has been experimentally confirmed with numerous experimental studies, which can be found in [55]. Several improvements and extensions have been suggested, such as the one proposed by Cole [281], who extended the roughness function to the outer layer through the law of the wake concept. An extensive review on the several roughness function corelations is provided by Flack and Schultz [88] and Andersson et al. [306].

$$U^+ = \frac{1}{\kappa}\ln y^+ + C - \Delta U^+, \qquad (4.6)$$

$$\Delta U^+ = \frac{1}{\kappa}\ln k_s^+ + C - B, \qquad (4.7)$$

where, C is the smooth-wall intercept, κ is the von Karman constant and was found by Schlichting [57] to be equal to 8.5.

4.3 Roughness models for turbulent flows

Apart from the wall functions approach utilising the roughness function, several other methods have been developed for obtaining computational predictions of the effects of surface roughness on turbulent flows. Stripf et al. [62] and Bons [36], have categorised these methods, which substantially vary both with respect to the employed method for accounting for wall roughness and in terms of the computational requirements. Based on their reviews, the surface roughness modelling methods fall within three major categories. The first method is related to the full resolution of the surface roughness within the computational domain, the second category is related to the *discrete element method (DEM)* approach, and the third is based on the equivalent sand-grain roughness concept.

Concerning the first method, the full resolution of the surface roughness profile within the computational grid eliminates the dependence on equivalent sand-grain roughness, and thus, the related uncertainty associated with its estimate [36]. Although theoretically this is the ultimate way of studying the influence of surface roughness, the full resolution of the roughness geometry results in significantly

increased computational cost. Consequently, the applicability of this method in 3D complexed turbomachinery flows, is limited, under the current computational capabilities. This method is usually applied to simplified small geometrical sections to carry out fundamental investigations on the interaction of surface elements with the near wall flow. Several examples have demonstrated the effectiveness of such a methodology, utilising RANS [31, 63, 307], LES [64, 65] or DNS [31, 63, 67–69, 71, 308] solvers.

The second category is related to the DEM approach, which is a popular alternative to equivalent sand-grain roughness-based models. Using this modelling strategy, additional quantities are introduced to account for blockage, drag and heat related effects induced by the wall roughness. Consequently, the dependence on equivalent sand-grain roughness and wall similarity is eliminated [36, 62]. Additionally, this method allows the application of different physical characteristics on the individual roughness elements. Early demonstrations of this modelling technique have been performed by Finson et al. [309], followed by several modifications, such as extending the applicability of the model for surfaces with irregular roughness [310]. However, one of the limitations of DEM is that is cannot be applied to 3D, unsteady flow fields, thus its employment in gas turbine applications remains limited [36].

The third and most widely adopted method for evaluating the effect of surface roughness on computational simulation of turbulent flows, involves the utilisation of equivalent sand-grain roughness-based models. Several different approaches within this wall framework have been developed. Since most of turbulent models involve the turbulent eddy viscosity (μ_t) in their formulation, a common practise to model the influence of surface roughness is to modify μ_t as a function of roughness height. Cebeci and Chang [311], following Rotta's [312] suggestion, modified the algebraic eddy viscosity model of Cebeci and Smith [313] to account for roughness effects. In the revised model, μ_t was increasing with increasing equivalent sand grain roughness, subsequently vanishing the influence of viscous damping near the wall. Feiereisen and Acharya [314] tuned the Cebeci and Chang model to cover directly measurable roughness quantities. Krogstad [315], Granville [316], Gbadebo et al. [317] and Blair [318] have also suggested and implemented similar methods.

Similar to the modification of μ_t approach, the influence of surface roughness, when one or two-equation turbulence models are implemented, is often simulated by incorporating surface roughness into the wall boundary condition of μ_t or ω. Lee and Paynter [319] edited the Spalart-Allmaras (SA) turbulence model by adopting an effective wall displacement analogous to Cebeci and Chang's code [311]. Concerning the two-equation turbulence models, such as k-ω or k-ε, Wilcox [58] modified the turbulent dissipation rate (ω) boundary condition to directly account for surface roughness effects, using the k-ω turbulent model. This method was recently employed by Huang et al., [60] providing heat transfer and skin friction predictions.

Finally, the effect of wall roughness can be indirectly accounted for, with the introduction of a roughness function that modifies the log-law wall equation, as discussed in Section 4.2.3 and 4.2.4. The main benefit of this method is the reduction in computational time requirements [284], which enables the investigation of complex flows and full-scale 3D geometries [59, 61, 320–322]. Demirel et al., [59] utilised this technique to simulate the hull resistance due to antifouling coatings, using a simplified geometry representing the hull of a ship. A similar investigation was conducted by Ohasi [321], who investigated the roughness effects on actual ship-scale. Orych et al. [322] compared several roughness models dependent on the wall function approach to evaluate their predictive capabilities. Moreover, Sakin and Karagoz [61], investigated the effects of surface roughness on the resultant swirling flow of a full-scale cyclone geometry. As the wall function approach is the employed method for the present computational investigation, this approach will be further discussed in the following Section 4.4.

It is worth noting that the serious drawback of equivalent sand-grain roughness-based models is that they rely on the equivalent roughness length scale. Apart from the uncertainty related to the conversion of the real surface roughness to the equivalent one, the latter is only applicable to skin-friction coefficients. Thus, for heat transfer predictions, different corelations of equivalent sand-grain roughness must be used. This issue has been thoroughly reviewed by Stripf et al. [62].

4.4 Description of the turbulence modelling method employed

To reduce the required computational cost of the performed simulations in Chapter 5, the Reynolds-Averaged Navier Stokes (RANS) turbulence modelling

method was preferred. Therefore, the average quantities were resolved while the impact of small-scale fluctuating structures was approximated based on the corresponding turbulence model. Subsequently, the realizable k-epsilon (k-ε) two-layer model was used to model the turbulence. The effect of surface roughness was modelled via the concept of *wall functions*, utilising a *roughness function* as described in Section 4.3. The calculations were carried out by using the commercially available *Simcenter STAR-CCM+ 2019.3 (Build 14.06.012)* CFD software. In the following Sections 4.4.1 and 4.4.2, the descriptions and the governing equations of the RANS and Realizable k-epsilon (k-ε) two-layer models are presented.

4.4.1 Reynolds-Averaged Navier Stokes (RANS)

RANS turbulence models provide closure relations for the Reynolds-Average Navier-Stokes equations that govern the transport of the mean flow quantities. To acquire the Reynolds-Averaged Navier-Stokes equation, each solution variable (χ) in the instantaneous Navier-Stokes equation is decomposed into its mean (or averaged) value ($\bar{\chi}$), and its fluctuating component (χ'), such as:

$$\chi = \bar{\chi} + \chi', \qquad (4.8)$$

where the variable χ represents velocity, pressure, energy, or species concentration [280].

To obtain the equations of the mean quantities, the decomposed solution variables are input to the Navier-Stokes equation. The averaging process resembles the time-averaging for steady-state situations [280]. For RANS turbulence models, the continuity (Equation 4.9), momentum (Equation 4.10), and energy conservation (Equation 4.11) equations for incompressible Newtonian fluids are defined as:

$$\frac{\partial U_i}{\partial x_i} = 0, \qquad (4.9)$$

$$\rho U_j \frac{\partial U_i}{\partial x_j} = -\frac{\partial P}{\partial x_i} + \frac{\partial}{\partial x_j}\left[\mu\left(\frac{\partial U_i}{\partial x_j} + \frac{\partial U_j}{\partial x_i}\right) - \rho\overline{U_i' U_j'}\right], \qquad (4.10)$$

$$\rho U_j \frac{\partial T}{\partial x_j} = \frac{\partial}{\partial x_j}\left[\frac{\mu}{Pr}\frac{\partial T}{\partial x_j} - \rho\overline{T' U_j'}\right], \qquad (4.11)$$

where ρ is density, T is temperature, U is velocity, P is pressure, μ is dynamic viscosity, Pr is Prandtl number, and $\overline{U_i' U_j'}$ and $\overline{T' U_j'}$ are the stress tensor and turbulent heat

fluxes, respectively, which are modelled via the selected turbulence model, as described in Section 4.4.2.

4.4.2 Realizable k-epsilon (*k-ε*) two-layer model

The *realizable k-epsilon (k-ε) two-layer* model, developed by Shih et al. [323], belongs to the two-equation eddy-viscosity turbulence models category. It is distinguished from the *standard k-epsilon (k-ε)* model due to the new formulation for the *turbulent viscosity* (μ_t) and the new transport equation for the *turbulent dissipation rate* (ε). Due to these improvements, the realizable k-ε model is characterised by superior performance, compared to standard k-ε, for flows involving rotation, boundary layer under strong pressure gradients, separation, and recirculation [280, 323, 324]. These characteristics makes it ideal for the underlying physics of the simulated case. The transport equations for k and ε for the realizable k-ε model are presented in Equation 4.12 and Equation 4.13, respectively [280, 323, 324]:

$$\frac{\partial}{\partial t}(\rho k) + \frac{\partial}{\partial x_j}(\rho k u_j) = \frac{\partial}{\partial x_j}\left[\left(\mu + \frac{\mu_t}{\sigma_k}\right)\frac{\partial k}{\partial x_j}\right] + G_k + G_b - \rho \cdot \varepsilon - Y_M + S_k, \qquad (4.12)$$

$$\frac{\partial}{\partial t}(\rho \varepsilon) + \frac{\partial}{\partial x_j}(\rho \varepsilon u_j) = \frac{\partial}{\partial x_j}\left[\left(\mu + \frac{\mu_t}{\sigma_\varepsilon}\right)\frac{\partial \varepsilon}{\partial x_j}\right] + \rho C_1 S_\varepsilon - \rho C_2 \frac{\varepsilon}{k + \sqrt{\nu\varepsilon}} + C_{1\varepsilon}\frac{\varepsilon}{k} C_{3\varepsilon} G_b + S_\varepsilon, \qquad (4.13)$$

where

$$C_1 = \max\left[0.43, \frac{\eta}{\eta + 5}\right], \qquad (4.14)$$

$$\eta = S\frac{k}{\varepsilon}, \qquad (4.15)$$

$$S = \sqrt{2 S_{ij} S_{ij}}, \qquad (4.16)$$

In Equation 4.12 and Equation 4.13, ρ is density, t is time, ε is turbulent dissipation rate, k is turbulent kinetic energy, u is velocity, μ is dynamic viscosity, ν is kinematic viscosity, μ_t is turbulent viscosity, σ_k (=1.0) and σ_ε (=1.2) is the turbulent Prandtl numbers for k and ε, respectively. Additionally, $C_{1\varepsilon}$ and C_2 are the default constants equal to 1.44 and 2, respectively, S_k and S_ε are user-defined source terms, whilst in

Equation 4.16 S_{ij} is the strain rate. G_k is the production of turbulent kinetic energy, G_b is the production of turbulent kinetic energy due to buoyancy, Y_M is the contribution of the fluctuating dilatation in compressible turbulence to the overall dissipation rate and $C_{3\varepsilon}$ is a model coefficient. These four parameters can be found in elsewhere [280, 324]. Other than the model constants, the k equation is the same as the standard k-ε model.

To model the turbulent viscosity (μ_t), all k-ε model use Equation 4.17, which is presented below:

$$\mu_t = \rho C_\mu \frac{k^2}{\varepsilon}, \qquad (4.17)$$

However, the realizable k-ε model employs a different formulation for the C_μ. This is another characteristic that differentiates it from standard k-ε and RNG k-ε. The new C_μ coefficient is no longer a constant and it is computed based on Equation 4.18 as follows:

$$C_\mu = \frac{1}{A_0 + A_s \frac{kU^*}{\varepsilon}}, \qquad (4.18)$$

where

$$U^* \equiv \sqrt{S_{ij}S_{ij} + \tilde{\Omega}_{ij}\tilde{\Omega}_{ij}}, \qquad (4.19)$$

and

$$\tilde{\Omega}_{ij} = \Omega_{ij} - 2\varepsilon_{ijk}\omega_k, \qquad (4.20)$$

$$\Omega_{ij} = \overline{\Omega_{\iota J}} - \varepsilon_{ijk}\omega_k, \qquad (4.21)$$

In Equation 4.21, the term $\overline{\Omega_{\iota J}}$ represents the mean rate-of-rotation tensor viewed in a rotating reference frame with an angular velocity ω_k. The model constant A_0 is equal to 4.04, whilst A_s is calculated per Equation 4.22:

$$A_s = \sqrt{6}\cos\varphi, \qquad (4.22)$$

where

$$\varphi = \frac{1}{3}\cos^{-1}(\sqrt{6}W), \qquad (4.23)$$

$$W = \frac{S_{ij}S_{jk}S_{ki}}{\tilde{S}^3}, \quad (4.24)$$

$$\tilde{S} = \sqrt{S_{ij}S_{jk}}, \quad (4.25)$$

$$S_{ij} = \frac{1}{2}\left(\frac{\partial u_j}{\partial x_i} + \frac{\partial u_i}{\partial x_j}\right), \quad (4.26)$$

Thus, C_μ is a function of the mean strain and rotation rates, the angular velocity for the system rotation, and the turbulence quantities k and ε.

Realizable k-ε model has been validated for a variety of flows, comprising rotating homogenous shear flows, free flows, such as jets and mixing layers, as well as channels, boundary layer and separated flows. For all the aforementioned cases, Realizable k-ε outperforms the standard k-ε, whilst it resolves the *round-jet anomaly* of standard k-ε. Consequently, the spreading rate for axisymmetric jets is predicted as effectively as that for planar jets [280, 323, 324].

The two-layer model extension was first proposed by Rodi [325], as an alternative for the low-Reynolds number approach, enabling the k-ε model to be applied in the viscous and buffer sublayers of the turbulent boundary layer, where the friction forces are dominated by viscosity. Based on this approach, the flow is divided in two layers and the turbulent dissipation rate (ε) and turbulent viscosity (μ_t) are modified accordingly based on their wall distance. In the near wall cells, turbulent dissipation rate (ε) is given by Equation 4.27, whilst in the region far from the wall, its values stem from its transport equation (Equation 4.12). Subsequently the two values are smoothly blended. Similar treatment is applied for the turbulent viscosity (μ_t). The turbulent kinetic energy (k) is solved within the entire domain without any changes. All the coefficients of the *realizable k-ε model two-layer* are identical to the previously presented ones for the *realizable k-ε*. In STAR-CCM+, there are three variants for the formulations of turbulent dissipation rate (ε) and turbulent viscosity (μ_t). For the present set of simulations, the *shear-driven (Wolfstein)* [326] formulation was employed. The equations for the near wall modelling of turbulent dissipation rate (ε) and turbulent viscosity (μ_t) are presented in Equation 4.27 and Equation 4.28, respectively.

$$\varepsilon = \frac{k^{\frac{3}{2}}}{\varepsilon_{2-layer}}, \quad (4.27)$$

$$\mu_t = \lambda \mu_{t,k-\varepsilon} + (1-\lambda)\mu \left(\frac{\mu_t}{\mu}\right)_{2-laer}, \quad (4.28)$$

where

$$\varepsilon_{2-layer} = c_1 d \left[1 - e^{\left(-\frac{Re_d}{2c_l}\right)}\right], \quad (4.29)$$

$$Re_d = \frac{\sqrt{k}d}{\nu}, \quad (4.30)$$

$$c_l = 0.42 C_\mu^{-\frac{3}{4}}, \quad (4.31)$$

and

$$\lambda = \frac{1}{2}\left[1 + \tanh \frac{Re_d - Re_y^*}{A}\right], \quad (4.32)$$

$$A = \frac{\left|\Delta Re_y\right|}{\operatorname{atanh} 0.98}, \quad (4.33)$$

$$\left(\frac{\mu_t}{\mu}\right)_{2-layer} = 0.42 Re_d C_\mu^{\frac{1}{4}} \left[1 - e^{\left(-\frac{Re_d}{70}\right)}\right], \quad (4.33)$$

In Equation 4.32 and Equation 4.33, Re^*_y and ΔRe_y are the model coefficients equal to 60 and 10, respectively, C_μ is obtained from Equation 4.18 and d is the distance to wall.

As discussed in Section 4.3, the effects of surface roughness can be modelled or resolved through various methods. For the present set of simulation, presented in Chapter 5, the influence of surface roughness on mean flow parameters was modelled through the employment of the *wall function* that incorporated the *roughness function*. Wall functions provide algebraic approximations of the main quantities, such as velocity, temperature and turbulence, for the inner layer (viscous, buffer, and logarithmic sublayers) of the turbulent boundary layer. As these approximations are independent of the turbulence model employed, wall functions are derived under universal conditions [280].

The main use of the wall function is to reduce the grid points of a volume domain and to avoid the requirements for resolving stiff, discretised equations, in the near wall region [284]. As explained in Section 2.1.2.1, at high Reynolds numbers, the thickness of the viscous sublayer is so thin that providing enough cells to accurately resolve this region of the flow would increase enormously the computational requirements. The wall function should not be viewed as a separate set of solutions overlayed onto the turbulence model, but as a common solution, between the wall function and the turbulence model, at the location where the two sets of equations merge. Although, the wall function is practically an overlap law on top of the turbulence model, fundamentally it represents a boundary condition. In that conception, the wall function represents the inner region of the boundary layer, whilst the turbulence model with the transport equations the outer region of the boundary layer. The region where the two solutions should emerge, forming a common region of validity, is anywhere within the logarithmic (or log-law) layer ($30 < y^+ < 500$). However, to achieve a smooth matching, the wall function can be equated as an equilibrium solution to the turbulence model transport equations. This equilibrium simplification holds more accurately and sufficiently for the flow regime close to the wall. Wall functions have been formed based on the classic understanding of turbulent boundary layer structure, and consequently their formulation is based on the *law of the wall* and the *law of the wake* concepts [284].

From the above analysis it can be concluded that, wall functions provide the boundary conditions of the wall-adjacent volume cells, in which the effect of wall on the inner layer of the turbulent boundary layer, is already modelled based on the *law of the wall* concept. Consequently, if the wall is rough, a *roughness function* is employed to modify accordingly the *law of the wall* and to provide the *wall similarity* (universal velocity defect law) concept, as discussed in Section 4.1. STAR-CCM+ provides a standard and a blended wall function. Since the wall functions are defined in terms of dimensionless parameters, they are independent of Reynolds number.

As the present computational investigation utilises the standard wall function to model the effect of rough wall, the wall function-turbulence model overlap region takes place in the logarithmic layer at $y^+ \approx 30$, since, as it can be seen from Equation 4.34, at the viscous sublayer, the formulation of wall function does not contain a roughness function. The standard wall-function formulations for velocity (u^+) and turbulence

dissipation rate (ε^+), are presented in Equation 4.34 and Equation 4.36, respectively, whilst the graphic representations of the shape of the corresponding functions across the y^+ value range is also provided for clarity [280]. For the turbulent kinetic energy (k), there are no wall functions available since it is strongly dependent on the Reynolds number [280].

- Non-dimensional velocity:

$$u^+ = \begin{cases} y^+, & y^+ \leq \approx 3 \\ \frac{1}{\kappa}\ln(E' y^+), & 30 \leq y^+ \leq 500 \end{cases}, \quad (4.34)$$

$$E' = \frac{E}{f} \quad (4.35)$$

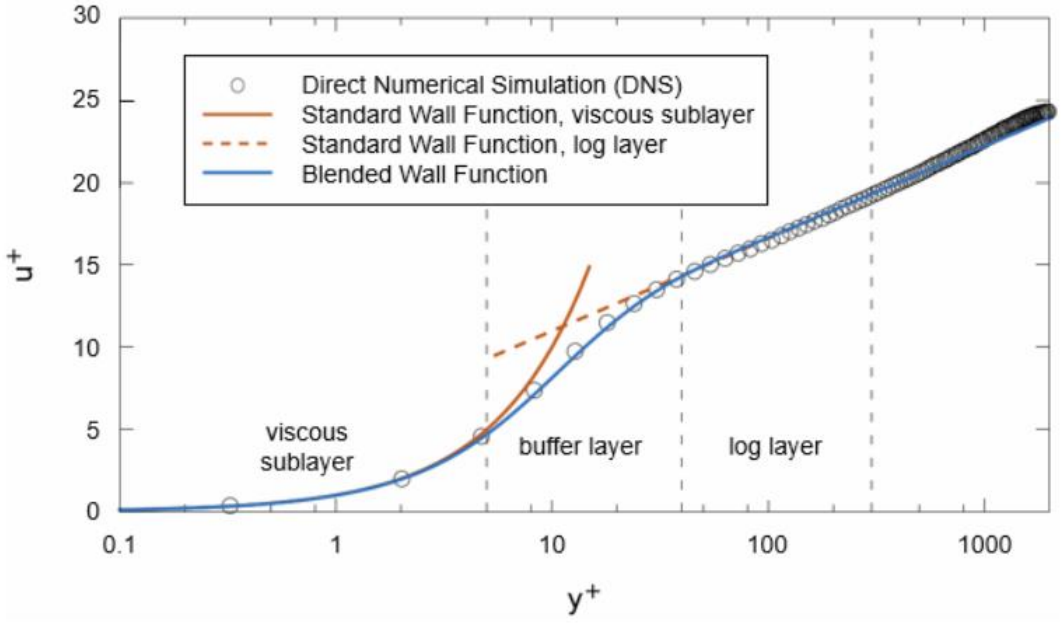

Figure 4.4.2-1 *Distribution of non-dimensional velocity (u^+), Source:* [280].

- Non-dimensional turbulent dissipation (ε^+) rate:

$$\varepsilon^+ = \begin{cases} \frac{2k^+}{(y^+)^2}, & y^+ \leq \approx 5 \\ \frac{1}{\kappa y^+}, & 30 \leq y^+ \leq 500 \end{cases}, \quad (4.36)$$

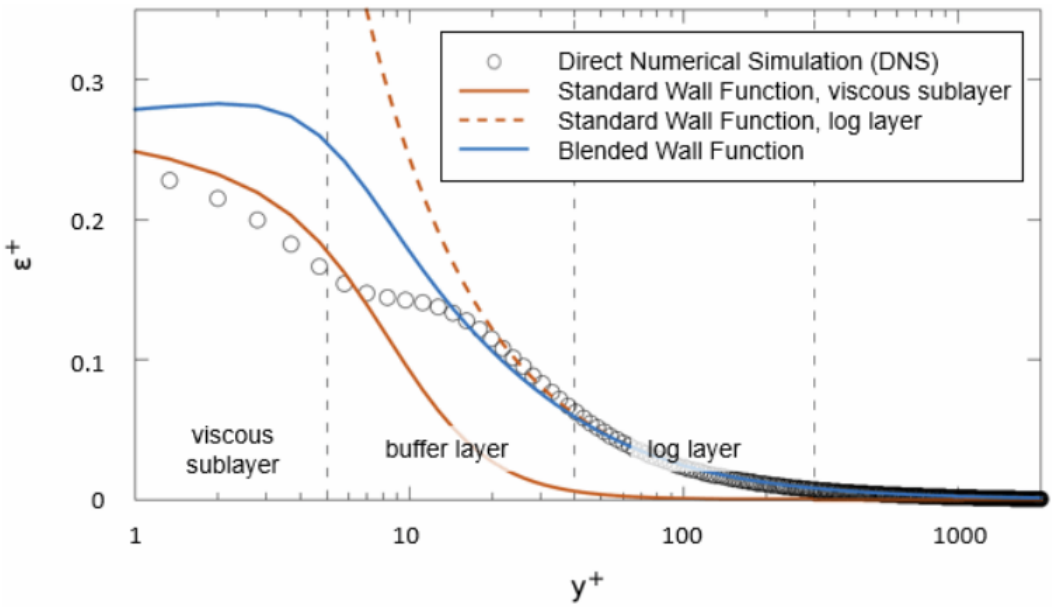

Figure 4.4.2-2 *Distribution of non-dimensional turbulent dissipation (ε^+), Source:* [280].

In the set of equation presented above, κ is the von Karman constant, E is the log offset and f' is the roughness function, as discussed in Section 4.2.4. The *roughness function* (f), which modifies the log offset (E), is a function of the *roughness Reynolds number* (k^+_s) (Equation 4.5). The roughness function is defined in Equation 4.37.

$$f = \begin{cases} 1 & ; k_s^+ \le k_{smooth}^+ \\ \left[B\left(\dfrac{k_s^+ - k_{smooth}^+}{k_{rough}^+ - k_{smooth}^+} \right) + C k_s^+ \right]^{\alpha} & ; k_{smooth}^+ < k_s^+ < k_{rough}^+, \\ B + C k_s^+ & ; k_s^+ > k_{rough}^+ \end{cases} \quad (4.37)$$

where

$$\alpha = \sin\left[\frac{\pi}{2} \frac{\log\left(\dfrac{k_s^+}{k_{smooth}^+} \right)}{\log\left(\dfrac{k_{rough}^+}{k_{smooth}^+} \right)} \right], \quad (4.38)$$

As shown in Equation 4.37, the roughness parameter is a function of equivalent sand-grain roughness, the concept of which was presented in Section 4.2.2. Additionally, the limits of the roughness function (f) are defined as the roughness Reynolds number (k^+_s) and represent the limits of the roughness regimes (discussed in Section 4.2.3). For the present numerical investigation, presented in Chapter 5, the default software values were used, such as $k^+_{smooth} = 2.25$ and $k^+_{rough} = 90$. These

values correspond to the roughness regime limits for equivalent sand-grain roughness, suggested by Cabeci and Bradshaw [301] and are also very close to the corresponding limits suggested by Ioselevich and Pilipenko [327]. For the model coefficients B and C, the default values, 0 and 0.253, were respectively used.

Finally, for the inlet boundary conditions of the computational domain employed in Chapter 5, the inlet turbulence intensity and inlet turbulent length scale has to be defined. Due to the absence of experimental data regarding these quantities, empirical correlations, frequently used for CFD simulations, were employed [324]. Therefore, the turbulence intensity (T_I) and turbulent length scale (T_L) were calculated based on Equation 4.39 and Equation 4.40, respectively, since the flows at inlet was assumed to be fully developed.

$$T_I = 0.16 Re_D^{-\frac{1}{8}}, \quad (4.39)$$

$$T_L = 0.07 D, \quad (4.40)$$

where, Re_D is the Reynolds number based on the mean flow velocity and inlet diameter and D is the inlet diameter.

4.5 Summary

The models, sub-models, and governing equations applicable for the problem described in this thesis have been introduced in this Chapter. The developed approaches regarding the numerical treatment of turbulent flows over smooth and rough surfaces have been presented and discussed. The approach selected will now be adopted in the following Chapter 5 to analyse its potential as an industrial modelling methodology to appraise the influence of surface roughness on the performance of a typical combustion geometry.

Chapter 5. Isothermal CFD; modelling of surface roughness of AM swirlers

In light of the previously suggested influence of surface roughness on combustion chemistry within industrial burners, and informing the design of further experimental investigations of the generic swirl burner required, an isothermal CFD study was undertaken to appraise the predictive capability, of the RANS Realizable k-epsilon (k-ε) model with respect to predicting surface roughness effects.

A two-layer model utilising the concept of wall function was adopted, to design and evaluate a methodology for investigating the effect of surface roughness, implemented in a computationally inexpensive way. It is worth emphasising that very few methodologies have been developed for the numerical investigation of surface roughness [62], and due to the excessive computational requirements, they are primarily applied to canonical flows and simplified geometries such as 2D channels and flat plates. The utilisation of wall functions along with a RANS Realizable k-ε two-layer model, facilitated a computationally inexpensive investigation of the effect of surface roughness on a full 3D burner geometry, which to the author's knowledge has not been previously undertaken.

The mesh parameters required were firstly investigated and satisfied to enable appropriate use of wall functions (Section 5.1). Subsequently, a mesh-independency study was conducted to specify the suitable cell size and total node number of the simulation domain, verifying such that the computed solution is independent of the grid resolution (Section 5.2). Finally, the validity of the physical model was assessed through comparison with 1D LDA measurements in isothermal flows, obtained for the three swirlers: *Machined* (1 μm), *AM-G* (5 μm) and *AM-R* (9 μm) as reported by Runyon et al. [29] (Section 5.3). Based on previous experimental results [29], the impact of surface roughness was associated with a reduction in the peak axial velocity and the shifting of the positive outwards flow towards the central axis of the burner. Thus, the validation assessment was extended to the observed flow pattern transitions. Potential sources of uncertainty and error that drive the accuracy of the CFD solver are also discussed (Section 5.4). Finally, the CFD results are discussed on reflection of the corresponding experimental data, providing a summary of the Chapter (Section 5.5).

5.1 Mesh requirements

The *wall function* modelling approach was used to account for wall roughness effects. According to this approach, the *roughness function* f modifies the *coefficient* E' that is used to reduce the logarithmic velocity profile at the fully turbulent log-law region of the boundary layer. The *roughness function* f is determined from the *roughness Reynolds number* k^+_s, which is a function of the *equivalent sand-grain roughness*, as detailed previously in Section 4.5. Specifically, this modelling approach, also referred as *high* y^+ *approach,* requires y^+ values higher than 30, as shown in the following Figure 5.1-1 (A) [280].

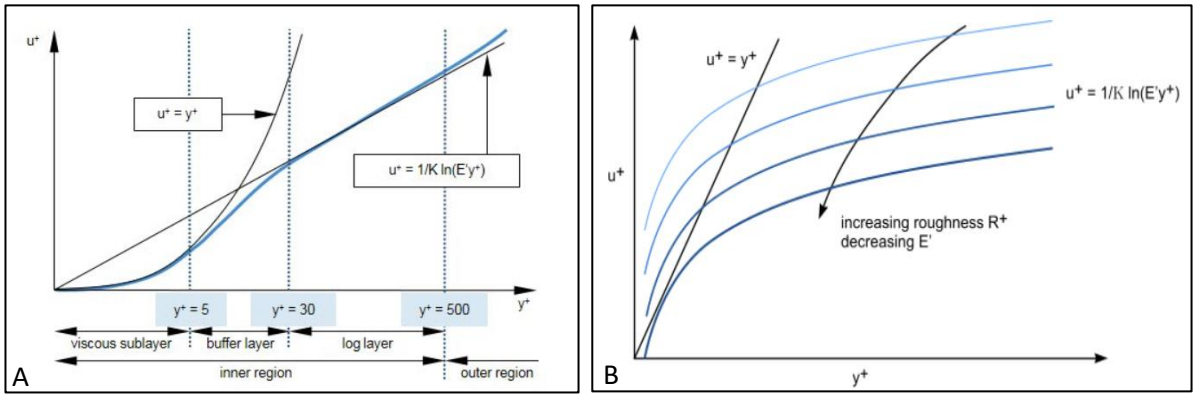

Figure 5.1-1 *(A): Schematic of the non-dimensional velocity* u^+ *distribution as a function of wall* y^+ *across the three sublayers of the inner region of the turbulent boundary layer. (B): The effect of decreasing coefficient E' on non-dimensional* u^+*. Source:* [280].

This approach assumes that the first near-wall cell lies within the logarithmic region (log-layer) of the boundary layer as illustrated in Figure 5.1-2. Therefore, the effect of surface roughness in the buffer and viscous sublayer is modelled and extrapolated to the first near-wall cell. The accuracy of the above-described methodology is mainly influenced by the level of agreement between the assumed parameters embodied in the wall functions (such as, the equivalent sand-grain roughness) and the actual parameters (such as, the measured surface roughness) that correspond to the simulation [36, 62, 280]. As described in Section 4.3, the main advantage of the *wall function* approach is the reduction of the required computational power since the spatial resolution of the near-wall region is reduced, and consequently, the number of near-wall cells required is decreased.

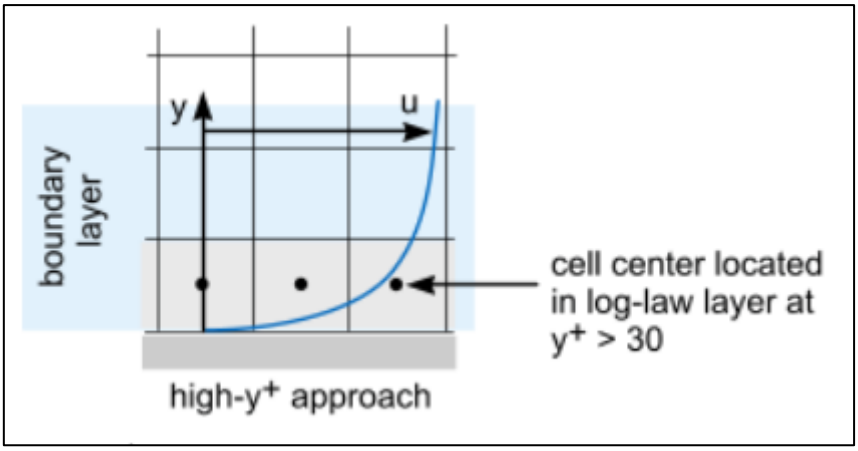

Figure 5.1-2 *Illustration of the near wall cell distribution across the boundary layer for the high y^+ approach, Source:* [280].

In *Simcenter STAR-CCM+ 2019.3 (Build 14.06.012)*, the modelling strategy above is the most computationally inexpensive approach to account for surface roughness effects. An alternative approach would require the full integration of the surface roughness to the wall parts in the computational domain; and the use of multiple prism layers (inflation layers) to fully resolve all the sub-layers of the turbulent boundary layer. Although theoretically this is the ultimate way of studying the effect of surface roughness, given the length-scales associated with the present surface roughness range (1-9 μm) and diameter of nozzle (40 mm), such a large length-scale ratio would demand very fine mesh resolution next to the wall, making the numerical simulation computationally expensive. Additionally, a third approach considered required the selection of the k-ω turbulence model and consequently the use of a much finer computational mesh. This is a verified, common approach that is usually employed in the literature, in which the *specific turbulent dissipation rate* function (ω) at the rough surface is modified to account for roughness effects using the equivalent sand-grain roughness term. However, the use of a significantly finer mesh to achieve a *wall* y^+ value close to unity, which is a requirement of the k-ω turbulence model, would significantly increase the computational cost of the simulations, if applied to the full 3D geometry of the burner. As the main aim of this investigation is to exploit a computationally inexpensive methodology, the Realizable k-ε two-layer turbulence model was preferred to k-ε elliptic blending model, which requires higher computational power, similar to the k-ω case.

To implement the wall functions approach, and thus, to model the viscous and buffer layer while resolving the log-law region, it is important to ensure that the vast

majority of the cells in the areas where surface roughness is studied, satisfy the meshing requirement of $y^+ > 30$. These areas are the flat and curved surfaces of the vanes of the swirler, as well as the top wall of the swirler and the inner wall of the nozzle as described in section 3.3.1. The $y^+ > 30$ assumption results from the logarithmic region of the turbulent boundary layer, as indicated in Figures 5.1-2. Since the cells adjacent to the wall must fall within this region, the minimum value that can be used is 30. The lower limit of acceptable y^+ range was targeted to maximise the resolution of the inherent fluid dynamics prevailed in the computational domain. The y^+ value requires initial simulation of computational fluid domain, as it is calculated from the value of friction velocity (u^*), which is computed as part of a flow solution. Thus, an *a posteriori* adjustment of the computational domain is often necessary to produce the required y^+ distribution [278]. Three meshes were produced in the mesh independency study, with the average y^+ values of the rough surfaces, as described above, listed in the following Table 5.1-1.

Table 5.1-1 *Average wall y^+ results for the three generated meshes.*

Mesh Type	Average y^+
Coarse mesh$_1$	≈32.99
Medium mesh$_2$	≈33.06
Fine mesh$_3$	≈33.07

The resultant values of the mesh refinement satisfy $y^+ > 30$ ensuring the adoption of wall functions. The y^+ values are significantly dependent on the flow velocity along the solid wall surfaces, imposing additional complexity to comply with the $y^+ > 30$ condition. For instance, the leading edge of the curved vanes result in lower y^+ values compared to the trailing edge, where the flow is further developed to turbulent and therefore the roughness sublayer of the turbulent boundary layer becomes thinner, resulting in higher y^+ values. To ensure $y^+ > 30$, a single prism layer along the wall surfaces was created. In Figure 5.1-3, a depiction of the near wall meshing with prism layers, depicting the vanes (left) and the nozzle (right).

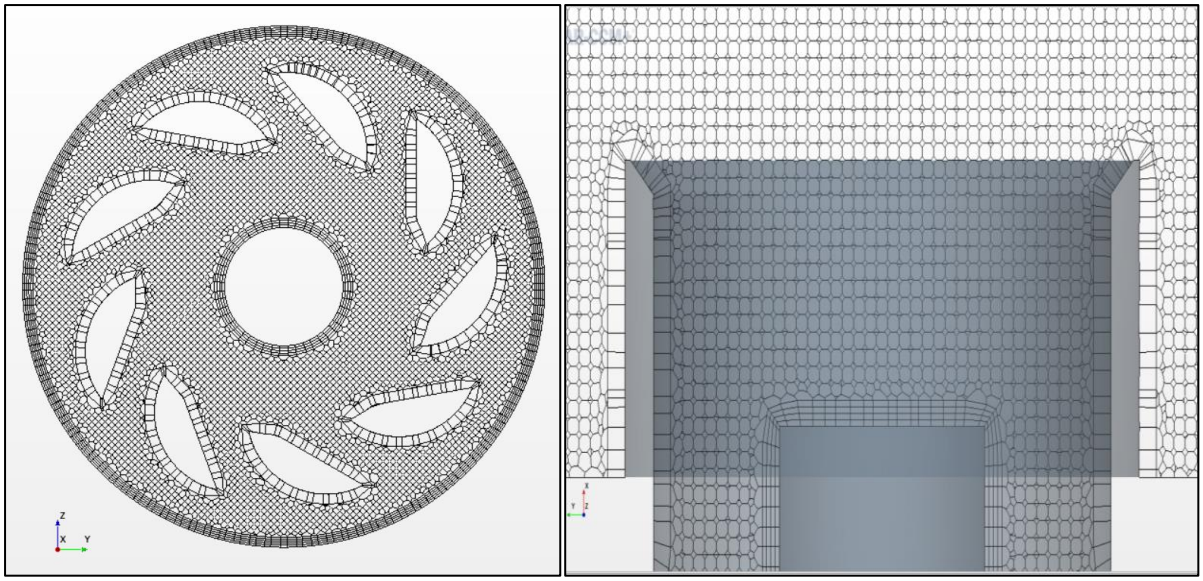

Figure 5.1-3 *Visual depiction of the near-wall mesh modelling indicating the single prism layer near the rough vanes (left) and nozzle (right).*

5.2 Mesh independency

The mesh independency - also referred as grid independency - is an important exercise that confirms the accuracy of converged CFD solutions to within a chosen tolerance. Through this process, it is shown that the predicted computational solution is independent of the spatial resolution of the computational grid. As discussed by Almohammadi et al. [328], the first step towards a mesh independent solution is to obtain both an iterative and a mesh converged solution. While the former concerns the number of iterations and the minimization of residuals, the latter requires the use of monitoring points, which are stabilised as the simulation progresses. The mesh independency exercise should precede the model validation. Once a “converged” solution is mesh independent, then the comparison with the experimental data can take place.

The convergence of a steady-state CFD solution can be assessed by using residual values and monitoring the flow quantities of interest. The assessment of residuals is a meticulous process, which is strongly related to the specific case investigated. As residuals are dependent upon the accuracy of the presumed initial conditions, in some cases, selecting an initial condition close to the desired solution, might limit the iterative reduction of residuals, and hence, maintain them at relatively higher levels. Hence, the mere evaluation of residuals as the satisfactory condition for a converged solution is problematic [280]. The automatically normalised residuals for

some of the variables, as produced by the solver, reduced to 10^{-4}, while the non-normalised analogous values were less than 10^{-5}. This is attributed to the combination of the simulated flow field (which included steep velocity gradients and vortices) and simulated geometry (which consists of sharp edges that could potentially increase the skewness angle and reduced the cell quality), thus reducing the stability of the simulation [324]. Subsequently, the mesh converged solution approach was also taken into consideration for evaluating the convergence of the simulation. For all simulations, monitoring points were placed in several locations around the simulation domain, allowing the visualisation of changes of the corresponding cell values per iteration. The mesh converged solution was achieved and the simulation stopping criterion was satisfied when the vast majority of the monitoring points in the main areas of interest were stabilised, with an iterative fluctuation of less than 1% noted.

Since it was confirmed that the computational solution was converged, the mesh independency study could then take place. For this set of simulations, in which the steady-state Reynolds Averaged Navier-Stokes equation with the Realizable k-ε two-layer model was utilised, the method of Grid Convergence Index (GCI) was selected to appraise mesh independency. The GCI method, which stems from the *General Richardson Extrapolation*, was first proposed by Roache [329] in 1994 and correlates the error resulting from systematic grid refinements or coarsening to the error resulting when doubling or halving the grid size, respectively. Therefore, the GCI method is used to estimate the percentage difference of the selected variable as the grid is further refined, and how far the solution is from the asymptotic range of convergence. The closer the GCI value is to 1, the closer the solution is to the asymptotic range. Although the GCI method can be applied on two consecutively refined grids, use of three grids is recommended to increase the accuracy of the estimation of the order of convergence.

Equation 5.1 presents the formulation of GCI:

$$GCI = \frac{F_s \times \left| \frac{f_1 - f_2}{f_2} \right|}{(r_k^p - 1)} \cdot 100\% \qquad (5.1)$$

In Equation 5.2, F_s is the safety factor with a value of 1.25, as indicated for GCI calculation of three refined grids, f_i corresponds to the value of the examined

parameter of the *i*-th grid, r_k is the ratio between two consecutively refined grids defined as:

$$r_k = \frac{N_{i+1}}{N_i} \qquad (5.2)$$

where *N* is the total number of cells in the *i*-th grid with p acquired from following Equation 5.3. The original formula for p as it is described by Roache [329] does not include the absolute function, however, due to the non-monotonic convergence of the computational simulation, the absence of the absolute function could potentially result to negative values, which cannot be used in the natural logarithm function. The introduction of the absolute function inside the logarithmic function allows estimation of the percentage difference even if f_1, f_2 *and* f_3 are not changing monotonically.

$$p = \frac{\ln\left|\frac{f_1 - f_2}{f_2 - f_3}\right|}{\ln r_k} \qquad (5.3)$$

Finally, the following ratio is calculated to quantify the level of grid convergence:

$$Convergence\ Index = \frac{GCI_{i,i-1}}{r_k^p \times GCI_{i+1,i}} \qquad (5.4)$$

When the *Convergence Index* ratio is closer to unity, the solution of the *i*-th grid is estimated to be within the asymptotic range of convergence [60, 330]. The present computational investigation focuses on the effect of surface roughness on the mean flow parameters such as axial velocity magnitudes, skin friction coefficient and pressure drop. Hence, it is sensible to perform the mesh independency study with respect to those scalars. Specifically, the magnitude of the axial velocity at points A (0.005 m, 0.01 m) and B (0.005 m, 0.02 m), where the x and y coordinates correspond to axial and radial displacements of the nozzle exit and burner centreline respectively, were input in the GCI algorithm. Furthermore, the average *Skin Friction Coefficient* (C_{fAVG}) and y^+ (y^+_{AVG}) from all surfaces of the computational domain, where roughness is present, as well as total *pressure drop* (ΔP), were chosen as the additional parameters examined by the GCI methodology, with used values presented in Table 5.2-1.

Table 5.2-1 *Mesh independency study results.*

Mesh		***Coarse***	***Medium***	***Fine***
Total cells		*≈3.8x10⁶*	*≈7.1x10⁶*	*≈13.3x10⁶*
r_k		-	*≈1.87*	*≈1.87*
V_{axial} ***(m/s)***				
A (0.005m, 0.01m)	$V_{axial,A}$	6.56	6.44	6.34
	$GCI_{i,i-1}$	-	0.1560%	0.1385%
	$\boldsymbol{GCI_{i,i-1}/[(r^p_k)GCI_{i+1,1}]}$	**-**	**0.9843**	-
B (0.005m, 0.02m)	$V_{axial,A}$	23.58	23.70	23.72
	$GCI_{i,i-1}$	-	0.0012%	0.0002%
	$\boldsymbol{GCI_{i,i-1}/[(r^p_k)GCI_{i+1,1}]}$	**-**	**1.0008**	-
Skin Friction Coefficient (C_f)	C_{fAVG-i}	0.28592	0.28548	0.28568
	$GCI_{i,i-1}$	-	0.0017%	0.0008%
	$\boldsymbol{GCI_{i,i-1}/[(r^p_k)GCI_{i+1,1}]}$	**-**	**0.98611**	-
$\boldsymbol{y^+_{AVG}}$ ***(-)***	$y+_{AVG}$	32.99	33.06	33.07
	$GCI_{i,i-1}$	-	0.0004%	0.00006%
	$\boldsymbol{GCI_{i,i-1}/[(r^p_k)GCI_{i+1,1}]}$	**-**	**1.0003**	-
Total ΔP (Pa)	τ_{wAVG-i}	714.02	714.73	714.97
	$GCI_{i,i-1}$	-	0.00064%	0.00022%
	$\boldsymbol{GCI_{i,i-1}/[(r^p_k)GCI_{i+1,1}]}$	**-**	**1.0003**	-

All Converged Index ratio values are very close to unity; hence, it is verified that the solution of the medium mesh, ($Mesh_2$), is within the asymptotic range of convergence.

In addition to the GCI method, the isothermal axial velocity profile across the radial displacement of the burner was plotted (Figure 5.2-1) and compared against the 1D LDA isothermal measurements at the analogous locations. All the three meshes are in good agreement with the experimental data. The highest positive outward velocities ($0.15\ \mathrm{m} < x < 0.2\ \mathrm{m}$) were slightly underpredicted resulting in a difference of ≈8%. This is due to the complexity of the flow in the specific region and the physical approximation errors associated with the boundary conditions of the simulation domain, such as the outlet pressure, inlet turbulence intensity and length scale, as well as the curvature correction function. Those potential sources of error are further discussed in Section 5.4.

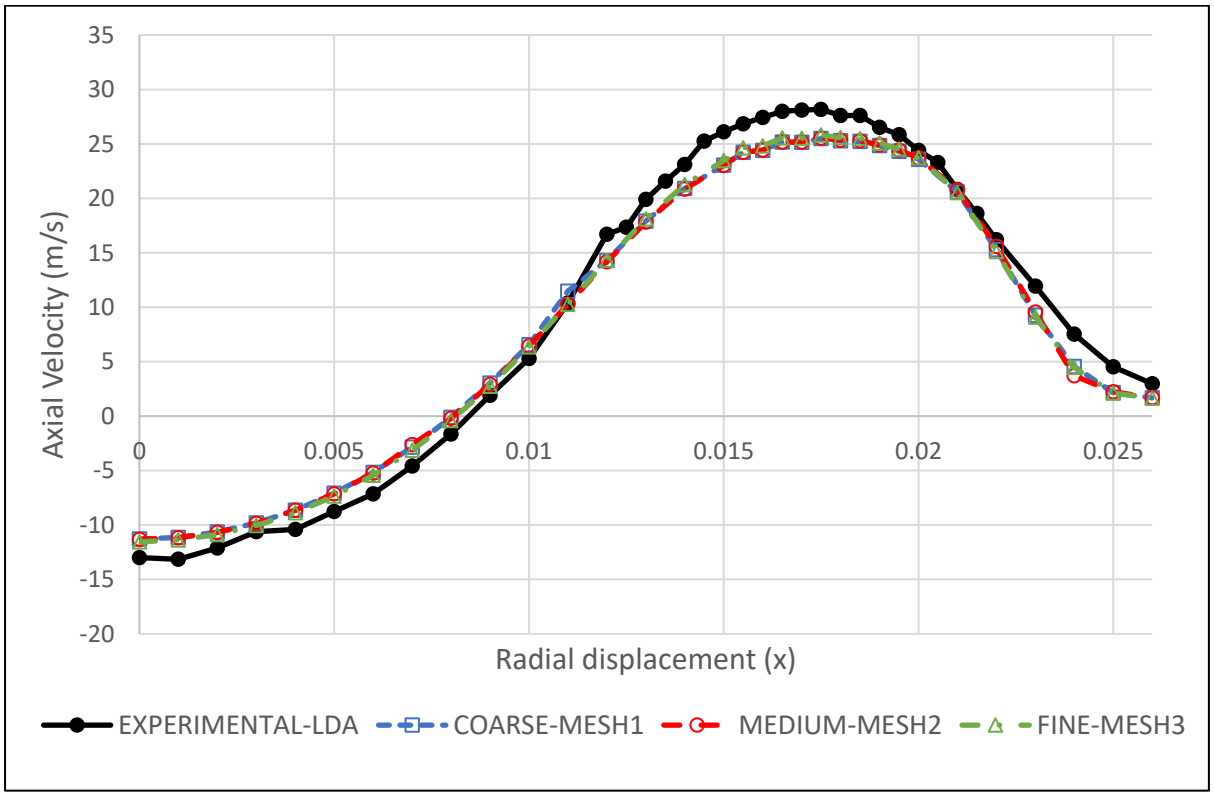

Figure 5.2-1 *Isothermal axial velocity comparison between the experimental LDA and the computationally predicted results for the coarse (mesh1), medium (mesh2) and fine (mesh3) meshes, using the Machined swirler.*

The medium-resolution computational grid (*Mesh*$_2$) was chosen over the high-resolution grid (*Mesh*$_3$) as it demands less computational power with minimal change in the accuracy of the predicted quantities of interest. Concerning the computational domain, which is presented in Figure 5.2-2, it is worth noting that the complete 3D geometry of the burner was simulated. The complete 3D geometry was preferred as

the alignment of the radial-tangential swirler in the circumferential direction (Figure 5.2-3), which consists of 9 vanes, renders the axisymmetric flow assumption invalid.

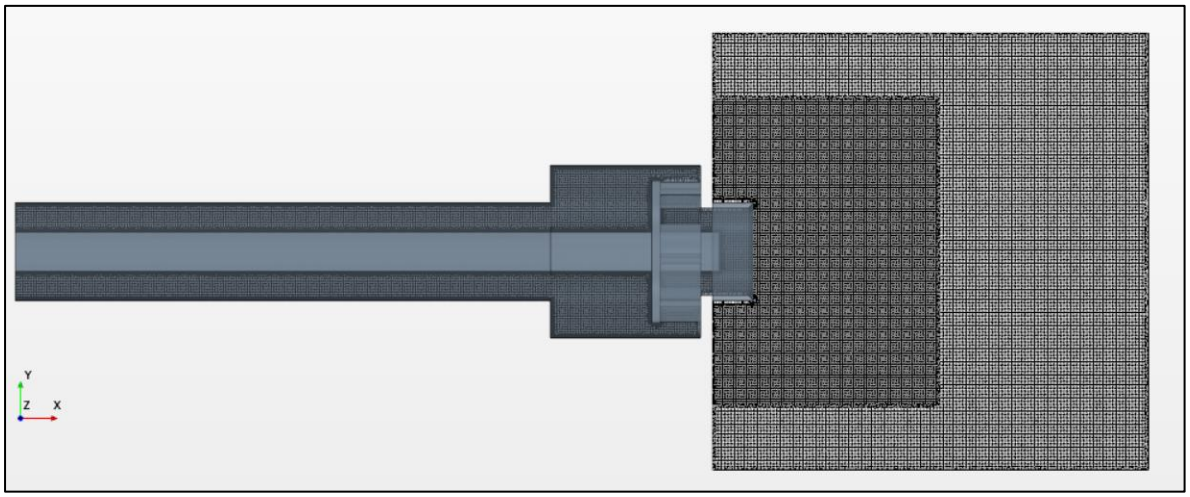

Figure 5.2-2 *Depiction of the full computational domain, illustrating the fined and default volume mesh.*

Concerning mesh characteristics, polyhedral elements were used for the generation of both surface and volume mesh, whilst prism layers were utilised at the inner edges of wall boundaries to provide the appropriate y^+ values. For the selected *Mesh*$_2$ grid, the default polyhedral base size and the minimum surface size were set at 0.009 m and 0.00135 m, respectively. To avoid the generation of unstructured mesh, surface and volume custom mesh control options were enabled. Consequently, the selected areas were refined to structured mesh, to improve mesh quality and ensure sufficient cell numbers enabling accurate flow representation across the narrow flow domain. Specifically, for the nozzle bluff body, the target and minimum surface sizes were both set at 0.001 m, whilst the 4 prism layers of total thickness 0.0025 m were generated around its internal edges. For the rest of the surfaces, excluding the nozzle, swirler and outlet surfaces, the target and minimum surface sizes were set at 0.001 m, whereas 5 prism layers were generated of total thickness of 0.0025 m. The assignment of an extra prism layer aimed to further improve the boundary layer resolution upstream of the area of interest, without significantly increasing the computational requirements. The prism layers, together with surface

and volume mesh's for the inlet plenum, mixing chamber, nozzle bluff body and swirler flange are presented in following Figure 5.2-3.

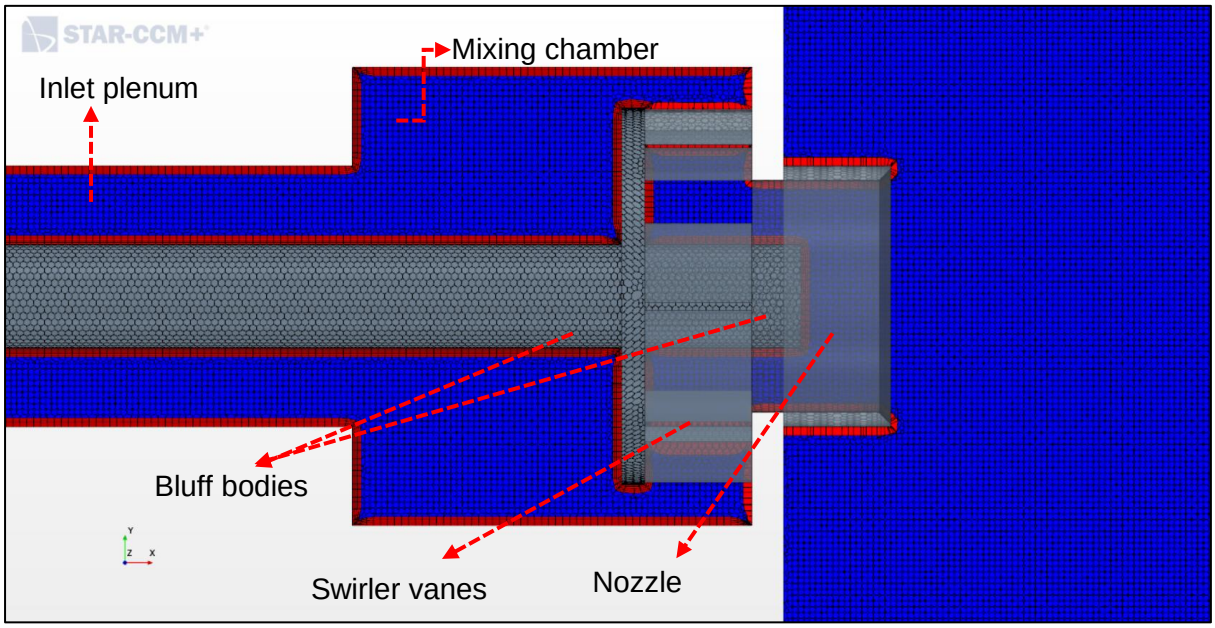

Figure 5.2-3 *Depiction of surface and volume mesh, highlighting the prism layers location in red colour.*

For the swirler and nozzle section of the swirler (Figure 5.2-4), the target and minimum surface size was set at 0.001 m and a single prism layer was assigned around the internal boundaries between the wall surfaces and the fluid volume domain, in order to keep the y^+ values over 30 and thus to implement the use of wall functions (Figures 5.2-3). With regard to the outlets, which are shown in Figure 5.2-5, both target and minimum surface sizes were set at 0.0025 m for outlet 3, whilst for outlet 1 and 2 the analogous values were set at 0.002 m and 0.001 m respectively. Finally, the fluid domain inside the nozzle and downstream of the swirler, was discretised to a cell size of 0.001 m and 0.0015 m, respectively, as indicated in Figure 5.2-2, based on the velocity variation.

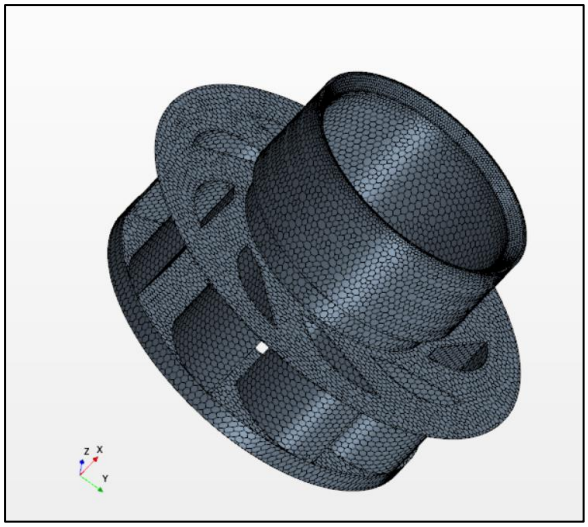

Figure 5.2-4 *Surface mesh representation of swirler*

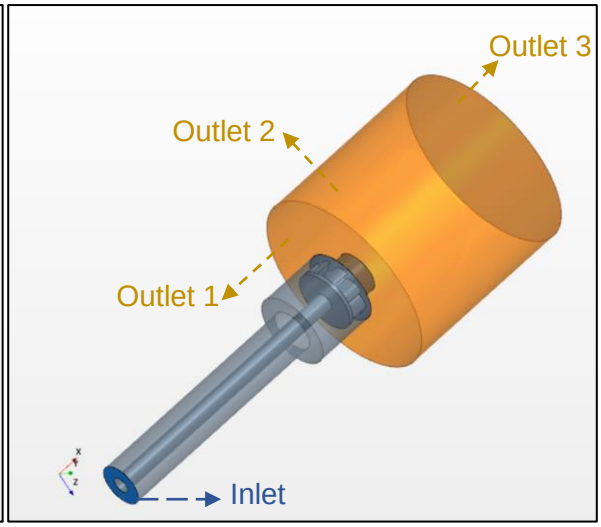

Figure 5.2-5 *Inlet and outlets of computational domain*

5.3 Evaluation of the predictive capability of the CFD model on capturing the effect of surface roughness

The aim of this section is to evaluate the effectiveness of the computational continua, which is comprised of the physics continua (RANS Realizable k-ε Two-layer model) and the mesh continua (high y^+ wall functions approach), in capturing the effect of surface roughness. Thus, examining if a robust methodology of investigating the effect of surface roughness can be employed in a computationally inexpensive way. This is highlighted by comparing the computationally derived axial velocity distribution with the analogous experimentally acquired one. Additionally, this section aims to provide an explanation regarding any changes in the isothermal flow field structures because of the impact of surface roughness.

The total mass flowrate for all simulations was equal to 0.0161 kg/s, yielding a bulk axial velocity of 19.17 m/s at the nozzle exit, at this condition the Reynolds number is equal to ≈17200, similar to the Reynolds number calculated for a defined CH_4 combustion case, at $\varphi=0.55$, [29]. The continuum temperature was set to 573 K to also be consistent with the experimental campaign and no heat losses through walls were assumed. The boundary condition inputs, together with the thermodynamic properties of air and the selected physical models that were used for all simulation cases, are analytically listed in Table 5.3-1. The thermodynamic properties of air were calculated based on the continuum temperature (573 K), whilst the inlet turbulence

intensity and turbulent length scale length scale were estimated per Equation 4.39 and 4.40, respectively (Section 4.4.2).

Table 5.3-1 *Boundary conditions, thermodynamic properties of air and physical models.*

Boundary Conditions	**Value**
Inlet mass flow rate (kg/s)	0.0161
Inlet turbulence intensity (%)	≈4.8
Inlet turbulent length scale (m)	0.00158
Outlets pressure (Pa)	101325.0 (atmospheric)
Continuum temperature (K)	573.0
Thermodynamic properties of Air	**Value**
Density (kg/m^3)	≈0.668
Dynamic viscosity (Pa·s)	≈2.985
Molecular Weight (kg/kmol)	28.9664
Specific heat [J/(kg·K)]	≈1046.0
Thermal Conductivity [W/(m·K)]	≈0.02603
Turbulent Prandtl Number (-)	≈0.70829
Physical Models	
Reynolds-Averaged Navier-Stokes	
Realizable k-ε Two-layer	
Ideal Gas	
Segregated Flow	
Segregated Fluid Isothermal	

In Figures 5.3-1, 5.3-2 and 5.3-3 the predicted isothermal axial velocity profiles of the three swirlers are compared against their 1D LDA experimental measurements. The experimental measurements, which can be found in [29], were conducted 5 mm above the exit of the nozzle, covering most of the radial dimension of the swirlers. The shape of the axial velocity distribution reveals the territory of the recirculation zone at this location. Specifically, the Central Recirculation Zone (CRZ) was located in radial coordinates ($0 \leq x \leq \approx 0.0085$ m) where the axial velocities range from negative values

to zero, followed by the free shear layer. The Positive Outwards Flow (POF) extended from $\approx 0.0085\ \mathrm{m} \leq x \leq 0.026\ \mathrm{m}$, peaking between $0.016\ \mathrm{m} \leq x \leq 0.018\ \mathrm{m}$.

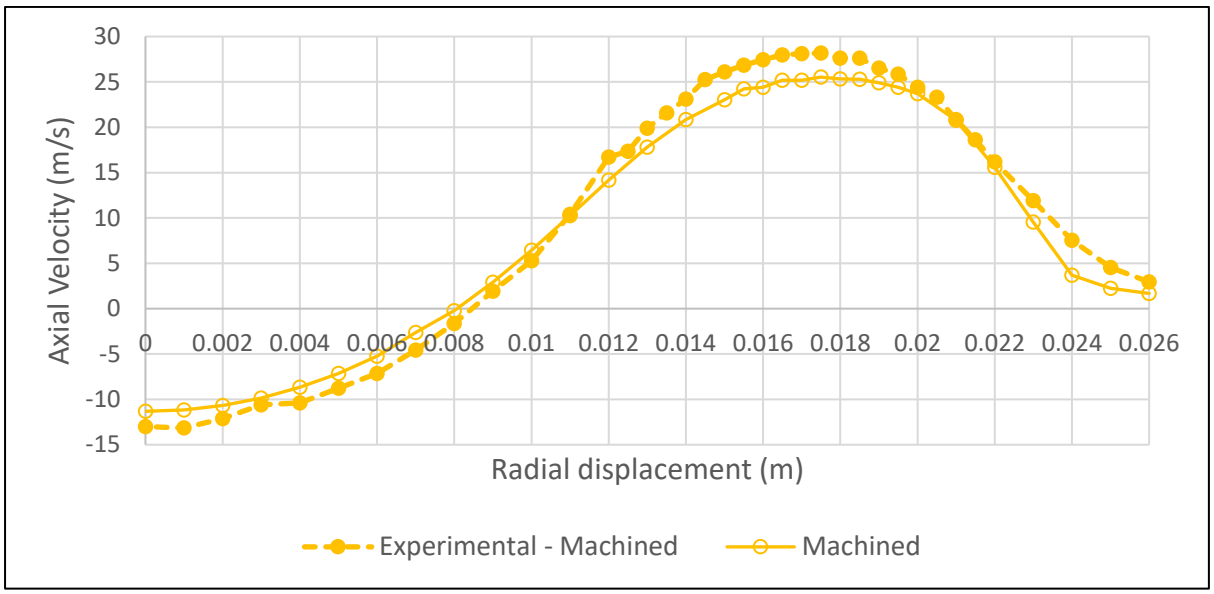

Figure 5.3-1 *Comparison of experimental Machined and CFD predicted Machined (1 μm) isothermal velocity profile.*

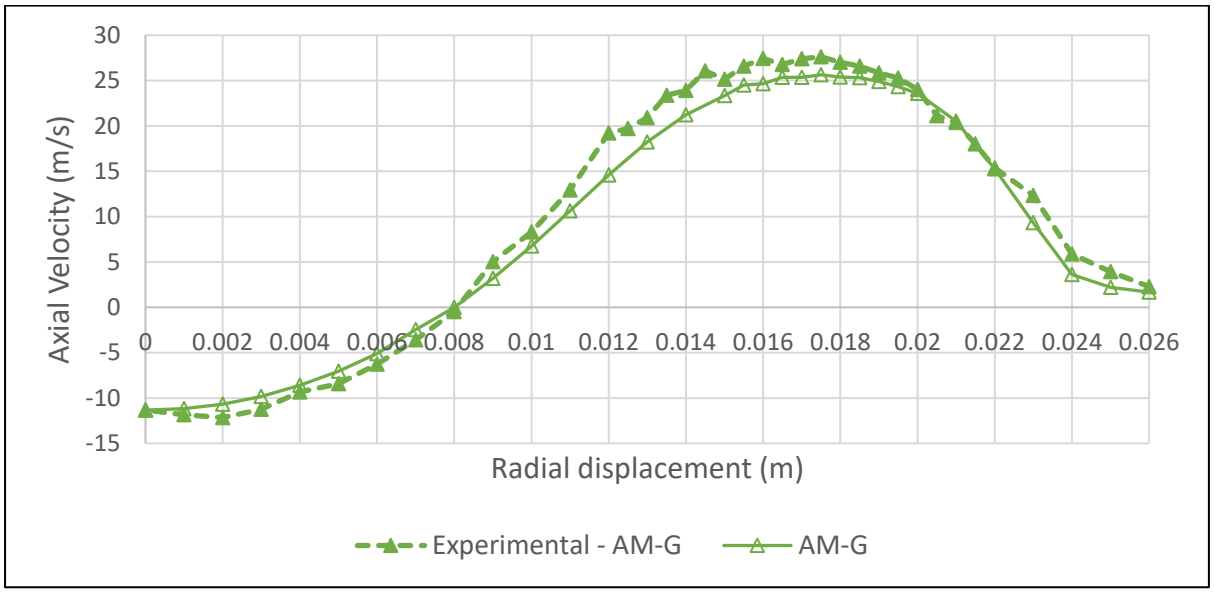

Figure 5.3-2 *Comparison of experimental AM-G and CFD predicted AM-G (5 μm) isothermal velocity profile.*

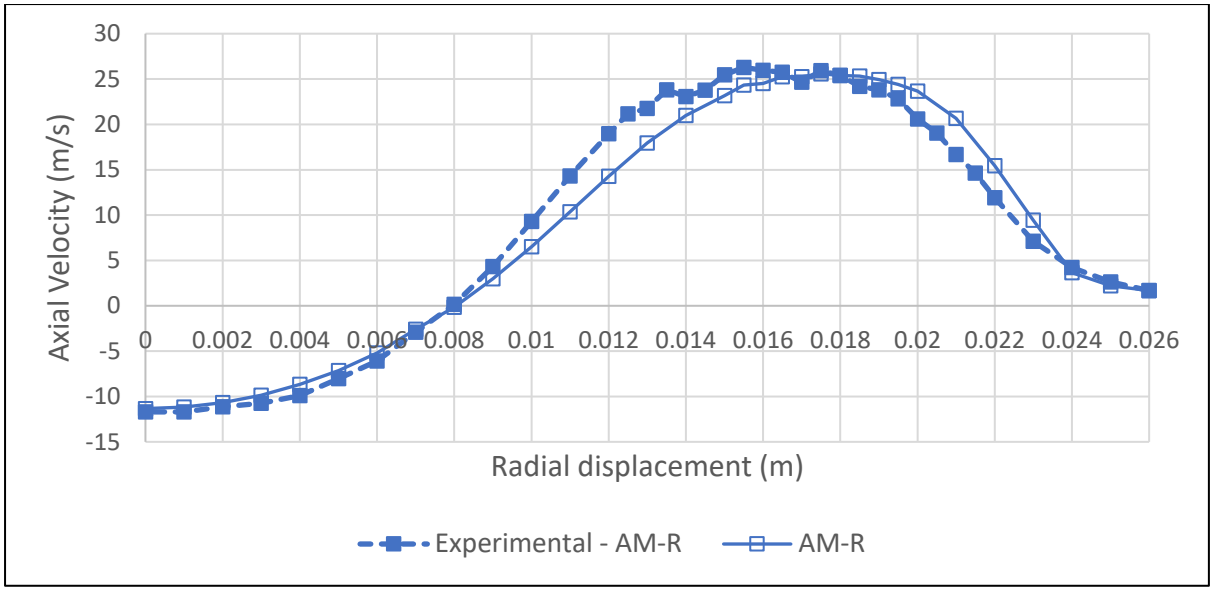

Figure 5.3-3 *Comparison of experimental AM-R and CFD predicted AM-R (9 μm) isothermal velocity profile.*

For all three cases, the isothermal axial velocity profiles obtained computationally were very similar, indicative of the CFD solver predicting little effect of surface roughness on the isothermal axial velocity distribution. Although the width of the POF appears correctly captured, its shifting towards the centreline of the burner, is underpredicted compared to the experimental data. Additionally, the peak axial velocity deficit was also subtlety lower than the empirically derived result. According to the experimental results in Figure 5.3-4, the surface roughness affected the isothermal velocity profile in two ways: by shifting the location of the POF towards the centreline of the burner and by decreasing the peak axial velocities. Hence, it is sensible to investigate the predictive capability of the solver in capturing those two phenomena separately.

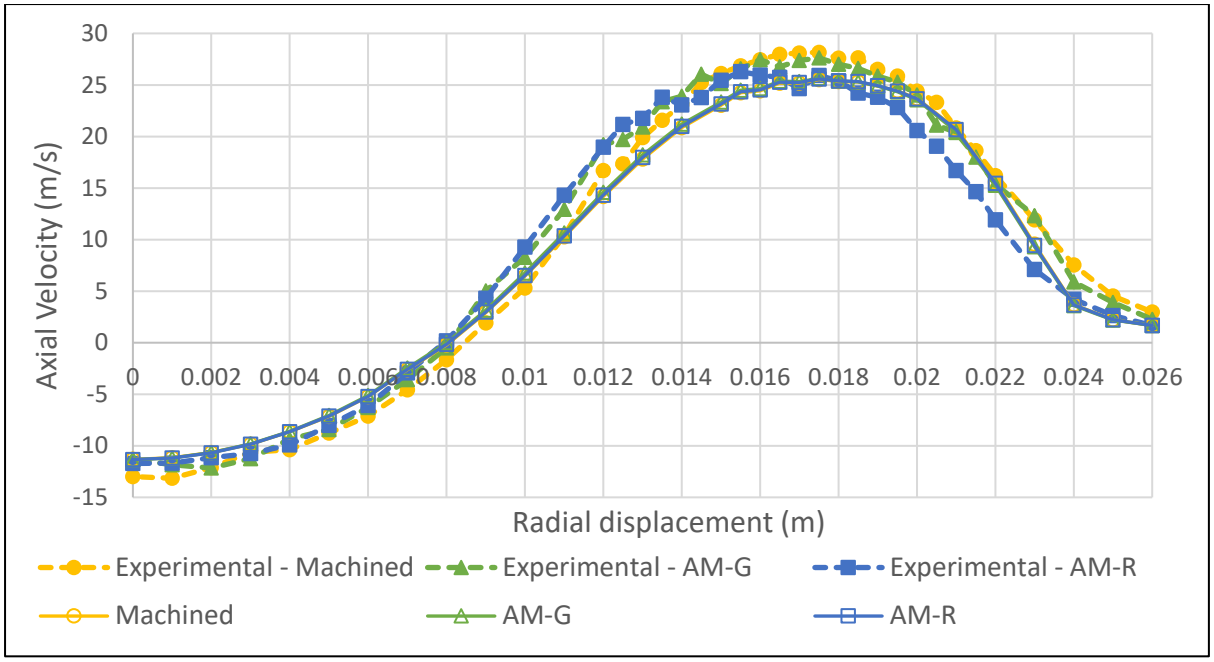

Figure 5.3-4 *Experimental vs CFD isothermal axial velocity profiles for Machined, AM-G and AM-R.*

A potential reason for disagreement, between the experimental and the CFD predicted profiles, is the dependence of the computational model on the *equivalent sand-grain roughness* and consequently on the algorithm that was used to convert the measured surface roughness to the equivalent one, rather than the inability of the CFD solver to capture this specific phenomenon. Referring to Section 4.3, there are multiple equations and algorithms to perform the task of converting the actual, measured surface roughness to the equivalent sand-grain one. A thorough review on this issue is published by Bons in [36]. For the current computational work, Equation 4.4 (Section 4.2.2) was used to perform the conversion as proposed by Adams et al. [297]. It is therefore presumed that the algorithm implemented for the roughness conversion underpredicted the equivalent sand-grain roughness value for the cases of the grit-blasted *(AM-G)* and raw *(AM-R)* swirlers. Consequently, the effect of surface roughness on mean flow parameters, such as the axial velocity and the momentum, was underestimated. However, as presented in Figures 5.3-5 and 5.3-6, where the predicted inner and outer shear layers are each respectively plotted against those experimentally measured, even for the low equivalent sand-grain roughness values, the shifting in POF was qualitatively captured by the computational scheme.

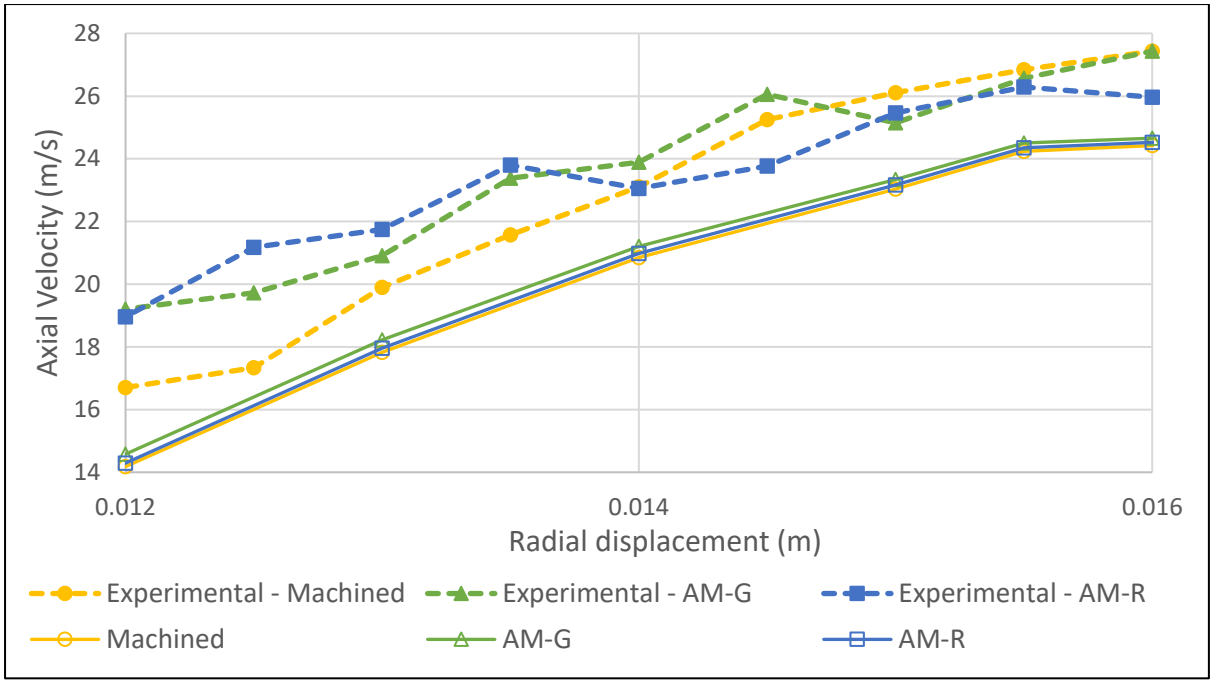

Figure 5.3-5 *Experimental vs CFD isothermal axial velocity profiles for Machined, AM-G and AM-R at inner shear layer location (0.012 m ≤ x ≤ 0.016 m).*

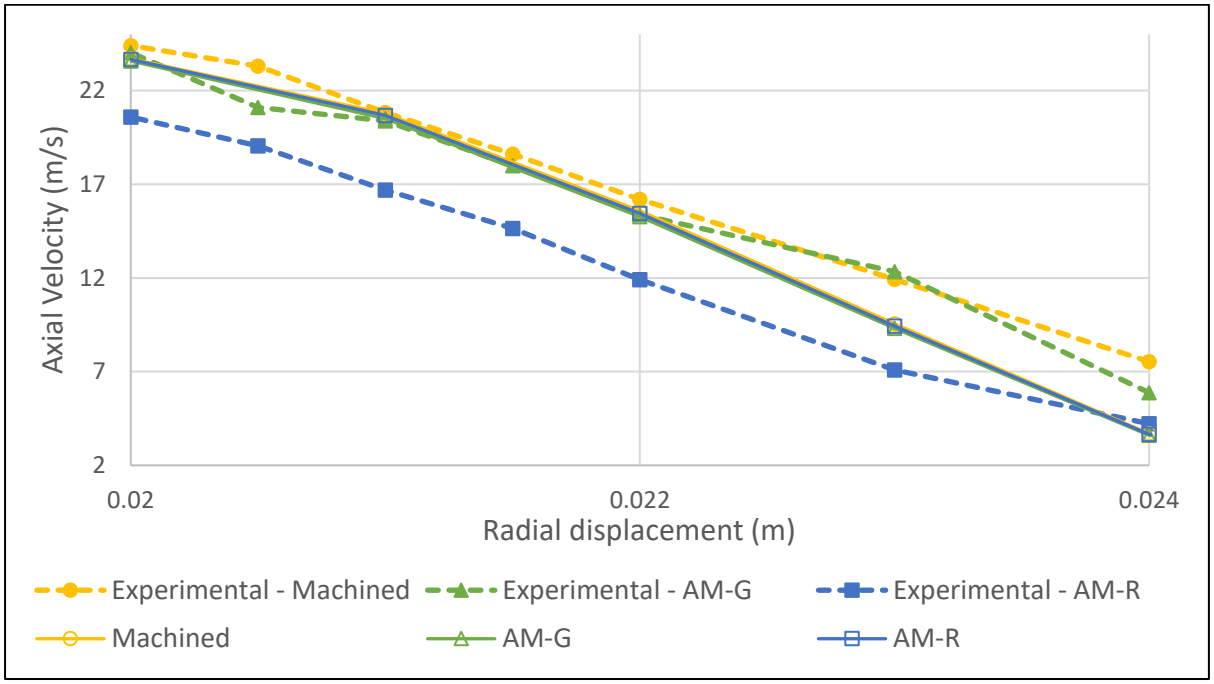

Figure 5.3-6 *Experimental vs CFD isothermal axial velocity profiles for Machined, AM-G and AM-R at outer shear layer location (0.02 m ≤ x ≤ 0.024 m).*

The validity of the hypothesis that the underprediction of the POF shifting stems from the underestimation of equivalent sand-grain roughness was further investigated, the results of which are presented in Figure 5.3-7. Here, higher equivalent sand-grain roughness values were assigned for the grit-blasted *(AM-G)* and raw *(AM-R)* swirlers.

Instead of employing different conversion algorithms to result in higher equivalent sand-grain values, the same generic conversion algorithm was purposely modified to increase the input roughness ten-fold resulting in a deliberately high equivalent sand-grain roughness. In this way, the underprediction of the equivalent roughness and thus of the POF shifting, due to the selected algorithm, would be highlighted. Additionally, since the post processing method applied to the swirlers was varying, different equations would have been required, which would increase further the complexity of the comparison. Thus, the use of the generic algorithm was favoured to minimise the variables compared.

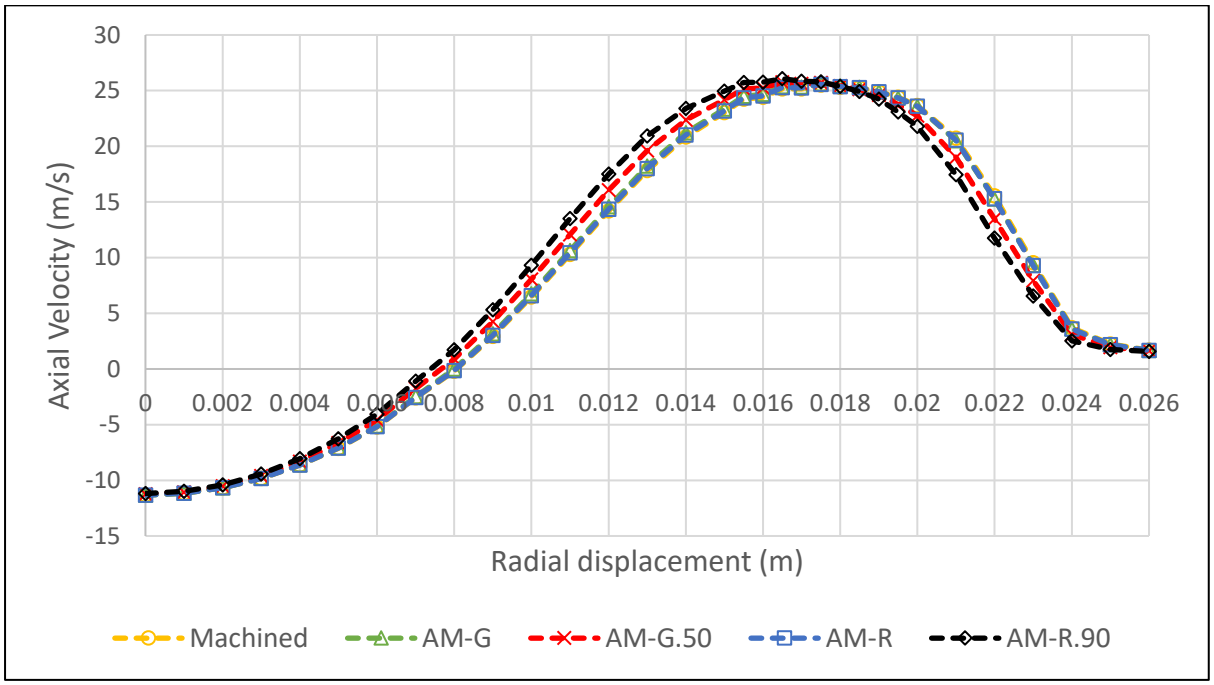

Figure 5.3-7 *Computationally predicted, isothermal axial velocity distribution for Machined (1μm), AM-G (5 μm), AM-G.50 (50 μm), AM-R (9 μm), and AM-R.90 (90 μm).*

The series labelled as *"AM-G.50"* and *"AM-R.90"* are indicative of the new surface roughness input in the conversion algorithm. For the *AM-G.50* case, the input value to the roughness conversion algorithm was 50 μm, instead of 5 μm that was initially assumed for the *AM-G* computational results. Accordingly, for the *AM-R.90*, the input value to the roughness conversion algorithm was 90 μm, instead of 9 μm that was previously used for the *AM-R* computational results. Those inputs consequently resulted in higher equivalent sand-grain roughness values. It is observed that for the surface roughness values of 50 μm and 90 μm, the CFD solver better captures the effect of surface roughness, whilst the POF is noticeably shifted towards the centreline of the burner and the CRZ size is reduced. Hence, as presented in Figure 5.3.1-8 and

5.3.1-9, the use of higher surface roughness values such as 50 μm and 90 μm, instead of 5 μm and 9 μm, significantly improved the predictive performance of the CFD solver. Therefore, it was presumed that the equivalent sand-grain roughness conversion algorithm that was employed for the cases of *AM-G* and *AM-R*, underestimated the converted value by an order of magnitude. Thus, it is concluded that the selection of the appropriate conversion algorithm has a major influence in the predictive capabilities of the CFD solver using this low computational power method.

In Figure 5.3-8, it is apparent that the consistency between the experimental LDA results *(Experimental – AM-R)* and the computational ones is significantly improved for the newly assigned surface roughness value of 90 μm *(AM-R.90)*. In the CRZ region ($0 \leq x \leq 0.008$ m) the predicted values deviated slightly from the experimental values. However, at the rest of the radial positions, the predicted velocity profile almost overlapped with the measured velocity profile and therefore the inwards shifting of the POF was effectively captured.

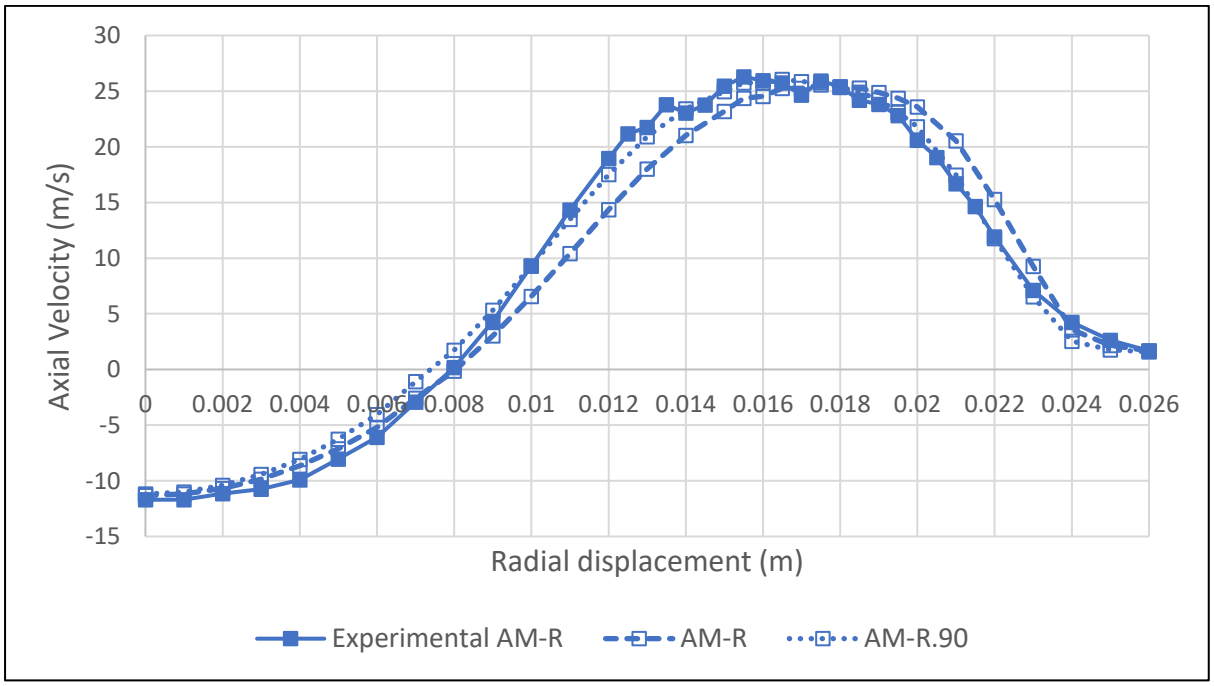

Figure 5.3-8 *Comparison of the computationally predicted, isothermal axial velocity distributions for Experimental AM-R, AM-R (9 μm) and AM-R.90 (90 μm).*

As can be seen from Figure 5.3-9, the level of agreement between the measured and predicted velocity profiles was enhanced for the *AM-G.50* case too. The inwards shifting of the POF was improved when a higher sand-grain value was input as also witnessed in Figure 5.3-7. However, overall, the inwards shifting of the POF for the

AM-G and *AM-R* swirlers under the influence of surface roughness was better captured by the CFD solver when higher values of surface roughness were assigned such as 50 μm and 90 μm instead of 5 μm and 9 μm respectively.

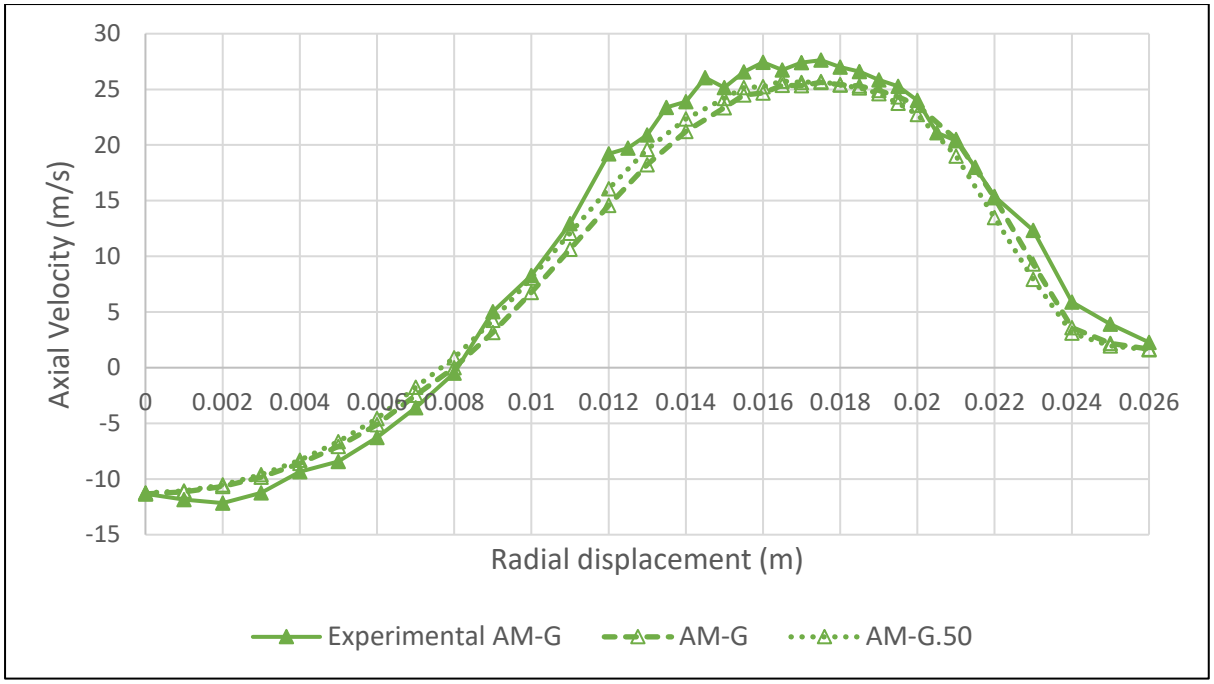

Figure 5.3-9 *Comparison of the computationally predicted, isothermal axial velocity distributions for Experimental AM-R, AM-G (5 μm) and AM-G.50 (50 μm).*

The inwards shifting of the POF and, hence, the reduction in CRZ size, with increased surface roughness is linked to the combined effect of Adverse Pressure Gradient (APG). This is generated due to the swirler geometry, and the increase in wall shear stress due to the increase in surface roughness. The former (APG) promotes a pressure-induced boundary layer separation, which is amplified by the surface roughness. In general, a mild APG region is generated at the trailing edge of the flat vanes, due to the shape of the vanes, whilst a second, stronger APG region is generated at the wake of the central bluff body inside the nozzle section of the swirler. This is demonstrated in following Figure 5.3-10, where the pressure distribution at the two locations is illustrated. At these regions, the boundary layer separation is favoured [57].

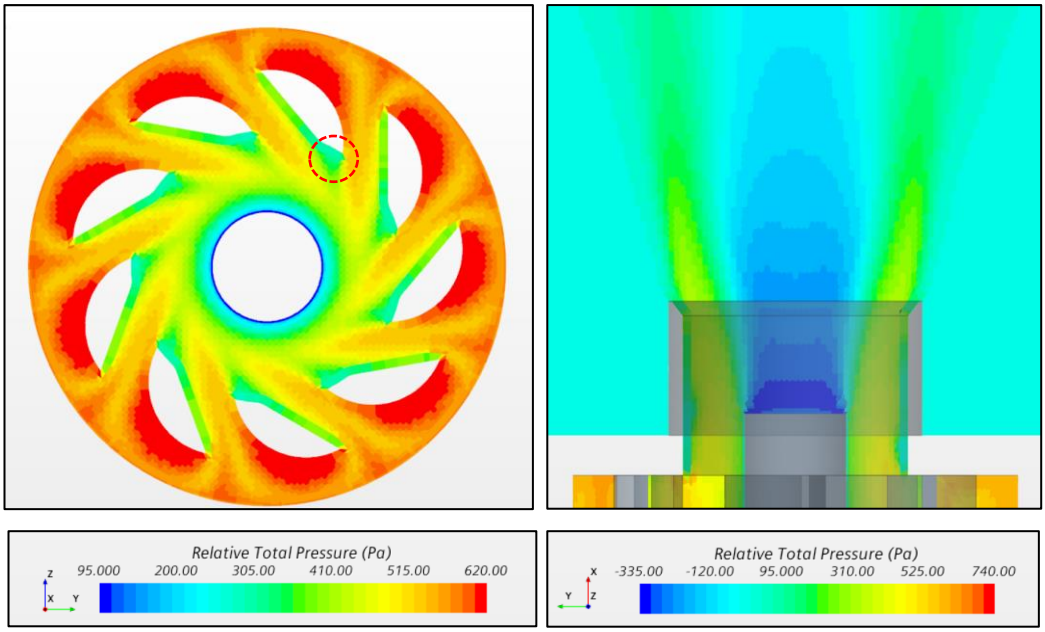

Figure 5.3-10 *Relative pressure distribution for the Machined swirler, indicating the Adverse Pressure Gradient (APG) regions formed at the trailing edge of flat vanes (left) and at the wake of central bluff body (right).*

Conversely, the increase in surface roughness results in higher wall shear stress and thus, higher momentum deficit near the wall since the fluid flow slows down by the friction forces. Due to the augmented momentum deficit, the displacement of the turbulent boundary layer increases, and the streamlines are displaced further away from the wall, resulting in a thicker boundary layer [57]. The thickened boundary layer of reduced momentum is more susceptible to separation [102]. Thus, at the location of the APG region, the thickened turbulent boundary layer, due to increased surface roughness, promotes flow separation and its streamlines are displaced further towards the direction of the APG region.

The predicted results of the *Machined* and *AM-R.90* cases were considered to visualise and explain this physical phenomenon since they had the largest surface roughness difference and therefore the most noticeable change in flow structures. The skin friction coefficient for those two cases is illustrated in Figures 5.3-11 and 5.3-12, for the swirler vane and swirler nozzle sections, respectively. To compute the skin friction coefficient, the free stream velocity and the density of working medium are required. The free stream velocity was estimated to be 22 m/s across the vanes and 44 m/s across the nozzle section, respectively, whilst the density of the air was calculated from its thermodynamic properties.

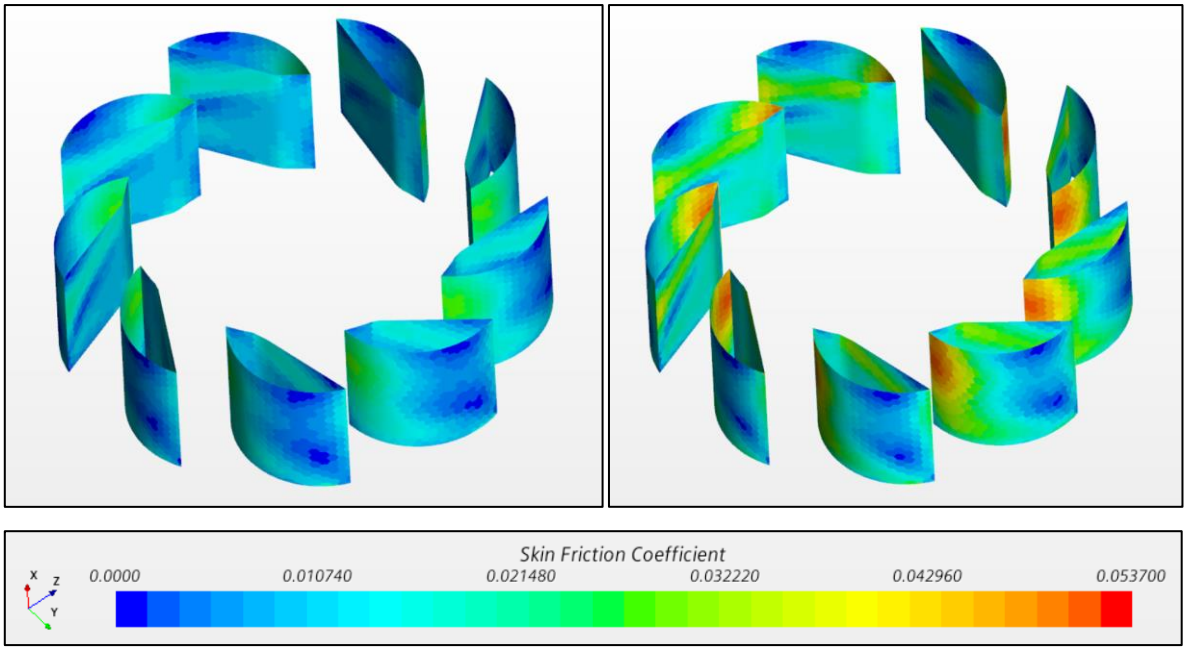

Figure 5.3-11 *Skin Friction Coefficient at the swirler vane section for the Machined (left) and AM-R.90 (right) cases.*

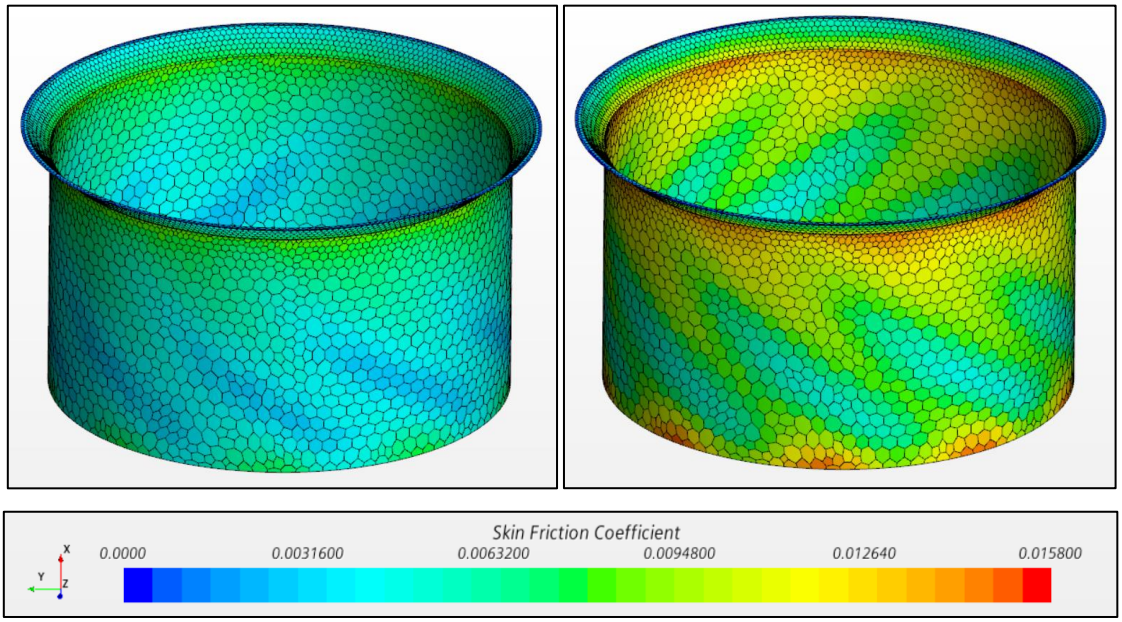

Figure 5.3-12 *Skin Friction Coefficient at the nozzle section for the Machined (left) and AM-R.90 (right) cases.*

Both for the vanes and for the nozzle of the swirler, the computed skin friction coefficient increases with higher surface roughness. The skin friction coefficient is analogous to the wall shear stress, which is a measure of the friction forces that are exerted from the wall on the fluid. These forces decelerate the flow near the wall and result in momentum deficit. Therefore, for the 90 μm case, where the skin friction is higher, the momentum deficit and, hence, the boundary layer displacement is higher,

resulting in a thicker boundary layer. This is visualised in Figures 5.3-13, where the iso-surface curves for the vanes and the nozzle section of the swirler are depicted. To facilitate the comparison of the results, the two contours that corresponds to the *AM-R.90* (red curved) and *Machined* (black curves) are overlayed on top of each other.

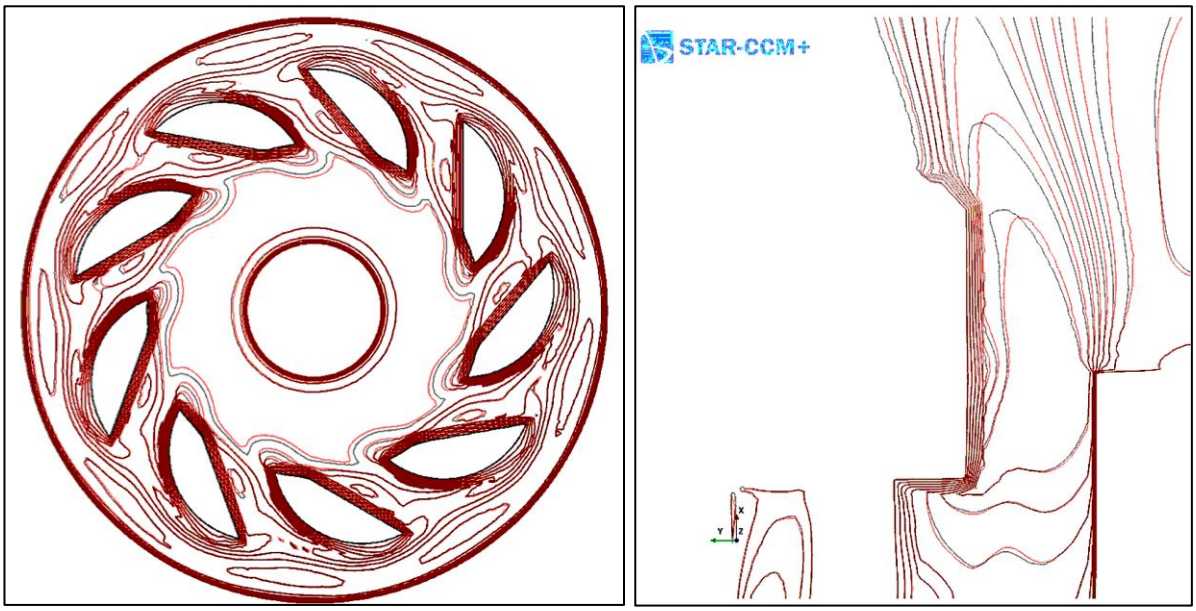

Figure 5.3-13 *Iso-surface lines for the vanes section (left) and the nozzle section (right) of the swirler, concerning the Machined (black) and the AM-R.90 (red) cases.*

Concerning the swirler vanes, it is observed that the size of the swirling flow region is smaller for the *AM-R.90* case (red curves) and the turbulent boundary layer at the trailing edge of the flat vane thickens when compared to the *Machined* case (black curves), becoming more susceptible to flow separation. This is also evident in Figure 5.3-12, where a sudden decrease in skin friction is predicted at the trailing edge of the flat vanes. For the *AM-R.90* swirler, the drop in skin friction at the APG region is steeper since the momentum deficit increases and the flow separation is promoted. Therefore, for the *AM-R.90* case, the displacement of the turbulent boundary layer is larger, shifting the swirling flow radially inward.

In the swirler nozzle section, the turbulent boundary layer attached to the wall thickens for the *AM-R.90* case due to the increased skin friction. The increased thickness of the turbulent boundary layer for the *AM-R.90* case, is also quantified in Figure 5.3.-14, where the *displacement thickness* (δ_1) of the turbulent boundary layer is plotted for the *Machined* and the *AM-R.90* case, within the swirler nozzle section and across its radial direction ($0.015\ \mathrm{m} \leq x \leq 0.019\ \mathrm{m}$). As shown, the displacement

thickness of the boundary layer increases for the *AM-R.90* case, compared to the *Machined* case. The increased boundary layer displacement, due to the increased momentum deficit, moves the streamlines of the *AM-R.90* case towards the centre of the burner, where the APG region is located. Therefore, for this case, the positive outwards flow (POF) is shifted towards the centre of the nozzle and the size of the CRZ reduces. After emerging from the nozzle, the flow expands less due to momentum deficit.

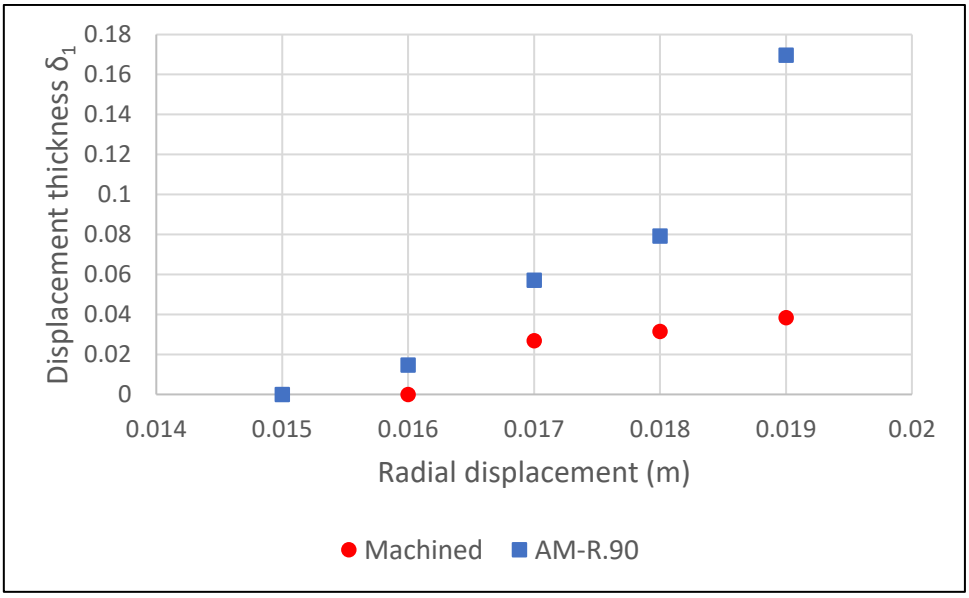

Figure 5.3-14 *Displacement thickness of the turbulent boundary layer for the Machined and AM-R.90 cases measured inside the swirler nozzle at 0.015 m ≤ x ≤ 0.019 m.*

It is noted that surface roughness promotes boundary layer transition (from laminar to turbulent) and therefore helps reduce separation, since the flow separates further downstream. However, in fully developed turbulent boundary layers with APG, surface roughness has the opposite effect as it increases the momentum deficit and therefore promotes the phenomenon of separation instead of delaying it [66]. This effect has also been shown recently using computationally expensive transient 2D numerical simulations by Jeong and Song [80]. The present simulation utilizing the Realizable k-ε Two-layer model, does not account for surface roughness induced boundary layer transition, as the turbulence model does not contain an intermittency model to describe such phenomenon. However, even without the promoted laminar-turbulent transition due to surface roughness, the boundary layer is turbulent at the APG region, as indicated by the CFD results in Figure 5.3.1-15, where the wall shear stress and the wall y^+ contour noticeably increase along the curved vanes of the

Machined swirler. This means that the boundary layer approaches the APG location being turbulent, regardless of the surface roughness condition. Thus, even if the model was able to capture the surface roughness induced boundary layer transition, it would only result in faster transition and would not improve the separation propensity at the APG region.

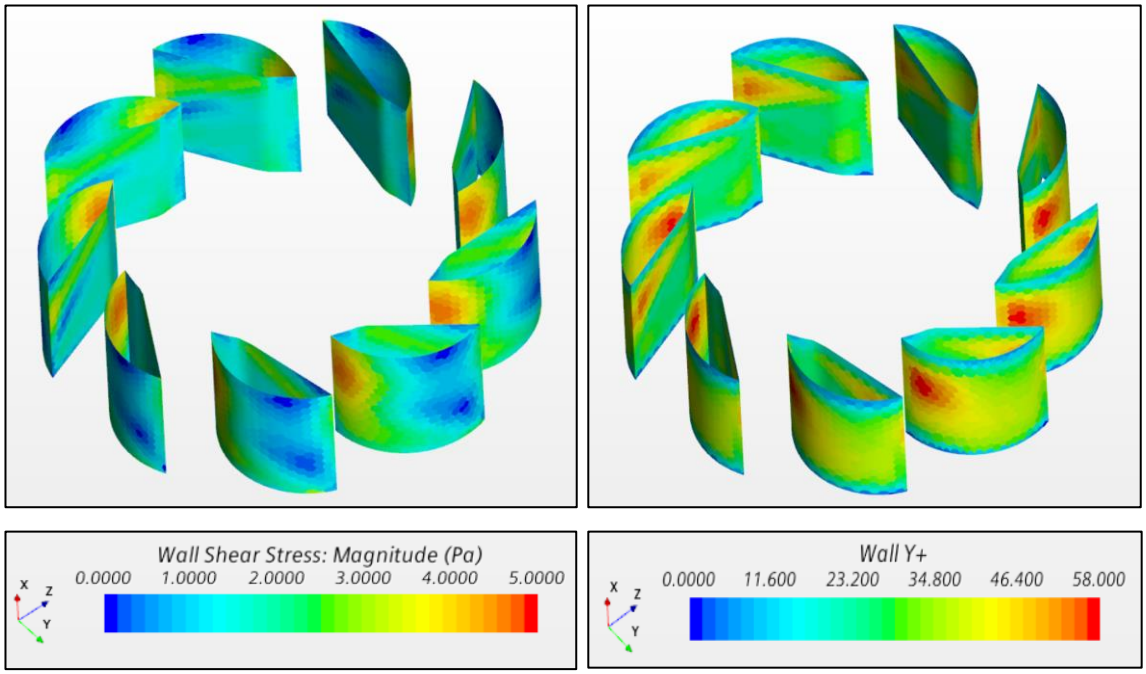

Figure 5.3-15 *Wall shear stress (left) and wall y+ (right) distributions for the Machined case at the swirler vanes section.*

It is worth pointing out that although the Realizable k-ε two-layer turbulence model has been developed and calibrated for fully developed turbulent flow, its transport equations do converge to a laminar solution at low Reynolds number and to a turbulent solution at sufficiently high Reynolds number. Consequently, the model equations do describe a transition between laminar and turbulent solution branches [278]. This transition is mainly due to the natural transition of the boundary layer, rather than due to the presence of surface roughness (*bypassed transition*) or other intermittent phenomena.

Since the effect of surface roughness on the inwards shifting of the POF has been captured and explained, further discussions here are concerned with the predictive capability of the computational continua on capturing the peak axial velocity deficit, due to the presence of the roughness elements.

The experimental findings that support the reduction in peak axial velocities are attributed to the increase in skin friction induced pressure drop (also referred as *skin friction drag*) due to the presence of surface roughness [29]. The experimentally measured pressure drop was 0.96 kPa for the *Machined* swirler and increased to 1.11 kPa for the *AM-R* one. Surface roughness increases wall shear stress and consequently skin friction, if the flow is in the transitional or fully turbulent regime and the roughness height is above the "admissible" surface roughness height (so-called "hydraulically smooth limit") [55, 57, 76, 84, 88, 305, 331]. In this context, the *Roughness Reynolds Number* was estimated for the rough wall surfaces of *AM-G* and *AM-R,* to investigate if the roughness heights are above the hydraulically smooth limit and hence, to verify the corresponding increase in skin friction and pressure drop.

As presented in Section 4.2, the categorisation of the roughness regimes was first proposed by Nikuradse [76] and it was based on the *Roughness Reynolds Number* ($k^+_s=k_s \cdot u^*/\nu$), where k_s is the equivalent sand-grain roughness, u^* is the friction velocity defined as the square root of the ratio of wall shear stress to density [$u^*=(\tau_w/\rho)^{1/2}$] and ν is the kinematic viscosity. The upper limit of hydraulically smooth (k^+_{smooth}) and lower limit of fully rough (k^+_{rough}) have been calculated by several researchers for several roughness features [36, 55]. For the case of equivalent sand-grain roughness, Ioselevich and Pilipenko [327], as well as Cebeci and Bradshaw [301] estimated k^+_{smooth} equal to 2.5 and 2.25, respectively, while k^+_{rough} was equal to 90 in both studies. The lower and upper limits of roughness function in the wall function formula were set to $k^+_{smooth} = 2.25$ and $k^+_{rough} = 90$, respectively, for all the simulated cases. By adding a user-defined function, the average roughness Reynolds number (k^+_s) was estimated for the cases of *Machined, AM-G.50* and *AM-R.90* and therefore, the roughness regime for the three different surface roughness cases could be extracted and are presented in Table 5.3-2.

Table 5.3-2 *Roughness Reynolds number (k^+_s) for the cases of Machined, AM-G.50 and AM-R.90, at the locations where surface roughness is assigned.*

Roughness Reynolds Number (k^+_s)					
Swirler case	**Nozzle inner wall**	**Swirler top wall**	**Flat vanes**	**Curved vanes**	**Average**
Machined	0.30	0.21	0.22	0.25	**0.25**
AM-G.50	20.01	13.94	14.36	16.05	**16.09**
AM-R.90	43.16	29.91	31.20	33.86	**34.53**

Based on k^+_s, the surface roughness for the *AM-G.50* and *AM-R.90* cases stays over the hydraulically smooth limit and within the transitionally rough regime on all the solid wall surfaces of the swirler. Therefore, it is expected that skin friction coefficient will be higher for those cases compared to the *Machined* case. Indeed, as shown in Table 5.3-3, the skin friction coefficients increase with surface roughness.

Table 5.3-3 *Skin Friction Coefficient (C_f) for the cases of Machined, AM-G.50 and AM-R.90, at the locations where surface roughness is assigned.*

Skin Friction Coefficient (C_f)					
Swirler case	**Nozzle inner wall**	**Swirler top wall**	**Flat vanes**	**Curved vanes**	**Average**
Machined	0.005	0.012	0.010	0.010	**0.009**
AM-G.50	0.008	0.017	0.015	0.016	**0.014**
AM-R.90	0.009	0.021	0.018	0.019	**0.017**

Due to the absence of experimental results related to skin friction coefficient calculation, the total pressure drop was further computed and compared to the analogous experimental measurements. The computation of the total pressure drop was based on the mass-flow average absolute total pressure difference between the inlet and the three outlets of the computational domain. The computational values and the percentage difference, with respect to the *Machined* case, are listed in Table 5.3-4.

Table 5.3-4 *Pressure-drop (ΔP) calculations for the cases of Machined, AM-G.50 and AM-R.90.*

Swirler case	**Pressure-drop (ΔP) (kPa)**	**% Difference**
Machined	0.714	0.00%
AM-G.50	0.717	0.33%
AM-R.90	0.718	0.54%

As expected, the total pressure drop increased with increased skin friction, due to higher surface roughness. Comparing the *Machined* to the *AM-R.90* case, an increase of 0.54% in total pressure drop is predicted. Although this level of increase is marginal, it may justify or contribute to the inconsistency with the experimental results with respect to the reduction in peak axial velocity with increased surface roughness, as, the experimental results reported a 15% increase in total pressure drop between the *Machined* and *AM-R* case, and therefore a noticeable reduction in peak axial

velocities. Assuming that the error related to the experimental measurements is insignificant, the underprediction in total pressure drop could be attributed to the physical approximation error related to the CFD inlet and outlet boundary conditions, as well as to the simplification of computational domain. Thus, it is sensible to investigate potential sources of error in the CFD method employed.

5.4 CFD uncertainty and error potential sources

Since the effect of surface roughness on the peak axial velocities and total pressure drop is underpredicted by the employed computational scheme, it is sensible to analyse the CFD related potential sources of uncertainty and error. While uncertainty is related to a *potential* deficiency in any part of the modelling process due to *lack of knowledge*, error is *identifiable* and *not* due to *lack of knowledge* [332]. Thus, uncertainty principally concerns the *lack of knowledge* with respect to the physical processes that embodied in the selected physical model. Often, a major factor of uncertainty in CFD simulation stems from turbulence modelling, as some concepts are not well understood. Sensitivity and uncertainty analysis, as well as several runs of the simulation with difference turbulence models can be applied to investigate the level of uncertainty. Regarding the potential CFD error sources, which are identifiable, and thus, can be recognized upon investigation, they fall into several categories such as *acknowledged* and *unacknowledged* errors, as well as *local* and *global* ones. The present analysis focuses on *acknowledged global* errors as they account for the whole computational domain and not *local* cells, whilst there are set procedures of identifying and resolving them. On the contrary, *unacknowledged errors* such as “computer bugs” and “usage errors” have no standard procedures of finding and removing them and thus, they are out of the scope of the present analysis [333].

The most influential *acknowledged errors* are *physical approximation errors, iterative convergence error* and *discretization errors.* The first category of errors is associated with the selected set of equation and boundary conditions that is used to simulate the problem and the deliberate simplifications of the model. As some physical phenomena often require modelling, they can significantly contribute to errors [333]. For this specific case, such errors might stem from:

- the use of wall functions, and thus, from the modelling of the viscous sublayer,

- the dependency on equivalent sand-grain roughness and its conversion algorithms,
- the simplification of heat transfer mechanisms, as adiabatic conditions were assumed,
- the estimation of inlet turbulent conditions from empirical correlations due to the absence of experimental data,
- the imprecise definition of the outlet pressure field due to the simplification of computational domain and the lack of experimental data.

Concerning the *iterative convergence error,* it exists as the iteratively progressing simulation must have a final point, and thus, this error scales to deviation of the solution at the end of the simulations. Finally, the *discretization errors*, which can be evaluated by the grid convergence (or mesh independency) study (Section 5.2), regarding errors related to algebraic expressions that are used to solve the governing equations within the discrete domain of space. Consequently, these errors tend to zero as grid spacing tends to zero and the total grid size tends to infinity. Although the mesh independence study (Section 5.2) showed that the solution for the selected mesh is within the asymptotic range of convergence, as the discretization error is also dependent on the mesh quality, several cell parameters such as *skewness angle, cell quality, aspect ratio* and *zonal boundary interfaces* might increase the level of discretization error [333]. The use of prism layers might have slightly contributed to this type of error, though the cell quality for both prism layer and polyhedral cells was refined at 100% for the vast majority of the volume domain. Additionally, high skewness angle at the cells located at the sharp edges of the vane and nozzle sections of the swirler might have further contributed to discretization errors [324].

Although the discussion and analysis of the isothermal computational results focuses on sources of error that are derived from the CFD modelling, it is noted that the experimental results, which are compared against the CFD ones, might also possess a percentage of error. Hence this paragraph is concerned with a short discussion of the possible sources of error related to the experimental investigation. The level of precision and accuracy of the axial velocity distribution could be limited as only one repeat was achieved for the acquisition of the axial velocity experimental results. Multiple sets of repeats would be necessary to improve the level of accuracy and precision, in terms of the resultant values and distribution, respectively. As

previously explained in Section 3, since the experimental measurements were conducted using 1D Laser Doppler Anemometry (LDA) there was the possibility for misalignment of measuring equipment, with respect to the measuring location. Therefore, a small displacement from the intended measurement location in the near-burner region where velocity gradients are steep and flow is highly turbulent, would alter the velocity profile, leading to mismatch with the predicted profile. As described in section 3, the measured axial velocity profile was shifted by ≈3.5 mm to agree with the generalised axisymmetric swirling flow pattern that requires the maximum negative velocity point to be in the centreline of the burner [149, 151, 152, 154]. Therefore, a similar misalignment regarding the measuring axial location might be the reason behind the disagreement of the peak axial velocities.

5.5 Non-isothermal (reacting) simulation – Challenges & Observations

The implementation of a reacting physical scheme to the aforementioned isothermal simulations, give rise to a number of challenges, particularly concerning the incorporation of surface roughness effects and the mapping of heat transfer.

Regarding the incorporation of surface roughness at the areas of interest, as described in Section 4.3, the concept of equivalent sand-grain roughness, and subsequently, the utilisation of the correct conversion algorithm cannot simultaneously account for both skin-friction and heat transfer related effects. Consequently, the use of a single sand-grain roughness correlation for the description of both skin-friction and heat transfer related effects is problematic. This is a well-known issue in the relevant literature as has been thoroughly detailed by Stripf et al. [62] and Bons [36, 310]. Under the present physical continua, which utilised the RANS equations set combined with the wall functions approach, the input of two different equivalent sand-grain roughness values, one representing the skin-friction related effects and another representative of the heat transfer ones, is prohibited. Hence, unless the equivalent sand-grain roughness value happens to be the same for representing both skin-friction and heat transfer effects, the use of a single value for simulating both aerodynamic and heat transfer roughness related effects, is limiting.

Apart from the issues arising from the simulation of the surface roughness effects, reacting CFD simulations include heat transfer models. In order for an accurate computational simulation of the flow structures and flame locations under

reaction conditions, the heat transfer from the flame to the boundaries of the computational domain (i.e. nozzle and quartz confinement) has to be accurately mapped and described. The estimation of heat transfer and heat loss from a system to its surrounding is a particularly challenging exercise to be undertaken, with several researchers using a rough estimate of the heat transfer coefficient in their CFD simulations Agostinelli et al. [267]. An extensive empirical investigation is necessary for heat loss calculations and heat transfer mapping, where the heat and aerodynamic profile, of the areas of interest, is closely examined. This is significantly challenging, especially in the near vicinity of the boundary walls and the outside of the experimental set-up. With a view to estimating the heat transfer characteristics of the present test rig, as described in Section 3.2, a further experimental campaign should be carried out, subsequently providing the required information to the CFD suite, such as the inner and outer wall temperatures, as well as the heat transfer coefficients and the environmental (ambient) temperature.

From initial evaluation of the effectiveness of the reacting CFD physical continua in capturing the surface roughness effects under combustion conditions, it was found that even without a detailed description of the prevailing heat transfer mechanisms, the shifting of the positive outwards flow was still effectively captured. The use of the same equivalent sand-grain roughness value as of the isothermal condition, suggested that the aerodynamic effect of heat transfer was still dominant under reaction conditions. However, the suitability of such value for accommodating both the heat transfer and skin-friction related effects had not been investigated. Additionally, the location of the flame was predicted inaccurately, when compared to the OH* chemiluminescence pictures, whereas the NOx emissions were slightly underpredicted. These inaccuracies can be attributed to the insufficient information related to the heat transfer mapping of the system, since the wall heat transfer effects majorly influence flame stabilisation and flame dynamics [267, 334].

5.6 Summary

The evaluation of the predictive capabilities of the computational continua (RANS realizable k-ε turbulence model with wall function), with respect to the influence of surface roughness, on swirling isothermal flow field has been successfully conducted. One objective of this research was to appraise the findings of a recent experimental study [29] on similar facilities which resulted in a recent patent application based on

improved combustion performance. Hence, computationally inexpensive methodology - suitable for industrial utilisation - for modelling and resolving the effect of surface roughness on flow structures was generated, and its effectiveness was evaluated by comparison between the computational and experimental axial velocity profiles. The mesh requirements were presented and the y^+ values reported, confirming the implementation of the wall function approach. To apply this computational method, the minimum y^+ value that can be used is 30. To prove that the computational results were independent of the spatial resolution of the generated computational domain, mesh independency was demonstrated. For all the selected parameters the CGI method showed that for the medium mesh ($mesh_2$) the solution best correlated the asymptotic range.

As shown in [29] the main effect of surface roughness on 3D isothermal swirling flow was the inwards shifting of the positive outwards flow (POF) and decrease in peak axial velocities. Therefore, the effectiveness of the CFD solver was evaluated based on those two observations. However, the performance of the computational continua is also dependent on the estimated equivalent sand-grain roughness value. This was confirmed by varying the equivalent sand-grain roughness value for the case of *AM-G* and *AM-R* swirlers, which significantly improved the velocity profiles predicted. Hence, it was concluded that the selection of the appropriate algorithm to convert the measured surface roughness to the equivalent sand-grain roughness is a key factor that affects the accuracy of predictions of mean flow quantities. Using the correct equivalent sand-grain roughness values, the inwards shifting of the POF and the reduction in CRZ size was highlighted. The transitioning flow pattern with increasing surface roughness was related to the augmented wall shear stress, which resulted in increased momentum deficit and thickened boundary layer. Consequently, the latter was more susceptible to separation at the regions where adverse pressure gradient (APG) was generated. Therefore, for the *AM-G.90* case, due to the combined effect of APG and rough wall, the flow was displaced further towards to APG region. That resulted in the inwards shifting of the positive outwards flow, which was effectively captured by the CFD and was also in good agreement with the experimental data.

In contrast, the Realizable k-ε Two-layer turbulence model significantly underpredicted the effect of surface roughness on pressure-drop, which increased marginally, compared to the experimental measurements in [29] which presented a

much higher pressure drop. Hence, reduction in the peak axial velocity with increased surface roughness, was not notably predicted by the computational simulations. Finally, the absence of experimental data related to the exact description of the inlet and outlet boundary conditions, the simplification of the experimental geometry and the assumption of adiabatic condition, constitute potential sources of CFD input error that further reduce the agreement between the CFD predictions and experimentally acquired results.

Chapter 6. Experimental investigation of the effect of surface roughness on a Generic Methane Burner

An experimental campaign was designed and successfully undertaken to identify the effect of surface roughness on pure methane (CH_4) premixed combustion under atmospheric pressure and elevated temperature ($150\ ^oC$) conditions, of relevance to practical burner designs. The aforementioned, two additively manufactured swirlers of average measured surface roughness of 5 μm *(AM-G)* and 9 μm *(AM-R)* together with a traditionally manufactured machined swirler of average measured surface roughness of 1 μm *(Machined)* were investigated, and their respective results were compared. As discussed earlier, the *AM-G* swirler had undergone grit-blasting, thus generating the reduced surface roughness compared to the *AM-R,* which was deployed without any post-processing. Within manufacturing tolerances, the geometrical parameters of the three swirlers were identical, excluding the differences in surface roughness, each presenting a swirl number of 0.8.

Initially the burner stability envelope and stable operating curves were identified, for each of the three swirlers, to investigate if there are significant differences in the lean blowoff (LBO) and flashback limit owing to the different surface roughness (Section 6.1). As discussed in Section 3.1, to maintain the thermal power the fuel flowrate was kept constant, with the oxidiser composition in the mixture either increased or decreased to approach the LBO and flashback limit respectively. For every test point NO_x emissions, temperature and OH^* chemiluminescence measurements were conducted which are reported in Sections 6.2 and 6.3. Finally, in Section 6.4, the CH_4 results are discussed, providing a summary of the significant findings.

Concerning the repeatability of the present experimental campaign, two full repeats of the experimental test points took place for the *Machined* and *AM-R* swirler cases. For the *AM-G* case, only one repeat was achieved due to lab-time constraints, brought about due to long-term covid lockdowns. Thus, for sections 6.2 and 6.3, the individual measurements for the quantities of interest, namely, *Inlet plenum temperature*, *NO_x emissions* and *Exhaust gas thermocouple temperature* of the first and second repeat are listed, followed by their corresponding averaged values. Vertical error-bars are used to represent the range of variation between the first and

the second repeat with respect to the average value. The standard deviation of the mean value of each individual measurement, over the recording period of 60 seconds, is also provided, confirming the “steady-state” conditions assumed as the measurements were collected.

With concern to the horizontal error-bars these are associated with the equivalence ratio, and represent the manufacturer reported uncertainty of the mass flow controllers estimated by the manufacturer to be ±0.5% of the actual flow. This results in a maximum uncertainty of ≈±1% with respect to the equivalence ratio when summing the air and fuel CMF controller uncertainties (±0.71% if summed in quadrature). As the equivalence ratio increases the uncertainty increases since the former is more susceptible to a slight deviation of the mass flow controller. It is noted that the deviation due to the repeatability error of the mass flow controllers is not considered for the calculation of horizontal error-bars.

6.1 Burner stability envelope

The first aspect of the CH_4 experimental campaign concerned the identification of the burner stability envelope and the estimation of the stable operating curve for the three swirlers. Through this exercise, the influence of surface roughness on LBO and flashback limit for the two additively manufactured swirlers *(AM-G & AM-R)* are compared against the conventionally manufactured machined one. As explained in Section 3.1, the limits of the stability map were identified through visual observation of the flame and careful examination of the various monitoring tools utilised in the system, such as pressure transducers, high-speed OH^* chemiluminescence photography and thermocouples. These diagnostics provided significant information about the condition of the system and assisted in the estimation of the limits of the stable operating curve. It is noted that to ensure safe operation of the research facility and to protect the experimental rig and apparatus from unwanted damage, the system was not driven to full flashback conditions. Rather, partial flashback was assumed as the limit of the operation, where the flame was unsteadily moving in and out of the nozzle burner. Specifically in the case of CH_4, the flashback phenomenon could not take place since for the current burner configuration and thermal power output (25 kW), the bulk flow velocity of the mixture was always higher than the flame speed. Thus, the flame was stabilised well above the nozzle exit even for stoichiometric conditions, where flame speed is at its maximum. A “technical flashback point” (TFP) was assumed as the

upper limit of the stable operating curve ($\varphi = 1.05$), even though this test point resulted in stable operation.

Under the specific experimental test conditions, the three swirlers of various surface roughness did not present any differences in terms of the burner stability envelope. Thus, the limits of the stable operating curves were identical for the three cases and correspond to $\varphi = 1.05 \pm 1\%$ (TFP) and $\varphi = 0.558 \pm 1\%$ (LBO). As can be observed in Figure 6.1-1, the stable operating curves of the three cases are totally overlapping. As discussed previously, the horizontal error-bars are related to the uncertainty of mass flowrate controller and consequently influence the equivalence ratio, which in turn dominates the resultant burning rate. For the present equivalence ratio range, the related error is sufficiently small. The LBO point is highlighted since it was characterised by the LBO instability, while for the rest of the points combustion under stable conditions should be expected. Thus, under the present experimental conditions the influence of the corresponding surface roughness range on the burner stability envelope of CH_4 is found to be negligible. This conclusion concurs with previous analogous investigations [29], which also found that the LBO instability of the three various surface roughness was the same under preheated CH_4 combustion at $300\ ^{o}C$. This is potentially due to the negligible effect that surface roughness has on the chemical and reciprocal flow timescale that define the Damköhler number ($Da = \tau_{flow}/\tau_{chem}$) (Section 2.3.5.1).

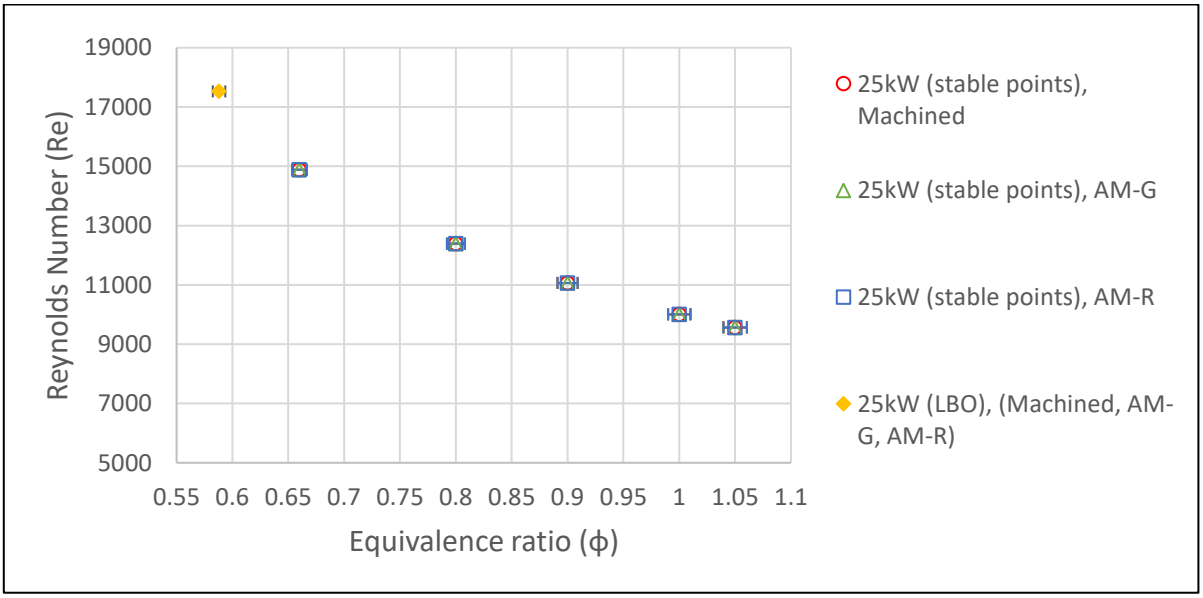

Figure 6.1-1 *Stable operating curves of 100%CH_4 combustion for Machined, AM-G and AM-R swirlers*

In Figure 6.1-2 the resultant stable operating curve for the 25 kW, *Machined* case, is compared against a 55 kW analogous one from previous experimental campaigns conducted by Runyon et al. [238]. The exact same swirler (*Machined*) was used at a higher inlet plenum temperature ($300\ ^{o}C$). Due to the higher volumetric flowrate of the mixture, since the thermal power output was 55 kW, the resultant Reynolds number is much higher and accordingly the 55 kW stability curved is located above the 25 kW one. A shift in the LBO limit towards a leaner equivalence ratio is observed also for the 55 kW case, because of the increased flame speed that is induced due to the higher inlet temperature. The shape of the stability curves for the two cases are similar, while it is demonstrated that even leaner equivalence ratios can be achieved for increased thermal power output and increased preheat temperature.

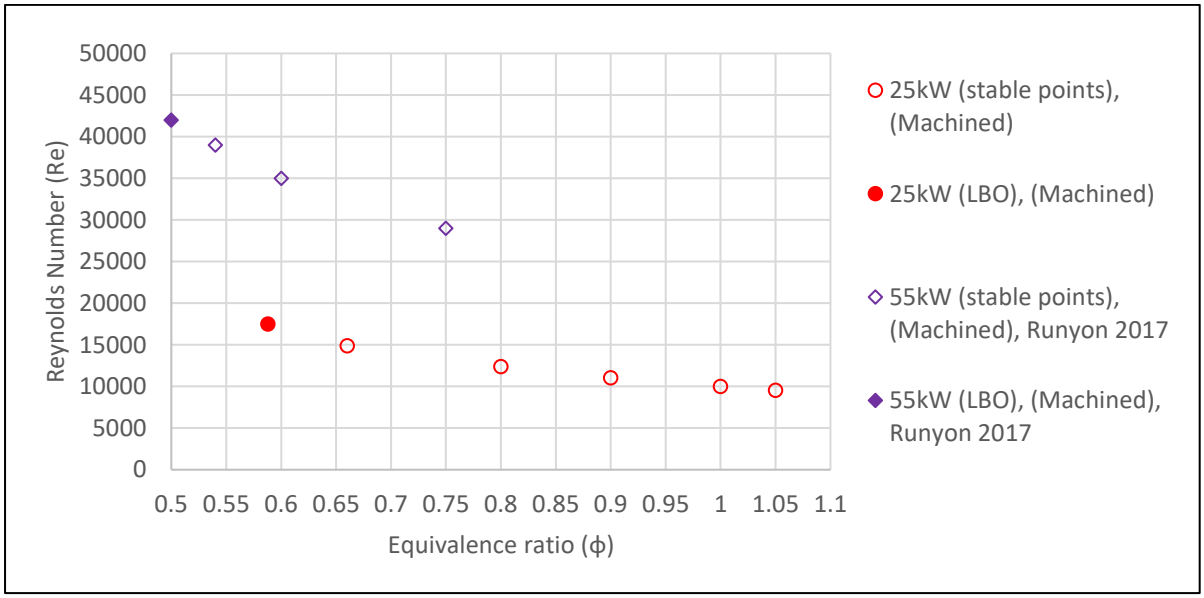

Figure 6.1-2 *Stable operating curves comparison of 25 kW and 55 kW machined swirler.*

6.2 Exhaust Gas Emissions

To identify the influence of surface roughness on the formation of NO_x emission, the latter was measured, for each test point, at the exhaust section of the burner, using a line probe as described in Chapter 3. A broad range of equivalence ratio *(φ)* was covered, ranging from the LBO *($\varphi = 0.558 \pm 1\%$)* to the maximum perceived laminar burning rate, which would be expected at slightly above the stoichiometric condition of CH_4 *($\varphi = 1.05 \pm 1\%$)*. For all the test points, the target inlet temperature of the mixture was set at $150\ ^{o}C$ (≈423 K) with an acceptable deviation of $\pm 5\ ^{o}C$ (1% of the inlet temperature in K) deemed acceptable in terms of limiting temperature impact. Again it is highlighted that the inlet plenum temperature measurements were taken using a

single point measuring thermocouple located at the entrance of the plenum and aligned with its centreline.

As the inlet temperature of the reactants significantly influences the formation of NO_x emissions [5], the first results presented concern the temperature measurements of the inlet plenum thermocouple across the equivalence ratio range investigated. This practise ensured that the reactants inlet temperature was within the predetermined acceptable range, and that any differences in NO_x emissions were not derived by variations in inlet plenum temperature. To verify that at each test-point the system was in “steady-state” condition over the 60 seconds measurement period, and therefore, the results are not biased by any relative changes in the equivalence ratio, the mean-average and its corresponding standard deviation over the recording period (60 seconds) is listed in Table 6.2-1. As the sampling rate of thermocouples was set at 10 Hz, 600 single measurements were conducted within a 60 second period. Thus, the listed values in columns “Temp” are the mean average value of these 600 samples. Since two experimental repeats were conducted for the *AM-R* and *Machined* case, two sets of individual results are presented in the corresponding columns, namely, “Repeat 1” and “Repeat 2”. As shown in Table 6.2-1, the standard deviation of the individual measurements is less than $1\ ^{o}C$ for all the cases across the range of the equivalence ratio, confirming that the system was stabilised and the measurements were conducted under “steady-state” operating conditions. As can be seen the largest standard deviation was $0.8\ ^{o}C$ and corresponds to the first repeat of the *Machined* swirler at $\varphi = 1.05$.

Table 6.2-1 *Inlet plenum temperature individual measurements and their corresponding standard deviation over the 60 seconds of recording period for CH_4/air mixtures.*

	AM-R (9 μm)				**AM-G (5 μm)**		**Machined (1 μm)**			
	Repeat 1 (^{o}C)		Repeat 2 (^{o}C)		Repeat 1 (^{o}C)		Repeat 1 (^{o}C)		Repeat 2 (^{o}C)	
Φ	Temp	**St. Dev**	Temp	**St. Dev**	Temp	**St. Dev**	Temp	**St. Dev**	Temp	**St. Dev**
0.558	152.2	**0.2**	150.3	**0.2**	150.4	**0.2**	150.2	**0.4**	145.9	**0.2**
0.66	153.8	**0.1**	146.9	**0.1**	147.3	**0.1**	146.7	**0.2**	147.9	**0.5**
0.80	145.8	**0.1**	147.2	**0.3**	152.0	**0.4**	154.3	**0.3**	153.8	**0.1**
0.90	147.7	**0.1**	151.1	**0.3**	149.7	**0.3**	147.0	**0.2**	148.9	**0.2**
1.00	147.1	**0.3**	150.2	**0.2**	147.9	**0.4**	147.3	**0.2**	151.1	**0.3**
1.05	146.2	**0.2**	145.7	**0.3**	148.0	**0.4**	148.5	**0.8**	150.8	**0.4**

As two repeats of the full set of test points were conducted for the *Machined* and *AM-R* cases, the level of repeatability of the current experimental campaign is extracted and the arithmetic average value between two repeats calculated (Table 6.2-2). For the case of *AM-G*, the calculation of arithmetic average is not applicable since only one repeat took place. Thus, the results of the first repeat are used for comparative purposes. For most test points, the inlet plenum temperature difference between the first and second repeat is marginal since the methodology for approaching each test condition was done using a consistent methodology. However, as the preheated air was used to heat up both the rig and the reactants mixture, controlling the exact temperature of the inlet plenum was challenging, thus for some equivalence ratios small variations are reported between the first and the second repeat of each swirler. The largest difference was observed for the *AM-R* case at $\varphi = 0.66$, where the inlet plenum temperature difference between "Repeat 1" and "Repeat 2" was $\approx 7\ ^{o}\mathrm{C}$. For the rest of the test points, the repeatability was generally tighter, with reported differences of less than $4\ ^{o}\mathrm{C}$.

Table 6.2-2 *Inlet plenum temperature individual measurements and averages for CH_4/air mixtures.*

	Inlet Plenum Temperature (°C)							
	AM-R (9 μm)			**AM-G (5 μm)**		**Machined (1 μm)**		
Φ	Repeat 1	Repeat 2	**Average**	**Repeat 1**	Average	Repeat 1	Repeat 2	**Average**
0.558	152.2	150.3	**151.3**	**150.4**	N/A	150.2	145.9	**148.1**
0.66	153.8	146.9	**150.4**	**147.3**	N/A	146.7	147.9	**147.3**
0.80	145.8	147.2	**146.5**	**152.0**	N/A	154.3	153.8	**154.1**
0.90	147.8	151.1	**149.4**	**149.7**	N/A	147.0	148.9	**147.9**
1.00	147.1	150.2	**148.7**	**147.9**	N/A	147.3	151.1	**149.2**
1.05	146.2	145.7	**146.0**	**148.0**	N/A	148.5	150.8	**149.6**

Table 6.2-2 demonstrates that all the inlet plenum temperatures were inside the acceptable range of $150 \pm 5\ ^{o}\mathrm{C}$. The average inlet plenum temperature difference between the three swirlers under the same equivalence ratio was generally low at $\approx 2.5\ ^{o}\mathrm{C}$. The largest variation, which was reported for the $\varphi = 0.8$ case between the *AM-R* swirler and the *Machined* one, was $\approx 7.5\ ^{o}\mathrm{C}$. This 1% range of inlet plenum temperature difference is expected to have a negligible effect on NO_x emissions. Thus, it is concluded that any observed differences in NO_x should not stem from discrepancies regarding the inlet plenum temperature.

Since it is expected that the present variation in inlet plenum temperature between the three swirler cases is negligible, it can be assumed that the three swirlers were tested under the same operating conditions (same equivalence ratio, pressure and inlet temperature). This is further supported by the oxygen (O_2) concentration levels of the exhaust gases for the three swirlers (Figure D-1), which were experimentally measured quasi-simultaneously with the inlet temperature and NO_x measurements. They demonstrate negligible variation in O_2 concentrations between the three swirlers, under the same equivalence ratio. Therefore, any variation in NO_x emissions is presumed to stem from either the different surface roughness or the combined standard error of the test apparatus.

The analysis of the NO_x emissions results is conducted similar to the previous section of inlet plenum temperatures. Thus, for each test point measurement, the individual mean average and its corresponding standard deviation over the sampling period of 60 seconds, are presented in Table 6.2-3. Since the sampling rate of the gas analyser system was 1 Hz, the values listed under the column "NO_x" correspond to the average of the 60 measurements conducted over the 60 second sampling period. The measurements have been normalised for dry, 15% O_2 to be compared to analogous measurements in the literature. As shown, the standard deviation is generally low, indicating that any noticeable differences do not stem from equivalence ratio transition, since the system was under "steady-state" operating conditions. The highest mean value standard deviation was 1.28 ppmv (7% of reading) and corresponds to the $\varphi = 0.80$, *AM-G,* repeat 2 case.

The present experimental results are in good agreement with previous experimental campaigns that were conducted with the exact same three swirlers under atmospheric pressure and elevated inlet temperature (573 K) [29]. NO_x emissions at $\varphi = 0.80$ are ≈20% lower compared to [29], since the present experimental campaign took place at a 26% lower inlet temperature (423 K) and outside the HPOC, where heat loss was anticipated to be higher.

Table 6.2-3 *NO_x individual measurements and their corresponding standard deviation over the 60 seconds of sampling period for CH_4/air mixtures.*

	AM-R (9 μm)				**AM-G (5 μm)**		**Machined (1 μm)**			
	Repeat 1 (ppmv)		Repeat 2 (ppmv)		Repeat 1 (ppmv)		Repeat 1 (ppmv)		Repeat 2 (ppmv)	
Φ	NOx	**St. Dev**	NOx	**St. Dev**	NOx	**St. Dev**	NOx	**St. Dev**	NOx	**St. Dev**
0.558	1.9	**0.02**	1.4	**0.03**	2.2	**0.11**	1.2	**0.08**	2.6	**0.14**
0.66	4.3	**0.03**	3.6	**0.64**	4.6	**0.03**	4.0	**0.06**	5.4	**0.06**
0.80	18.0	**0.33**	18.4	**0.28**	18.9	**1.28**	16.2	**0.90**	18.3	**0.13**
0.90	40.5	**0.49**	42.3	**1.23**	42.5	**1.00**	40.6	**0.76**	37.1	**1.10**
1.00	47.1	**0.60**	51.0	**0.84**	48.0	**0.50**	51.0	**0.67**	47.3	**0.88**
1.05	33.7	**0.54**	33.8	**0.52**	34.8	**0.81**	38.2	**0.66**	34.9	**0.22**

As expected, NO_x emissions increase with equivalence ratio for all the three swirlers until the stoichiometric condition ($\varphi = 1.00$), indicating that NO_x production is dominated by the thermal NO_x pathway. A further decrease in air, above the stoichiometric condition results in a decrease in NO_x emissions due to the drop in adiabatic flame temperature. As explained, the fuel flowrate (thermal power) was kept constant, while the oxidiser flowrate was either increased or decreased to account for the changes in equivalence ratio. Hence, as the oxidiser composition in the mixture was reducing to approach a richer equivalence ratio, whilst the bulk flow velocity and the resulted Reynolds Number was also reducing. This approach was specifically selected to observe the influence of surface roughness, in terms of NO_x emissions, at low and high Reynolds respectively and it was also the method proposed and utilised by Runyon et al. [29].

To demonstrate the level of repeatability and to investigate if there were in fact significant differences in the NO_x emissions, due to the presence of surface roughness, the average values of the first and second experimental repeat are listed in Table 6.2-4. Similar to the inlet plenum temperatures results, for the case of *AM-G,* only one set of data was collected, hence, the “Repeat 1” results are used for comparison. It can be observed that especially for the leaner equivalence ratios ($\varphi \leq 0.66$), the NO_x measurements are extremely low, and therefore, the percentage

difference between the two repeats appears high, but is within the uncertainty of the NO_x measurement at this concentration.

For instance, for the *Machined,* $\varphi = 0.558$ case, under the same operating conditions, the resultant NO_x reading was increased by more than 100%, from repeat 1 to repeat 2. Similarly, for the *AM-R*, $\varphi = 0.558$ case, the NO_x emissions reading was reduced by ≈25% from repeat 1 to repeat 2. As the equivalence ratio increases the percentage difference between the first and second repeat is reduced. The variation between first and second repeat is ranging ≈2-4 ppmv on average, which is ≈5-10% of the average mean values, but again these deviations are within the expected uncertainty of the measurement given known repeatability and drift offset of the analyser. Therefore, the relative difference between *AM-R, AM-G* and *Machined* is less than 2 ppmv on average, with the difference likely insignificant and driven by the relative uncertainty of the measurements. This is demonstrated further in Figure 6.2-1, where the average NO_x values are plotted.

Table 6.2-4 *NO_x emissions individual measurements and averages for CH_4/air mixtures.*

	NOx emissions, dry, 15% O_2 (ppmv)							
	AM-R (9 µm)			**AM-G (5 µm)**		**Machined (1 µm)**		
Φ	Repeat 1	Repeat 2	**Average**	**Repeat 1**	Average	Repeat 1	Repeat 2	**Average**
0.558	1.89	1.39	**1.64**	**2.22**	N/A	1.23	2.62	**1.92**
0.66	4.30	3.62	**3.96**	**4.58**	N/A	4.04	5.37	**4.71**
0.80	17.98	18.36	**18.17**	**18.90**	N/A	16.17	18.27	**17.22**
0.90	40.47	42.34	**41.40**	**42.49**	N/A	40.57	37.06	**38.82**
1.00	47.12	50.97	**49.05**	**47.96**	N/A	51.03	47.31	**49.17**
1.05	33.72	33.79	**33.75**	**34.79**	N/A	38.22	34.94	**36.58**

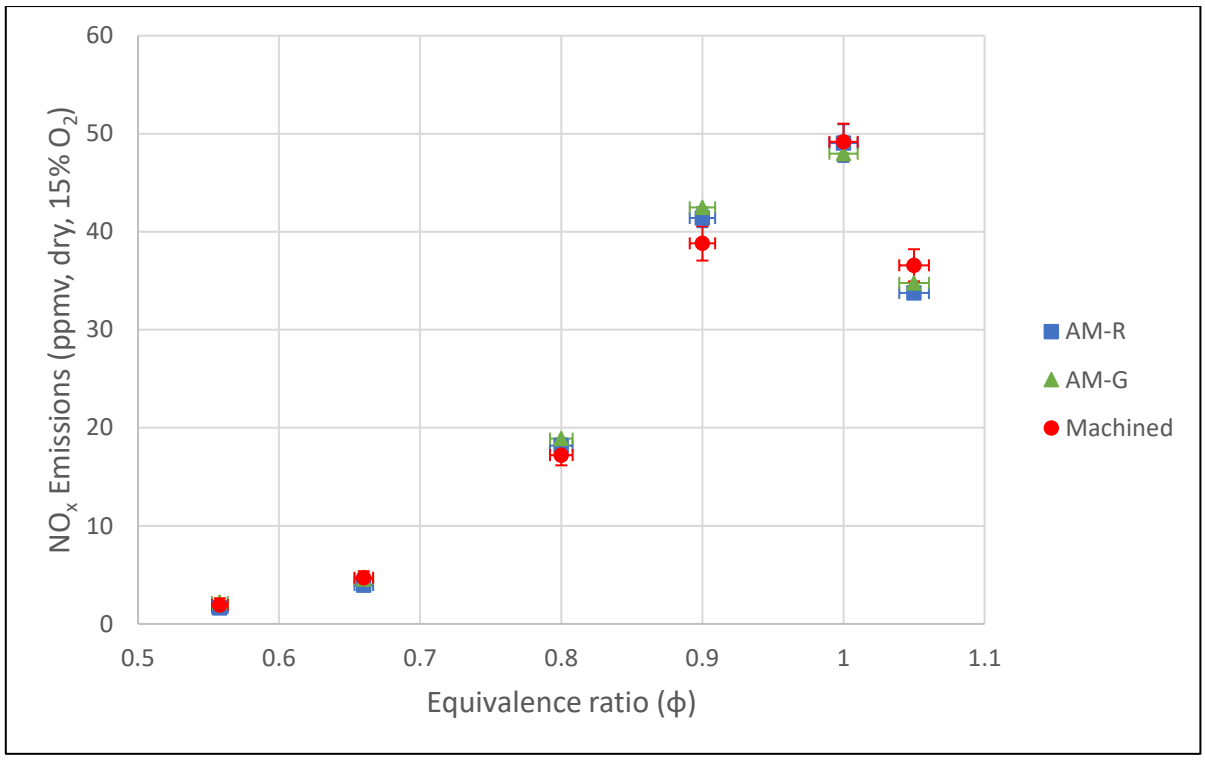

Figure 6.2-1 *Average NO_x emissions indicating the level of repeatability between the first and second repeat for CH_4/air mixtures.*

Vertical error-bars, corresponding to the range of variation between the first and second repeat, are used to visualise the level of repeatability. It is observed that in most of the test points, the average NO_x values of the three swirler cases have over-lapped error-bars of uncertainty. It is worth pointing out that the systematic error of the gas analyser due to calibration process, variation in span-gas and "drift" of the reference values due to extended operation, has not been considered for the calculation of the uncertainty error-bars. In fact, taking into consideration these uncertainty factors, as well as the standard deviations of Table 6.2-3, the level of repeatability would be further reduced, resulting in significant uncertainty with respect to NO_x emissions and preventing the extraction of any significant differences due to the presence of surface roughness.

It is noted that previous experimental work [29] conducted at higher inlet temperature (573 K) showed that NO_x emissions varied albeit modestly with surface roughness, particularly for the richer equivalence ratios. This was attributed to the alteration of the aerodynamic flow field, which affects the residense time and hence the NO_x formation. For the present experimental campaign with the limited number of experimental repeats, the results indicate that there are not significant differences in

NO_x due to variation in surface roughness. The contrast with the previous experimental work may stem from the difference in inlet plenum temperature, meaning the NO_x analyser was measuring at a lower concentration, with a higher relative uncertainty in this study, which made observation of any subtle trend unviable. However, the density of the mixture was also higher and therefore the overall bulk flow velocity was lower, resulting in a lower Reynolds number. As such, the resultant boundary layer was thicker [57] and the ratio between the latter and the roughness length scale was larger. Thus, the effect of surface roughness on the aerodynamic flow field, which influences the resident time and consequently the NO_x formation, is expected to be reduced [76].

6.3 Temperature & OH^* Chemiluminescence

The analysis of the temperature thermocouples and OH^* chemiluminescence time-averaged data was conducted in parallel concurrently. The combined analysis of those two data-collection sources reveals and explains interesting trends with respect to the surface roughness effect on swirling premixed combustion. As explained in Section 3.2.2, temperature measurements were taken using *K-type* pre-calibrated thermocouples. The average recorded "steady-state" period of each test point was 60 seconds with temperature measurements recorded at a frequency of 10 Hz. To reach a "steady-state" condition, a minimum period of 5 minutes was employed for each equivalence ratio change before any data was collected, with temperature readings closely monitored to estimate the level of stabilisation and convergence following the equivalence ratio change. The initialisation of temperature recordings took place quasi simultaneously with the initialisation of the OH^* chemiluminescence recordings, assuring comparability of results. The temperature measurements that were conducted during the experimental campaign correlate to single-point measurements, conducted at the centreline of exhaust system. Thus, any extrapolation of the following presented trends in the radial direction of the burner is invalid. This is a limiting characteristic of the measuring set-up, as trends can only be extracted for the centreline of the burner, near the exhaust gas analysis probe location. However, as part of the experimental aim was to reproduce the high-pressure industrial burner, allowing comparison of previous results, an analogous measuring set-up was required.

To prove the validity of the assumption that the system was at "steady-state" conditions when the data were collected, for each experimental repeat and test point, the mean exhaust thermocouple temperature measurement and its corresponding

standard deviation over the recording period of 60 seconds is listed in Table 6.3-1. For most of the test points the standard deviation over the recording period is less than 1 ^{o}C, demonstrating that the NO_x, temperature and OH^* chemiluminescent measurements were taken under "steady-state" conditions. Even for the cases where temperature at the exhaust thermocouple was deviating more than 1 ^{o}C, the relative difference as a percentage of the absolute temperature value is less than 0.1%. It is noted that for both repeats the *AM-R* case results in higher exhaust gas thermocouple readings. The *Machined* swirler case is located either below or above the *AM-G* swirler.

Table 6.3-1 *Exhaust temperature thermocouple individual measurements and their corresponding standard deviation over the 60 seconds of recording period for CH_4/air mixtures*

	AM-R (9 μm)				**AM-G (5 μm)**		**Machined (1 μm)**			
	Repeat 1 (^{o}C)		Repeat 2 (^{o}C)		Repeat 1 (^{o}C)		Repeat 1 (^{o}C)		Repeat 2 (^{o}C)	
Φ	Temp	**St. Dev**	Temp	**St. Dev**	Temp	**St. Dev**	Temp	**St. Dev**	Temp	**St. Dev**
0.558	935.2	**0.6**	925.0	**0.8**	910.0	**0.6**	900.7	**3.6**	904.0	**0.4**
0.66	982.1	**0.5**	969.4	**0.8**	950.5	**0.6**	939.8	**4.6**	931.7	**2.1**
0.80	1,058.7	**1.0**	1,033.8	**0.6**	1,003.2	**3.4**	1,015.3	**1.5**	1,002.3	**0.8**
0.90	1,092.5	**0.8**	1,075.8	**0.9**	1,052.2	**0.6**	1,050.8	**1.1**	1,039.6	**0.6**
1.00	1,112.3	**0.5**	1,094.2	**0.7**	1,067.6	**1.0**	1,075.2	**1.3**	1,060.7	**0.7**
1.05	1,094.3	**0.5**	1,079.0	**0.5**	1,050.3	**1.3**	1,046.1	**4.9**	1,044.0	**0.7**

Similar to the analysis in Section 6.2, the level of repeatability can be derived for the cases of *AM-R* and *Machined.* The arithmetic average between the first and the second experimental repeat was calculated as listed in Table 6.3-2. For both cases, the variation is less than 20 ^{o}C, which is around 2% of the average values. For the *AM-G* case, since only one repeat was carried out, the corresponding values are considered for comparison. As presented in Figure 6.3-1, the range of vertical error-bars, which are used to visualise the range of variation between the first and the second experimental repeat, is limited. Additionally, since the standard deviation of the mean value of each individual measurement is small (Table 6.3-1), noticeable differences, with respect to the exhaust temperature of the three swirlers, can be extracted from this data set.

Table 6.3-2 *Exhaust thermocouple temperature individual measurements and averages for CH_4/air mixture*

	Exhaust Thermocouple (°C)							
	AM-R (9 μm)			AM-G (5 μm)		Machined (1 μm)		
Φ	Repeat 1	Repeat 2	**Average**	**Repeat 1**	Average	Repeat 1	Repeat 2	**Average**
0.558	935.2	925.0	**930.1**	**910.0**	N/A	900.7	904.0	**902.3**
0.66	982.1	969.4	**975.8**	**950.5**	N/A	939.8	931.7	**935.7**
0.80	1058.7	1033.8	**1046.2**	**1003.2**	N/A	1015.3	1002.3	**1008.8**
0.90	1092.5	1075.8	**1084.1**	**1052.2**	N/A	1050.9	1039.6	**1045.2**
1.00	1112.3	1094.2	**1103.2**	**1067.6**	N/A	1075.2	1060.7	**1068.0**
1.05	1094.3	1079.0	**1086.6**	**1050.3**	N/A	1046.1	1044.0	**1045.0**

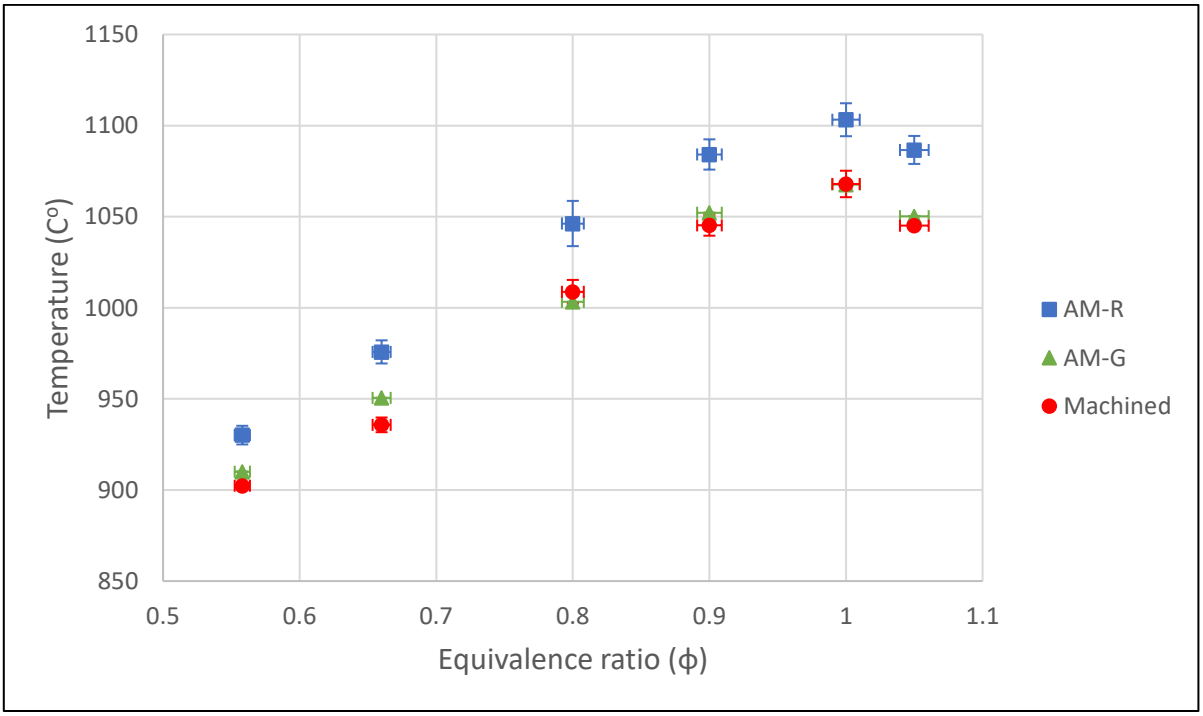

Figure 6.3-1 *Average exhaust thermocouple temperature indicating the level of repeatability for CH_4/air mixtures.*

It is apparent that the *AM-R* surface roughness swirler resulted in higher temperatures at the location of the exhaust thermocouple across the range of the equivalence ratio, while the *AM-G* and *Machined* cases were predominantly at similar levels and within the range of uncertainty. Only for very lean equivalence ratios ($\varphi < 0.66$) was the *AM-G* swirler distinguishable from the *Machined* case by ≈ 12 °C on average. The *AM-R* swirler resulted in significantly higher temperature, compared to the other two swirlers, with a difference of ≈ 40 °C on average across the equivalence

ratio range. The increasing temperature trend, before peaking at stoichiometric equivalence ratio, is followed by all swirlers irrespective of the surface roughness conditions. As expected, a slight drop in temperature is recorded as the mixture becomes fuel rich ($\varphi > 1$).

As the flowrate was only seen to deviate slightly (±0.5%), the difference in the exhaust thermocouple temperature likely does not stem from differences in equivalence ratio, which differed by ≈±1% as indicated by the horizontal error-bars. Additionally, as shown in Table 6.2-2, the presumed inlet temperature for the three swirlers deviated by only 2-3 ^{o}C for most of the equivalence ratios investigated. This difference is not large enough to justify the ≈ 40 ^{o}C change in the exhaust temperature. This is supported further by comparing the inlet temperatures of *AM-R* and *Machined* at $\varphi = 0.8$ and $\varphi = 1.05$ with the exhaust temperatures at the corresponding equivalence ratios in Table 6.3-3:

Table 6.3-3 *Comparison of inlet and exhaust average temperature readings for φ=0.80 and φ=1.05 for CH_4/air mixtures*

	φ = 0.80		**φ = 1.05**	
Surface roughness	Inlet Plenum	Exhaust Gas	Inlet Plenum	Exhaust Gas
AM-R (9 μm)	146.5^{o}C	1046.2^{o}C	146.0^{o}C	1086.6^{o}C
Machined (1 μm)	154.0^{o}C	1008.8^{o}C	149.6^{o}C	1045.0^{o}C
Difference	**-7.5**^{o}C	**37.4**^{o}C	**-3.6**^{o}C	**41.6**^{o}C

Although the difference between the two swirlers for the inlet plenum temperature was -7.5 ^{o}C for $\varphi = 0.8$ and reduced to -3.6 ^{o}C for $\varphi = 1.05$, the corresponding difference at the exhaust thermocouple increased from 37.4 ^{o}C to 41.6 ^{o}C. Thus, it can be assumed that the effect of the current range of deviation in the inlet plenum temperature has negligible effect on the exhaust gas thermocouple reading, and the difference that is recorded does not stem from the small differences in inlet plenum temperatures. Furthermore, the Reynolds number for both swirlers was only a function of the equivalence ratio and as the flowrates were identical for the three cases (*AM-R, AM-G, Machined*), the temperature difference does not come from deviation in mass flowrate, which could increase the temperature of the flame, and thus, the exhaust thermocouple reading.

Hence, since it is proven that the temperature differences identified by the exhaust thermocouple should not stem from changes in the chemistry of the flame that are derived by fluctuation of the equivalence ratio or inlet plenum temperature, it is proposed that the differences may have arisen due to alteration of the aerodynamic flow field. However, as the bulk flow velocity was identical for the three swirlers under the same equivalence ratio, it is further hypothesised that the variation in the surface roughness has changed the stabilisation position of the flame, moving it closer to the exhaust thermocouple for the *AM-R* case, thus resulting in the higher observed temperature. An alternative explanation would be that the exhaust thermocouple had been misplaced for the case of *AM-R*. However, this is not considered a likely explanation since its radial and axial location, as well as its orientation, were fixed at the exhaust hat and confirmed prior to each test. Therefore, the hypothesis that the stabilisation position of the flame was altered due to the presence of the increased surface roughness required further investigation.

To investigate the validity of this hypothesis, OH^* chemiluminescence measurements of the flames were undertaken within the experimental campaign. The overall shape and location of the flame was visualised through capturing the light emissions from OH^* radicals emanating from the flame front, as described in Section 3.2.3. The resulted time-averaged line-of-sight frames were spatially resolved using a corresponding Abel deconvolution algorithm via MATLAB software as has been successfully used in previous studies [29, 239–241, 260, 261, 269]. Hence, the time-averaged locations and intensities of OH^* radicals were quantified, revealing the location of the flame. To accelerate the post-processing time and because the camera is capturing the 2D side view of the flame which is assumed to be axisymmetric with respect to its central axis, only half (left side) of the flame was input into the Abel algorithm, as described in Section 3.2.3. The final Abel results, of the OH^* chemiluminescence data acquisition system corresponding to $\varphi = 0.558$ (LBO), $\varphi = 0.80$ and $\varphi = 1.00$, are presented in Figure 5.3.2-2. The camera frame rate was set at 4000 Hz, though only the first 2000 frames were used, thus the following OH^* pictures are time-averaged over a period of 0.5 seconds.

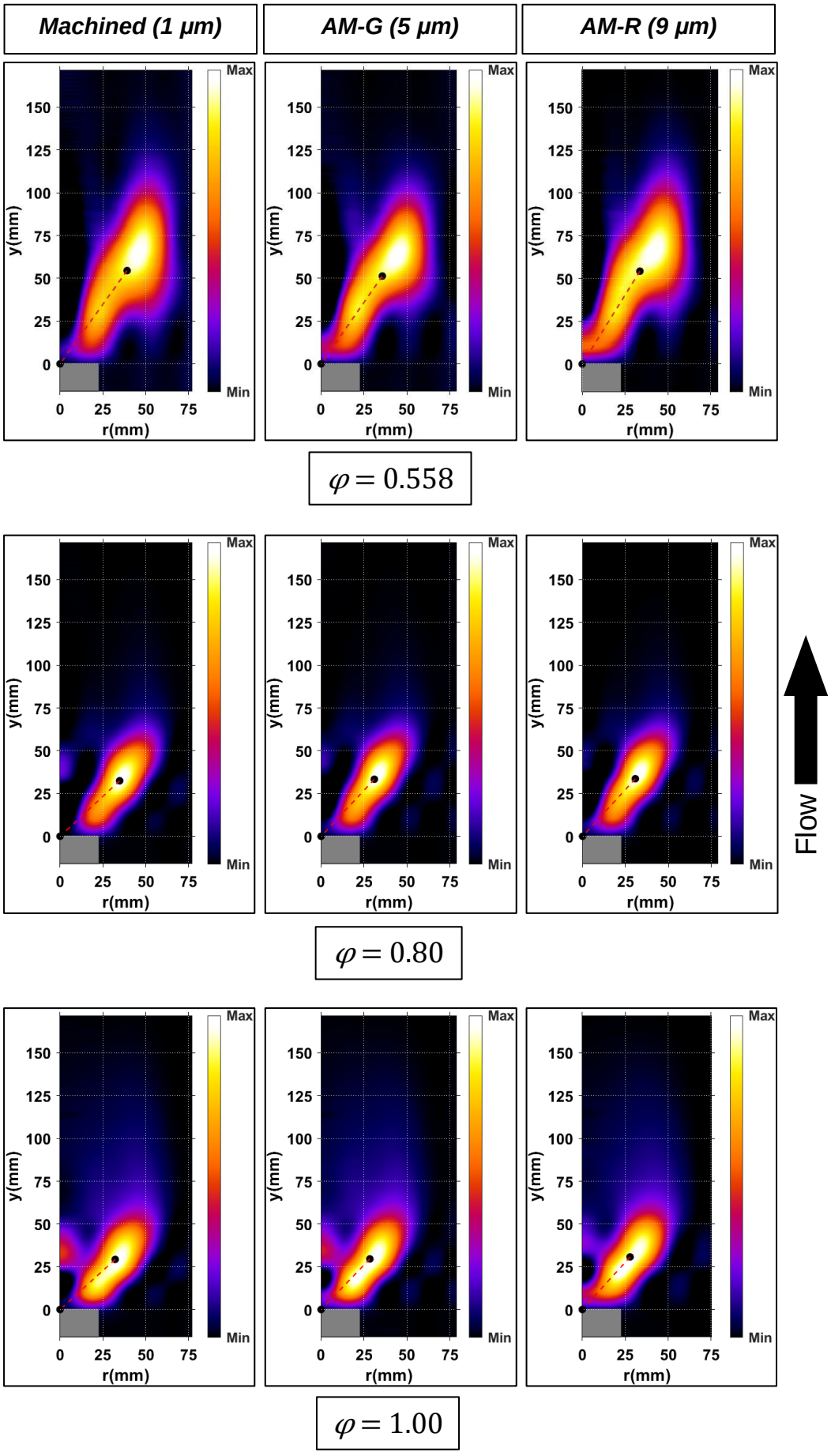

Figure 6.3-2 *Deconvoluted OH^* chemiluminescence results for the three swirlers at φ = 0.558, φ=0.80 and φ = 1.00 for CH_4/air flames.*

The profiles of the Abel deconvoluted flame images are revealed quantitively. As would be expected, a reduction in the size of the flame was observed as the equivalence ratio was increased approaching stoichiometry, and the chemical kinetics of the flame are improving. Consequently, the peak intensity region covered a higher percentage of flame area with increased equivalence ratio. As the bulk flow velocity was reduced, the flame stabilised closer to the nozzle exit. Although for $\varphi = 0.558$, the flame was close to transitioning from a V-shape to M-shape flame, for the rest of the equivalence ratios investigated, a clear V-shape was established. Furthermore, an increase in flame angle with respect to the vertical axis was noted as the equivalence ratio increased from $\varphi = 0.558$ to $\varphi = 0.80$.

To quantify the effects of surface roughness on flame shape and location, and to calculate the displacement of the flame, the Abel transformation algorithm was modified so that the *weighted centroid* of the flame could be located, as explained in Section 3.2.3.1. This was calculated based on the binary trace of the Abel deconvoluted image and represents the centroid of a region based on both its shape and its pixel intensity distribution. Thus, by specifying the weighted centroid for each flame, and by comparing it to the swirler with different surface roughness, the change in flame locations as a function of surface roughness could be highlighted. The corresponding x and y coordinates of the weighted centroids for the resulted Abel images were plotted in Figure 5.3.2-3 across the equivalence ratio range investigated, and for the three swirlers with different surface roughness (*Machined, AM-G* and *AM-R*).

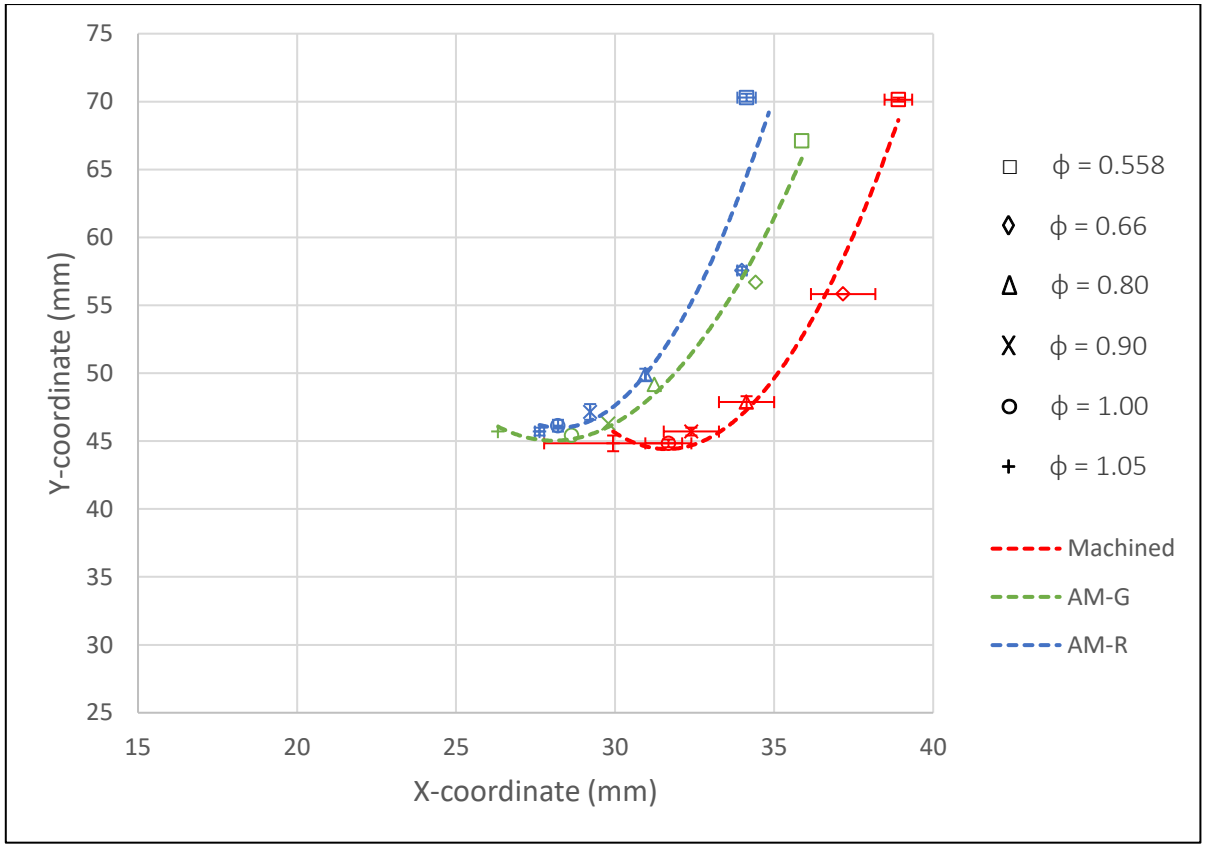

Figure 6.3-3 *Flame centroids cartesian coordinates across the investigated equivalence ratio for the Machined (1μm), AM-G (5μm) and AM-R (9μm) swirlers, for CH_4/air mixtures.*

It is apparent that as the equivalence ratio was increased and the bulk flow velocity was reduced, due to the decrease in the mass flowrate of air, the flame location was altered and the flame stabilised closer to the exit of the nozzle. Hence, from LBO ($\varphi = 0.558 \pm 1\%$) to $\varphi = 1.05$, the y-coordinate of the centroid of the flame was decreased by ≈25 mm, for all three swirlers. This change seems to be independent of the surface roughness and mainly influenced by the change in Reynolds Number due to the reduction in bulk flow velocity. For the case of *AM-R*, the flame centroid is lifted marginally, compared to the *AM-G* and *Machined* case, where the flame seems to stabilise in a similar location with regards to the y-axis.

By contrast, a significant change with respect to the x-coordinate of the flame centroids was noted for all the equivalence ratios. For the *Machined* case, the flame centroid was located closer to the outlet wall boundary of the burner, whilst for higher surface roughness values, the location of the flame centroid shifts radial towards the centreline of the burner. Quantitively, the *AM-R* flame centroids were ≈4 mm closer to the central vertical axis of the flame compared to those *Machined*, while the flame centroids for the *AM-G* swirler were stabilised somewhere in-between the other two.

It is noted that due to the single repeat that was conducted for the *AM-G* case, the repeatability of the corresponding results cannot be verified and thus the level of accuracy is unknown.

The larger difference between the x-coordinates of *Machined* and *AM-R* was identified at the LBO limit ($\varphi = 0.558$). This is sensible since at this equivalence ratio the Reynolds number was at its largest and so the surface roughness for this case was expected to be more influential due to increased surface roughness/boundary layer thickness ratio. For the rest of the equivalence ratio range, the difference between the centroids of the two swirlers is reduced, reaching its minimum at $\varphi = 1.05$. Regarding the centroids of the *AM-G* swirler, their distribution lies closer to the *AM-R* centroids, rather than to the *Machined* ones, particularly at higher equivalence ratios. For $\varphi = 1.05$, the *AM-G* centroid is the closest to the burner central axis, being further displaced compared to *AM-R.*

The observation, with respect to the shifting of the flame centroids towards the central vertical axis of the burner, is in qualitative agreement with the previous experimental findings published by Runyon et al. 2019 [29], utilising the same swirlers and a burner of similar bulk geometric characteristics, but at higher inlet plenum temperature ($300\ ^{o}\mathrm{C}$). Moreover, the modelling results that were presented in the Chapter 5 are also consistent with the findings of the present experimental programme, since the model results clearly show that the distribution of the axial velocity has been shifted towards the centreline of the burner as the surface roughness is systematically increased, as shown in Figure 5.3-7. The consistency between CFD and empirical findings validates further the effectiveness of the developed CFD modelling concept. Therefore, as the flame stabilises closer to the centreline of the burner for increased surface roughness, the hot gases from the flame are closer to the exhaust thermocouple, which consequently records higher temperatures. This increase in temperature corresponds only to the single point, where the thermocouple is located, and should not be confused with the spatially averaged temperature value across the diameter of the exhaust. The latter is expected to be similar for the three swirlers, as the resultant NO_x emissions were also within similar levels.

6.4 Summary

This experimental campaign concerned the investigation of the impact of surface roughness on the premixed atmospheric combustion of pure methane (CH_4) at elevated temperature ($150\ ^oC$). The aim of this Chapter was to assess the impact of swirler surface roughness and burner characteristics, whilst presenting benchmark dataset against other fuels appraised later in Chapter 7. Three swirlers of various surface roughness, namely, *Machined* (1 μm)*, AM-G* (5 μm) and *AM-R* (9 μm)*,* where tested over a wide range of equivalence ratio. Temperature, NO_x and OH^* chemiluminescence measurements were carried out, while the burner stability envelope was also identified.

The stable operating curves and the LBO limits were measured for practical applications as well as to ensure safe operation during experimental programme. All three swirlers resulted in the same stable operating curves and LBO limit, and therefore, it is concluded that the surface roughness did not noticeably affect the combustion stability and the Damköhler number, which is defined as the ratio of flow to chemical timescale.

Concerning the NO_x emissions measurements that were conducted using an industry standard gas analyser (CLD), again no significant differences were reported for the three swirlers. Due to the limited number of repeats, and the very small concentrations of NO_x emissions at lean equivalence ratios, the differences that were reported were within the range of uncertainty of the gas analyser. Thus, no clear trends could be discerned with respect to the influence of surface roughness on NO_x emissions.

Temperature measurements were undertaken, at the inlet plenum and exhaust section of the system, using a single point measuring thermocouple at each location. Significant differences were recorded with increased surface roughness. The readings of the inlet plenum thermocouple verified that all the test points were within the acceptable range of $150 \pm 5\ ^oC$. Additionally, it was demonstrated that the system was under “steady-state” conditions when the measurements were conducted. The exhaust thermocouple readings revealed the interesting trend, according to which, the increase in surface roughness resulted in higher exhaust thermocouple values measured at a set point on the centreline. Since for the three various surface

roughness swirlers the operating conditions (inlet plenum temperature, pressure and equivalence ratio) were identical, while NO_x emissions were recorded at similar levels, it is postulated that the difference in exhaust thermocouple measurements stemmed from a change in flame stabilization position rather than from a change in flame chemistry.

To investigate this hypothesis, OH^* chemiluminescence measurements were re-analysed. To facilitate the comparison, the centroid of the flame was calculated from the binary trace of the Abel converted image. The calculation of the centroid was performed using a suitable open-source MATLAB algorithm generated as part of this study, and discussed Section 3.2.5.1, taking into consideration both the shape of the flame and its spatial intensity distribution. Subsequently, the cartesian coordinates of the flame centroids for each of the three swirlers were plotted and compared across the equivalence ratio range investigated. The comparison showed that with increased surface roughness, the flame centroid shifts inwards, towards the centerline of the burner. Consequently, it is sensible for the exhaust thermocouple, which is aligned with the central vertical axis of the burner, to record higher temperature values for increased surface roughness, since the flame is sitting closer to the centerline of the burner and thus, the hot gases of the flame are closer to the thermocouple. This finding agrees well with previous experimental finding that were conducted using the same swirlers at higher temperature conditions ($300\ ^oC$), as well as, with the modelling results in Chapter 5 which also showed a noticeable shift of the axial velocity towards the centerline of the burner as surface roughness increases, which further supports the use of the developed CFD modelling concept.

The increase in exhaust thermocouple temperature readings for increased surface roughness corresponds only to the specific experimental measuring location. As the stable operating curves were identical for the three swirlers, whilst the emissions measurements resulted in similar NO_x levels, it is concluded that the range of surface roughness investigated did not result in significant differences in flame chemistry. Consequently, the spatially averaged exhaust gas temperature was expected to be similar for the three surface roughness cases. In practical terms, under the investigated combustion conditions, the overall performance of the two AM swirlers was therefore seen to at least match that of the traditionally manufactured one.

Chapter 7. Experimental investigation of the effect of surface roughness on alternative fuels (H_2) and fuel blends (CH_4/H_2) combustion

This Chapter builds upon Chapter 5 & 6, investigating the potential impact of surface roughness upon combustion characteristics for alternative fuels relevant towards decarbonised power. Specifically premixed combustion of both pure hydrogen (100% H_2) and a methane/hydrogen blend (23%$_{vol}CH_4$/77%$_{vol}H_2$) was investigated. The study again employed ambient pressure and elevated temperature (150 ^oC) conditions, of relevance to practical burners designs, with the impact of the same three swirlers *(AM-G, AM-R* and *Machined)* tested, and their respective results compared with the combustion performance of the swirlers, utilising premixtures of high H_2 fuels (77-100%), benchmarked against the analogous pure CH_4 results. In this way, the influence of the surface roughness length-scale range on different thermo-diffusive properties was highlighted. Again, for all test points, the mass flowrate of fuel was kept constant, and adjusted for each fuel concentration to maintain a constant thermal power output of 25 kW. The methane/hydrogen blend (23%$_{vol}CH_4$/77%$_{vol}H_2$) was deliberately chosen to ensure each fuel component contributed roughly 12.5 kW of thermal power output, based on their lower heating value.

The experimental procedure was carried out in the same manner as for the pure CH_4 case as described in Chapter 6. The burner stability envelope and stable operating curves were again identified, for both the pure H_2 and CH_4/H_2 blend, to determine if there are major differences in the lean blow-off (LBO) and flashback limit owing to the different surface roughness (Section 7.1). As the fuel flowrate was maintained constant, the oxidiser composition in the mixture was again either increased or decreased to approach the LBO and flashback limit, respectively. NO_x emissions, temperature and OH^* chemiluminescence measurements were conducted at each test point and are reported in Sections 7.2 and 7.3, for the pure H_2 and the fuel blend, respectively. Subsequently, in Section 7.4, the complete set of results for the two alternative fuel mixtures is discussed, leading to a summary of the salient findings.

To evaluate the level of repeatability of the experimental results, two experimental repeats were undertaken for all the test points. Thus, similar to the CH_4 results

presented in Chapter 6, the individual measurements for the quantities of interest, concerning, *Inlet plenum temperature, NO_x emissions and Exhaust gas thermocouple temperature* of the first and second repeat are listed, followed by their respective averaged values. The range of uncertainty between the first and second repeat, with respect to the average value, is again represented by vertical error-bars. The standard deviation of the mean value of each individual measurement, over the recording period of 60 seconds, is also provided, verifying that the system was under "steady-state" conditions, when the measurements were collected.

Concerning the horizontal error-bars that are related to the equivalence ratio, they again represent the uncertainty error of the Coriolis mass flow controllers (≈±1%) in terms of equivalence ratio as discussed previously in Chapter 6. It is again noted that the deviation due to the repeatability error of the mass flow controllers is expected to be insignificant across the duration of the experimental investigation, thus, it is not considered for the calculation of horizontal error-bars.

7.1 Burner stability envelope

The initial aspect of this experimental campaign regarded the determination of the burner stability envelopes and the estimation of the stable operating curves for the three different surface roughness swirlers, as previously conducted for the pure CH_4 case. The impact of surface roughness on LBO and flashback limits for the two AM swirlers (*AM-G* & *AM-R*), are again compared against the benchmark, traditionally manufactured *Machined* part. Moreover, the influence of pure H_2 and CH_4/H_2 combustion on the stability envelope is compared against analogous baseline results of pure CH_4, to highlight any differences stemming from the thermo-diffusive properties of hydrogen. The estimation of the limits of the burner stability envelopes was conducted in a similar manner to the previous CH_4 investigation, utilising the same diagnostic equipment, including pressure transducers, thermocouples and high-speed OH^* chemiluminescence photography. The latter was particularly important for monitoring the pure H_2 flame since its visible emissions are very limited [335].

For both cases, the LBO and flashback stability limits were identified. In contrast to the pure CH_4 results reported in Chapter 6, which did not flashback under the specific burner configuration, flashback events were observed for both the 100% H_2 and 23%$_{vol}$$CH_4$/77%$_{vol}$$H_2$ blend. The burner was driven to complete flashback, and the

corresponding measurements were conducted, before the fuel flowrate was cut off to extinguish the flame and to protect the experimental apparatus. The thermal power output was kept constant at 25 kW throughout, while again the air was preheated at 150 ± 5 ^{o}C, similar to the CH_4 benchmark. To assess the level of repeatability, two experimental repeats were conducted, with their results showing good agreement. Additionally, horizontal error-bars were used to indicate the level of uncertainty with respect to the flowrate of the mass flow controllers. The resultant burner stability envelopes and stable operating curves for the 100% H_2 and 23%$_{vol}CH_4$/77%$_{vol}H_2$ combustion are presented in Figure 7.1-1 and 7.2-2, respectively.

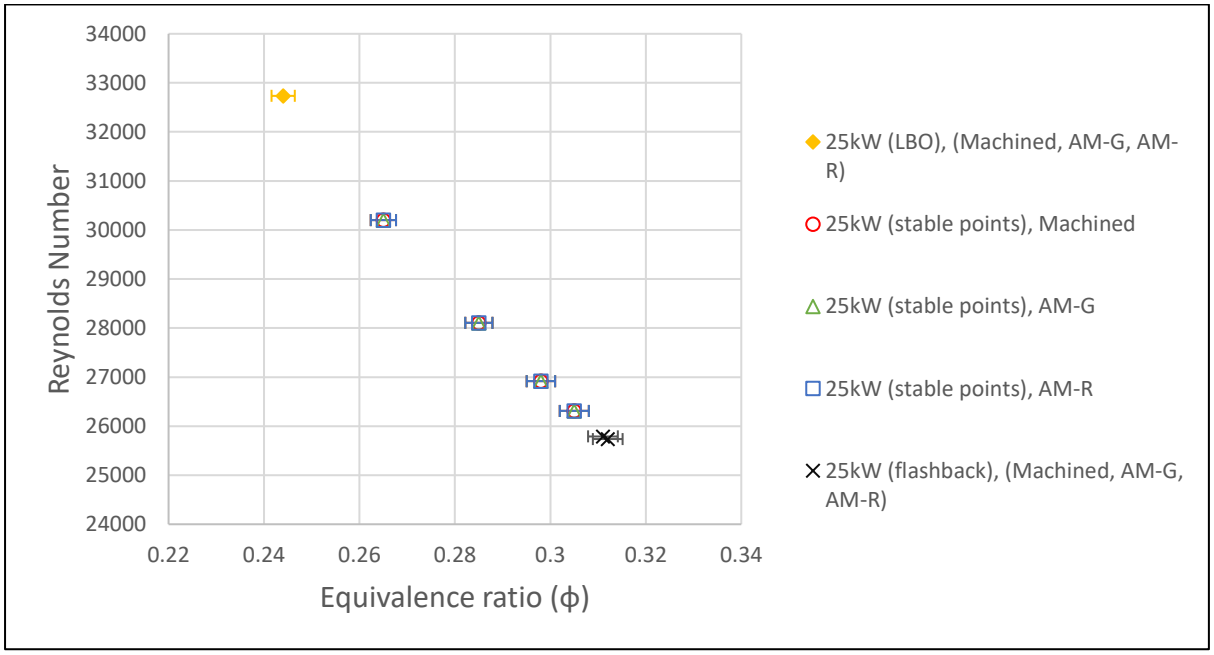

Figure 7.1-1 *Stable operating curves of 100%H_2 combustion for Machined, AM-G and AM-R swirlers.*

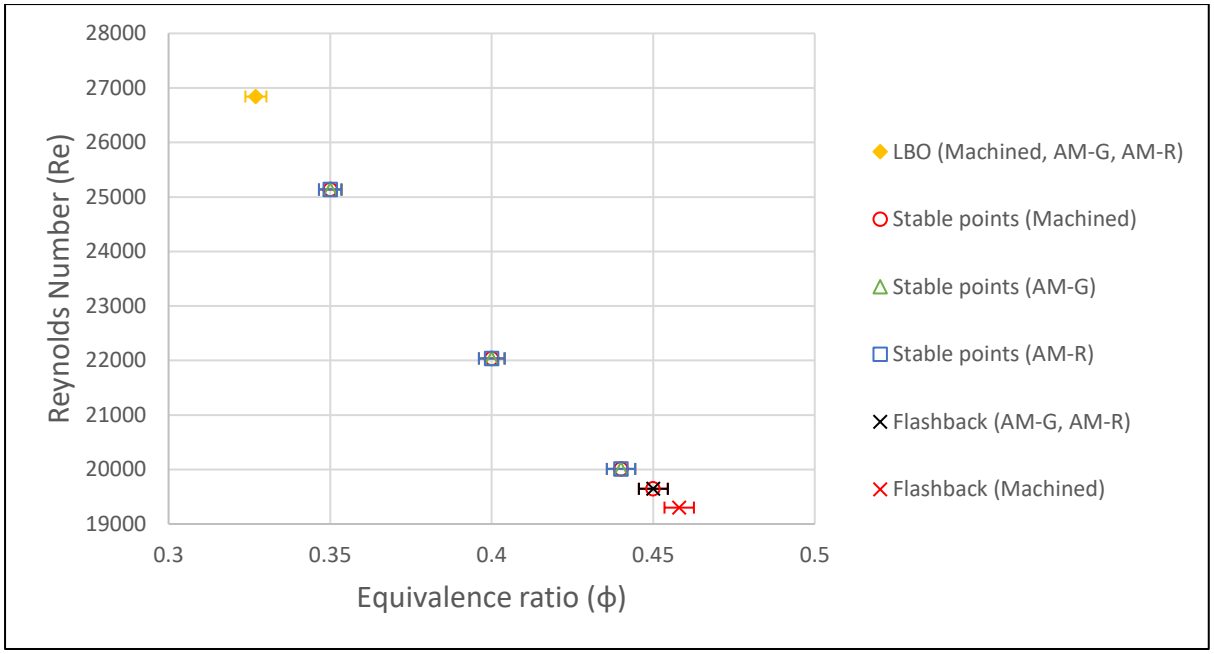

Figure 7.1-2 *Stable operating curves of 23%$_{vol}$CH$_4$/77%$_{vol}$H$_2$ combustion for Machined, AM-G and AM-R swirlers.*

As explained in Section 3.1, the LBO limits were identified by increasing the oxidizer concentration in the mixture, while maintaining constant fuel flowrate. This resulted in an increase in Reynolds number whilst the combustion intensity was reduced due to the decrease in equivalence ratio. Under these conditions, the LBO limits for the pure H_2 case and the CH_4/H_2 blend were identified at $\varphi = 0.244 \pm 1\%$ and $\varphi = 0.327 \pm 1\%$, respectively, as shown in the relevant Figures 7.1-1 and 7.1-2. The resultant LBO instabilities were characterised from lifted flames which underwent rapid extinction and reignition events. These events are potentially attributed to the imbalance between the rate of entrainment of reactants into the recirculation zone and the rate of burning of reactants. Both for the case of pure H_2 and for the case of CH_4/H_2, surface roughness seemed to have minimal effect on LBO instability, since for the three swirlers the LBO was realized under nominally similar equivalence ratios and were characterized by the same instability mechanism. Therefore, it was concluded that for the two fuel mixtures, surface roughness had negligible influence on the ratio of reciprocal to chemical timescales, which is commonly defined as the Damköhler number ($D_a = \tau_{flow}/\tau_{chem}$).

Maintaining a constant thermal power output under the same burner configuration, while switching from 100% CH_4 to 23%$_{vol}$$CH_4$/77%$_{vol}$$H_2$ and eventually to 100% H_2, required different quantities of fuel and air to be introduced to the system,

to account for the different stoichiometry and heating values of the mixtures. Consequently, the stable operating curves spread across varying equivalence ratios, based on the fuel composition. As can be seen in Figure 7.1-1 and Figure 7.1-2, an increase in H_2 percentage in the fuel mix shifted the burner stability envelope towards leaner equivalence ratios. This is attributed to the higher diffusivity, reaction rate and burning velocities that are associated with the H_2 addition. Hence, the lean flammability limits were extended, and the LBO occurred at leaner conditions. This is consistent with several experimental studies in the literature [116, 117, 121–123]. The LBO limit was lowered by around 41% for 77%$_{vol}H_2$ *($\varphi = 0.327 \pm 1\%$)* enrichment in CH_4 and almost 60% for 100% H_2 *($\varphi = 0.244 \pm 1\%$)*, compared to baseline 100% CH_4 *($\varphi = 0.558 \pm 1\%$)*. Due to the thermo-diffusive characteristics of H_2, which are characterised by $Le << 1$ under lean turbulent conditions, the flame stretch accelerates the flame resulting in higher burning velocities [124]. Thus, the resistance of the flame to combustion instabilities is improved [107, 124]. The increased H_2 concentration in the mixture not only improved the blow-off performance of the burner, but also enhanced its emissions performance. Due to the shifting of the stable operating curve towards leaner equivalence ratio, the flame temperature was reduced and so, as expected, thermal NO_x concentrations at the exhaust were also decreased, as described in Sections 7.2.1 and 7.3.1.

With increased percentage of H_2 in the mixture, the range of the burner stability envelope decreased. As shown in Figures 7.1-1 and 7.1-2, for 23%$_{vol}CH_4$/77%$_{vol}H_2$ and 100% H_2 the stable operating curves, of the *Machined* swirler, ranged from $0.327 < \varphi < 0.458$ and $0.244 < \varphi < 0.312$, respectively. This is qualitatively consistent with previous experimental studies utilising the generic swirl burner under atmospheric conditions, though, with different H_2 enrichment percentages [155, 238]. In comparison, the analogous range for pure CH_4 was $0.558 < \varphi < 1.05$, though it is again noted that richer equivalence ratios could have been achieved under the same burner configuration for the CH_4 case. The extremely narrow stable operation curves of high H_2 concentration fuels sets a major challenge for large scale power plants considering utilising these fuels. Small variations in air/fuel mixture concentration, inlet temperature and pressure, which are often difficult to control, could potentially result in blow-off or flashback phenomena, jeopardising the power plant's operation. This is particularly pertinent during the identification of the flashback limits of the three swirlers for the

100% H_2. As the stable operating curve range is extremely narrow and the influence of mixture variation on flame stability is significantly higher, to identify the exact equivalence ratio which initiates the flashback event and to distinguish it from a previous stable operation point, was challenging. For this reason, as demonstrated in Figure 7.1-1, the flashback limits for the three swirlers under 100% H_2 combustion were found to commonly lie between $\varphi = 0.311 \pm 1\%$ and $\varphi = 0.312 \pm 1\%$, since at both equivalence ratios, the flame was very unstable and partial or complete flashback events occurred. This range is well within the uncertainty range of the mass flow controllers, as indicated in Figure 7.1-1 via the horizontal error-bars.

The difference in flashback limits due to surface roughness was expected to be small, due to the small range of surface roughness investigated, guided by the original experimental study and hence focus of this research (Runyon et al., [29]). Hence, small air flow adjustments were necessary to identify the corresponding flashback limits. However, due to the high sensitivity of high H_2 concentration fuels to small air/fuel variations, the standard error of uncertainty of the mass flow controllers (±1% of resultant equivalence ratio), was larger than the level of variation in airflow required to highlight the surface roughness effect on flashback. This is particularly evident in Figure 7.1-2, where the flashback limits of the 23%$_{vol}$$CH_4$/77%$_{vol}$$H_2$ blend for both the *AM-G* and *AM-R* swirlers were at $\varphi = 0.450 \pm 1\%$, whilst for the *Machined* one at $\varphi = 0.458 \pm 1\%$. As observed on Figure 7.1-2, although the flashback limit for the *Machined* swirler was at a slightly richer equivalence ratio, the horizontal error-bars are marginally overlapping, indicating this observation is within the range of uncertainty. Particularly for this case, complete flashback events were observed for all three swirlers, approximately 2 minutes after approaching the test point. Since the flame was located very near and marginally within the burner nozzle exit, due to the flame radiation, the nozzle of the swirler started to glow indicating excessive heat transfer from the flame to the nozzle surface. This acted as a preheater for the fresh reactants, further increasing their burning velocity and initiating the flashback event. This phenomenon was commonly observed for the three swirlers.

Concluding the initial part of the alternative fuels study for the three swirlers, across the surface roughness range did not affect the LBO instability mechanism or shift the LBO limit either for 100% H_2 or 23%$_{vol}$$CH_4$/77%$_{vol}$$H_2$ combustion. The surface roughness seemed to have an effect only on the flashback limit of 23%$_{vol}$$CH_4$/77%$_{vol}$$H_2$

blend, however, even this difference is within the range of uncertainty and does not necessarily indicate significant improvement in combustion performance. In general, the addition of H_2 into the mixture affected the burner stability envelope by shifting it towards leaner equivalence ratios and by making it narrower. For both alternative fuel cases (100% H_2 and 23%$_{vol}CH_4$/77%$_{vol}H_2$) the swirlers manufactured using additive layer *(AM-R* and *AM-G)* resulted in combustion performance with respect to the burner stability envelope and the stable operating curves similar to the traditionally manufactured *Machined* swirler. From a practical perspective for potential manufacturers of additive layer parts, this indicates that there is negligible performance advantage in post-manufacture surface finishing for the alternative fuels studied in this thesis, which could be significant in leading to product cost reductions.

7.2 Single component fuel (H_2)

7.2.1 Exhaust Gas Emissions

Similar to the experimental investigation undertaken for the benchmark of pure CH_4 in Section 6.2, the NO_x emissions resulting from pure H_2 combustion were measured using a calibrated, industrial standard gas analyser, as described in Section 3.2.6, across a range of equivalence ratios where the flame was stabilised. As the same support structure was used for the water-cooled gas analysis probe, the mounting position of the latter was identical. As shown in Section 7.1, the stability envelope of the burner for H_2 combustion was substantially narrower compared to the analogous CH_4 test, thus, the equivalence ratio *(φ)* ranged from $\varphi = 0.244 \pm 1\%$ (LBO) to $\varphi = 0.312 \pm 1\%$ (flashback). Inlet plenum temperature measurements were again conducted using the single measuring point thermocouple that had previously employed for the CH_4 testing. Since the H_2 programme was undertaken with the same burner, the inlet plenum thermocouple was mounted at the exact same location as described in Section 3.2.4. The target inlet plenum temperature was again set at 150 ^{o}C, with a tolerable deviation of ± 5 ^{o}C.

The analysis of the experimental data was generated using similar protocols as previously. Thus, prior to the presentation of NO_x emissions measurements, individual measurements within the inlet plenum for each test point and each repeat are presented in Table 7.2.1-1. Since NO_x emissions are influenced by the inlet temperature of the reactants [5], it is important to ensure that any observed difference in NO_x does not stem from inconsistencies related to the preheat temperature of the

mixture. All the values listed in Table 7.2.1-1 are within the target range of 150 ± 5 °C. The larger difference in inlet plenum temperatures with respect to the same swirler and different equivalence ratios, was recorded for the first repeat of the *AM-R,* where the inlet temperature increased from 146 °C to 153 °C and the equivalence ratio reduced from $\varphi = 0.312$ to $\varphi = 0.244$. By contrast, the largest difference in inlet plenum temperature, under the same equivalence ratio and for different swirlers was noted between the first experimental repeat of the *AM-R* and the *Machined* cases, at $\varphi = 0.311$. For these conditions, the relative temperature difference was ≈ 5°C. Moreover, for each individual measurement, the standard deviation over the recording period (60 seconds) was evaluated. As shown in Table 7.2.1-1, the standard deviation calculated is less than 1 °C for all the test points, confirming that the system was under "steady-state" conditions when the measurements took place.

Table 7.2.1-1 *Inlet plenum temperature individual measurements and their corresponding standard deviation over the 60 seconds of recording period for H_2/air mixtures*

	AM-R (9 μm)				**AM-G (5 μm)**				**Machined (1 μm)**			
	Repeat 1 (°C)		Repeat 2 (°C)		Repeat 1 (°C)		Repeat 2 (°C)		Repeat 1 (°C)		Repeat 2 (°C)	
Φ	Temp	**St. Dev**	Temp	**St. Dev**	Temp	**St. Dev**	Temp	**St. Dev**	Temp	**St. Dev**	Temp	**St. Dev**
0.244	153.5	**0.1**	153.2	**0.1**	153.7	**0.1**	153.2	**0.2**	152.5	**0.1**	152.3	**0.2**
0.265	149.1	**0.2**	151.2	**0.1**	150.3	**0.2**	148.8	**0.2**	150.0	**0.1**	152.1	**0.1**
0.285	147.5	**0.1**	149.0	**0.1**	149.0	**0.1**	147.8	**0.2**	151.0	**0.1**	149.2	**0.1**
0.298	147.4	**0.3**	147.9	**0.1**	149.0	**0.3**	148.9	**0.2**	149.8	**0.1**	147.1	**0.1**
0.305	147.5	**0.1**	149.1	**0.1**	148.8	**0.1**	148.3	**0.1**	148.8	**0.2**	149.0	**0.1**
0.311	147.4	**0.1**	149.5	**0.1**	149.2	**0.1**	148.5	**0.1**	152.3	**0.1**	149.1	**0.1**
0.312	146.3	**0.1**	148.8	**0.1**	149.5	**0.1**	149.5	**0.1**	150.0	**0.1**	147.5	**0.1**

As shown in Table 7.2.1-2, the level of repeatability is very good, whilst all the inlet plenum temperatures were within the acceptable range of 150 ± 5 °C. The larger deviation between first and second repeat corresponds to the *Machined* swirler at $\varphi = 0.311$, where the inlet plenum temperature difference between the two experimental repeats was ≈3.2 °C. This level of inconsistency is expected to have a negligible effect on flame properties. Since the level of repeatability is high, the average value of the two experimental repeats was utilised for the rest of the analysis. It is noted that compared to the comparative results for CH_4 combustion, the level of repeatability was increased. The average inlet plenum differences between the three swirlers under the

same equivalence ratio was generally very low at $\approx 1.5\ ^{o}\mathrm{C}$. The largest variation, which was noted for the $\varphi = 0.311$ case between the *AM-R* swirler and the *Machined* one, was $\approx 2.2\ ^{o}\mathrm{C}$, and again was expected to have a negligible impact on resultant NO_x emissions.

Table 7.2.1-2 *Inlet plenum temperature individual measurements and averages for H_2/air mixtures.*

	Inlet plenum temperature (°C)								
	AM-R (9 μm)			**AM-G (5 μm)**			**Machined (1 μm)**		
Φ	Repeat 1	Repeat 2	**Average**	Repeat 1	Repeat 2	**Average**	Repeat 1	Repeat 2	**Average**
0.244	153.5	153.2	**153.3**	153.7	153.2	**153.5**	152.5	152.3	**152.4**
0.265	149.1	151.2	**150.1**	150.3	148.8	**149.5**	150.0	152.1	**151.0**
0.285	147.5	149.0	**148.3**	149.0	147.8	**148.4**	151.0	149.2	**150.1**
0.298	147.4	147.9	**147.6**	149.0	148.9	**149.0**	149.8	147.1	**148.4**
0.305	147.5	149.1	**148.3**	148.8	148.3	**148.5**	148.8	149.0	**148.9**
0.311	147.4	149.5	**148.5**	149.2	148.5	**148.9**	152.3	149.1	**150.7**
0.312	146.3	148.8	**147.6**	149.5	149.5	**149.5**	150.0	147.5	**148.8**

Thus, it can be assumed that the three swirlers were tested under the same operating conditions (same equivalence ratio, pressure and temperature), as the pure CH_4 case. This is further validated by the oxygen (O_2) concentration levels of the exhaust gases for the three swirlers (Figure D-2), which were recorded quasi-simultaneously with the inlet temperature and NO_x measurements, showing negligible variation in O_2 concentrations under the same equivalence ratio. Hence, any difference in reported NO_x emissions is presumed to stem from either the variation in surface roughness or the standard error of the measuring apparatus. As the standard deviation is low, it is ensured that the system was under “steady-state” operating conditions, and thus, any noticeable difference in NO_x should not be linked to equivalence ratio variation. It is noted that the standard deviation was significantly lower compared to the CH_4 cases presented in Table 6.2-1, since, for the majority of test points, it was less than 0.1 ppmv, with minimum exceptions (*AM-R,* $\varphi = 0.285$ and *Machined,* $\varphi = 0.305$*,* repeat 1), where it rose to maximum of 0.13 ppmv.

For the three swirler cases, the average relative increase in NO_x, from the LBO limit at $\varphi = 0.244 \pm 1\%$ to the flashback limit at $\varphi = 0.312 \pm 1\%$*,* was equal to ≈1 ppmv. In contrast, the analogous relative increase under CH_4 combustion was equal to more than 30 ppmv. Not only the relative increase in NO_x emissions across the investigated

equivalence ratio was much lower for the pure H_2 case, but the absolute NO_x emissions values too. The highest NO_x values, which were recorded for the *AM-R* and *AM-G* swirlers at $\varphi = 0.312$ and for the *Machined* one at $\varphi = 0.311$, were an order of magnitude lower compared to the analogous values for pure CH_4 at $\varphi = 1.00$.

Table 7.2.1-3 *NO_x individual measurements and their corresponding standard deviation over the 60 seconds of sampling period for H_2/air mixtures.*

	AM-R (9 μm)				**AM-G (5 μm)**				**Machined (1 μm)**			
	Repeat 1 (ppmv)		Repeat 2 (ppmv)		Repeat 1 (ppmv)		Repeat 2 (ppmv)		Repeat 1 (ppmv)		Repeat 2 (ppmv)	
Φ	NOx	**St. Dev**	NOx	**St. Dev**	NOx	**St. Dev**	NOx	**St. Dev**	NOx	**St. Dev**	NOx	**St. Dev**
0.244	2.50	**0.04**	2.09	**0.03**	1.33	**0.04**	0.96	**0.04**	1.80	**0.03**	1.43	**0.03**
0.265	2.19	**0.09**	1.93	**0.03**	1.20	**0.04**	0.96	**0.03**	1.62	**0.03**	1.84	**0.03**
0.285	2.00	**0.13**	1.75	**0.11**	1.03	**0.03**	1.08	**0.04**	2.79	**0.03**	1.25	**0.02**
0.298	2.69	**0.03**	1.98	**0.03**	1.66	**0.04**	1.22	**0.04**	2.87	**0.03**	1.99	**0.04**
0.305	3.01	**0.04**	2.33	**0.04**	2.08	**0.04**	1.32	**0.04**	1.90	**0.12**	2.38	**0.03**
0.311	3.11	**0.10**	2.38	**0.08**	2.25	**0.05**	1.41	**0.06**	2.94	**0.05**	2.20	**0.05**
0.312	3.24	**0.04**	2.56	**0.03**	2.84	**0.03**	1.75	**0.06**	2.45	**0.02**	2.03	**0.18**

Although 100% H_2 combustion is associated with higher flame temperatures compared to 100% CH_4 combustion [115, 116, 132, 144], and thus, an increase in NO_x emissions should be expected, this increase was offset by the shifting of the stable operating curves towards leaner equivalence ratios. Since the burner stability envelope was significantly narrower (and leaner) for the pure H_2 case, it was therefore expected that both the relative increase in NO_x (from LBO to flashback) and the absolute NO_x values are significantly lower than the analogous CH_4 case. These observations are consistent with previous experimental studies investigating the effect of H_2 enrichment in CH_4, with respect to NO_x emissions [122, 145].

To estimate the level of repeatability and to examine if there were in fact significant differences in resultant NO_x, due to the presence of surface roughness, the average values of the first and second experimental repeat are listed in the following Table 7.2.1-4. For all the three swirlers, the average difference across the equivalence ratio range investigated, between the two experimental repeats was less than 1ppmv, resulting in good repeatability. However, from Table 7.2.1-3, it is observed that the concentration of NO_x emissions under 100% H_2 combustion was extremely low, whilst its relative difference across the burner stability envelope was ≈1 ppmv. As the uncertainty of the gas analyser is generally estimated at ≈±2 ppmv, these differences

in NO_x emissions fall within the range of uncertainty of the measuring equipment. This is evident in Table 7.2.1-4 and Figure 7.2.1-1 where for some cases, NO_x emissions are marginally reducing with increasing equivalence ratio.

Table 7.2.1-4 *NO_x emissions individual measurements and averages for H_2/air mixtures.*

	NOx emissions, dry, 15% O_2 (ppmv)								
	AM-R (9 μm)			**AM-G (5 μm)**			**Machined (1 μm)**		
Φ	Repeat 1	Repeat 2	**Average**	Repeat 1	Repeat 2	**Average**	Repeat 1	Repeat 2	**Average**
0.244	2.50	2.09	**2.30**	1.33	0.96	**1.14**	1.80	1.43	**1.62**
0.265	2.19	1.93	**2.06**	1.20	0.96	**1.08**	1.62	1.84	**1.73**
0.285	2.00	1.75	**1.87**	1.03	1.08	**1.05**	2.79	1.25	**2.02**
0.298	2.69	1.98	**2.34**	1.66	1.22	**1.44**	2.87	1.99	**2.43**
0.305	3.01	2.33	**2.67**	2.08	1.32	**1.70**	1.90	2.38	**2.14**
0.311	3.11	2.38	**2.75**	2.25	1.41	**1.83**	2.94	2.20	**2.57**
0.312	3.24	2.56	**2.90**	2.84	1.75	**2.30**	2.45	2.03	**2.24**

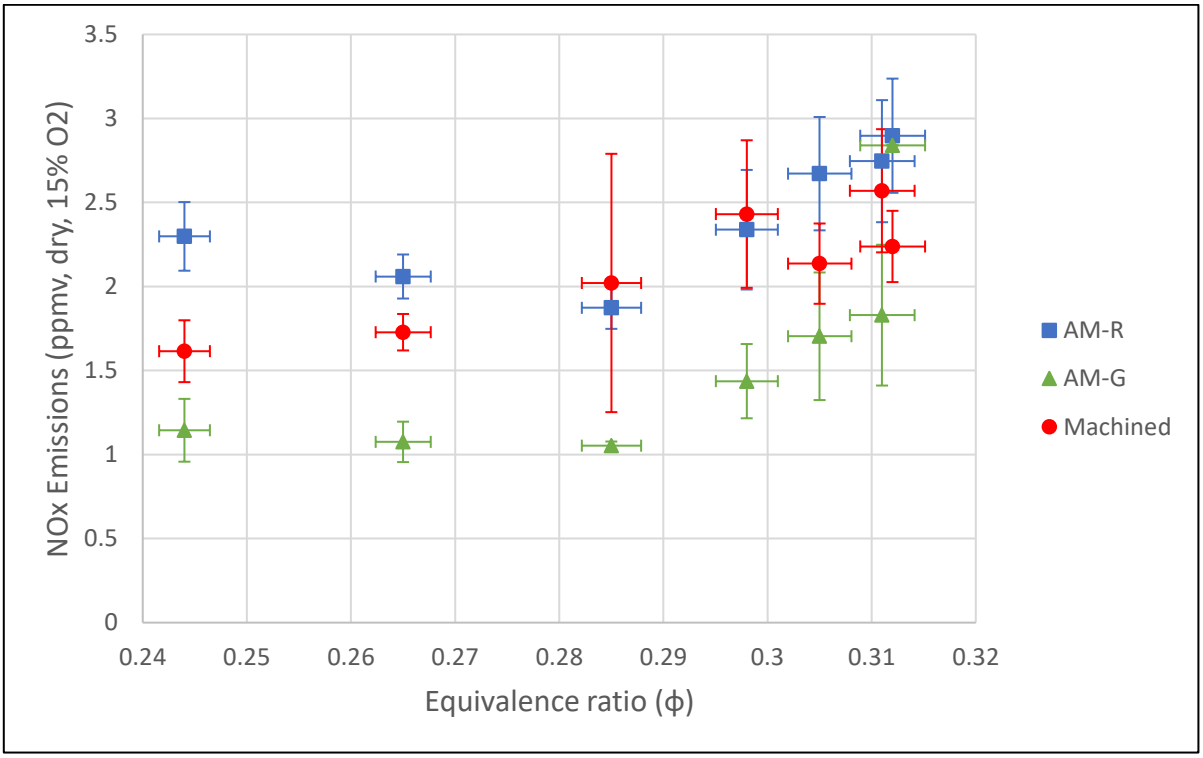

Figure 7.2.1-1 *Average NO_x emissions indicating the level of repeatability between the first and second repeat for H_2/air mixtures.*

Vertical error-bars, corresponding to the range of variation between the first and second experimental repeat, are used to visualise the level of repeatability. It is observed that at leaner equivalence ratios *($\varphi = 0.244$ and $\varphi = 0.265$),* repeatability was improved compared to relatively richer equivalence ratios, where most of the

vertical error-bars are overlapping. It is again worth noting that, as for the pure CH_4 case, the systematic error of the gas analyser due to calibration process, inconsistencies in span-gas and "drift" of the reference values due to prolonged period of operation, has not been taken into consideration. Thus, considering these error factors, the uncertainty bars presented in Figure 7.2.1-1 are of a similar order as the values being measured. For the *Machined* and *AM-R* cases, the average NO_x values were within similar levels, with a marginal difference of less than 0.5 ppmv, for the majority of the test points. Additionally, the resultant NO_x emissions for most of the *AM-G* case test points, were apparently lower compared - by less than 1 ppmv - to the other two cases. However, as stated above, these differences are less than 2 ppmv, which is roughly estimated as the uncertainty range of the equipment. Due to these low levels of NO_x concentration, which are low in the context of emissions legislation [5], and its small relative differences between the three cases, the extraction of significant trends due to the presence of surface roughness is prevented. Higher level of precision would have been required to effectively capture such small variations in NO_x emissions, however at these very low NO_x conditions, this was not deemed necessary. Hence, under practical operating conditions, such a range of surface roughness should be expected to result in negligible difference in NO_x emissions.

7.2.2 Temperature & OH^* Chemiluminescence

As for the pure CH_4 experimental investigation, temperature and OH^* chemiluminescence data were collected in parallel, for the three swirlers with different surface roughness, for the 100% H_2 and 23%$_{vol}$$CH_4$/77%$_{vol}$$H_2$ fuels. The experimental procedure for acquiring the experimental data was identical to the 100% CH_4 case allowing comparison of the respective measurements. The same *K-type* thermocouple used for the pure CH_4 testing, were utilised for the alternative fuel experimental investigations too. The recording period of the thermocouple was 60 seconds with a frequency of 10 Hz, and the data were recorded under "steady-state" conditions. A waiting period of a minimum of 5 minutes was applied for each test point transition to ensure that the "steady-state" condition is satisfied, whilst the temperatures diagnostics were also closely monitored. Hence, the recording process was initiated only when these conditions were satisfied. Consequently, the change in temperature due to the transition from one test point to another was minimised. The initialisation of temperature recordings occurred quasi-simultaneously with the initialisation of the OH^*

chemiluminescence recordings, assuring the combined analysis of the results, again consistent with the 100% CH_4 combustion case. It is worth pointing out that the experimental temperature recordings presented correspond to single-point measurements taken at the centreline of the burner, under a fixed axial position near the exhaust section, as described in Section 3.2.4. Therefore, any extrapolation of the trends presented in the radial direction of the burner is not possible.

To confirm that the system was indeed in “steady-state” when the data were recorded, for each experimental repeat and each test point, the mean exhaust thermocouple temperature measurement and its corresponding standard deviation over the recording period of 60 seconds is listed in Table 7.2.2-1. For the set of results presented, the largest standard deviation was 1.7 ^{o}C, reaffirming that NO_x, temperature and chemiluminescence measurements were carried out under “steady-state” conditions. The range of standard deviation is generally very low, with the overwhelming majority of the calculated deviations less than 0.1% of the measured temperature.

Table 7.2.2-1 *Exhaust temperature thermocouple individual measurements and their corresponding standard deviation over the 60 seconds of recording period for the H_2/air mixtures.*

	AM-R (9 μm)				**AM-G (5 μm)**				**Machined (1 μm)**			
	Repeat 1 (^{o}C)		Repeat 2 (^{o}C)		Repeat 1 (^{o}C)		Repeat 2 (^{o}C)		Repeat 1 (^{o}C)		Repeat 2 (^{o}C)	
Φ	Temp	**St. Dev**	Temp	**St. Dev**	Temp	**St. Dev**	Temp	**St. Dev**	Temp	**St. Dev**	Temp	**St. Dev**
0.244	738.2	**0.2**	719.9	**0.3**	703.9	**0.3**	704.1	**0.3**	698.2	**0.2**	700.0	**0.2**
0.265	763.5	**0.3**	742.5	**0.3**	724.2	**0.2**	725.8	**1.2**	718.8	**0.3**	720.4	**0.4**
0.285	786.7	**0.4**	760.1	**1.2**	738.6	**0.9**	740.8	**1.6**	742.3	**0.2**	740.9	**0.3**
0.298	802.9	**0.3**	780.0	**0.3**	759.3	**0.6**	762.6	**0.4**	756.1	**0.3**	755.9	**0.3**
0.305	807.2	**0.3**	788.0	**0.4**	767.1	**0.3**	771.1	**0.5**	763.6	**0.3**	764.4	**0.4**
0.311	813.0	**0.5**	795.5	**0.6**	772.5	**0.2**	776.3	**0.6**	769.9	**0.4**	770.6	**0.4**
0.312	813.2	**0.6**	795.8	**0.6**	770.1	**0.2**	773.9	**0.2**	771.3	**0.4**	770.4	**0.3**

To evaluate the level of repeatability, the exhaust thermocouple measurements together with their arithmetic average between the two experimental repeats are listed in Table 7.2.2-2. For the *AM-R* swirler, the variation between the two experimental repeats, across the range of equivalence ratio investigated was $\approx 20\ ^{o}C$, on average. For the cases of *Machined* and *AM-G*, the level of repeatability was significantly improved, since the analogous variation was $\approx 1.0\ ^{o}C$ and $\approx 2.7\ ^{o}C$, respectively. Since,

the deviation between the two experimental repeats was low for the three cases, the average exhaust thermocouple temperatures were extracted and used for the rest of the analysis. As presented in Figure 7.2.2-1, where the average temperatures are plotted, the range of the vertical error-bars used to visualise the range of variation between the two experimental repeats, is limited. Thus, a noticeable trend can be distinguished.

Table 7.2.2-2 *Exhaust thermocouple temperature individual measurements and averages for H_2/air mixtures.*

	Exhaust Thermocouple (ºC)								
	AM-R (9 µm)			**AM-G (5 µm)**			**Machined (1 µm)**		
Φ	Repeat 1	Repeat 2	**Average**	Repeat 1	Repeat 2	**Average**	Repeat 1	Repeat 2	**Average**
0.244	738.2	719.9	**729.0**	703.9	704.1	**704.0**	698.2	700.0	**699.1**
0.265	763.5	742.5	**753.0**	724.2	725.8	**725.0**	718.8	720.4	**719.6**
0.285	786.7	760.1	**773.4**	738.6	740.8	**739.7**	742.3	740.9	**741.6**
0.298	802.9	780.0	**791.5**	759.3	762.6	**760.9**	756.1	755.9	**756.0**
0.305	807.2	788.0	**797.6**	767.1	771.1	**769.1**	763.6	764.4	**764.0**
0.311	813.0	795.5	**804.2**	772.5	776.3	**774.4**	769.9	770.6	**770.3**
0.312	813.2	795.8	**804.5**	770.1	773.9	**772.0**	771.3	770.4	**770.9**

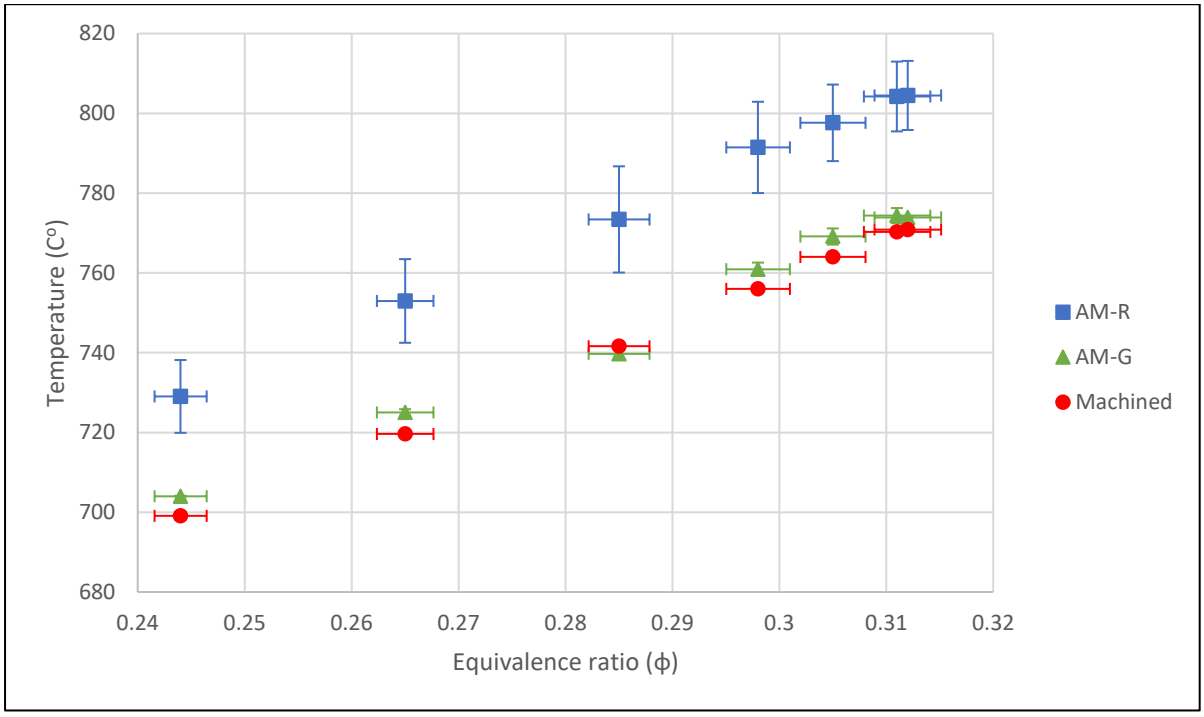

Figure 7.2.2-1 *Average exhaust thermocouple temperature indicating the level of repeatability for H_2/air mixtures.*

From Figure 7.2.2-1 it is apparent that for all the three cases, the recorded exhaust thermocouple average temperatures increase with equivalence ratio, due to increase in flame temperature. For 100% H_2 combustion, the resultant temperatures are significantly lower compared to the analogous results for 100% CH_4 presented in Figure 6.3-1. This is consistent with the lower NO_x emissions recorded under pure H_2 combustion. Regarding the relative temperature difference between the three swirlers, it was observed that the average exhaust thermocouple temperature increases with surface roughness. Therefore, the *AM-R* swirler, resulted in the highest temperatures, followed by the *AM-G* and the *Machined.* The relative difference between the *AM-G* and *Machined* was significantly lower ($\approx 5\ ^{o}C$), compared to the *AM-R*, which was differentiated by more than $\approx 25\ ^{o}C$ from the *Machined* swirler. Only for $\varphi = 0.285$, the *Machined* swirler resulted in higher temperature, of approximately $2\ ^{o}C$ compared to *AM-G*. Both the range of relative difference between *Machined – AM-G* and *Machined – AM-R* was reduced compared to the 100% CH_4 case, in which, the corresponding difference in exhaust thermocouple average temperature was $\approx 12\ ^{o}C$ and $\approx 40\ ^{o}C$, respectively.

As indicated in Figure 7.2.2-1 by the horizontal error-bars, the equivalence ratio only deviated by ±1%. Moreover, the difference in the inlet plenum temperatures between the three swirlers, as listed in Table 7.2.1-2, only differed by $\approx 1.5\ ^{o}C$ for the majority of the equivalence ratios investigated, whilst the highest difference recorded was $\approx 4.9\ ^{o}C$. The range of deviation with respect to the equivalence ratio and inlet plenum temperature does not justify the difference of $\approx 25\ ^{o}C$ recorded in the exhaust thermocouple from a flame chemistry viewpoint. This is further supported by the following Table 7.2.2-3, where the inlet plenum temperatures, recorded under the first experimental repeat of *AM-R* and *Machined* at $\varphi = 0.244$ and $\varphi = 0.311$, are compared with the exhaust thermocouple temperatures at the corresponding equivalence ratios.

Table 7.2.2-3 *Comparison of inlet and exhaust average temperature readings for $\varphi = 0.244$ and $\varphi = 0.311$ for H_2/air mixtures.*

	φ = 0.244		**φ = 0.311**	
Surface roughness	Inlet Plenum	Exhaust Gas	Inlet Plenum	Exhaust Gas
AM-R (9 μm)	153.5°C	738.2°C	147.4°C	813.0°C
Machined (1 μm)	152.5°C	698.2°C	152.3°C	769.9°C
Difference	1.0°C	40.0°C	-4.9°C	43.1°C

Although the inlet plenum temperature difference, between the two swirlers, was $1.0\ ^{o}C$ for $\varphi = 0.244$, and decreased to -4.9 ^{o}C for $\varphi = 0.305$, the respective exhaust thermocouple temperature difference was increased from $40\ ^{o}C$ to $43.1\ ^{o}C$. Therefore, it can be presumed that the current range of deviation in inlet plenum temperature had minimum influence on the exhaust thermocouple temperature reading, and the difference that was recorded did not stem from the small differences in inlet plenum temperatures. Additionally, as the equivalence ratio could only deviate marginally (±1%), the temperature difference in the exhaust thermocouple readings did not stem from variation in the composition of the premixture, which could potentially increase the temperature of the flame, and thus, the recorded exhaust thermocouple temperatures.

Therefore, as for the pure CH_4 case, it is shown that the relative temperature differences identified by the exhaust thermocouple across different swirlers, are not dominated by changes in flame chemistry driven by fluctuations of the equivalence ratio or inlet plenum temperature. Consequently, the recorded temperature differences stem from an alteration of the aerodynamic flow field. However, as the equivalence ratio could only deviate marginally, the variation in bulk flow velocities for the three swirler should be insignificant. Thus, it is hypothesised that as for the pure CH_4 case, the variation in surface roughness must have changed the stabilisation position of the flame, moving it closer to the exhaust thermocouple for the *AM-R* case. The validity of this hypothesis was appraised in the same manner as in Chapter 6. Hence, the OH^* chemiluminescence data were examined to quantify the location of the flame.

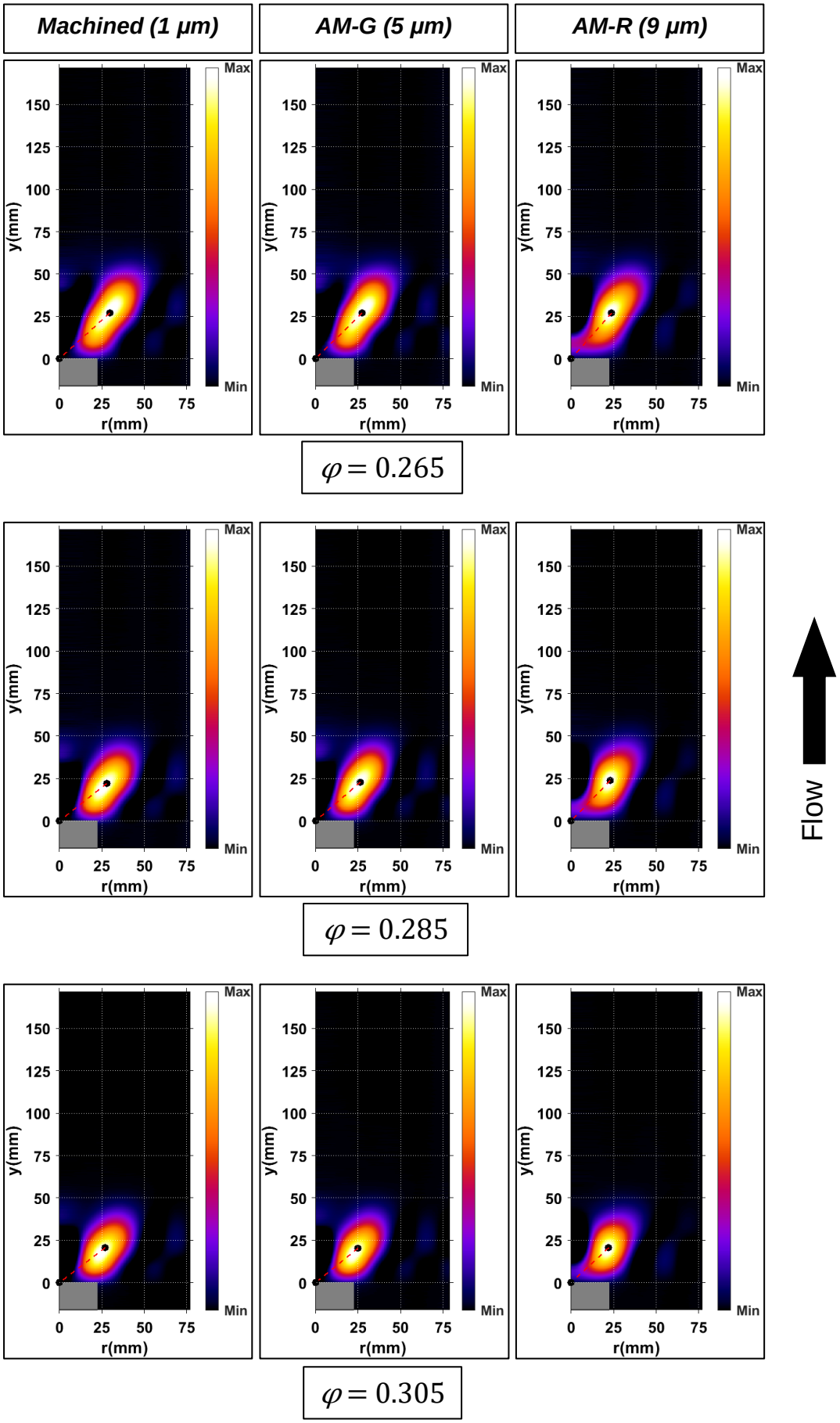

Figure 7.2.2-2 *Deconvoluted OH^* chemiluminescence results for the three swirlers at $\varphi = 0.265$, $\varphi = 0.285$ and $\varphi = 0.305$ for H_2/air flames.*

The profiles of the Abel deconvoluted flame images are revealed quantitively. A reduction in the size of the flame was evident for relatively richer equivalence ratios due to the improved chemical kinetics. However, this reduction was much less profound compared to the analogous for pure CH_4 combustion. This was attributed to the much more compact flames that characterise H_2 combustion, and the narrower range of the burner stability envelope, which inhibited large changes in Reynolds number, and therefore, in the resultant flow field. Consequently, the change in peak intensity area with increasing equivalence ratio was minimal. Similar to the CH_4 case, with increased equivalence ratio, the flame stabilises closer to the nozzle due to the increased flame speed. However, the overall size of the flame was much smaller compared to the analogous for 100% methane flame.

To quantify the influence of surface roughness on flame shape and location, and to determine the displacement of the flame, the *weighted centroid* function is introduced. Through this function, the flame centroid was estimated, as explained in Section 3.2.5.1. The corresponding cartesian coordinates of the weighted centroids for the resulted Abel images were plotted in Figure 7.2.2-3 across the burner stability envelope, and for the three swirlers of different surface roughness.

As the air flowrate was reduced, with corresponding increase in equivalence ratio, the flame was anchored closer to the nozzle exit, due to the augmented burning rate. Therefore, from LBO *($\varphi = 0.244 \pm 1\%$)* to flashback *($\varphi = 0.312 \pm 1\%$)*, the y-coordinate of the centroid of the flame was reduced by ≈15 mm, for all the three swirlers. The comparative reduction for CH_4 was ≈25 mm, as the flame stabilised further downstream. This was attributed to the balance between bulk flow velocity and flame burning velocity, and therefore, was heavily dependent upon equivalence ratio, while surface roughness seemed to have a negligible effect. Thus, for all the swirlers, the y-coordinates were observed at similar levels, across the equivalence ratio range studied.

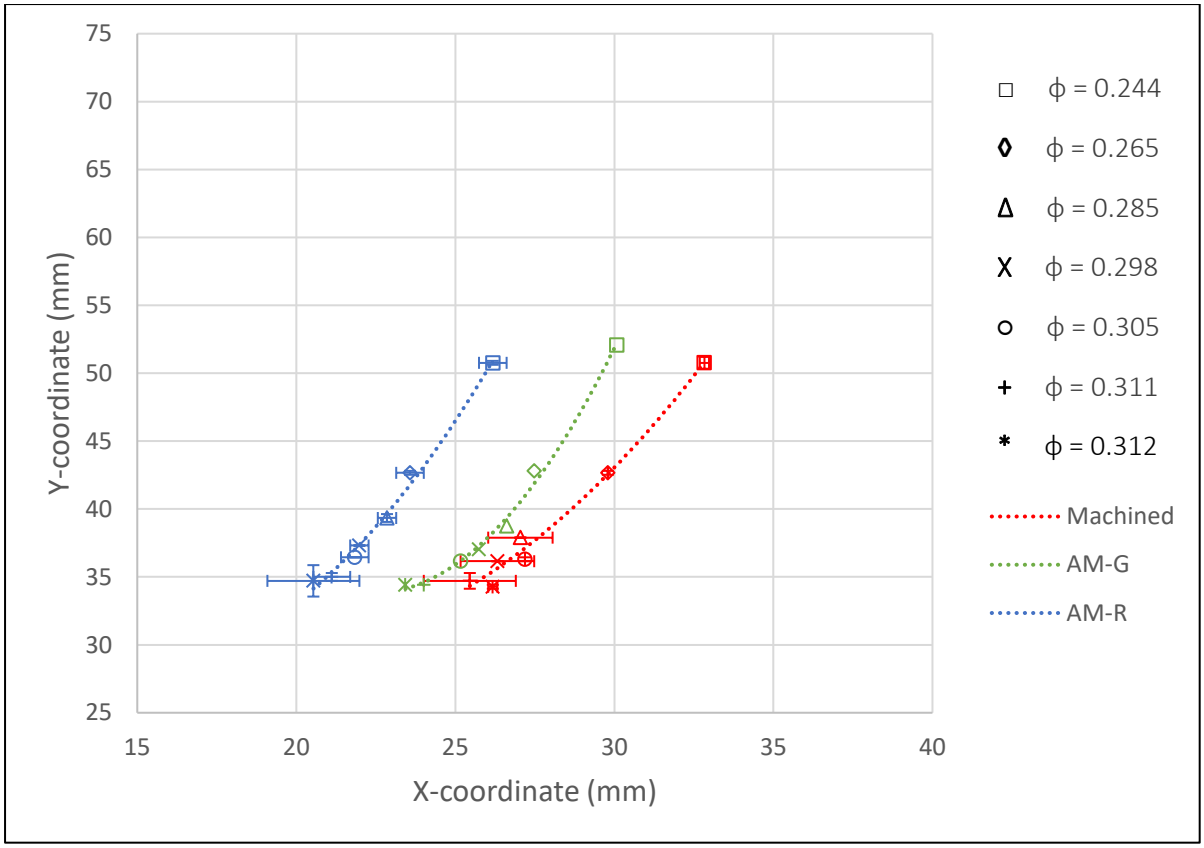

Figure 7.2.2-3 *Flame centroids cartesian coordinates across the investigated equivalence ratio for the Machined (1 μm), AM-G (5 μm) and AM-R (9 μm) swirlers, for H_2/air fuel mixtures.*

By contrast, surface roughness was observed to have a major influence on the x-coordinate of flame centroids. With increase in surface roughness, again the flame centroids were observed to shift radially towards the centreline of the burner. Quantitively, the *AM-R* flame centroids were ≈6 mm closer to the central vertical axis of the burner compared to the *Machined* ones, while the flame centroids for the *AM-G* swirler were found somewhere in-between the two. This observation is qualitatively consistent with the previous results presented in Section 6.3 regarding 100% CH_4 combustion. It is noted that for both fuel cases the AM-G centroids lie between the other 2, however, for this case, they are much closer to the Machined ones.

The effect of surface roughness on shifting the flame centroids towards the centreline of the burner was found to be larger closer to the LBO limit ($\varphi = 0.244 \pm 1\%$). This is attributed to the higher bulk flow velocity, which reduced the boundary-layer thickness and increased the surface roughness/boundary layer thickness ratio. As this ratio increases, the surface roughness is expected to be more influential on mean flow quantities, such as the displacement of the boundary layer, which results to the radial shifting of the flame position. For the rest of the burner stability envelope, the difference

between the centroid of the swirlers reduces, reaching its minimum at the flashback limit ($\varphi = 0.312 \pm 1\%$). Thus, surface roughness slightly influenced the angle at which the flame displaces, as indicated in Figure 7.2.2-3. Concerning the *AM-G* swirler, its centroids lie closer to those *Machined*, especially at relatively richer equivalence ratios.

This potentially explains the marginal differences in the exhaust thermocouple average temperature since the position of the stabilisation of the flame obviously directly affects the static exhaust thermocouple temperature reading. As observed for the pure CH_4 case, with higher surface roughness, the stabilisation location of the flame was shifted towards the centreline of the burner. Thus, the hot gases from the flame were closer to the exhaust thermocouple, which consequently, records higher temperatures than the mean exhaust temperature. The higher recorded temperatures for the swirler of increased surface roughness, are only related to the specific measuring point, on which the exhaust thermocouple is located, and should not be confused with the spatially average exhaust gas temperature.

7.3 Methane Hydrogen fuel blend

7.3.1 Exhaust Gas Emissions

As well as investigating the effect of surface roughness on NO_x formation of single conventional (CH_4) and alternative (H_2) fuels, the present experimental campaign examines the respective performance of the three various surface roughness swirlers under lean premixed combustion of a fuel blend consisting of $23\%_{vol}CH_4/77\%_{vol}H_2$. The comparison of these results with those reported earlier in the Chapter related to pure CH_4 and H_2 cases, is justified since the same experimental rig and burner configuration was used. Therefore, the same support structure and water-cooled probe was utilised for the sampling of NO_x emissions, whilst the same thermocouples were mounted at the same positions around the rig. As discussed in Section 7.1, the introduction of CH_4 in the fuel premixture shifted the burner stability envelope towards richer equivalence ratios and closer to the pure CH_4 case, whilst the swirlers were not seen to significantly change the stability envelope beyond the uncertainty of the mass flow controllers used to determine it.

Since the stable operating curves were shifted to relatively richer equivalence ratios, NO_x emissions were expected to be slightly higher, compared to the pure H_2

case but still significantly lower compared to pure CH_4 one. The approach for analysing the results related to CH_4/H_2 combustion was conducted similarly to those discussed Sections 6.2 and 7.2. Hence, prior to the presentation of NO_x measurements, the individual inlet plenum measurements for each test point and each experimental repeat are presented in Table 7.3.1-1. As NO_x emissions are influenced by the inlet temperature of the reactants [5], Table 7.3.1-1 is presented to demonstrate that the temperature recorded by the inlet plenum thermocouple were within the acceptable target range of 150 ± 5 °C. The largest difference in inlet plenum temperatures, across different swirlers, under the same equivalence ratio, was found between the first experimental repeat of *AM-R* and *Machined* cases at $\varphi = 0.44$, for which the temperature difference was ≈ 8.4 °C.

Furthermore, the standard deviation over the recording period of (60 seconds) was extracted. As presented in Table 7.3.1-1, the standard deviation calculated was less than 0.5 °C for all the test points, confirming that the system was in "steady-state" when the measurements were recorded. Moreover, a marginal difference in flashback limit between the conventional swirler *(Machined)*, and the two manufactured by additive layer *(AM-G* and *AM-R),* was observed and results in an absence of experimental data with respect to the $\varphi = 0.458$ for these swirlers as indicated by the N/A inputs in the table.

Table 7.3.1-1 *Inlet plenum temperature individual measurements and their corresponding standard deviation over the 60 seconds of recording period for CH_4/H_2 fuel mixtures.*

	AM-R (9 µm)				**AM-G (5 µm)**				**Machined (1 µm)**			
	Repeat 1 (°C)		Repeat 2 (°C)		Repeat 1 (°C)		Repeat 2 (°C)		Repeat 1 (°C)		Repeat 2 (°C)	
Φ	Temp	**St. Dev**	Temp	**St. Dev**	Temp	**St. Dev**	Temp	**St. Dev**	Temp	**St. Dev**	Temp	**St. Dev**
0.327	152.9	**0.1**	151.1	**0.2**	152.1	**0.1**	154.0	**0.1**	154.3	**0.1**	153.1	**0.1**
0.35	152.9	**0.1**	153.3	**0.1**	152.6	**0.1**	153.4	**0.1**	154.2	**0.2**	154.0	**0.2**
0.40	148.0	**0.1**	150.9	**0.1**	149.7	**0.1**	151.5	**0.1**	151.8	**0.2**	150.2	**0.3**
0.44	146.3	**0.1**	147.0	**0.1**	147.2	**0.1**	148.0	**0.1**	154.7	**0.2**	150.3	**0.1**
0.45	146.8	**0.1**	148.0	**0.1**	146.6	**0.1**	148.2	**0.1**	151.0	**0.1**	147.6	**0.1**
0.458	N/A	**N/A**	N/A	**N/A**	N/A	**N/A**	N/A	**N/A**	149.3	**2.0**	148.6	**1.9**

It is observed that the level of repeatability was generally high, whilst all values presented were within the acceptable target range of 150 ± 5 °C. The larger variation between the two repeats corresponds to the *Machined* swirler at $\varphi = 0.44$, where the

inlet plenum temperature difference was $\approx 4.4\ ^{o}C$. This level of inlet plenum temperature variation was expected to have a negligible effect on resultant NO_x formation. Since for the rest of test points, the difference between the two experimental repeats is less than 4.4 ^{o}C, the average arithmetic value between the two experimental runs was extracted and used for the rest of the analysis. With respect to the average inlet plenum temperatures of the three swirlers, their relative difference across the vast majority of test points was $\approx 1.5\ ^{o}C$, excluding the larger variation, which was noted for $\varphi = 0.44$ between the *AM-R* swirler and the *Machined* one. The latter was $\approx 5.9\ ^{o}C$ and expected to have negligible impact on resultant NO_x emissions.

Since the inlet plenum temperature variation between the three swirlers was low, and thus, expected to have a negligible effect on resultant NO_x emissions, it was assumed that the three swirlers were tested under the same operating conditions. This is further quantified by the oxygen (O_2) concentration levels of the exhaust gases for the three swirlers (Figure D-3), which were empirically obtained quasi-simultaneously with the inlet temperature and NO_x measurements, presenting negligible variation in O_2 concentrations under the same equivalence ratio. Therefore, any noticeable difference in NO_x should result from either the difference in surface roughness or due to the standard error of the measuring equipment.

Table 7.3.1-2 *Inlet plenum temperature individual measurements and averages for CH_4/H_2 fuel mixtures.*

	Inlet plenum temperature (^{o}C)								
	AM-R (9 μm)			**AM-G (5 μm)**			**Machined (1 μm)**		
Φ	Repeat 1	Repeat 2	**Average**	Repeat 1	Repeat 2	**Average**	Repeat 1	Repeat 2	**Average**
0.327	152.9	151.1	**152.0**	152.1	154.0	**153.0**	154.3	153.1	**153.7**
0.35	152.9	153.3	**153.1**	152.6	153.4	**153.0**	154.2	154.0	**154.1**
0.40	148.0	150.9	**149.5**	149.7	151.5	**150.6**	151.8	150.2	**151.0**
0.44	146.3	147.0	**146.7**	147.2	148.0	**147.6**	154.7	150.3	**152.5**
0.45	146.8	148.0	**147.4**	146.6	148.2	**147.4**	151.0	147.6	**149.3**
0.458	N/A	N/A	**N/A**	N/A	N/A	**N/A**	149.3	148.6	**149.0**

For each measurement, the individual arithmetic average, and its corresponding standard deviation over the sampling period of 60 seconds, are presented in Table 7.3.1-3. The sampling rate was consistent with the previous experimental investigation regarding pure CH_4 and pure H_2, thus set at 1 Hz and the measurements have been normalised for dry, 15% O_2, to allow comparison with the

results reported in Section 6.2 and 7.2.1. The resultant standard deviations of the individual NO_x measurements were calculated to ensure that the system was in "steady-state". As presented in Table 7.3.1-3, the standard deviation was less than 0.2 ppmv at all experimental conditions, confirming that the system was stabilised as the measurements were taken. For the cases where the recorded NO_x emissions were lower than 1ppmv, the corresponding standard deviation also reduced to ≈0.03 ppmv.

Table 7.3.1-3 *NO_x individual measurements and their corresponding standard deviation over the 60 seconds of sampling period for CH_4/H_2 fuel mixtures.*

	AM-R (9 μm)				**AM-G (5 μm)**				**Machined (1 μm)**			
	Repeat 1 (ppmv)		Repeat 2 (ppmv)		Repeat 1 (ppmv)		Repeat 2 (ppmv)		Repeat 1 (ppmv)		Repeat 2 (ppmv)	
Φ	NOx	**St. Dev**	NOx	**St. Dev**	NOx	**St. Dev**	NOx	**St. Dev**	NOx	**St. Dev**	NOx	**St. Dev**
0.327	0.39	**0.04**	2.69	**0.03**	2.65	**0.03**	1.08	**0.03**	1.19	**0.03**	0.68	**0.02**
0.35	0.40	**0.02**	2.50	**0.04**	2.55	**0.04**	1.13	**0.04**	1.02	**0.03**	0.71	**0.13**
0.40	0.83	**0.07**	2.30	**0.02**	2.84	**0.03**	1.39	**0.11**	1.09	**0.11**	1.16	**0.14**
0.44	1.03	**0.18**	2.64	**0.04**	3.00	**0.04**	1.66	**0.14**	2.07	**0.14**	1.37	**0.03**
0.45	1.44	**0.03**	2.66	**0.04**	3.16	**0.04**	1.76	**0.13**	2.25	**0.05**	1.30	**0.07**
0.458	N/A	**N/A**	N/A	**N/A**	N/A	**N/A**	N/A	**N/A**	1.31	**0.16**	1.30	**0.04**

Consistent with the 100%H_2 case, the relative increase in NO_x emissions for the 23%$_{vol}CH_4$/77%$_{vol}H_2$ blend, across the range of the stable operating curves, was calculated ≈1 ppmv, on average. As presented in Table 7.3.1-4, where the NO_x emissions for the two experimental repeats were listed together with their mean value, the resultant NO_x emissions were at the same levels as for the 100%H_2 case, ranging from 0.94 ppmv (lower reported NO_x, corresponding to *Machined,* $\varphi = 0.327$) to 2.46 ppmv (highest reported NO_x corresponding to *AM-G,* $\varphi = 0.45$). This observation indicates that although the percentage of CH_4 in the CH_4/H_2 mixture was increased to the extent that both fuels contributed 12.5 kW of thermal power, whilst the stable operating curves had been shifted to relatively richer equivalence ratios, the flame temperature was still low, and the NO_x formation was dominated by the prompt and N_2O NO_x pathways. Therefore, for the CH_4/H_2 blend, NO_x emissions were maintained within similar to 100% H_2 levels (1-2 ppmv), whilst stability control was enhanced, due to the wider burner stability envelope. However, the 23%$_{vol}CH_4$/77%$_{vol}H_2$ mixture composition produces carbon emissions, which the 100% H_2 does not.

Table 7.3.1-4 *NO_x emissions individual measurements and averages for CH_4/H_2 fuel mixtures.*

	NOx emissions, dry, 15% O_2 (ppmv)								
	AM-R (9 μm)			**AM-G (5 μm)**			**Machined (1 μm)**		
Φ	Repeat 1	Repeat 2	**Average**	Repeat 1	Repeat 2	**Average**	Repeat 1	Repeat 2	**Average**
0.327	0.39	2.69	**1.54**	2.65	1.08	**1.87**	1.19	0.68	**0.94**
0.35	0.40	2.50	**1.45**	2.55	1.13	**1.84**	1.02	0.71	**0.87**
0.40	0.83	2.30	**1.56**	2.84	1.39	**2.11**	1.09	1.16	**1.13**
0.44	1.03	2.64	**1.83**	3.00	1.66	**2.33**	2.07	1.37	**1.72**
0.45	1.44	2.66	**2.05**	3.16	1.76	**2.46**	2.25	1.30	**1.77**
0.458	N/A	N/A	**N/A**	N/A	N/A	**N/A**	1.31	1.30	**1.31**

With respect to repeatability, as indicated in Table 7.3.1-4, for the *AM-R* and *AM-G* cases, the absolute difference between the two experimental repeats was calculated on average equal to ≈1 ppmv. Although this corresponds to a relative percentage difference of more than 100% for some cases, considering that the range of uncertainty for the gas analyser is roughly estimated to ±2 ppmv, it can be concluded that the level of repeatability was good. As the difference in NO_x emissions between LBO and flashback, as well as the relative differences between the three swirlers was less than the range of uncertainty of the measuring equipment, the extraction of significant trends with respect to the effect of surface roughness on NO_x emissions was not possible. This is evident in Figure 7.3.1-1, where the average NO_x values for the three swirlers are plotted across the respective stable operating curves.

Although the *Machined* swirler appears to consistently result in lower NO_x, followed by the *AM-R* and *AM-G*, the relative difference between the three swirlers was ≈1 ppmv, which is less than the range of uncertainty of the NO_x analyser. Moreover, as the overalapping vertical error-bars indicate, the level of variation between the two experimental repeats was larger than the relative difference of their average values. Therefore, it is again concluded that the current range of surface roughness, under the present operating conditions, exerts negligible influence on NO_x emissions, that is, the three swirlers result in similar NO_x emissions levels.

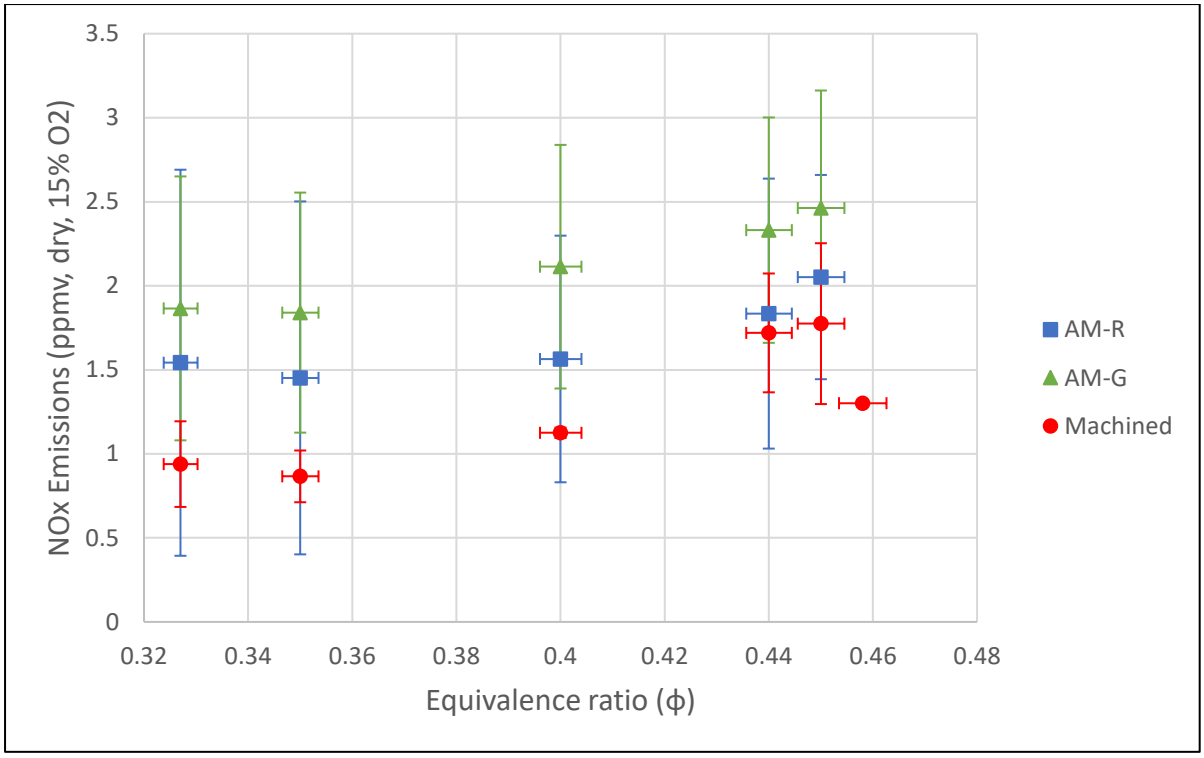

Figure 7.3.1-1 *Average NO_x emissions indicating the level of repeatability between the first and second repeat for CH_4/H_2 fuel mixtures.*

7.3.2 Temperature & OH^* Chemiluminescence

With regard to the temperature and OH^* chemiluminescence measurements, similar to the investigation of pure CH_4 and pure H_2 combustion, these two datasets were collected concurrently, and the same methodology was followed, to minimise the deviation in temperature due to the transition from one test point to another, as described in Section 6.3 and 7.2.2.

To verify that the system was operating in "steady-state" as the measurements were conducted, for each experimental repeat and test point, the mean exhaust thermocouple temperature measurement and its respective standard deviation over the recording period of 60 seconds was listed in Table 7.3.2-1. As indicated, for the current set of results, the standard deviations were ranging from 0.3 ^{o}C (first experimental repeat, *AM-G,* $\varphi = 0.327$) to 2.6 ^{o}C (first experimental repeat, *Machined*, $\varphi = 0.40$). These values correspond to less than 0.5% deviation of the respective recorded values. Thus, it was confirmed that NO_x, temperature and chemiluminescence measurements took place under "steady-state" operation.

Table 7.3.2-1 *Exhaust temperature thermocouple individual measurements and their corresponding standard deviation over the 60 seconds of recording period for CH_4/H_2 fuel mixtures.*

	AM-R (9 μm)				**AM-G (5 μm)**				**Machined (1 μm)**			
	Repeat 1 (°C)		Repeat 2 (°C)		Repeat 1 (°C)		Repeat 2 (°C)		Repeat 1 (°C)		Repeat 2 (°C)	
Φ	Temp	**St. Dev**	Temp	**St. Dev**	Temp	**St. Dev**	Temp	**St. Dev**	Temp	**St. Dev**	Temp	**St. Dev**
0.327	812.7	**0.4**	797.3	**0.4**	779.3	**0.3**	781.8	**0.6**	775.4	**0.4**	775.0	**0.3**
0.35	821.3	**0.7**	806.3	**0.4**	788.1	**0.8**	788.2	**1.3**	786.7	**2.2**	783.3	**0.7**
0.40	859.5	**0.6**	847.6	**1.2**	822.7	**0.9**	826.9	**2.1**	812.2	**2.6**	821.3	**1.0**
0.44	886.9	**1.4**	879.4	**1.5**	856.9	**2.5**	860.1	**1.7**	859.3	**1.4**	853.6	**1.7**
0.45	892.1	**1.0**	886.0	**0.9**	857.7	**0.9**	864.5	**1.8**	862.8	**0.9**	852.9	**1.3**
0.458	N/A	**N/A**	N/A	**N/A**	N/A	**N/A**	N/A	**N/A**	863.4	**1.1**	864.2	**1.3**

The level of repeatability, regarding the exhaust thermocouple measurements, was also evaluated based on Table 7.3.2-2, where the individual measurements, together with their arithmetic averages are listed. With respect to the *AM-R* swirler, the variation between the two experimental repeats, across the range of the burner stability envelope was calculated $\approx 11\ ^{o}C$, on average. Similarly, for the cases of *AM-G* and *Machined*, the analogous values were $\approx 3\ ^{o}C$ and $\approx 6\ ^{o}C$, respectively. For the *AM-R* case, which resulted the worst out of the three swirlers, with respect to repeatability, the level of variation between the two experimental repeat is still less than 2% of the measured values, on average. Thus, it was concluded that the level of repeatability was generally acceptable.

Table 7.3.2-2 *Exhaust thermocouple temperature individual measurements and averages for CH_4/H_2 fuel mixtures.*

	Exhaust Thermocouple (°C)								
	AM-R (9 μm)			**AM-G (5 μm)**			**Machined (1 μm)**		
Φ	Repeat 1	Repeat 2	**Average**	Repeat 1	Repeat 2	**Average**	Repeat 1	Repeat 2	**Average**
0.327	812.7	797.3	**805.0**	779.3	781.8	**780.5**	775.4	775.0	**775.2**
0.35	821.3	806.3	**813.8**	788.1	788.2	**788.2**	786.7	783.3	**785.0**
0.40	859.5	847.6	**853.6**	822.7	826.9	**824.8**	812.2	821.3	**816.8**
0.44	886.9	879.4	**883.2**	856.9	860.1	**858.5**	859.3	853.6	**856.5**
0.45	892.1	886.0	**889.1**	857.7	864.5	**861.1**	862.8	852.9	**857.8**
0.458	N/A	N/A	**N/A**	N/A	N/A	**N/A**	863.4	864.2	**863.4**

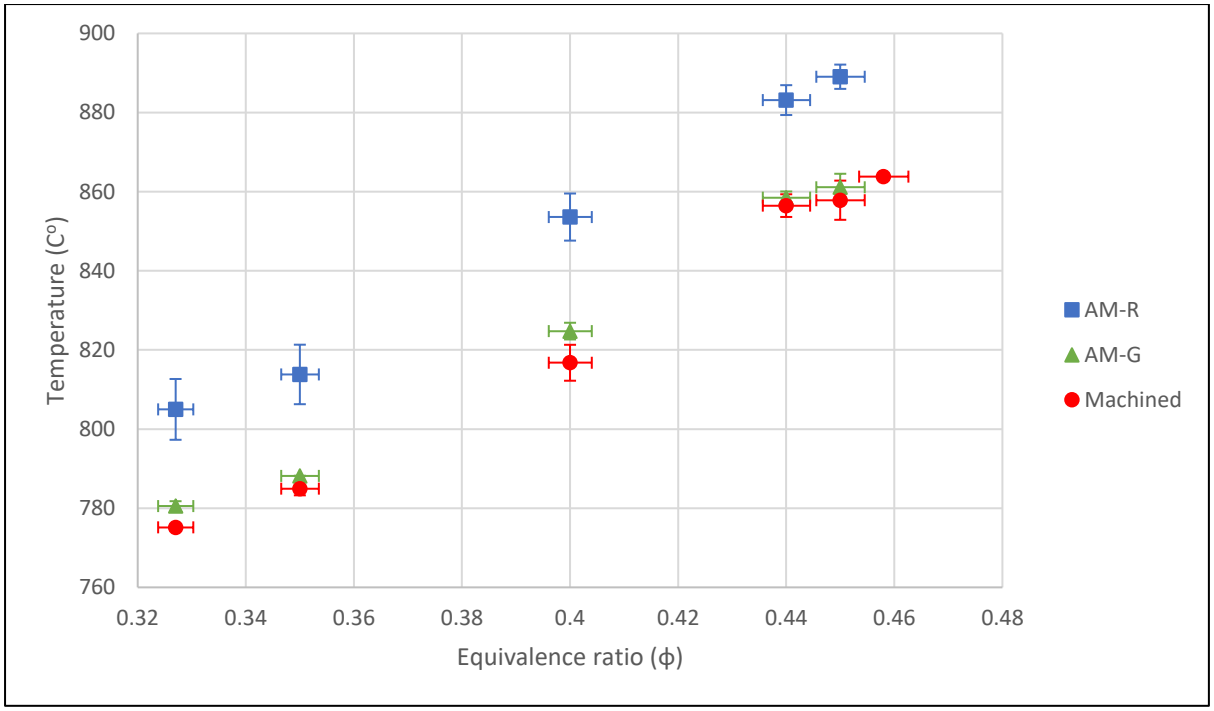

Figure 7.3.2-1 *Average exhaust thermocouple temperature indicating the level of repeatability for CH_4/H_2 fuel mixtures.*

As the level of repeatability was high, the exhaust thermocouple average temperatures were extracted (Table 7.3.2-2) and plotted in Figure 7.3.2-1. Vertical error-bars are used to visual the deviation between the two experimental repeats. It is apparent from the figure that due to the low range of deviation, significant trends concerning the effect of surface roughness on exhaust thermocouple average temperature can be extracted. Similar to the previous experimental investigation of 100% CH_4 and 100% H_2 combustion, the recorded temperatures increased with increasing equivalence ratio, due to the higher flame temperature. Compared to pure H_2 case, a modest increase of ≈11% was noted for the exhaust thermocouple temperatures, across the burner stability envelope. This was attributed to the wider burner stability envelope of CH_4/H_2 operation and the increased levels of flame radiation. Compared to pure CH_4, the resultant exhaust thermocouple average temperatures of CH_4/H_2 blend were still lower (≈15%), resulting, as previously shown, in lower NO_x emissions, due to leaner equivalence ratio operating window.

With regards to the relative temperature difference between the three swirlers of various surface roughness, the *AM-R* swirler was characterised by higher exhaust thermocouple temperatures across the range of the burner stability envelope. Its relative difference compared to the other two swirlers, which resulted in similar

temperature levels, was $\approx 28.5\ ^{o}C$, on average. For other two swirlers, a small difference of $\approx 4.4\ ^{o}C$, on average, was noted. The range of the relative difference between the three swirlers was found closer to the comparator for the pure H_2 case, rather than for the pure CH_4 one where it was ≈30% higher.

As the horizontal error-bars indicate in Figure 7.3.2-1, the equivalence ratio could deviate by 1%. In addition, the relative difference in inlet plenum temperature for the three swirlers, as presented in Table 7.3.1-2, was $\approx 1.5\ ^{o}C$ on average, with the largest difference being 5.9 ^{o}C. This level of variation in inlet plenum temperature and equivalence ratio was too small to result in an average difference of $\approx 28.5\ ^{o}C$ in the exhaust thermocouple. This was further supported through the following comparison in Table 7.3.2-3. Specifically for the first experimental repeat of the $\varphi = 0.40$ case, the relative difference in terms of exhaust thermocouple temperature between the *AM-R* swirler and the *Machined* one was calculated at $\approx 47.3\ ^{o}C$. Therefore, to verify that such relative difference in exhaust thermocouple average temperature was not linked to inconsistencies concerning the inlet boundary conditions, in Table 7.3.2-3, the resultant inlet plenum and exhaust thermocouple temperatures for the two swirler cases *(AM-G* and *Machined),* were compared against each other for $\varphi = 0.40$ and $\varphi = 0.45$.

Table 7.3.2-3 *Comparison of inlet and exhaust average temperature readings for φ=0.40 and φ=0.45 for CH_4/H_2 fuel mixtures.*

	φ = 0.40		**φ = 0.45**	
Surface roughness	Inlet Plenum	Exhaust Gas	Inlet Plenum	Exhaust Gas
AM-R (9 μm)	148.0^{o}C	859.5^{o}C	146.8^{o}C	892.1^{o}C
Machined (1 μm)	151.8^{o}C	812.2^{o}C	151.0^{o}C	862.8^{o}C
Difference	**-3.8**^{o}C	**47.3**^{o}C	**-4.2**^{o}C	**29.3**^{o}C

As indicated in Table 7.3.2-3, although the relative difference, in inlet plenum temperature, for the two swirlers was marginally increased between $\varphi = 0.40$ and $\varphi = 0.45$ from -3.8 ^{o}C to -4.2 ^{o}C, the corresponding difference in exhaust thermocouple temperature was significantly reduced from $47.3\ ^{o}C$ to $29.3\ ^{o}C$. Thus, it can be assumed that the effect of the current range of deviation in inlet plenum temperatures has negligible effect on exhaust thermocouple readings, and the relative difference that is recorded does not stem from inlet plenum temperature variations. Additionally, based

on the uncertainty rating of the mass flow controller, the equivalence ratio could only deviate slightly (±1%), which was not enough to alter the temperature of the flame, and thus, to augment the exhaust temperatures. Consequently, under the present conditions, the bulk flow velocity was majorly influenced only from the equivalence ratio, and therefore, was almost identical for the three swirlers under the same equivalence ratio.

Similarly to the pure CH_4 and H_2 cases, it was again hypothesised that the difference in exhaust thermocouple average temperature between the three swirlers, was linked to the change of the stabilised *location* of the flame, as a result of surface roughness. To investigate the validity of this hypothesis, analysis of the OH^* chemiluminescence photography was again utilised. The final Abel results, of the OH^* chemiluminescence data acquisition system corresponding to $\varphi = 0.35$, $\varphi = 0.40$ and $\varphi = 0.44$, are presented in Figure 7.3.2-2. The camera frame rate was set at 4000 Hz, though only the first 2000 frames were used, thus the following OH^* pictures are time-averaged over a period of 0.5 seconds.

Utilising the Abel deconvolution algorithm, the profiles of the flame were revealed quantitatively. Similar to the pure H_2 and the pure CH_4 cases, the flame size was reduced with increased equivalence ratio due to the improved chemical kinetics. It was observed that the dimensions of the flame were significantly altered from $\varphi = 0.35$ to $\varphi = 0.44$. At the leaner equivalence ratio, the flame dimensions were similar to the ones of pure CH_4, whilst for relatively richer equivalence ratio, they were closer to the size of pure H_2 flames. The significant reduction in flame size with increasing equivalence ratio was potentially attributed to the reduction in Reynolds number and increased burning velocities. This combination resulted in reduction in the CRZ size. Similar to the previous cases of 100% H_2 and 100% CH_4 combustion, the flame stabilised closer to the burner nozzle exit as it approached its flashback point and the flame speed was increased.

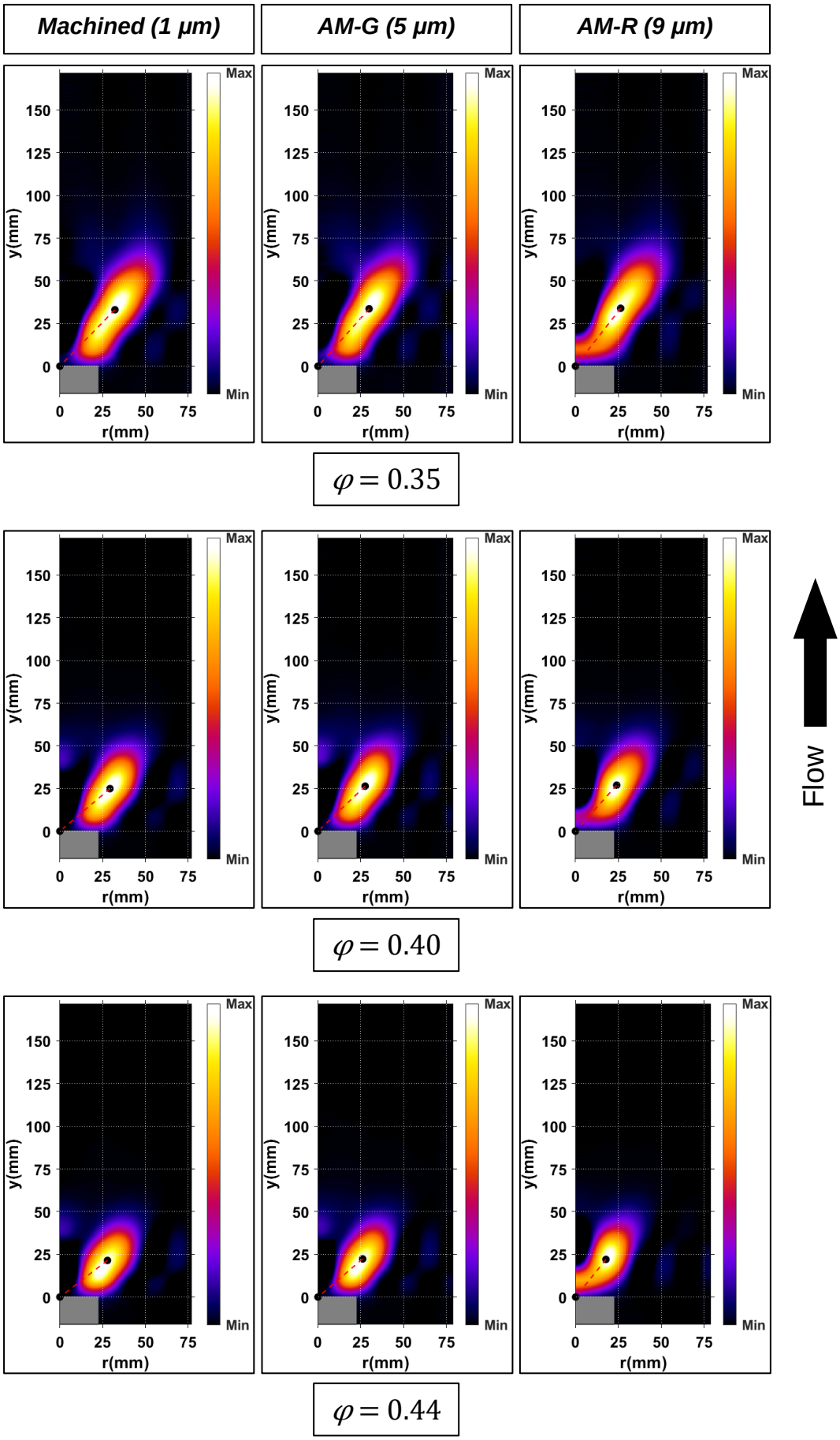

Figure 7.3.2-2 *Deconvoluted OH^* chemiluminescence results for the three swirlers at φ=0.35, φ=0.40 and φ=0.44 for CH_4/H_2 flames.*

To quantify further the effect of surface roughness on flame shape and location, and to estimate the displacement of the flame, the *weighted centroid* function was applied to the corresponding image processing algorithm. As explained in Section 3.2.5.1, via this function the flame centroid could be located based on the binary trace of the Abel deconvoluted image. The resultant point represented the centroid of the flame region based on both the shape of the region and its pixel intensity distribution. Hence, by locating the weighted centroid for each flame, and by comparing it to the swirler with different surface roughness, the change in flame locations as a function of surface roughness was highlighted. The corresponding x and y coordinates of the weighted centroids for the resultant Abel images were plotted in the following Figure 7.3.2-3 across the burner stability envelope, and for the three swirlers of different surface roughness (*Machined, AM-G* and *AM-R*).

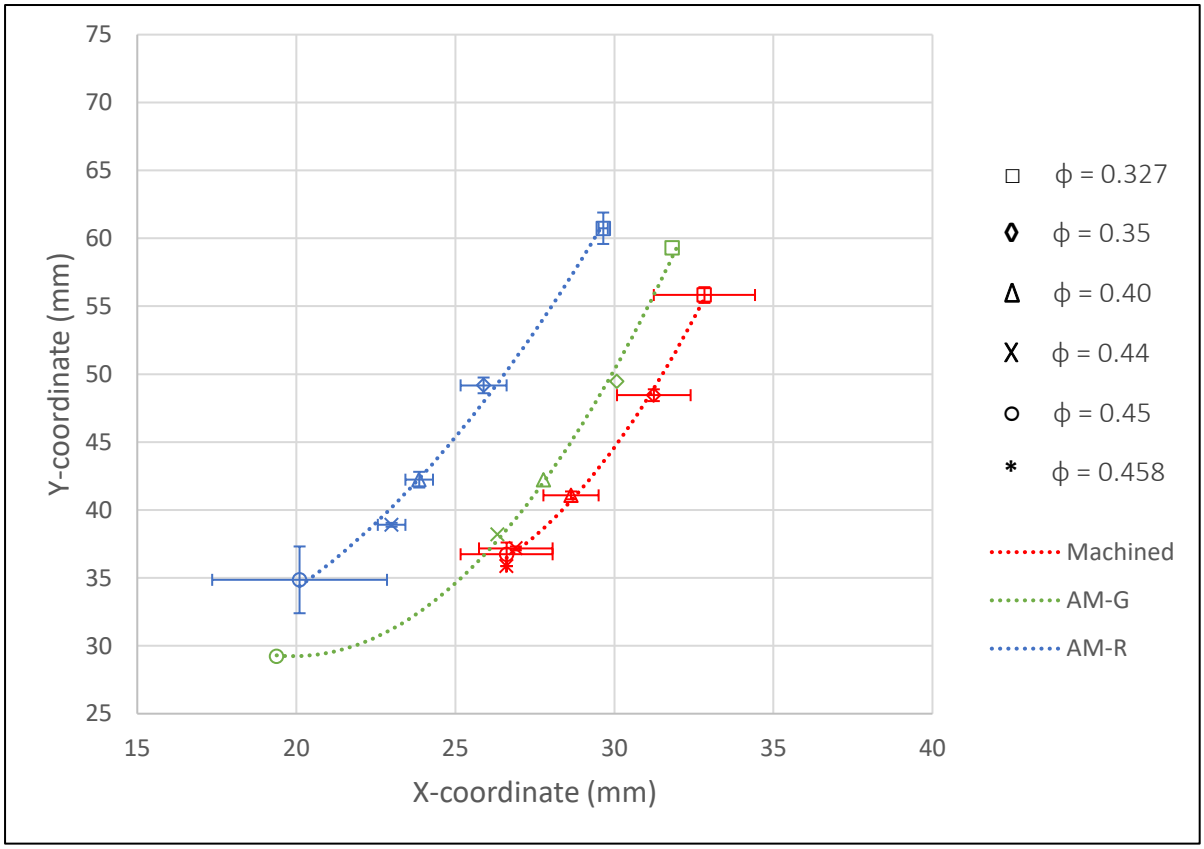

Figure 7.3.2-3 *Flame centroids cartesian coordinates across the investigated equivalence ratio for the Machined (1 μm), AM-G (5 μm) and AM-R (9 μm) swirlers, for CH_4/H_2 fuel mixtures.*

As the air flowrate was reduced, and therefore, the equivalence ratio increased, the flame was displaced closer to the burner nozzle exit, due to the increase in flame speeds and the reduction in bulk flow velocity of the reactants. Thus, across the burner stability envelope, the flame was displaced, on average, by ≈30-20 mm, based on the

swirler case. Specifically, the *AM-G* swirler resulted in noticeably larger displacement range (≈30 mm), compared to the other two. The analysis indicated that for this swirler, the flame stabilisation position before the flashback event, was the closest to the burner exit. The swirler of the highest surface roughness *(AM-R),* resulted in slightly smaller displacement (≈25 mm), from LBO to flashback, whilst the smoothest of the three swirlers *(Machined)*, corresponded to the narrower displacement range (≈22 mm). However, taking into consideration the level of variation between the two experimental repeats, which may be visualised through the vertical and horizontal error-bars, the difference between the *AM-R* and the *Machined* cases, in terms of their displacement, was marginal. In contrast with the CH_4/H_2 blend, both previous fuels showed minimum influence of surface roughness on the reduction of y-coordinates of flame centroid with increasing equivalence ratio. The current set of results indicates a fair influence of surface roughness on the displacement range of the flame in the y-axis. The latter is found to be closer to the pure CH_4 case, in which the respective value was ≈25 mm for all three swirlers.

Moreover, the surface roughness was found to have an even greater influence on the determination of the x-coordinates of the flame centroids. With increased surface roughness, the flame centroids were again radially shifted towards the centreline of the burner. This shift was found higher at leaner equivalence ratios, where the Reynolds number was higher, and was attributed to increased surface roughness to boundary layer thickness ratio. The flame centroids, corresponding to the *AM-R* swirler, were found ≈4 mm closer to the central vertical axis of the burner, compared to those *Machined*. This is in qualitative agreement with the previous results concerning 100% H_2 and 100% CH_4 combustion. It is worth pointing out that the analogous difference for the CH_4 case was also found at ≈4 mm, though, for the CH_4/H_2 case, the horizontal error-bars, and thus the level of measurement inaccuracy, were larger. Consistent with the two previous fuel cases, the flame centroids for the *AM-G* swirler lay in-between the *AM-G* and *Machined*, but closer to the latter.

This potentially explains the marginal differences in exhaust thermocouple average temperatures between these two swirlers. In general, the observation that the flame centroids were shifted radially towards the centreline of the burner with increased surface roughness, was in qualitative agreement with the previous investigation of single fuels. Similarly, as the flame is displaced towards the burner

centreline for the *AM-R* swirler, its peak flame temperature was closer to the exhaust thermocouple, thus explaining the higher temperatures measured. Again, this increase in temperature corresponds only to the single point, in which the exhaust thermocouple is measuring, and should not be confused with the spatially average exhaust gas temperature.

7.4 Summary

The second part of the experimental study regarded the impact of surface roughness on lean premixed (LPM) atmospheric combustion of 100% H_2 and 23%CH_4/77%H_2, at elevated inlet temperature ($150\ ^{o}C$). The aim of this Chapter was to assess the influence of swirler surface roughness and burner characteristics, whilst comparing the resultant combustion against the 100% CH_4 case presented in Chapter 6. The same three swirlers, namely, *Machined* (1 μm)*, AM-G* (5 μm) and *AM-R* (9 μm)*,* were again appraised over a wide range of equivalence ratio. Temperature, NO_x and OH^* chemiluminescence measurements were carried out, while the burner stability envelopes were also identified.

The burner was driven from LBO to full flashback conditions, and the stable operating curves were determined for the three swirlers and the two fuel cases. The investigated scale of surface roughness was found to have no distinctive effect on LBO limits, as all swirler presented the same LBO limit, which was commonly characterised by rapid flame extinction and reignition events. With increased H_2 percentage in fuel mixture, the burner stability envelope was shifted towards leaner equivalence ratio, due to the higher diffusivity, reaction rate and burning velocity. Consequently, compared to CH_4, the LBO was extended by 41% for the CH_4/H_2 blend and 60% for the pure H_2 case. Conversely, the stable operating curve was narrower for increased H_2 percentage in the mixture. Thus, the transition from stable operation to flashback conditions was steeper, suggesting a further challenge for large scale power generation applications utilizing high content H_2 fuels. Although for pure H_2 the flashback limits were identical for the three surface roughness cases, for the CH_4/H_2 blend small differences were noted, though within the range of measuring uncertainty. However, it was concluded that the investigated range of surface roughness had no significant influence on the burner stability envelope under any fuel case.

Concerning the NO_x performance of the burner, for both cases the resultant NO_x emissions, under the same thermal power conditions (25 kW), were significantly lower compared to 100% CH_4 combustion, across the investigated range of equivalence ratio. This was credited to the shift of burner stability envelope towards leaner conditions, which consequently reduced the temperature of the flame and minimised thermal NO_x. For the CH_4/H_2 blend, although the stable operating curve was across richer equivalence ratios compared to pure H_2, the resultant NO_x emissions were found to be within similar to pure H_2 levels (1-2 ppmv). This indicates that although the flame temperature was slightly higher, since the burner stability envelope was shifted to slightly richer equivalence ratios, it was still below the threshold of thermal NO_x production. Thus, CH_4/H_2 combustion, maintained NO_x similar to pure H_2 levels, whilst presenting enhanced stability control due to its wider burner stability envelope. Due to the very low concentration of NO_x emissions, (well below regulatory limits) under both 100% H_2 and 23%CH_4/77%H_2 combustion, the extraction of significant trends with respect to surface roughness was not possible.

The reduced exhaust thermocouple temperatures recorded for the pure H_2 and the CH_4/H_2 blend, indicated that the exhaust gas temperature, and consequently the flame temperature, were in fact lower, compared to pure CH_4, due to leaner combustion conditions. The effect of surface roughness on the exhaust thermocouple temperature was common for the two fuel cases, and qualitatively consistent with the previous CH_4 case. The *AM-R* swirler resulted in distinctively higher exhaust thermocouple temperatures, followed by the *AM-G* and the *Machined*, which in general resulted in similar temperature readings. The significant increase in exhaust thermocouple temperature recorded for the *AM-R* swirler stemmed from its flame position, which was located closer to the centreline. As ascertained from the flames OH^* centroids, at increased surface roughness, the flame position was radially shifted towards the centreline of the burner, which is consistent with the pure CH_4 case. Therefore, the hot gases from the flame were closer to the exhaust thermocouple, which consequently recorded higher temperatures.

These higher temperatures correspond only to the specific experimental measuring position, where the exhaust thermocouple is located, and should not be confused with the spatial averaged temperature value across the diameter of the exhaust. With this explanation, it is not surprising that an increase in temperature at a

single position does not correspond with an increase in NO_x at the exhaust. These flame location trends are fully consistent with the isothermal CFD in Chapter 5, where again increased surface roughness was predicted to radially shift the positive outwards flow towards the centreline of the burner.

In practical terms, under the specific combustion conditions and consistent with the pure CH_4 case, the surface roughness range investigated did not appear to influence flame chemistry, as the three swirlers resulted in similar levels of NO_x emissions. Since, the effect of surface roughness on burner stability envelopes was also found negligible, it was concluded that the combustion performance of swirlers manufactured by additive layers was as good as the traditionally manufactured one. Therefore, the *AM-R* swirler (9 μm), which did not undergo any post-processing activity results in similar combustion performance for all the investigate fuels and fuel blends, to the *AM-G* (5 μm) and the *Machined* (1 μm), which had to undergo post-processing activities to reduce their surface roughness, and thus, they are associated with higher production cost. Additionally, the radially inwards shifting of the flame position for the *AM-R* swirler could potentially be advantageous due to keeping the flame further away from the wall, thus reducing the wall temperature of the combustor.

Chapter 8. Conclusions & Future work

Additive Manufacturing (AM) as an emerging new manufacturing technology, allows for manufacturing of fuel-flexible gas turbine components, of reduced production time and cost, with specific built-in characteristics that can facilitate the utilisation of high-hydrogen content fuels. To efficiently design and fabricate the future gas turbine burners, their surface texture parameters, including surface roughness, should be modelled effectively and empirically appraised with respect to their combustion performance. However, the impact of surface roughness on a 3D CFD analysis of gas turbine burners has to date generally been neglected, as the empirical evidence of surface roughness effects on combustion phenomena is very limited.

This thesis, therefore aimed to gain an understanding, through computational (CFD) and empirical appraisal, on the influence of surface roughness on combustion performance and emissions of an AM combustor utilising high hydrogen-content fuels. The following conclusions and recommendations have been deduced.

8.1 Additive manufacturing (AM) and gas turbine (GT) systems:

With its expanding usage and applications, the AM techniques has also offered unique opportunities for GT OEMs and research institutions to develop, manufacture, and investigate innovative gas turbine components. The new design and fabrication options aim to support and accelerate the transition towards the utilisation of low-carbon fuels in GTs. This requires fuel-flexible, ecologically friendly, and highly efficient combustion systems. The most essential findings are:

8.1.1 AM for Academic combustion research:

- Although academic interest in AM has increased exponentially in the last 15 years, the specific focus on AM for combustion applications has generally remained low.
- Increasing access to SLM machines results in utilisation of AM methods for research across a broad range of applications.
- Low Technology Readiness Level (TRL) components are fabricated by AM to deliver fundamental combustion research.
- The fabrication of high TRL components is currently limited, though, supported by significant number of investments.

8.1.2 AM for micro gas turbines (MGTs):

- The size of MGTs is regarded ideal for AM techniques, enabling multiple component integration and fabrication of multifunction structures, whilst promoting freedom of design, material savings and reduced production tooling cost.
- Utilising AM for the fabrication of geometrically optimised complex recuperators out of high-temperature metals, the efficiency of MGTs is enhanced due to advanced heat transfer performance.
- The critical challenges that must be addressed for MGTs' essential components include cost of AM equipment and primary resources, consistency, and surface finish.
- Further research must be focused on interaction and development of new metals and alloys, AM process modelling and advanced CFD methodologies for surface roughness and flow interaction in microchannels.

8.1.3 AM for industrial gas turbines (GTs):

- The majority of GT OEMs invest in, produce, and test additively fabricated injectors, fuel/air mixers and cooling components.
- OEMs already utilise AM for developing on-engine combustion parts to combust high hydrogen (H_2) fuels.
- AM technology is regarded essential for improving efficiency in production of GT components.
- The critical challenges that must be overcome include "out of the box" thinking combined with in-depth AM design knowledge and innovative cooling and mixing designs to promote low-carbon fuels utilisation.
- Future research is likely to comprise new materials, extension of AM components life, and training in AM design and digital tools to enable faster development of GT parts.

8.2 Experimental facilities:

During the experimental investigation undertaken exclusively at Cardiff University's Gas Turbine Research Centre, new facilities were developed, commissioned, and utilised, whilst new diagnostic apparatus was installed, to deliver the relevant research objectives.

- A new atmospheric pressure generic swirl burner (APGSB) was manufactured at Cardiff University through conventional manufacturing methods, giving attention to maintaining the similar bulk geometric characteristics with the HPGSB-2 burner, and assembled in vertical orientation at GTRC. However, when compared to HPGSB-2, the new burner offers practicability, permitting safely-managed and time-saving burner maintenance, operations and disassembly with full optical access to the flame, and option for retrofitting to existing GTRC facilities.
- Other than the new optical access APGSB and the investigated swirlers of constant swirl number ($S_N = 0.8$) and different surface roughness, the new experimental rig was integrated with diagnostic system comprising high-precision Coriolis mass-flow controllers, shielded *k-type* thermocouples positions in various locations around the system, an inlet air preheater, a water-cooled probe for exhaust gas measurements and a high-speed chemiluminescence photography suite.

8.3 Methodologies:

A set of numerical, empirical and image processing methodologies have been developed and implemented to computationally evaluate the influence of surface roughness on the isothermal swirling flow field, and to empirically observe and quantify the impact of surface roughness on burner characteristics and combustion performance. These methods include:

- A computationally inexpensive numerical methodology, developed and implemented to evaluate the influence of surface roughness on isothermal swirling flow, and to assess its predictive capabilities based on the findings of a recent experimental campaign. With this method, a RANS k-epsilon (k-ε) two-layer turbulence model was adopted with the mesh requirements concerning the appropriate use of wall functions. The effect of surface roughness on mean flow quantities was modelled using a roughness parameter, which was a function of the equivalent sand-grain roughness.
- An empirical method for appraising the effect of surface roughness on the combustion performance and burner characteristics of a generic swirl burner utilising traditional, low and zero carbon fuels. Maintaining a constant fuel flowrate, whilst gradually varying the inlet air, the impact of surface roughness

on lean blow-off (LBO) and flashback limits, was observed. Non-intrusive diagnostic tools, such as high-speed OH^* chemiluminescence photography was utilised, while NO_x emissions and temperature measurements were collected.

- A novel image processing technique was developed and applied to each OH^* chemiluminescence (CL) data set to quantify the effect of surface roughness on flame shape and location. An Abel deconvolution algorithm was primarily employed to reconstruct the 2D radial distribution of the chemiluminescence intensity along the flame. Subsequently, an image processing MATLAB function was utilised on each binary Abel deconvoluted image to find flame centre coordinates, based on both pixel value and locations, revealing the effect of surface roughness on flame displacement.
- During the development of the OH^* CL image processing technique, an optical medium-related effect, which resulted in an amplified pixels intensity distribution in the left side of the 2D images, was also reported.

8.4 Evaluation of CFD predictive capabilities and numerical investigation of surface roughness effects:

Surface roughness is an important design parameter that critically influences gas turbine operation. The AM technology enables the integration of surface finish during the fabrication stage of components, with reduced cost and time associated with post-processing tasks. Subsequently, to allow CFD to serve as a powerful design tool for AM derived parts, methodologies effectively capturing the influence of surface roughness on relevant to practical conditions flows, are required. Although flows over rough surfaces have been extensively investigated using computational fluid dynamic approaches with several numerical models developed, most research studies have been limited to simplified geometries. Few studies have incorporated surface roughness into their numerical models, and investigated its effect on flow fields of full-scale gas turbine burners. To enable the vast adoption of CFD as a design tool for AM components in the power generation industry, computationally efficient and inexpensive methodologies, which account for the effect of surface roughness using full burner geometry, must be developed.

Consequently, the first objective of the present thesis was to evaluate the predictive capabilities of a computationally inexpensive methodology for the investigation of the effects of surface roughness on isothermal swirling flow, for the full 3D geometry of an

industrial AM burner. The accuracy of the employed method was validated by comparing the predicted axial velocity data with the experimental data collected at 5 mm above the burner. The following conclusions can be drawn:

- The computational continua employed utilised the RANS realisable k-ε turbulence model with the wall function approach, to model the effects of surface roughness. Hence, the near-wall volume resolution, for the surfaces where roughness was applied, was reduced, using larger cells of y^+ values of approximately 30.
- The predictive capabilities of the model were evaluated based on the two predominant effects of surface roughness, which were the inwards shifting of the positive outwards flow (POF) and the decrease in peak axial velocities.
- The predictive performance of the computational method utilised was significantly affected by the equivalent sand-grain roughness value, and consequently, by the employed roughness conversion algorithm.
- Using the correct equivalent sand-grain roughness values, the shifting of POF was effectively captured and correlated very well with the experimental results, proving the efficiency of the computational methodology employed. By contrast, the decrease in peak axial velocities was significantly underpredicted.
- With increasing surface roughness, the turbulent boundary became more susceptible to separation. The adverse pressure gradient (APG) generated, due to the geometry of the burner, near the turbulent boundary layer regions, eventually displaced the turbulent boundary layer and thus the POF towards the centreline of the burner. This observation agrees well with similar observations in the literature [66, 80, 102].
- Imprecise definition of the boundary conditions due to the lack of experimental data, the simplification of the experimental geometry and the assumption of adiabatic heat transfer, constitute potential sources of physical approximation errors that reduce further the agreement between CFD and experimental results.

8.5 Empirical investigation of surface roughness effects:

The growth of AM market has accelerated the fabrication of innovative GT components including combustors. Both academia and OEMs research and invest

in AM to facilitate the development of GT systems of enhanced fuel flexibility. Other than environmental, operation, and economic advantages, AM offers "manufacturable" surface finish, minimising the cost associated with post-processing tasks, while reducing lead-time. Moreover, aerodynamic and heat transfer related performance improvements due to novel, accurate and highly controllable surface finishes, may be also achieved. However, the influence of surface roughness on burner characteristics and combustion performance is significantly overlooked.

Therefore, the present thesis empirically appraised the impact of surface roughness on lean premixed (LPM) combustion performance and burner characteristics of a generic swirl burner utilising traditional (100% CH_4), low-carbon (23%$_{vol}$$CH_4$/77%$_{vol}$$H_2$), and zero-carbon (100% H_2) fuels, under ambient pressure and elevated inlet temperature ($150\ ^{o}C$) conditions, relevant to practical burner designs. To appraise the effect of surface roughness, the performance of a conventionally manufactured *Machined* swirler ($R_a = 1\ \mu m$), was compared against an AM swirler (*AM-R*) that had *not* undergone any post processing ($R_a = 9\ \mu m$), and an AM swirler (*AM-G*) that was subject manual grit-blasting post-processing, thus resulting in reduced surface roughness ($R_a = 5\ \mu m$). The most significant findings of the empirical investigation are summarised as follows:

8.5.1 Burner stability envelope:

- Although 100% H_2 LPM combustion resulted in narrower burner stability envelopes, subsequently reducing the operational flexibility, and increasing flashback and LBO propensity, it was demonstrated that 100%H_2 LPM stable combustion is achievable.
- The three swirlers of different surface roughness, yielded identical LBO limits. The LBO limit was extended by 41% for 23%$_{vol}$$CH_4$/77%$_{vol}$$H_2$ and 60% for 100% H_2 combustion, compared to 100% CH_4.
- For the 100% CH_4 case, the flashback limits for the three swirlers were identical. The same observation was reported for the 100% H_2 case. For the CH_4/H_2 fuel blend case, small differences were noted, though within the range of measuring uncertainty.
- The range of surface roughness (1-9 μm) investigated had no significant influence on the burner stability envelope for any of the fuel types studied.

8.5.2 NO_x emissions:

- With increasing percentages of H_2 in the mixture, NO_x emissions were reducing due to the lower flame temperatures, driven by operating at leaner equivalence ratios. For 100% H_2 and 23%$_{vol}CH_4$/77%$_{vol}H_2$, NO_x emissions were extremely low (0.5-2 ppmv) and within the uncertainty range of the measuring equipment. For this reason, the extraction of significant trends with respect to the influence of surface roughness on NO_x emissions, was prevented.
- For the 100% CH_4 case, the highest values of NO_x emissions (≈50 ppmv) were recorded when stoichiometric conditions were approached. However, the differences in NO_x emissions due to surface roughness still remained negligible and within the range of measuring uncertainty.
- Although the negligible differences in NO_x and relatively high measuring uncertainties prevented the extraction of significant trends with respect to the effect of surface roughness on NO_x formation, it was demonstrated that combustion of pure H_2 and CH_4/H_2 blend, of H_2-rich fuel, is achievable and within statutory limits for NO_x.

8.5.3 Exhaust thermocouple temperatures & OH^* chemiluminescence:

- A single point measuring thermocouple was placed at the centreline of the exhaust section of the burner to measure the temperature of the hot product gas stream.
- The *AM-R* swirler of the higher surface roughness (9 μm), systematically resulted in higher exhaust temperatures, followed by the *AM-G* (5 μm) and the *Machined* (1 μm), which were within similar levels. This trend was consistent under any fuel type, and unexpected under the conditions deployed.
- To explain this observation, the Abel deconvoluted images from the OH^* chemiluminescence measurements were re-evaluated and the centroids of the OH^* binary trace of the deconvoluted flame images were quantified in cartesian coordinates.
- It was found that with increasing surface roughness, the flame centroid locations, and hence, the flame, were shifted inwards and stabilised closer to the centreline of the burner, yielding high exhaust temperature readings for the *AM-R* case.

- This observation was further supported by the numerical data extracted from the isothermal CFD simulations. Well-matched numerical and experimental data increases the confidence level of the reported results.
- This temperature increase corresponds only to the measuring point location and should not be confused with the spatially averaged temperature value across the diameter of the exhaust. The latter was expected to be similar for the three swirlers, since NO_x emissions were within similar levels.
- The inwards shifting of the flame towards the centreline of the burner could potentially have a beneficial impact on the combustor structure, by keeping the flame further away from the wall, thus reducing the cooling requirements.

Overall, the range of surface roughness investigated in the present study (1-9 μm), did not significantly improve the burner stability envelope characteristics or the NO_x emissions performance of the burner, under any fuel type. Consequently, the associated post processing activities for the reduction of surface roughness across the range 1 μm – 9 μm, should not be considered essential. The “raw”, AM fabricated *AM-R* swirler (9 μm), performed just as well as the conventionally *Machined* swirler (1 μm) and the AM fabricated *AM-G* (5 μm) one, which had undergone post-processing to reduce their surface roughness, thus resulting in higher production cost. This cost can be minimised by using the *AM-R* swirler.

8.6 Future work and recommendations

As a result of the present thesis, several recommendations for further study, categorised in numerical and empirical related ones, can be made:

8.6.1 Numerical related recommendations for further study:

- Expansion of the employed isothermal simulation to combustion, maintaining the same mesh strategy concerning the y^+ criterion, to appraise the predictive capabilities of the new model with respect to the effect of surface roughness, based on the NO_x emissions and the flame position results obtained from this empirical investigation.
- Utilisation of the several thermocouple measurements around the experimental rig as inputs to the computational model, to estimate the heat loss performance of the burner, with a view to improving the numerical combustion predictions.

- Assessing the predictive capacity of the model at elevated pressures, while maintaining the same Reynolds number, and thus, the same mesh and y^+ values.
- Development of a set of simulations where roughness is isolated to a specific region of the burner, with a view to identifying in which region the influence of roughness is dominant. Subsequently, roughness can be applied only on specific regions of the surface (i.e. at the leading edge of the vane and not on the whole vane surface).

8.6.2 Empirical related recommendations for further study:

- Development and appraisal of burner characteristic and combustion performance of AM swirlers of higher surface roughness or roughness of different pattern (such as riblets or sharkskin geometry), under the same conditions.
- Development of an AM swirler with a modular structure, for which the vanes and the nozzle sections can be replaced and mixed with analogous components of different roughness values, with a view to providing an optimised combination of surface roughness around the swirler. The ideal combination could be determined prior to testing through CFD simulations. Additionally, if a modular swirler is utilised, a transparent nozzle could replace the current nozzle, to investigate the flashback mechanisms in detail for pure H_2 and CH_4/H_2 blends of high H_2 content.
- Using a combination of high-speed PIV and OH^* CL, to investigate the turbulent flow-surface roughness interaction. The boundary condition parameters including turbulence intensity and velocity profiles will be accurately captured for different flow conditions to limit the physical approximation errors. Additionally, the pressure could be scaled up with mass flowrates, to maintain a constant Reynolds number and to investigate the effect of elevated pressure on surface roughness/turbulent flow interaction, as well as on combustion performance and burner characteristics of H_2 and CH_4/H_2 blends of high H_2 content.
- To map the radial distribution of the exhaust gas temperature, a series of thermocouples will be placed at different radial positions across the exhaust section.

- To manufacture and deploy a new calibration target for OH^* CL calibration, with a view to quantify the optical medium-related effect, reported for OH^* CL measurements.

References

1. Ritchie, H., Roser, M., Rosado, P.: Energy, https://ourworldindata.org/energy
2. BP: BP Statistical Review of World Energy 2022,(71st edition). [online] London: BP Statistical Review of World Energy. 1–60 (2022)
3. Smil, V.: Energy Transitions: Global and National Perspectives. Praeger (2017)
4. EPA: Air Pollution Emissions Overview, https://www3.epa.gov/airquality/emissns.html
5. Lefebvre, A.H., Ballal, D.R.: Gas Turbine Combustion. CRC Press (2010)
6. Law, C.K.: Combustion Physics. Cambridge University Press (2006)
7. EPA: Overview of Greenhouse Gases, https://www.epa.gov/ghgemissions/overview-greenhouse-gases
8. European Political Strategy Centre: 10 Trends Reshaping Climate and Energy. https://op.europa.eu/en/publication-detail/-/publication/a6014988-10d2-11ea-8c1f-01aa75ed71a1/language-en (2018)
9. Parray, J.A., Filho, W.L.: Climate Change and Microbiome Dynamics. Carbon Cycle Feedbacks. Springer (2023)
10. Foulquie, M.: The energy trilemma comes back to bite, https://eutc.org/the-energy-trilemma-comes-back-to-bite/
11. Liu, H., Khan, I., Zakari, A., Alharthi, M.: Roles of trilemma in the world energy sector and transition towards sustainable energy: A study of economic growth and the environment. Energy Policy. 170, 113238 (2022). https://doi.org/10.1016/j.enpol.2022.113238
12. Swart, R., Raes, F.: Making integration of adaptation and mitigation work: Mainstreaming into sustainable development policies? Climate Policy. 7, 288–303 (2007). https://doi.org/10.1080/14693062.2007.9685657
13. Yue, M., Lambert, H., Pahon, E., Roche, R., Jemei, S., Hissel, D.: Hydrogen energy systems: A critical review of technologies, applications, trends and challenges. Renewable and Sustainable Energy Reviews. 146, 111180 (2021). https://doi.org/10.1016/j.rser.2021.111180
14. Wulf, C., Linßen, J., Zapp, P.: Review of power-to-gas projects in Europe. Energy Procedia. 155, 367–378 (2018). https://doi.org/10.1016/j.egypro.2018.11.041
15. Tlili, O., Mansilla, C., Frimat, D., Perez, Y.: Hydrogen market penetration feasibility assessment: Mobility and natural gas markets in the US, Europe, China and Japan. Int J Hydrogen Energy. 44, 16048–16068 (2019). https://doi.org/10.1016/j.ijhydene.2019.04.226
16. Bmp-greengas: Key technology – power-to-gas, https://www.bmp-greengas.com/knowledge/key-technology-power-to-gas/
17. I.E.A: The Future of Hydrogen - Seizing today's opportunities. (2019). https://www.iea.org/reports/the-future-of-hydrogen

18. Pivovar, B.: H2 at Scale: Deeply Decarbonizing Our Energy System. (2016). https://www.hydrogen.energy.gov/pdfs/htac_apr16_10_pivovar.pdf

19. ETN Global: HYDROGEN GAS TURBINES. 28. (2020). https://etn.global/wp-content/uploads/2020/01/ETN-Hydrogen-Gas-Turbines-report.pdf

20. Tang, C., Zhang, Y., Huang, Z.: Progress in combustion investigations of hydrogen enriched hydrocarbons. Renewable and Sustainable Energy Reviews. 30, 195–216 (2014). https://doi.org/10.1016/j.rser.2013.10.005

21. National Academies of Sciences, Engineering, and Medicine, .: Advanced Technologies for Gas Turbines. The National Academies Press., Washington, DC (2020)

22. Ngo, T.D., Kashani, A., Imbalzano, G., Nguyen, K.T.Q., Hui, D.: Additive manufacturing (3D printing): A review of materials, methods, applications and challenges. Compos B Eng. 143, 172–196 (2018). https://doi.org/10.1016/j.compositesb.2018.02.012

23. Runyon, J., Psomoglou, I., Kahraman, R., Jones, A.: Additive Manufacture and the Gas Turbine Combustor: Challenges and Opportunities To Enable Low-Carbon Fuel Flexibility. Gas turbines in a carbon-neutral society 10th International Gas Turbine Conference. 1–17 (2021)

24. CFM Internation: The LEAP Engine, https://www.cfmaeroengines.com/engines/leap/

25. Goldmeer, J.: Power to Gas: Hydrogen for power generation. General Electric Company. 19 (2019). https://www.ge.com/content/dam/gepower/global/en_US/documents/fuel-flexibility/GEA33861%20Power%20to%20Gas%20-%20Hydrogen%20for%20Power%20Generation.pdf

26. Sher, D.: 'AM2020, Baker Hughes looks to advance additive manufacturing for sustainable energy production,' https://www.3dprintingmedia.network/baker-hughes- am2020/

27. York, W., Hughes, M., Berry, J., Russell, T., Lau, Y.C., Liu, S., Arnett, M.D., Peck, A., Tralshawala, N., Benjamin, M., Iduate, M., Kittleson, J., Garcia-, A., Delvaux, J., Casanova, F., Lacy, B., Brzek, B., Palafox, P., Ding, B., Badding, B., Mcduffie, D.: Advanced IGCC/Hydrogen Gas Turbine Development (Final Technical Report of US Department of Energy). 1–183, DE-FC26-05NT42643 (2015)

28. Fu, W., Haberland, C., Klapdor, E.V., Rule, D., Piegert, S.: STREAMLINED FRAMEWORKS FOR ADVANCING METAL BASED ADDITIVE MANUFACTURING TECHNOLOGIES IN GAS TURBINE INDUSTRY. In: Proceedings of the 1st Global Power and Propulsion Forum. , Zurich, Switzerland (2017)

29. Runyon, J., Giles, A., Marsh, R., Pugh, D., Goktepe, B., Morris, S., Pugh, D., Bowen, P., Steven, M.: Characterization of ALM Swirl Burner Surface Roughness and Its Effects on Flame Stability Using High-Speed Diagnostics. In: Proceedings of the ASME Turbo Expo. pp. 1–13 (2019)

30. Giuliani, F., Paulitsch, N., Cozzi, D., Görtler, M., Andracher, L.: An assessment on the benefits of additive manufacturing regarding new swirler geometries for gas turbine burners. Proceedings of the ASME Turbo Expo. 4A-2018, 1–12 (2018). https://doi.org/10.1115/GT201875165

31. Bons, J.P., McClain, S.T., Wang, Z.J., Chi, X., Shih, T.I.: A comparison of approximate versus exact geometrical representations of roughness for CFD calculations of cf and St. J Turbomach. 130, (2008). https://doi.org/10.1115/1.2752190

32. Mumtaz, K.A., Hopkinson, N.: Selective Laser Melting of thin wall parts using pulse shaping. J Mater Process Technol. 210, 279–287 (2010). https://doi.org/10.1016/j.jmatprotec.2009.09.011

33. Darcy, H.: Recherches Experimentales Relatives au Mouvement de l'eau dans les Tuyaux (Experimental Research Relating to the Movement of Water in Pipes). , Paris (1857)

34. Fanning, J.T.: A treatise on hydraulic and water supply engineering. (1886)

35. Zhang, Q., Ligrani, P.M.: Aerodynamic losses of a cambered turbine vane: Influences of surface roughness and freestream turbulence intensity. J Turbomach. 128, 536–546 (2006). https://doi.org/10.1115/1.2185125

36. Bons, J.P.: A review of surface roughness effects in gas turbines. J Turbomach. 132, 1–16 (2010). https://doi.org/10.1115/1.3066315

37. Hummel, F., Lötzerich, M., Cardamone, P., Fottner, L.: Surface roughness effects on turbine blade aerodynamics. J Turbomach. 127, 453–461 (2005). https://doi.org/10.1115/1.1860377

38. Zhang, W., Melcher, R., Travitzky, N., Bordia, R.K., Greil, P.: Three-dimensional printing of complex-shaped alumina/ glass composites. Adv Eng Mater. 11, 1039–1043 (2009). https://doi.org/10.1002/adem.200900213

39. Bammert, K., Sandstede, H.: Influences of Manufacturing Tolerances and Surface Roughness of Blades on the Performance of Turbines. J Eng Gas Turbine Power. 98, 29–36 (1976)

40. Li, P., Guo, D., Huang, X.: Heat transfer enhancement , entropy generation and temperature uniformity analyses of shark-skin bionic modified microchannel heat sink. Int J Heat Mass Transf. 146, 118846 (2020). https://doi.org/10.1016/j.ijheatmasstransfer.2019.118846

41. Dean, B., Bhushan, B.: Shark-Skin Surfaces for Fluid-Drag Reduction in Turbulent Flow : A Review. (2016). https://doi.org/10.1098/rsta.2010.0201

42. Liu, W., Ni, H., Wang, P., Zhou, Y.: An investigation on the drag reduction performance of bioinspired pipeline surfaces with transverse microgrooves. 24–40 (2020). https://doi.org/10.3762/bjnano.11.3

43. Domel, A.G., Saadat, M., Weaver, J.C., Haj-hariri, H., Bertoldi, K., Lauder, G.: Shark skin-inspired designs that improve aerodynamic performance. 1–9 (2018)

44. Dean, B., Bhushan, B.: Shark-skin surfaces for fluid-drag reduction in turbulent flow : a review. 4775–4806 (2010). https://doi.org/10.1098/rsta.2010.0201

45. Hatem, F.A., Alsaegh, A.S., Al-Faham, M., Valera-Medina, A.: Enhancement flame flashback resistance against CIVB and BLF in swirl burners. Energy Procedia. 142, 1071–1076 (2017). https://doi.org/10.1016/j.egypro.2017.12.358

46. Al-Fahham, M., Amer Hatem, F., Al-Dulami, Z., Medina, A.V., Bigot, S.: Experimental study to enhance swirl burner against boundary layer flashback. Energy Procedia. 142, 1534–1538 (2017). https://doi.org/10.1016/j.egypro.2017.12.604

47. Ramesh, K.N., Sharma, T.K., Prasad, G.A.: Latest Advancements in Heat Transfer Enhancement in the Micro - channel Heat Sinks: A Review. Springer Netherlands (2021)

48. Kadivar, M., Tormey, D., Mcgranaghan, G.: CFD of roughness effects on laminar heat transfer applied to additive manufactured minichannels. Heat and Mass Transfer. (2022). https://doi.org/10.1007/s00231-022-03268-1

49. Soleimani, S., Eckels, S.: review of drag reduction and heat transfer enhancement by riblet surfaces in closed and open channel fl ow. International Journal of Thermofluids. 9, 100053 (2021). https://doi.org/10.1016/j.ijft.2020.100053

50. Sadek Tadros, Dr.A.A., Ritter, Dr.G.W., Drews, C.D., Ryan, D.: Additive Manufacturing of Fuel Injectors. Final Technical Report, EWI. (2017). https://www.osti.gov/biblio/1406179

51. du Plessis, A., Broeckhoven, C., Yadroitsava, I., Yadroitsev, I., Hands, C.H., Kunju, R., Bhate, D.: Beautiful and Functional: A Review of Biomimetic Design in Additive Manufacturing. Addit Manuf. 27, 408–427 (2019). https://doi.org/10.1016/j.addma.2019.03.033

52. Gebisa, A.W., Lemu, H.G.: Additive manufacturing for the manufacture of gas turbine engine components: Literature review and future perspectives. Proceedings of the ASME Turbo Expo. 6, 1–10 (2018). https://doi.org/10.1115/GT2018-76686

53. Al-fahham, M.A.H.: A modelling and experimental study to reduce boundary layer flashback with microstructure. PhD Thesis - Cardiff University. 18, 273–288 (2017)

54. Maeda, S., Fujisawa, M., Ienaga, S., Hirahara, K., Obara, T.: Effect of sandpaper-like small wall roughness on deflagration-to-detonation transition in a hydrogen-oxygen mixture. Proceedings of the Combustion Institute. 37, 3609–3616 (2019). https://doi.org/10.1016/j.proci.2018.07.119

55. Kadivar, M., Tormey, D., McGranaghan, G.: A review on turbulent flow over rough surfaces: Fundamentals and theories. International Journal of Thermofluids. 10, 100077 (2021). https://doi.org/10.1016/j.ijft.2021.100077

56. Kapsis, M., He, L., Li, Y.S., Valero, O., Wells, R., Krishnababu, S., Gupta, G., Kapat, J., Schaenzer, M.: Multiscale Parallelized Computational Fluid Dynamics Modeling Toward Resolving Manufacturable Roughness. J Eng Gas Turbine Power. 142, (2020). https://doi.org/10.1115/1.4045481

57. Schlichting, H., Gersten, K.: Boundary Layer Theory 9th Edition. Springer (2017)

58. Wilcox, D.C.: Turbulence Modelling for CFD 3rd Edition. D C W Industries (2006)

59. Demirel, Y.K., Khorasanchi, M., Turan, O., Incecik, A., Schultz, M.P.: A CFD model for the frictional resistance prediction of antifouling coatings. Ocean Engineering. 89, 21–31 (2014). https://doi.org/10.1016/j.oceaneng.2014.07.017

60. Huang, H., Sun, T., Zhang, G., Liu, M., Zhou, B.: The effects of rough surfaces on heat transfer and flow structures for turbulent round jet impingement. International Journal of Thermal Sciences. 166, 106982 (2021). https://doi.org/10.1016/j.ijthermalsci.2021.106982

61. SAKİN, A., KARAGÖZ, İ.: Numerical Investigation Of Surface Roughness Effects On The Flow Field In A Swirl Flow. Uludağ University Journal of The Faculty of Engineering. 19, 1 (2014). https://doi.org/10.17482/uujfe.47749

62. Stripf, M., Schulz, A., Bauer, H.J.: Modeling of rough-wall boundary layer transition and heat transfer on turbine airfoils. J Turbomach. 130, (2008). https://doi.org/10.1115/1.2750675

63. Wang, Z.J., Chi, X., Shih, T., Bons, J.: Direct Simulation of Surface Roughness Effects with a RANS and DES Approach on Viscous Adaptive Cartesian Grids. 1–12 (2012). https://doi.org/10.2514/6.2004-2420

64. Martin, S., Bhushan, B.: Fluid flow analysis of a shark-inspired microstructure. J Fluid Mech. 756, 5–29 (2014). https://doi.org/10.1017/jfm.2014.447

65. Martin, S., Bhushan, B.: Modeling and optimization of shark-inspired riblet geometries for low drag applications. J Colloid Interface Sci. 474, 206–215 (2016). https://doi.org/10.1016/j.jcis.2016.04.019

66. Wu, W., Piomelli, U.: Effects of surface roughness on a separating turbulent boundary layer. J Fluid Mech. 841, 552–580 (2018). https://doi.org/10.1017/jfm.2018.101

67. Napoli, E., Armenio, V., de Marchis, M.: The effect of the slope of irregularly distributed roughness elements on turbulent wall-bounded flows. J Fluid Mech. 613, 385–394 (2008). https://doi.org/10.1017/S0022112008003571

68. Okabayashi, K., Hirai, K., Takeuchi, S., Kajishima, T.: Direct numerical simulation of turbulent flow above zigzag riblets. AIP Adv. 8, (2018). https://doi.org/10.1063/1.5049714

69. Kuwata, Y., Kawaguchi, Y.: Direct numerical simulation of turbulence over systematically varied irregular rough surfaces. J Fluid Mech. 862, 781–815 (2019). https://doi.org/10.1017/jfm.2018.953

70. Croce, G., D'agaro, P., Nonino, C.: Three-dimensional roughness effect on microchannel heat transfer and pressure drop. Int J Heat Mass Transf. 50, 5249–5259 (2007). https://doi.org/10.1016/j.ijheatmasstransfer.2007.06.021

71. Rawool, A.S., Mitra, S.K., Kandlikar, S.G.: Numerical simulation of flow through microchannels with designed roughness. Microfluid Nanofluidics. 2, 215–221 (2006). https://doi.org/10.1007/s10404-005-0064-5

72. Kharati-Koopaee, M., Zare, M.: Effect of aligned and offset roughness patterns on the fluid flow and heat transfer within microchannels consist of sinusoidal structured roughness. International Journal of Thermal Sciences. 90, 9–23 (2015). https://doi.org/10.1016/j.ijthermalsci.2014.11.031

73. Ansari, M.Q., Zhou, G.: Influence of structured surface roughness peaks on flow and heat transfer performances of micro- and mini-channels. International Communications in Heat and Mass Transfer. 110, 104428 (2020). https://doi.org/10.1016/j.icheatmasstransfer.2019.104428

74. Randles, A., Frakes, D.H., Leopold, J.A.: Computational Fluid Dynamics and Additive Manufacturing to Diagnose and Treat Cardiovascular Disease. Trends Biotechnol. 1049–1061 (2017). https://doi.org/10.1016/j.tibtech.2017.08.008.Computational

75. Reynolds, O.: An experimental investigation of the circumstances which determine whether the motion of water shall be direct or sinuous, and of the law of resistance in parallel channels. Philos Trans R Soc Lond. 174, 935–982 (1883). https://doi.org/10.1098/rstl.1883.0029

76. Nikuradse, J.: Laws of Flow in Rough Pipes. NACA (1950)

77. Prandtl, L.: Motion of fluids with very low viscosity. Houille Blance. 28, 75–82 (1903)

78. Blasius, H.: The boundary layers in fluids with little friction. NACA (1908)

79. Velocity boundary layer, https://www.nuclear-power.com/nuclear-engineering/fluid-dynamics/boundary-layer/velocity-boundary-layer-thermal-boundary-layer/

80. Song, S.J., Jeong, H.: Surface Roughness Impact on Boundary Layer Transition and Loss Mechanisms over a Flat-Plate under a Low-Pressure Turbine Pressure Gradient. J Turbomach. 144, 1–13 (2022). https://doi.org/10.1115/1.4051937

81. Roberts, S.K., Yaras, M.I.: Boundary-layer transition affected by surface roughness and free-stream turbulence. Journal of Fluids Engineering, Transactions of the ASME. 127, 449–457 (2005). https://doi.org/10.1115/1.1906266

82. Bechert, D.W., Bruse, M., Hage, W.: Experiments with three-dimensional riblets as an idealized model of shark skin. 28, 403–412 (2000)

83. TANI, I.: Drag Reduction by Riblet Viewed as Roughness Problem. Proceedings of the Japan Academy, Series B. 64, 4 (1988). https://doi.org/https://doi.org/10.2183/pjab.64.21

84. Jiménez, J.: Turbulent flows over rough walls. Annu Rev Fluid Mech. 36, 173–196 (2004). https://doi.org/10.1146/annurev.fluid.36.050802.122103

85. COLEBROOK, C.F., BLENCH, T., CHATLEY, H., ESSEX, E.H., FINNIECOME, J.R., LACEY, G., WILLIAMSON, J., MACDONALD, G.G.: Correspondence. Turbulent Flow in Pipes, With Particular Reference To the Transition Region Between the Smooth and Rough Pipe Laws. (Includes Plates). Journal of the Institution of Civil Engineers. 12, 393–422 (1939). https://doi.org/10.1680/ijoti.1939.14509

86. Moody, F.L.: Friction Factor for Pipe Flow. Transactions of the American Society of Mechanical Engineers, 66, 671-681. (1944)

87. Gregory, J.M., McEnery, J.A.: Process-based friction factor for pipe flow. Open J. Fluid Dyn. 219–230 (2017). https://doi.org/10.4236/ojfd.2017.72015.

88. Flack, K., Schultz, M.: Review of Hydraulic Roughness Scales in the Fully Rough Regime. Journal of Fluids Engineering-transactions of The Asme. 132, 41203 (2010). https://doi.org/10.1115/1.4001492

89. Brown, G.O.: The history of the Darcy-Weisbach equation for pipe flow resistance. Proceedings of the Environmental and Water Resources History. 40650, 34–43 (2002). https://doi.org/10.1061/40650(2003)4

90. LaViolette, M.: On the history, science, and technology included in the Moody diagram. J. Fluids Eng. Trans. ASME. (2017). https://doi.org/10.1115/1.4035116.

91. Taylor, J.B., Carrano, A.L., Kandlikar, S.G.: Characterization of the effect of surface roughness and texture on fluid flow - Past, present, and future. Proceedings of the 3rd International Conference on Microchannels and Minichannels, 2005. PART A, 11–18 (2005). https://doi.org/10.1016/j.ijthermalsci.2006.01.004

92. Gloss, D., Herwig, H.: Wall roughness effects in laminar flows: An often ignored though significant issue. Exp Fluids. 49, 461–470 (2010). https://doi.org/10.1007/s00348-009-0811-6

93. Kandlikar, S., Schmitt, D.: Characterization of surface roughness effects on pressure drop in single-phase flow in minichannels. Physics of Fluids. 17, (2005). https://doi.org/10.1063/1.1896985

94. Mayle, R.E.: The Role of Laminar-Turbulent Transition in Gas Turbine Engines. Volume 5: Manufacturing Materials and Metallurgy; Ceramics; Structures and Dynamics; Controls, Diagnostics and Instrumentation; Education; IGTI Scholar Award; General. V005T17A001 (1991). https://doi.org/10.1115/91-GT-261

95. Yang, Z.: On bypass transition in separation bubbles: a review. Propulsion and Power Research. 8, 23–34 (2019). https://doi.org/10.1016/j.jppr.2018.12.004

96. Jacobs, R.G., Durbin, P.A.: Simulations of bypass transition. J Fluid Mech. 428, 185–212 (2001). https://doi.org/10.1017/S0022112000002469

97. Durbin, P.A.: Perspectives on the Phenomenology and Modeling of Boundary Layer Transition. Flow Turbul Combust. 99, 1–23 (2017). https://doi.org/10.1007/s10494-017-9819-9

98. Wei, L., Ge, X., George, J., Durbin, P.: Modeling of laminar-turbulent transition in boundary layers and rough turbine blades. J Turbomach. 139, 1–8 (2017). https://doi.org/10.1115/1.4037670

99. Wei, L., Ge, X., George, J., Durbin, P.: Modeling transition on smooth and rough blades. American Society of Mechanical Engineers, Fluids Engineering Division (Publication) FEDSM. 1A-2016, 1–9 (2016). https://doi.org/10.1115/FEDSM2016-7563

100. Boyle, R.J., Stripf, M.: Simplified approach to predicting rough surface transition. J Turbomach. 131, 1–11 (2009). https://doi.org/10.1115/1.3072521

101. Boyle, R.J., Senytiko, R.G.: Measurements and Predictions of Surface Roughness Effects on the Turbine Vane Aerodynamics. Turbo Expo: Power for Land, Sea and Air. 6, (2009)

102. Durbin, P.A., Medic, G., Seo, J.M., Eaton, J.K., Song, S.: Rough Wall Modification of Two-Layer k — ε. Journal of Fluids Engineering, Transactions of the ASME. 123, 16–21 (2001). https://doi.org/10.1115/1.1343086

103. Liu, F., Gülder, Ö.L.: Effects of pressure and preheat on super-adiabatic flame temperatures in rich premixed methane/air flames. Combustion Science and Technology. 180, 437–452 (2008). https://doi.org/10.1080/00102200701741285

104. Malkogianni, A., Tourlidakis, A.: Influence of the air preheat temperature and the fuel preheat temperature in the adiabatic flame temperature for gaseous fuels of low heating value. 1–9 (2012)

105. Pizzuti, L., Martins, C.A., dos Santos, L.R., Guerra, D.R.S.: Laminar Burning Velocity of Methane/Air Mixtures and Flame Propagation Speed Close to the Chamber Wall. Energy Procedia. 120, 126–133 (2017). https://doi.org/10.1016/j.egypro.2017.07.145

106. Konnov, A.A.: The temperature and pressure dependence of the laminar burning velocity: Experiments and modelling. Proceedings of the European Combustion Meeting 2015. (2015)

107. Fairweather, M., Ormsby, M.P., Sheppard, C.G.W., Woolley, R.: Turbulent burning rates of methane and methane-hydrogen mixtures. Combust Flame. 156, 780–790 (2009). https://doi.org/10.1016/j.combustflame.2009.02.001

108. Ebaid, M.S.Y., Al-Khishali, K.J.M.: Measurements of the laminar burning velocity for propane: Air mixtures. Advances in Mechanical Engineering. 8, 1–17 (2016). https://doi.org/10.1177/1687814016648826

109. Damköhler, G.: The effect of turbulence on the flame velocity in gas mixture. 46, 22A (1947). https://doi.org/10.1097/00152192-198911000-00004

110. Shelkin, K.I.: On combustion in a turbulent flow. Journal of Technical Physics. 13, 520–530 (1943)

111. Ballal, D.R., Lefebvre, A.H.: The structure and propagation of turbulent flames. Proceedings of the Royal Society of London. A. Mathematical and Physical Sciences. 344, 217–234 (1975). https://doi.org/10.1098/rspa.1975.0099

112. Matalon, M.: Flame Stretch and Lewis Number Effects, https://www.princeton.edu, (2011)

113. van den Schoor, F.: Influence of pressure and temperature on flammability limits of combustible gases in air. PhD thesis - Katholieke Universiteit Leuven (2007)

114. Rashwan, S.S., Nemitallah, M.A., Habib, M.A.: Review on Premixed Combustion Technology: Stability, Emission Control, Applications, and Numerical Case Study. Energy and Fuels. 30, 9981–10014 (2016). https://doi.org/10.1021/acs.energyfuels.6b02386

115. Karim, G.A., Wierzba, I., Al-Alousi, Y.: Methane-hydrogen mixtures as fuels. Int J Hydrogen Energy. 21, 625–631 (1996). https://doi.org/10.1016/0360-3199(95)00134-4

116. Kim, H.S., Arghode, V.K., Linck, M.B., Gupta, A.K.: Hydrogen addition effects in a confined swirl-stabilized methane-air flame. Int J Hydrogen Energy. 34, 1054–1062 (2009). https://doi.org/10.1016/j.ijhydene.2008.10.034

117. Liu, X., Bertsch, M., Subash, A.A., Yu, S., Szasz, R.Z., Li, Z., Petersson, P., Bai, X.S., Aldén, M., Lörstad, D.: Investigation of turbulent premixed methane/air and hydrogen-enriched methane/air flames in a laboratory-scale gas turbine model combustor. Int J Hydrogen Energy. 46, 13377–13388 (2021). https://doi.org/10.1016/j.ijhydene.2021.01.087

118. Chen, Z.: Effects of hydrogen addition on the propagation of spherical methane/air flames: A computational study. Int J Hydrogen Energy. 34, 6558–6567 (2009). https://doi.org/10.1016/j.ijhydene.2009.06.001

119. Zhang, Y., Huang, Z., Wei, L., Zhang, J., Law, C.K.: Experimental and modeling study on ignition delays of lean mixtures of methane, hydrogen, oxygen, and argon at elevated pressures. Combust Flame. 159, 918–931 (2012). https://doi.org/10.1016/j.combustflame.2011.09.010

120. Halter, F., Chauveau, C., Gökalp, I.: Characterization of the effects of hydrogen addition in premixed methane/air flames. Int J Hydrogen Energy. 32, 2585–2592 (2007). https://doi.org/10.1016/j.ijhydene.2006.11.033

121. Kim, H.S., Arghode, V.K., Gupta, A.K.: Flame characteristics of hydrogen-enriched methane-air premixed swirling flames. Int J Hydrogen Energy. 34, 1063–1073 (2009). https://doi.org/10.1016/j.ijhydene.2008.10.035

122. Tuncer, O., Acharya, S., Uhm, J.H.: Dynamics, NOx and flashback characteristics of confined premixed hydrogen-enriched methane flames. Int J Hydrogen Energy. 34, 496–506 (2009). https://doi.org/10.1016/j.ijhydene.2008.09.075

123. Schefer, R.W.: Hydrogen enrichment for improved lean flame stability. Int J Hydrogen Energy. 28, 1131–1141 (2003). https://doi.org/10.1016/S0360-3199(02)00199-4

124. Lapalme, D., Lemaire, R., Seers, P.: Assessment of the method for calculating the Lewis number of H2/CO/CH4 mixtures and comparison with experimental results. Int J Hydrogen Energy. 42, 8314–8328 (2017). https://doi.org/10.1016/j.ijhydene.2017.01.099

125. Schefer, R.W., Wicksall, D.M., Agrawal, A.K.: Combustion of hydrogen-enriched methane in a lean premixed swirl-stabilized burner. Proceedings of the Combustion Institute. 29, 843–851 (2002). https://doi.org/10.1016/s1540-7489(02)80108-0

126. Shanbhogue, S.J., Sanusi, Y.S., Taamallah, S., Habib, M.A., Mokheimer, E.M.A., Ghoniem, A.F.: Flame macrostructures, combustion instability and extinction strain scaling in swirl-stabilized premixed CH 4 /H 2 combustion. Combust Flame. 163, 494–507 (2016). https://doi.org/10.1016/j.combustflame.2015.10.026

127. Rørtveit, G.J., Zepter, K., Skreiberg, Ø., Fossum, M., Hustad, J.E.: A comparison of low-NOx burners for combustion of methane and hydrogen mixtures. Proceedings of the Combustion Institute. 29, 1123–1129 (2002). https://doi.org/10.1016/S1540-7489(02)80142-0

128. Bagdanavicius, A., Bowen, P., Syred, N., Crayford, A.: Turbulent flame structure of methane-hydrogen mixtures at elevated temperature and pressure. Combustion Science and Technology. 185, 350–361 (2013). https://doi.org/10.1080/00102202.2012.718005

129. Lantz, A., Collin, R., Alden, M., Lindholm, A., Larfeldt, J., Lorstad, D.: Investigation of hydrogen enriched natural gas flames in a SGT-700/800 burner using oh PLIF and chemiluminescence imaging. J Eng Gas Turbine Power. 137, 1–8 (2015). https://doi.org/10.1115/1.4028462

130. Strakey, P., Sidwell, T., Ontko, J.: Investigation of the effects of hydrogen addition on lean extinction in a swirl stabilized combustor. Proceedings of the Combustion Institute. 31 II, 3173–3180 (2007). https://doi.org/10.1016/j.proci.2006.07.077

131. Syred, N., Abdulsada, M., Griffiths, A., O'Doherty, T., Bowen, P.: The effect of hydrogen containing fuel blends upon flashback in swirl burners. Appl Energy. 89, 106–110 (2012). https://doi.org/10.1016/j.apenergy.2011.01.057

132. Choudhuri, A.R., Gollahalli, S.R.: Combustion characteristics of hydrogen-hydrocarbon hybrid fuels. Int J Hydrogen Energy. 25, 451–462 (2000). https://doi.org/10.1016/S0360-3199(99)00027-0

133. Hu, E., Huang, Z., He, J., Miao, H.: Experimental and numerical study on laminar burning velocities and flame instabilities of hydrogen-air mixtures at elevated pressures and temperatures. Int J Hydrogen Energy. 34, 8741–8755 (2009). https://doi.org/10.1016/j.ijhydene.2009.08.044

134. di Sarli, V., di Benedetto, A.: Laminar burning velocity of hydrogen-methane/air premixed flames. Int J Hydrogen Energy. 32, 637–646 (2007). https://doi.org/10.1016/j.ijhydene.2006.05.016

135. Mehdi Zitouni, S.-E.: Combustion Characteristics of Lean Premixed Methane / Higher Hydrocarbon / Hydrogen Flames. (2020)

136. Lammel, G., Graßl, H.: Greenhouse effect of NOX. Environmental Science and Pollution Research. 2, 40–45 (1995). https://doi.org/10.1007/BF02987512

137. Nicol, D., Malte, P.C., Lai, J., Marinov, N.N., Pratt, D.T., Corr, R.A.: NOx sensitivities for gas turbine engines operated on lean-premixed combustion and conventional diffusion flames. ASME 1992 International Gas Turbine and Aeroengine Congress and Exposition, GT 1992. 3, (1992). https://doi.org/10.1115/92-GT-115

138. Maughan, J.R., Luts, A., Bautista, P.J.: A dry low NOx combustor for the MS3002 regenerative gas turbine. Proceedings of the ASME Turbo Expo. 3, (1994). https://doi.org/10.1115/94-GT-252

139. Klippenstein, S.J., Pfeifle, M., Jasper, A.W., Glarborg, P.: Theory and modeling of relevance to prompt-NO formation at high pressure. Combust Flame. 195, 3–17 (2018). https://doi.org/10.1016/j.combustflame.2018.04.029

140. Park, S.: Pressure effect on NO emission in methane/air lean-premixed flames. Journal of Mechanical Science and Technology. 33, 3031–3038 (2019). https://doi.org/10.1007/s12206-019-0553-1

141. de Persis, S., Idir, M., Molet, J., Pillier, L.: Effect of hydrogen addition on NOx formation in high-pressure counter-flow premixed CH4/air flames. (2019)

142. Coppens, F.H.V., de Ruyck, J., Konnov, A.A.: Effects of hydrogen enrichment on adiabatic burning velocity and NO formation in methane + air flames. Exp Therm Fluid Sci. 31, 437–444 (2007). https://doi.org/10.1016/j.expthermflusci.2006.04.012

143. Coppens, F.H.V., de Ruyck, J., Konnov, A.A.: The effects of composition on burning velocity and nitric oxide formation in laminar premixed flames of CH4 + H2 + O2 + N2. Combust Flame. 149, 409–417 (2007). https://doi.org/10.1016/j.combustflame.2007.02.004

144. Hawkes, E.R., Chen, J.H.: Direct numerical simulation of hydrogen-enriched lean premixed methane-air flames. Combust Flame. 138, 242–258 (2004). https://doi.org/10.1016/j.combustflame.2004.04.010

145. Griebel, P., Boschek, E., Jansohn, P.: Lean blowout limits and NOx emissions of turbulent, lean premixed, hydrogen-enriched methane/air flames at high pressure. J Eng Gas Turbine Power. 129, 404–410 (2007). https://doi.org/10.1115/1.2436568

146. Wang, J., Huang, Z., Tang, C., Miao, H., Wang, X.: Numerical study of the effect of hydrogen addition on methane – air mixtures combustion. Int J Hydrogen Energy. 34, 1084–1096 (2009). https://doi.org/10.1016/j.ijhydene.2008.11.010

147. Zahedi, P., Yousefi, K.: Effects of pressure and carbon dioxide, hydrogen and nitrogen concentration on laminar burning velocities and NO formation of methane-air mixtures. Journal of Mechanical Science and Technology. 28, 377–386 (2014). https://doi.org/10.1007/s12206-013-0970-5

148. Guo, H., Smallwood, G.J., Liu, F., Ju, Y., Gülder, Ö.L.: The effect of hydrogen addition on flammability limit and NOx emission in ultra-lean counterflow CH4/air premixed flames.

Proceedings of the Combustion Institute. 30, 303–311 (2005). https://doi.org/10.1016/j.proci.2004.08.177

149. Syred, N.: A review of oscillation mechanisms and the role of the precessing vortex core (PVC) in swirl combustion systems. Prog Energy Combust Sci. 32, 93–161 (2006). https://doi.org/10.1016/j.pecs.2005.10.002

150. Huang, Y., Yang, V.: Dynamics and stability of lean-premixed swirl-stabilized combustion. Prog Energy Combust Sci. 35, 293–364 (2009). https://doi.org/10.1016/j.pecs.2009.01.002

151. Syred, N., Beer, J.M.: Combustion in Swirling Flows: A Review. J Phys Conf Ser. 891, 143–201 (2017). https://doi.org/10.1088/1742-6596/891/1/012237

152. Alekseenko, S. v., Kuibin, P.A., Okulov, V.L., Shtork, S.I.: Helical vortices in swirl flow, Journal of Fluid Mechanics, Volume 382, pp. 195 - 243 (1999)

153. Wang, S., Yang, V., Hsiao, G., Hsieh, S.Y., Mongia, H.C.: Large-eddy simulations of gas-turbine swirl injector flow dynamics. J Fluid Mech. 583, 99–122 (2007). https://doi.org/10.1017/S0022112007006155

154. Roux, S., Lartigue, G., Poinsot, T., Meier, U., Bérat, C.: Studies of mean and unsteady flow in a swirled combustor using experiments, acoustic analysis, and large eddy simulations. Combust Flame. 141, 40–54 (2005). https://doi.org/10.1016/j.combustflame.2004.12.007

155. Abdulsada, M., Syred, N., Bowen, P., O'Doherty, T., Griffiths, A., Marsh, R., Crayford, A.: Effect of exhaust confinement and fuel type upon the blowoff limits and fuel switching ability of swirl combustors. Appl Therm Eng. 48, 426–435 (2012). https://doi.org/10.1016/j.applthermaleng.2012.04.042

156. Syred, N., Giles, A., Lewis, J., Abdulsada, M., Valera Medina, A., Marsh, R., Bowen, P.J., Griffiths, A.J.: Effect of inlet and outlet configurations on blow-off and flashback with premixed combustion for methane and a high hydrogen content fuel in a generic swirl burner. Appl Energy. 116, 288–296 (2014). https://doi.org/10.1016/j.apenergy.2013.11.071

157. Lieuwen, T., McDonell, V., Santavicca, D., Sattelmayer, T.: Burner development and operability issues associated with steady flowing syngas fired combustors. Combustion Science and Technology. 180, 1169–1192 (2008). https://doi.org/10.1080/00102200801963375

158. Muruganandam, T.M., Nair, S., Neumeier, Y., Lieuwen, T., Seitzman, J.M.: Optical and acoustic sensing of lean blowout precursors. 38th AIAA/ASME/SAE/ASEE Joint Propulsion Conference and Exhibit. (2002). https://doi.org/10.2514/6.2002-3732

159. Stöhr, M., Boxx, I., Carter, C., Meier, W.: Dynamics of lean blowout of a swirl-stabilized flame in a gas turbine model combustor. Proceedings of the Combustion Institute. 33, 2953–2960 (2011). https://doi.org/10.1016/j.proci.2010.06.103

160. Radhakrishnan, K., Heywood, J.B., Tabaczynski, R.J.: Premixed turbulent flame blowoff velocity correlation based on coherent structures in turbulent flows. Combust Flame. 42, 19–33 (1981). https://doi.org/10.1016/0010-2180(81)90139-5

161. Cavaliere, D.E., Kariuki, J., Mastorakos, E.: A comparison of the blow-off behaviour of swirl-stabilized premixed, non-premixed and spray flames. Flow Turbul Combust. 91, 347–372 (2013). https://doi.org/10.1007/s10494-013-9470-z

162. Hubschmid, W., Bombach, R., Inauen, A., Güthe, F., Schenker, S., Tylli, N., Kreutner, W.: Thermoacoustically driven flame motion and heat release variation in a swirl-stabilized gas turbine burner investigated by LIF and chemiluminescence. Exp Fluids. 45, 167–182 (2008). https://doi.org/10.1007/s00348-008-0497-1

163. Arndt, C.M., Severin, M., Dem, C., Stöhr, M., Steinberg, A.M., Meier, W.: Experimental analysis of thermo-acoustic instabilities in a generic gas turbine combustor by phase-correlated PIV, chemiluminescence, and laser Raman scattering measurements. Exp Fluids. 56, 1–23 (2015). https://doi.org/10.1007/s00348-015-1929-3

164. Nicoud, F., Poinsot, T.: Thermoacoustic instabilities: Should the Rayleigh criterion be extended to include entropy changes? Combust Flame. 142, 153–159 (2005). https://doi.org/10.1016/j.combustflame.2005.02.013

165. Nassini, P.C., Pampaloni, D., Meloni, R., Andreini, A.: Lean blow-out prediction in an industrial gas turbine combustor through a LES-based CFD analysis. Combust Flame. 229, 111391 (2021). https://doi.org/10.1016/j.combustflame.2021.02.037

166. Kariuki, J., Dowlut, A., Yuan, R., Balachandran, R., Mastorakos, E.: Heat release imaging in turbulent premixed methane-air flames close to blow-off. Proceedings of the Combustion Institute. 35, 1443–1450 (2015). https://doi.org/10.1016/j.proci.2014.05.144

167. Griebel, P., Boschek, E., Jansohn, P.: Lean blowout limits and NOx emissions of turbulent, lean premixed, hydrogen-enriched methane/air flames at high pressure. J Eng Gas Turbine Power. 129, 404–410 (2007). https://doi.org/10.1115/1.2436568

168. McDonell, V.: Lean combustion in gas turbines 2nd Edition. Technology and Control, Pages 147-201. Elsevier Inc. (2016)

169. Kalantari, A., McDonell, V.: Boundary layer flashback of non-swirling premixed flames: Mechanisms, fundamental research, and recent advances. Prog Energy Combust Sci. 61, 249–292 (2017). https://doi.org/10.1016/j.pecs.2017.03.001

170. Kwon, O.C., Faeth, G.M.: Flame/stretch interactions of premixed hydrogen-fueled flames: Measurements and predictions. Combust Flame. 124, 590–610 (2001). https://doi.org/10.1016/S0010-2180(00)00229-7

171. LEWIS, B., von ELBE, G.: Structure and stability of burner flames. journal of chemical physics. 11, 75 (1943). https://doi.org/10.1039/tf9494500781

172. Ebi, D.: Boundary Layer Flashback of Swirl Flames. Dissertation: UT Austin. (2016)

173. Eichler, C.T.: Flame Flashback in Wall Boundary Layers of Premixed Combustion Systems. PhD thesis – Technische Universität München (2011)

174. Gruber, A., Sankaran, R., Hawkes, E.R., Chen, J.H.: Turbulent flame-wall interaction: A direct numerical simulation study. J Fluid Mech. 658, 5–32 (2010). https://doi.org/10.1017/S0022112010001278

175. Hoferichter, V.: Boundary Layer Flashback in Premixed Combustion Systems. PhD thesis: Technische Universität München (2017)

176. Baumgartner, G.: Flame Flashback in Premixed Hydrogen-Air Combustion Systems. PhD thesis: Technische Universität München (2014)

177. Tober, J.: Boundary layer flashback prediction of a low emissions full hydrogen burner for gas turbine applications. MSc thesis: Faculty of Mechanical Engineering Department of Process and Energy Delft, University of Technology (2019)

178. Leibovich, S.: The structure of vortex breakdown. Annu Rev Fluid Mech. 221–246 (1978). https://doi.org/10.1090/gsm/146/03

179. McCue, T.: Significant 3D Printing Forecast Surges to $35.6 Billion, https://www.forbes.com/sites/tjmccue/2019/03/27/wohlers- report-2019-forecasts-35-6-billion-in-3d-printing-industry- growth-by-2024

180. Markets-SmarTech-Publishing: SmarTech Analysis Annual Additive Manufacturing Market Summary Report Says AM Market Grew to Over $10B Worldwide in 2019, https://www.globenewswire.com/news- release/2020/01/08/1968056/0/en/SmarTech-Analysis- Annual-Additive-Manufacturing-Market-Summary- Report-Says-AM-Market-Grew-to-Over-10B-Worldwide- in-2019.html

181. European Comission: CORDIS, https://cordis.europa.eu

182. UKRI Gateway to Research (GtR): UK Research and Innovation, https://gtr.ukri.org

183. European Comission: Oxide Dispersion Strengthened Materials for the Additive Manufacture of High Temperature Components in Power Generation (OXIGEN), https://cordis.europa.eu/project/id/310279

184. European Comission: Advanced materials for lean burn combustion tiles using laser- Additive Layer Manufacturing (L-ALM) (ASLAM), https://cordis.europa.eu/project/id/619993

185. Frazier, W.E.: Metal additive manufacturing: A review. J Mater Eng Perform. 23, 1917–1928 (2014). https://doi.org/10.1007/s11665-014-0958-z

186. Sireesha, M., Lee, J., Kiran, A.S.K., Babu, V.J., Kee, B.B.T., Ramakrishna, S.: A review on additive manufacturing and its way into the oil and gas industry. RSC Adv. 8, 22460–22468 (2018)

187. Gas to Power Journal: GE gets $1.3m grant to speed up timeline of 3D-printed components. Gas Power Technology Quarterly. 8 (2020)

188. Thomas, D.: Costs, benefits, and adoption of additive manufacturing: a supply chain perspective. The International Journal of Advanced Manufacturing Technology. 85, 1857-1876. (2016)

189. Schmidt, M., Merklein, M., Bourel, D., Dimitrov, D., Hausotte, T., Wegener, K., Overmeyer, L., Vollertsen, F., Levy, G.: Laser based additive manufacturing industry and academia. CIRP Annals. 66, 561–583 (2017)

190. Wood, S.: Monash Centre for Additive Manufacturing (MCAM). Materials Australia. 50, 34–35 (2017)

191. Science in Public (2015), www.scienceinpublic.com.au/monash-uni/photos- jet-engine

192. Boyette, W.R., Guiberti, T.F., Magnotti, G., Roberts, W.L.: Structure of turbulent nonpremixed syngas flames at high pressure. Proceedings of the Combustion Institute. 37, 2207–2214 (2019). https://doi.org/10.1016/j.proci.2018.09.004

193. Rivera, J., Gordon, R., Brouzet, D., Talei, M.: Exhaust CO emissions of a laminar premixed propane-air flame interacting with cold gas jets. Combust Flame. 210, 374–388 (2019)

194. Knadler, M., Caley, T., Lee, J.G., Jung, S., Kim, S., Park, H.: Validation of a physics-based low-order thermo-acoustic model of combustion driven oscillations in a liquid fueled gas turbine combustor. Proceedings of the ASME Turbo Expo. 4A-2018, (2018). https://doi.org/10.1115/GT201875559

195. Hodzic, E., Yu, S., Subash, A.A., Liu, X., Liu, X., Szasz, R.Z., Bai, X.S., Li, Z., Alden, M.: Numerical and experimental investigation of the cecost swirl burner. Proceedings of the ASME Turbo Expo. 4A-2018, 1–12 (2018). https://doi.org/10.1115/GT201875760

196. Vashahi, F., Rezaei, S., Lee, J.: Unsteady Aspects of Multi-Interacting Swirlers Using POD Analysis. In: ASME Turbomachinery Technical Conference and Exposition. , Oslo, Norway, 11-15 June (2018)

197. Crayford, A.P., Lacan, F., Runyon, J., Bowen, P.J., Balwadkar, S., Harper, J., Pugh, D.G.: Manufacture, characterization and stability limits of an AM prefilming air-blast atomizer. Proceedings of the ASME Turbo Expo. 4B-2019, 1–9 (2019). https://doi.org/10.1115/GT2019-91624

198. An, Q., Kheirkhah, S., Bergthorson, J., Yun, S., Hwang, J., Lee, W.J., Kim, M.K., Cho, J.H., Kim, H.S., Vena, P.: Flame stabilization mechanisms and shape transitions in a 3D printed, hydrogen enriched, methane/air low-swirl burner. Int J Hydrogen Energy. 46, 14764–14779 (2021)

199. Fan, Y., Tsujimura, T., Iki, N., Kurata, O., Furutani, H.: Investigation of non-premixed hydrogen-oxygen impinged jet flame under steam dilution. Proceedings of the ASME Turbo Expo. 3B-2021, 1–6 (2021). https://doi.org/10.1115/GT2021-59425

200. Delimont, J., White, S., Andrews, N.: Design of a 1 MW Direct-Fired Combustor for a sCO2 Power Cycle. In: ASME Turbomachinery Technical Conference and Exposition (2021)

201. Sotov, A.V., Agapovichev, A.V., Smelov, V.G., Kokareva, V.V., Zenina, M.V.: Investigation of the Ni-Co-Cr alloy microstructure for the manufacturing of combustion chamber GTE by selective laser melting. International Journal of Advanced Manufacturing Technology. 101, 3047–3053 (2019)

202. Samara University: A serial gas turbine engine with 3D-printed combustion chamber was tested at university, https://www.eurekalert.org/pub_releases/2018-09/su- asg091418.php

203. UK Research and Innovation: Storage of Ammonia For Energy (SAFE) - AGT Pilot, https://gtr.ukri.org/projects?ref=EP%2FT009314%2F1

204. Enagi, I.I., Al-attab, K.A., Zainal, Z.A.: Combustion chamber design and performance for micro gas turbine application. Fuel Processing Technology. 166, 258–268 (2017). https://doi.org/10.1016/j.fuproc.2017.05.037

205. Boukhanouf, R.: Small combined heat and power (CHP) systems for commercial buildings and institutions. Small and Micro Combined Heat and Power (CHP) Systems: Advanced Design, Performance, Materials and Applications. 365–394 (2011). https://doi.org/10.1533/9780857092755.3.365

206. Bhatia, S.C.: Advanced Renewable Energy Systems. Woodhead Publishing India., Delhi (2014)

207. Sung, T., Kim, S., Kim, K.C.: Thermoeconomic analysis of a biogas-fueled micro-gas turbine with a bottoming organic Rankine cycle for a sewage sludge and food waste treatment plant in the Republic of Korea. Appl Therm Eng. 127, 963–974 (2017). https://doi.org/10.1016/j.applthermaleng.2017.08.106

208. Kurata, O., Iki, N., Inoue, T., Matsunuma, T., Tsujimura, T., Furutani, H., Kawano, M., Arai, K., Okafor, E.C., Hayakawa, A., Kobayashi, H.: Development of a wide range-operable, rich-lean low-NOx combustor for NH 3 fuel gas-turbine power generation. Proceedings of the Combustion Institute. 37, 4587–4595 (2019). https://doi.org/10.1016/j.proci.2018.09.012

209. Fuel Cells Works: DLR, Aurelia and REWAG Sign Cooperation Agreement to Push Forward the Use of Hydrogen Fuel in Micro Gas Turbines, https://fuelcellsworks.com/news/dlr-aurelia-and-rewag-sign-cooperation-agreement-to-push-forward-the-use-of-hydrogen-fuel-in-micro-gas-turbines/

210. European Turbine Network (ETN): Micro Gas Turbine Technology Summary, https://etn.global/wp-content/uploads/2018/02/MGT-Technology-Summary-final-for-the-website.pdf

211. Delgado Camacho, D., Clayton, P., O'Brien, W.J., Seepersad, C., Juenger, M., Ferron, R., Salamone, S.: Applications of additive manufacturing in the construction industry – A forward-looking review. Autom Constr. 89, 110–119 (2018). https://doi.org/10.1016/j.autcon.2017.12.031

212. Klein, E., Ling, J., Aute, V., Hwang, Y., Radermacher, R.: A Review of Recent Advances in Additively Manufactured Heat Exchangers. International Refrigeration and Air Conditioning Conference. 1–10 (2018)

213. Kennedy, I., Chen, Z., Ceen, B., Jones, S., Copeland, C.D.: Experimental investigation of an inverted Brayton cycle for exhaust gas energy recovery. J Eng Gas Turbine Power. 141, 1–11 (2019). https://doi.org/10.1115/1.4041109

214. Gerstler, W.D., Erno, D.: 'Introduction of an additively manufactured multi-furcating heat exchanger. In: 16th IEEE Intersociety Conference on Thermal and Thermomechanical Phenomena in Electronic Systems (ITherm). , Orlando, Florida (2017)

215. EOS: Euro-K - 3D printed micro-burners for the optimized combustion of gaseous and liquid fuel, 'Euro-K - 3D printed micro-burners for the optimized combustion of gaseous and liquid fuel

216. HiETA Technologies: Combustion and Fuel Delivery, https://www.hieta.biz/products/combustion-fuel-delivery/

217. Jones, S.L., Smith, C.: Combustion Chamber and Heat Exchanger, https://ppubs.uspto.gov/pubwebapp/static/pages/landing.html, (2020)

218. Adamou, A., Kennedy, I., Farmer, B., Hussein, A., Copeland, C.: Experimental and computational analysis of an additive manufactured vaporization injector for a micro-gas turbine. Proceedings of the ASME Turbo Expo. 4A-2019, 1–12 (2019). https://doi.org/10.1115/GT2019-90245

219. Jafari, D., Wits, W.W.: The utilization of selective laser melting technology on heat transfer devices for thermal energy conversion applications: A review. Renewable and Sustainable Energy Reviews. 91, 420–442 (2018). https://doi.org/10.1016/j.rser.2018.03.109

220. Zhang, X., Keramati, H., Arie, M., Singer, F., Tiwari, R., Shooshtari, A., Ohadi, M.: Recent developments in high temperature heat exchangers: A review. Frontiers in Heat and Mass Transfer. 11, (2018). https://doi.org/10.5098/hmt.11.18

221. Linstrand, N.: This Swedish scientist works towards fulfilling Siemens' 2030 hydrogen pledge, https://new.siemens.com/global/en/company/stories/energy/hydrogen-capable-gas-turbine.html

222. Bothien, M.R., Ciani, A., Wood, J.P., Fruechtel, G.: Toward Decarbonized Power Generation with Gas Turbines by Using Sequential Combustion for Burning Hydrogen. J Eng Gas Turbine Power. 141, 1–10 (2019). https://doi.org/10.1115/1.4045256

223. Dodo, S., Karishuku, M., Yagi, N., Asai, T., Akiyama, Y.: Dry Low-NOx Combustion Technology for Novel Clean Coal Power Generation Aiming at the Realization of a Low Carbon Society. Mitsubishi Heavy Industries Technical Review. 52, 24–31 (2015)

224. Tekin, N., Ashikaga, M., Horikawa, A., Funke, H.: Enhancement of fuel flexibility of industrial gas turbines by development of innovative hydrogen combustion systems. Gas of Energy. Issue 2. (2018)

225. Brooks, R.: GE, Siemens Invest, Re-Commit to Metal Manufacturing, https://www.industryweek.com/industryweek- wire/foundry-management-technology/article/21981747/ge-siemens-invest-recommit- to-metal-manufacturing

226. Flin, D.: 3D printed parts in serial production, https://gasturbineworld.com/3d-printed-parts-in-serial-production/

227. Roan, A.J.: Mitsubishi anticipates metal AM industry, https://www.metaltechnews.com/story/2020/12/09/tech-bytes/mitsubishi-anticipates-metal-am-industry/408.html

228. Andersson, O., Graichen, A., Brodin, H., Navrotsky, V.: Developing Additive Manufacturing Technology for Burner Repair. J Eng Gas Turbine Power. 139, 1–9 (2017). https://doi.org/10.1115/1.4034235

229. Fantozzi, G., Kinell, M., Carrera, S.R., Nilsson, J., Kuesters, Y.: Experimental study on pressure losses in porous materials. J Eng Gas Turbine Power. 141, 1–8 (2019). https://doi.org/10.1115/1.4040868

230. Sieger, M.: A New Dimension for Industry: How 3D Printing is Doing Its Part to Reduce Greenhouse Emissions, https://www.ge.com/news/reports/new-dimension-industry-3d-printing-part-reduce-greenhouse-emissions

231. Kellner, T.: Land of Silk and Lasers: Bespoke 3D Printing Factory for the Oil & Gas Industry Thrives in Italy's Fashion Heartland, https://www.ge.com/news/reports/land-of-silk-and-lasers-bespoke-3d-printing-factory-thrives-in-italys-fashion-heartland

232. Larfeldt, J., Andersson, M., Larsson, A., Moëll, D.: Hydrogen Co-Firing in Siemens Low NOx Industrial Gas Turbines. In: POWER-GEN Europe. , Cologne, Germany (2017)

233. Panfili, G., Balestrino, C., Handy, S.: SGT-A35 (Industrial RB211) enhanced by additive manufacturing (AM) technology. In: 11th Petrobras Turbomachinery Forum. , Rio De Janeiro, Brazil (2019)

234. Ciani, A., Wood, J.P., Maurer, M., Bunkute, B., Pennell, D., Riazantsev, S., Früchtel, G.: Center Body Burner for Sequential Combustion: Superior Performance at Lower Emissions. In: ASME Turbomachinery Technical Conference and Exposition (2021)

235. Patel, S.: 3-D Printed Gas Turbine Technology Marks 'Game Changing' Milestone, https://www.powermag.com/3-d-printed-gas-turbine-technology-marks-game-changing-milestone/

236. Prandi, R.: One More GE's GT26 HE Upgrade, https://www.dieselgasturbine.com/news/One-More-GE-s-GT26-HE-Upgrade/7009340.article

237. Walton, R.: GE GT26 HE upgrade completed at Uniper UK plant, coming to Singapore, Buenos Aires, https://www.power-eng.com/om/plant-optimization/new-ge-gt26-he-upgrade-shows-benefits-in-uniper-uk-plant-testing/

238. Runyon, J.: Gas Turbine Fuel Flexibility: Pressurized Swirl Flame Stability, Thermoacoustics, and Emissions, PhD thesis: Cardiff University (2017)

239. Runyon, J., Marsh, R., Pugh, D., Bowen, P., Giles, A., Morris, S., Valera-Medina, A.: Experimental analysis of confinement and swirl effects on premixed ch4-h2 flame behavior in a pressurized generic swirl burner. Proceedings of the ASME Turbo Expo. Part F1300, 1–12 (2017). https://doi.org/10.1115/GT2017-64794

240. Pugh, D., Bowen, P., Crayford, A., Marsh, R., Runyon, J., Morris, S., Giles, A.: Catalytic Influence of Water Vapor on Lean Blow-Off and NOx Reduction for Pressurized Swirling Syngas Flames. J Eng Gas Turbine Power. 140, 1–10 (2018). https://doi.org/10.1115/1.4038417

241. Pugh, D.G., Bowen, P.J., Marsh, R., Crayford, A.P., Runyon, J., Morris, S., Valera-Medina, A., Giles, A.: Dissociative influence of H2O vapour/spray on lean blowoff and NOx reduction for heavily carbonaceous syngas swirling flames. Combust Flame. 177, 37–48 (2017). https://doi.org/10.1016/j.combustflame.2016.11.010

242. MATWEB: Special Metals INCONEL® Alloy 625, https://www.matweb.com/search/datasheet_print.aspx?matguid=4a194f59f35a427dbc5009f043349cb5

243. MATWEB: AISI Type 304 Stainless Steel, https://www.matweb.com/search/datasheet_print.aspx?matguid=bd20a4281ae3430d97cfbebf6904ec50

244. Chigier, N.A., Beér, J.M.: Velocity and static-pressure distributions in swirling air jets issuing from annular and divergent nozzles. Journal of Fluids Engineering, Transactions of the ASME. 86, 788–796 (1964). https://doi.org/10.1115/1.3655954

245. Kychakoff, G., Howe, R.D., Hanson, R.K., Drake, M.C., Pitz, R.W., Lapp, M., Murray Penney, C.: Visualization of turbulent flame fronts with planar laser-induced fluorescence. Science (1979). 224, 375–377 (1984). https://doi.org/10.1126/science.224.4647.382

246. Daily, J.W.: Laser induced fluorescence spectroscopy in flames. Prog Energy Combust Sci. 23, 133–199 (1997). https://doi.org/10.1016/S0360-1285(97)00008-7

247. Barlow, R.S.: Laser diagnostics and their interplay with computations to understand turbulent combustion. Proceedings of the Combustion Institute. 31 I, 49–75 (2007). https://doi.org/10.1016/j.proci.2006.08.122

248. Lantz, A., Collin, R., Alden, M., Lindholm, A., Larfeldt, J., Lorstad, D.: Investigation of hydrogen enriched natural gas flames in a SGT-700/800 burner using oh PLIF and chemiluminescence imaging. J Eng Gas Turbine Power. 137, 1–8 (2015). https://doi.org/10.1115/1.4028462

249. Witzel, B.: Application of Optical Diagnostics to Support the Development of Industrial Gas Turbine Combustors, VGB PowerTech (2015)

250. Guethe, F., Guyot, D., Singla, G., Noiray, N., Schuermans, B.: Chemiluminescence as diagnostic tool in the development of gas turbines. Appl Phys B. 107, 619–636 (2012). https://doi.org/10.1007/s00340-012-4984-y

251. Liu, Y., Tan, J., Wan, M., Zhang, L., Yao, X.: Quantitative Measurement of OH∗ and CH∗ Chemiluminescence in Jet Diffusion Flames. ACS Omega. 5, 15922–15930 (2020). https://doi.org/10.1021/acsomega.0c01093

252. Gámiz-Gracia, L., García-Campaña, A.M., Huertas-Pérez, J.F., Lara, F.J.: Chemiluminescence detection in liquid chromatography: Applications to clinical, pharmaceutical, environmental and food analysis-A review. Anal Chim Acta. 640, 7–28 (2009). https://doi.org/10.1016/j.aca.2009.03.017

253. H . P . Broida and A . G . Gaydon Source: The Mechanism of Formation of OH , CH and HCO in Flame Spectra , Using Deuterium as Tracer Author (s). In: Proceedings of the Royal Society of London Series A, Mathematical and Physical Sciences. pp. 60–69. Royal Society (1953)

254. Walsh, K.T., Long, M.B., Tanoff, M.A., Smooke, M.D.: Experimental and computational study of CH, CH*, AND OH* in an axisymmetric laminar diffusion flame. Symposium (International) on Combustion. 27, 615–623 (1998). https://doi.org/10.1016/S0082-0784(98)80453-0

255. Tinaut, F. v., Reyes, M., Giménez, B., Pastor, J. v.: Measurements of OH* and CH* chemiluminescence in premixed flames in a constant volume combustion bomb under autoignition conditions. Energy and Fuels. 25, 119–129 (2011). https://doi.org/10.1021/ef1013456

256. Lauer, M., Sattelmayer, T.: Heat release calculation in a turbulent swirl flame from laser and chemiluminescence measurements. 14th Int Symp on Applications of Laser Techniques to Fluid Mechanics. 7–10 (2008)

257. Guyot, D., Guethe, F., Schuermans, B., Lacarelle, A., Paschereit, C.O.: CH*/OH* Chemiluminescence response of an atmospheric premixed flame under varying operating conditions. Proceedings of the ASME Turbo Expo, 1–12 (2010)

258. Witzel, B., Huth, M., Schulz, C.: Application of optical diagnostics as an experimental tool for the development of combustors for stationary gas turbines. (2014)

259. Nori, V., Seitzman, J.: Evaluation of chemiluminescence as a combustion diagnostic under varying operating conditions. 46th AIAA Aerospace Sciences Meeting and Exhibit. 1–14 (2008). https://doi.org/10.2514/6.2008-953

260. Marsh, R., Runyon, J., Giles, A., Morris, S., Pugh, D., Valera-Medina, A., Bowen, P.: Premixed methane oxycombustion in nitrogen and carbon dioxide atmospheres: Measurement of operating limits, flame location and emissions. Proceedings of the Combustion Institute. Proceedings of the Combustion Institute. 36, 3949–3958 (2017). https://doi.org/10.1016/j.proci.2016.06.057

261. Marsh, R., Giles, A., Runyon, J., Pugh, D., Bowen, P., Morris, S., Best, T., Finney, K., Pourkashanian, M.: Selective Exhaust Gas Recycling for Carbon Capture Applications: Combustion and Operability Measurement. *The Future of Gas Turbine Technology 8th International Gas Turbine* Conference, Brussels, Belgium1–9 (2016)

262. Haber, L.C., Vandsburger, U., Saunders, W.R., Khanna, V.K.: An examination of the relationship between chemiluminescent light emissions and heat release rate under non-adiabatic conditions. Proceedings of the ASME Turbo Expo. 2, 1–8 (2000). https://doi.org/10.1115/2000-GT-0121

263. Hardalupas, Y., Orain, M.: Local measurements of the time-dependent heat release rate and equivalence ratio using chemiluminescent emission from a flame. Combust Flame. 139, 188–207 (2004). https://doi.org/10.1016/j.combustflame.2004.08.003

264. Najm, H.N., Paul, P.H., Mueller, C.J., Wyckoff, P.S.: On the Adequacy of Certain Experimental Observables as Measurements of Flame Burning Rate. Combust Flame. 113, 312–332 (1998). https://doi.org/10.1016/s0010-2180(97)00209-5

265. Haber, L.C.: An investigation into the origin, measurement and application of chemiluminescent light emissions from premixed flames. MSc Thesis: Faculty of the Virginia Polytechnic Institute and State University (2000)

266. Ikeda, Y., Kurahashi, T., Kawahara, N., Tomita, E.: Temperature Measurements of Laminar Propane / Air Premixed Flame Using Detailed OH* Spectra Intensity Ratio. 12th International Symposium on Applications of Laser Techniques to Fluid Mechanics. 1–11 (2004)

267. Agostinelli, P.W., Laera, D., Boxx, I., Gicquel, L., Poinsot, T.: Impact of wall heat transfer in Large Eddy Simulation of flame dynamics in a swirled combustion chamber. Combust Flame. 234, 111728 (2021). https://doi.org/10.1016/j.combustflame.2021.111728

268. Agostinelli, P.W., Kwah, Y.H., Richard, S., Exilard, G., Dawson, J.R., Gicquel, L., Poinsot, T.: Numerical and experimental flame stabilization analysis in the new spinning combustion technology framework. Proceedings of the ASME Turbo Expo. 4A-2020, (2020). https://doi.org/10.1115/GT2020-15035

269. Runyon, J., Marsh, R., Sevcenco, Y., Pugh, D., Morris, S.: Development and Commissioning of a Chemiluminescence Imaging System for an Optically-Accessible High-Pressure Generic Swirl Burner. 7th European Combustion Meeting. 1–6 (2015)

270. Valera-Medina, A., Marsh, R., Runyon, J., Pugh, D., Beasley, P., Hughes, T., Bowen, P.: Ammonia–methane combustion in tangential swirl burners for gas turbine power generation. Appl Energy. 185, 1362–1371 (2017). https://doi.org/10.1016/j.apenergy.2016.02.073

271. Valera-Medina, A., Morris, S., Runyon, J., Pugh, D.G., Marsh, R., Beasley, P., Hughes, T.: Ammonia, Methane and Hydrogen for Gas Turbines. Energy Procedia. 75, 118–123 (2015). https://doi.org/10.1016/j.egypro.2015.07.205

272. Kurji, H., Valera-Medina, A., Runyon, J., Giles, A., Pugh, D., Marsh, R., Cerone, N., Zimbardi, F., Valerio, V.: Combustion characteristics of biodiesel saturated with pyrolysis oil for power generation in gas turbines. Renew Energy. 99, 443–451 (2016). https://doi.org/10.1016/j.renene.2016.07.036

273. Dribinski, V., Ossadtchi, A., Mandelshtam, V.A., Reisler, H.: Reconstruction of Abel-transformable images: The Gaussian basis-set expansion Abel transform method. Review of Scientific Instruments. 73, 2634 (2002). https://doi.org/10.1063/1.1482156

274. Higgins, B., McQuay, M.Q., Lacas, F., Rolon, J.C., Darabiha, N., Candel, S.: Systematic measurements of OH chemiluminescence for fuel-lean, high-pressure, premixed, laminar flames. Fuel. 80, 67–74 (2001). https://doi.org/10.1016/S0016-2361(00)00069-7

275. Killer, C.: Abel Inversion Algorithm, https://www.mathworks.com/matlabcentral/fileexchange/43639-abel-inversion-algorithm

276. Pretzel, G.: A New Method for Numerical Abel-Inversion. Zeitschrift für Naturforschung A. 46, 639–641 (1991)

277. Stopper, U., Aigner, M., Meier, W., Sadanandan, R., Stöhr, M., Kim, I.S.: Flow field and combustion characterization of premixed gas turbine flames by planar laser techniques. J Eng Gas Turbine Power. 131, 1–8 (2009). https://doi.org/10.1115/1.2969093

278. Durbin, P.A., Pettersson Reif, B.A.: Statistical Theory and Modeling for Turbulent Flows. John Wiley &Sons, Ltd (2011)

279. Townsend, A.A.: The structure of turbulent shear flow. Journal of Fluid Mechanics, Volume 1, Issue 5, pp. 554 - 560 (1976)

280. Siemens: Simcenter STAR-CCM+ user guide. (2019)

281. Coles, D.: The law of the wake in the turbulent boundary layer. J Fluid Mech. 1, 191–226 (1956). https://doi.org/10.1017/S0022112056000135

282. Spalding, D.B.: A Single Formula for the “Law of the Wall.” J Appl Phys. 28 (3): 455-458 (1961)

283. Reichardt, H.: Vollstaandige darstellung der turbulenten geschwindigkeitsvertei- lung in glatten leitungen. journal of applied Mathematics ans Mechanics. (1951). https://doi.org/10.1002/zamm.19510310704.

284. Durbin, P.A.: Limiters and wall treatments in applied turbulence modeling. Fluid Dyn Res. 41, (2009). https://doi.org/10.1088/0169-5983/41/1/012203

285. Kim, T., Blois, G., Best, J.L., Christensen, K.T.: PIV measurements of turbulent flow overlying large, cubic- and hexagonally-packed hemisphere arrays. Journal of Hydraulic Research. 58, 363–383 (2020). https://doi.org/10.1080/00221686.2019.1581671

286. Laufer, J.: The structure of turbulence in fully developed pipe flow. NACA (1953)

287. Deshmukh, D., Samad, A.: CFD-based analysis for finding critical wall roughness on centrifugal pump at design and off-design conditions. Journal of the Brazilian Society of Mechanical Sciences and Engineering. 41, 1–18 (2019). https://doi.org/10.1007/s40430-018-1557-y

288. Flack, K.A., Schultz, M.P.: Roughness effects on wall-bounded turbulent flows. Physics of Fluids. 26, (2014). https://doi.org/10.1063/1.4896280

289. Busse, A., Thakkar, M., Sandham, N.D.: Reynolds-number dependence of the near-wall flow over irregular rough surfaces. J Fluid Mech. 810, 196–224 (2017). https://doi.org/10.1017/jfm.2016.680

290. Thakkar, M., Busse, A., Sandham, N.D.: Direct numerical simulation of turbulent channel flow over a surrogate for Nikuradse-type roughness. J Fluid Mech. 837, R11–R111 (2018). https://doi.org/10.1017/jfm.2017.873

291. Krogstad, P., Antonia, R.A.: Structure of turbulent boundary layers on smooth and rough walls. J Fluid Mech. 277, 1–21 (1994). https://doi.org/10.1017/S0022112094002661

292. Krogstad, P.A., Antonia, R.A., Browne, L.W.B.: Comparison between rough and smooth-wall turbulent boundary layers. J Fluid Mech. 245, 599–617 (1992). https://doi.org/10.1017/S0022112092000594

293. Flack, K.A., Schultz, M.P., Shapiro, T.A.: Experimental support for Townsend's Reynolds number similarity hypothesis on rough walls. Physics of Fluids. 17, (2005). https://doi.org/10.1063/1.1843135

294. Castro, I.P.: Rough-wall boundary layers: Mean flow universality. J Fluid Mech. 585, 469–485 (2007). https://doi.org/10.1017/S0022112007006921

295. Raja, J., Muralikrishnan, B., Fu, S.: Recent advances in separation of roughness, waviness and form. Precis Eng. 26, 222–235 (2002). https://doi.org/10.1016/S0141-6359(02)00103-4

296. Leach, Richard K.. "Characterisation of Areal Surface Texture." Characterisation of Areal Surface Texture (2013).

297. Adams, T., Grant, C., Watson, H.: A Simple Algorithm to Relate Measured Surface Roughness to Equivalent Sand-grain Roughness. International Journal of Mechanical Engineering and Mechatronics. 1, (2012). https://doi.org/10.11159/ijmem.2012.008

298. Schlichting, H.: Experimental investigation of the problem of surface roughness. NACA (1936).

299. Coleman, H.W., Hodge, B.K., Taylor, R.P.: A re-evaluation of schlichting's surface roughness experiment. Journal of Fluids Engineering, Transactions of the ASME. 106, 60–65 (1984). https://doi.org/10.1115/1.3242406

300. Schultz, M.P., Flack, K.A.: Outer layer similarity in fully rough turbulent boundary layers. Exp Fluids. 38, 328–340 (2005). https://doi.org/10.1007/s00348-004-0903-2

301. Cebeci, T., Bradshaw, P.: Momentum Transfer in Boundary Layers. McGraw Hill (1977)

302. Clauser, F.H.: Turbulent Boundary Layers in Adverse Pressure Gradients. Aeronotical Sciencies archive. 21, (1954)

303. Volino, R.J., Schultz, M.P., Flack, K.A.: Turbulence structure in a boundary layer with two-dimensional roughness. J Fluid Mech. 635, 75–101 (2009). https://doi.org/10.1017/S0022112009007617

304. Wu, Y., Christensen, K.T.: Spatial structure of a turbulent boundary layer with irregular surface roughness. J Fluid Mech. 655, 380–418 (2010). https://doi.org/10.1017/S0022112010000960

305. Hama, Francis R.. "Boundary Layer characteristics for smooth and rough surfaces." (1954).

306. Andersson, J., Oliveira, D.R., Yeginbayeva, I., Leer-Andersen, M., Bensow, R.E.: Review and comparison of methods to model ship hull roughness. Applied Ocean Research. 99, 102119 (2020). https://doi.org/10.1016/j.apor.2020.102119

307. DeGroot, C.T., Wang, C., Floryan, J.M.: Drag Reduction Due to Streamwise Grooves in Turbulent Channel Flow. Journal of Fluids Engineering, Transactions of the ASME. 138, (2016). https://doi.org/10.1115/1.4034098

308. Benschop, H.O.G., Breugem, W.P.: Drag reduction by herringbone riblet texture in direct numerical simulations of turbulent channel flow. Journal of Turbulence. 18, 717–759 (2017). https://doi.org/10.1080/14685248.2017.1319951

309. Finson, M.L., Wu, P.K.S.: Analysis of Rough Wall Turbulent Heating With Application to Blunted Flight Vehicles. 17th Aerospace Sciences Meeting. (1979). https://doi.org/doi.org/10.2514/6.1979-8

310. McClain, S.T., Hodge, B.K., Bons, J.P.: Predicting skin friction and heat transfer for turbulent flow over real gas turbine surface roughness using the discrete element method. J Turbomach. 126, 259–267 (2004). https://doi.org/10.1115/1.1740779

311. Cebeci, T., Chang, K.: Calculation of incompressible rough-wall boundary-layer flows. AIAA. 730–735 (1978). https://doi.org/10.2514/3.7571

312. Rotta, J.C.: Turbulent Boundary Layers in Incompressible Flow. Progress in Aeronautical Sciences. 2, 1–120 (1962)

313. Smith, A., Cebeci, T.: Numerical solution of the turbulent-boundary layer equations. (1967). https://doi.org/doi: 10.21236/ad0656430

314. Feiereisen, W.J., Acharya, M.: Modeling of Transition and Surface Roughness Effects in Boundary-Layer Flows. AIAA. 1642–1649 (1986)

315. Krogstad, P.: Modification of the van Driest Damping Function to Include the Effects of Surface Roughness. AIAA. 888–894 (1990)

316. Granville, P.S.: Mixing-Length Formulations for Turbulent Boundary Layers Over Arbitrarily Rough Surfaces. J. Ship Res. (1985)

317. Gbadebo, S.A., Hynes, T.P., Cumpsty, N.A.: Influence of Surface on Three-Dimensional Separation in Axial Compressors. ASME. (2004)

318. Blair, M.F.: An Experimental Study of Heat Transfer in a Large-Scale Turbine Rotor Passage. ASME J. Turbomach. 1–13 (1994)

319. Lee, J., Paynter, G.C.: Modified Spalart-Allmaras One-Equation Turbulence Model for Rough Wall Boundary Layers. J. Propul. Power. (1996)

320. Prakash, A.: RANS Computation of Heat Transfer Over Rough Surfaces. MSc thesis: Department of Mechanical Engineering, Polytechnique Montréal. (2019). https://publications.polymtl.ca/3922/

321. Ohashi, K.: Numerical study of roughness model effect including low-Reynolds number model and wall function method at actual ship scale. Journal of Marine Science and Technology (Japan). 26, 24–36 (2021). https://doi.org/10.1007/s00773-020-00718-5

322. Orych, M., Werner, S., Larsson, L.: Roughness effect modelling for wall resolved RANS – Comparison of methods for marine hydrodynamics. Ocean Engineering. 266, 112778 (2022). https://doi.org/10.1016/j.oceaneng.2022.112778

323. Shih, T., Liou, W.W., Shabbir, A., Yang, Z., Zhu, J.: A NEW k-ε EDDY VISCOSITY MODEL FOR HIGH REYNOLDS NUMBER TURBULENT FLOWS. Computers Fluids. 24, 227–238 (1994)

324. ANSYS FLUENT 12 . 0 UDF Manual. (2009)

325. Rodi, W.: Experience with two-layer models combining the k-epsilon model with a one-equation model near the wall. In: 29th Aerospace Sciences Meeting (1991)

326. Wolfshtein, M.: The velocity and temperature distribution in one-dimensional flow with turbulence augmentation and pressure gradient. Int J Heat Mass Transf. 12, 301–318 (1969)

327. Ioselevich, V.A., Pilipenko, V.N.: Logarithmic velocity profile for flow of a weak polymer solution near a rough surface. Soviet Physics Doklady. 18, 790 (1974)

328. Almohammadi, K.M., Ingham, D.B., Ma, L., Pourkashan, M.: Computational fluid dynamics (CFD) mesh independency techniques for a straight blade vertical axis wind turbine. Energy. 58, 483–493 (2013). https://doi.org/10.1016/j.energy.2013.06.012

329. Roache, P.J.: Perspective: A method for uniform reporting of grid refinement studies. Journal of Fluids Engineering, Transactions of the ASME. 116, 405–413 (1994). https://doi.org/10.1115/1.2910291

330. Ortega-Casanova, J., Castillo-Sanchez, S.I.: On using axisymmetric turbulent impinging jets swirling as Burger's vortex for heat transfer applications. Single and multi-objective vortex parameters optimization. Appl Therm Eng. 121, 103–114 (2017). https://doi.org/10.1016/j.applthermaleng.2017.04.031

331. Shockling, M.A., Allen, J.J., Smits, A.J.: Roughness effects in turbulent pipe flow. J Fluid Mech. 564, 267–285 (2006). https://doi.org/10.1017/S0022112006001467

332. Guide for the Verification and Validation of Computational Fluid Dynamics Simulations. American Institute of Aeronautics and Astronautics (1998)

333. Tu J; Yeoh G-H; Liu C, 'CFD Solution Analysis: Essentials', in Computational Fluid Dynamics, Elsevier, pp. 211 - 253, (2019). http://dx.doi.org/10.1016/b978-0-08-101127-0.00006-4

334. Kaess, R., Polifke, W., Poinsot, T., Noiray, N., Durox, D., Schuller, T., Candel, S.: CFD-based Mapping of the Thermo-acoustic Stability of a Laminar Premix Burner. Center for Turbulence Research Proceedings of the Summer Program. 289–302 (2008)

335. Schefer, R.W., Kulatilaka, W.D., Patterson, B.D., Settersten, T.B.: Visible emission of hydrogen flames. Combust Flame. 156, 1234–1241 (2009). https://doi.org/10.1016/j.combustflame.2009.01.011

Appendix

A. Operating conditions

The various operating conditions, in terms of flowrates for the inlet air and inlet fuel, for the investigated test points are listed in Tables 1-1, 1-2, and 1-3, for 100%CH_4, 100%H_2 and 23%$_{vol}CH_4$/77%$_{vol}H_2$, respectively.

Table A-1 *Analytical mass flowrates of inlet air and CH_4, and resultant equivalence ratios for the investigated test points.*

Equivalence ratio (φ)	Inlet Air (g/s)	CH_4 (g/s)
0.558	15.40	0.5
0.66	13.00	0.5
0.8	10.74	0.5
0.9	9.55	0.5
1	8.58	0.5
8.18	8.18	0.5

Table A-2 *Analytical mass flowrates of inlet air and H_2, and resultant equivalence ratios for the investigated test points.*

Equivalence ratio (φ)	Inlet Air (g/s)	H2 (g/s)
0.244	29.2	0.208
0.265	26.9	0.208
0.285	25.00	0.208
0.298	23.92	0.208
0.305	23.37	0.208
0.311	22.90	0.208
0.312	22.85	0.208

Table A-3 *Analytical mass flowrates of inlet air, CH_4 and H_2, and resultant equivalence ratios for the investigated test points.*

Equivalence ratio (φ)	Inlet Air (g/s)	CH_4 (g/s)	H_2 (g/s)
0.327	24.00	0.249	0.105
0.35	22.45	0.249	0.105
0.40	19.64	0.249	0.105
0.44	17.80	0.249	0.105
0.45	17.47	0.249	0.105
0.458	17.15	0.249	0.105

B. Equivalent sand-grain roughness

The equivalence sand grain roughness values utilised for the computational investigation of roughness are listed in Table 2-1. As explained the Section 4.2.2, these values were calculated from Equation 4.4 using the surface roughness values measured by Runyon et al. [29].

Table B-1 *Analytical mass flowrates of inlet air, CH_4 and H_2, and resultant equivalence ratios for the investigated test points.*

Equivalent sand grain roughness *(k_s)* (μm)				
Swirler	**Nozzle ID**	**Swirler Base**	**Swirler Curve**	**Swirler Flat**
Machined	8.76	10.96	4.18	8.87
AM-G	34.72	48.48	30.47	32.80
AM-R	54.43	76.39	48.91	46.86
AM-G.50	347.20	484.80	304.70	328.00
AM-R.90	544.30	763.90	489.10	468.60

C. Image processing algorithms

C.1. Chemiluminescence image temporal average MATLAB algorithm:

The function *MeanImageCalculation* calculates the temporal averaged (mean) image for a defined set of .TIF images. The files are exported as matrices to be used in the subsequent function presented in Section C.2. The temporal averaged image is normalised by its peak intensity, prior to export. Additionally, the centroid of the binary trace of the mean image is also estimated and overlayed on top of the mean image,

which is additionally exported as .TIF. The estimation of the mean image centroid is based on both the shape and the pixel intensity.

```
function MeanImageCalculation

% Calls dialogue box for user to provide .TIF image files
[file,path] = uigetfile('*.tif','MultiSelect','on');
if isequal(file,0)
   disp('User selected Cancel');
else
   disp(['User selected ', fullfile(path,file)]);
end

% File accessing and mean image calculation
NumFiles = length(file);
FirstImage = imread(file{1,1});
[Y1,X1] = size(FirstImage);
MeanImage = zeros([Y1 X1]);
for i = 1: NumFiles
   Image = imread(file{1,i});
   MeanImage = MeanImage+im2double(Image);
end
MeanImage = MeanImage./NumFiles;

% Image intensity normalisation
MeanImage = MeanImage./max(MeanImage(:));

% Binarization of mean image centroid estimation
[counts,~] = imhist(MeanImage,64);
T = otsuthresh(counts);
BinaryMeanImage = imbinarize(MeanImage,T);

% Estimation of binary mean image centroid
stat = regionprops(BinaryMeanImage,'Area');
statCentroid = regionprops(BinaryMeanImage,MeanImage,'WeightedCentroid');
centroids = cat(1,statCentroid.WeightedCentroid);
areas = cat(1,stat.Area);
CentXPix = round(centroids(1,1),0);
CentYPix = round(centroids(1,2),0);
```

```
% Projection of mean image
imshow(MeanImage);
```

C.2. Chemiluminescence image Abel deconvolution MATLAB algorithm

The employed Abel deconvolution function, denoted as *HalfAbel*, was provided by Killer [275]. This function calculates the Abel deconvolution of one half of the input chemiluminescence image, with the underlying assumption that the image input is symmetrical about its central vertical axis. To run the function, four variables are required to be input by the user. The first variable is the matrix of the temporal averaged chemiluminescence image, calculated by the algorithm provided in Section C1. The second input required is the variable *R*, representing the radius of the image in millimetres, which is calculated based on the spatial resolution of the image. Additionally, the third input required is the horizontal central pixel (CentXPix), whilst, the user must also indicate if the half image used for Abel deconvolution should be defined from the central pixel to the right edge (1) or from the central pixel to the left edge (2). The subsequent function called by the main function *HalfAbel* can be found in [275]. A new addition to the code is the estimation of the centroid of the binary trace of the Abel image. This action was performed using the *regionprops.centroid* function provided by MATLAB. The estimation of the Abel binary image centroid was based on both the shape and the pixel intensity.

```
function [ImAbel] = HalfAbel(Image, R, CentXPix, WhichWay)

[i, j] = size (Image);
n = (j/2) + 1;

if WhichWay == 1
       NewEdge = (2*(j-CentXPix));

       %Initialize output image matrix
       ImAbel = zeros(i, NewEdge);
       k = (NewEdge/2) - 1;

       %For loop cycles through each row of the input image
       for z = 1:i

              %Extract single image row
              A = Image(z, CentXPix:j);

              %Convert image row to double precision
              A2 = im2double(A, 'indexed');

              %Calls the Abel inversion function one row at a time with an
```

```
            %input of 5 cosinus expansions in the Fourier-series-like
            %expansion
            [f_rec , X] = abel_inversion(A2,R,5);

            %Add the Abel deconvoluted row to the output matrix
            ImAbel(z, (NewEdge/2):NewEdge) = f_rec(:,1);

            %Rotate the Abel deconvoluted row about the central axis
            f_rec = flipud(f_rec);
            ImAbel(z, 1:k) = f_rec(2:(NewEdge/2),1);
      end
end

if WhichWay == 2
      NewEdge = (2*CentXPix);
      ImAbel = zeros(i, NewEdge);
      k = (NewEdge/2) - 1;

      %For loop cycles through each row in the input image
      for z = 1:i

            %Extract single image row
            A = Image(z, 1:(CentXPix+1));
            A = fliplr(A);

            %Convert image row to double precision
            A2 = im2double(A, 'indexed');

            %Calls the Abel inversion function one row at a time with an input
            %of 5 cosinus expansions in the Fourier-series-like expansion
            [f_rec , X] = abel_inversion(A2,R,5);

            %Add the Abel deconvoluted row to the output matrix
            ImAbel(z, (NewEdge/2):NewEdge) = f_rec(:,1);

            %Rotate the Abel deconvulted row about the central axis
            f_rec = flipud(f_rec);
            ImAbel(z, 1:k) = f_rec(2:(NewEdge/2),1);
      end
end

CentXPix2=Xcentr;

%Binarization of ABEL image
AbelBinaryImage = imbinarize(ImAbel,'global');

%Crop of ABEL binary image to take the right side
CropZone = [(CentXPix2) 1 X1 Y1];
AbelCroppedBinaryImage = imcrop(AbelBinaryImage,CropZone);

%Estimation of binary ABEL image centroid
Abelstat = regionprops(AbelCroppedBinaryImage,'Centroid');
FlameCentre = cat(1,Abelstat.Centroid);

End
```

D. Oxygen (O_2) measurements

In Figures D-1, D-2 and D-3, the average oxygen (O_2) concentrations, between the first and the second experimental repeat of the three swirlers of different surface roughness, are presented for the 100% CH_4, the 77%$_{vol}H_2$/23%$_{vol}CH_4$ and the 100% H_2 cases, respectively. The sampling of O_2 emissions from the exhaust gas section of the burner took place quasi-simultaneously with the rest of the NO_x and temperature measurements. The O_2 concentrations are presented as a percentage of the exhaust gas for each equivalence ratio tested. The horizontal error-bars represent the uncertainty due to the standard error of the mass flow controllers, whereas the vertical error-bars represent the deviation between the two experimental repeats.

It is observed that for the three swirlers tested the measured O_2 levels are only marginally different under the same equivalence ratio. These differences which, for the vast majority of the cases, are less than 5% of the absolute plotted value and less than 0.5% of the total O_2 concentration, are sensible and can be attributed to the mass flow controller inaccuracy, as well as to the gas analyser standard measurement error. This trend was consistent under any fuel type studied. Consequently, it is presumed that the three swirlers were tested under the same operating conditions.

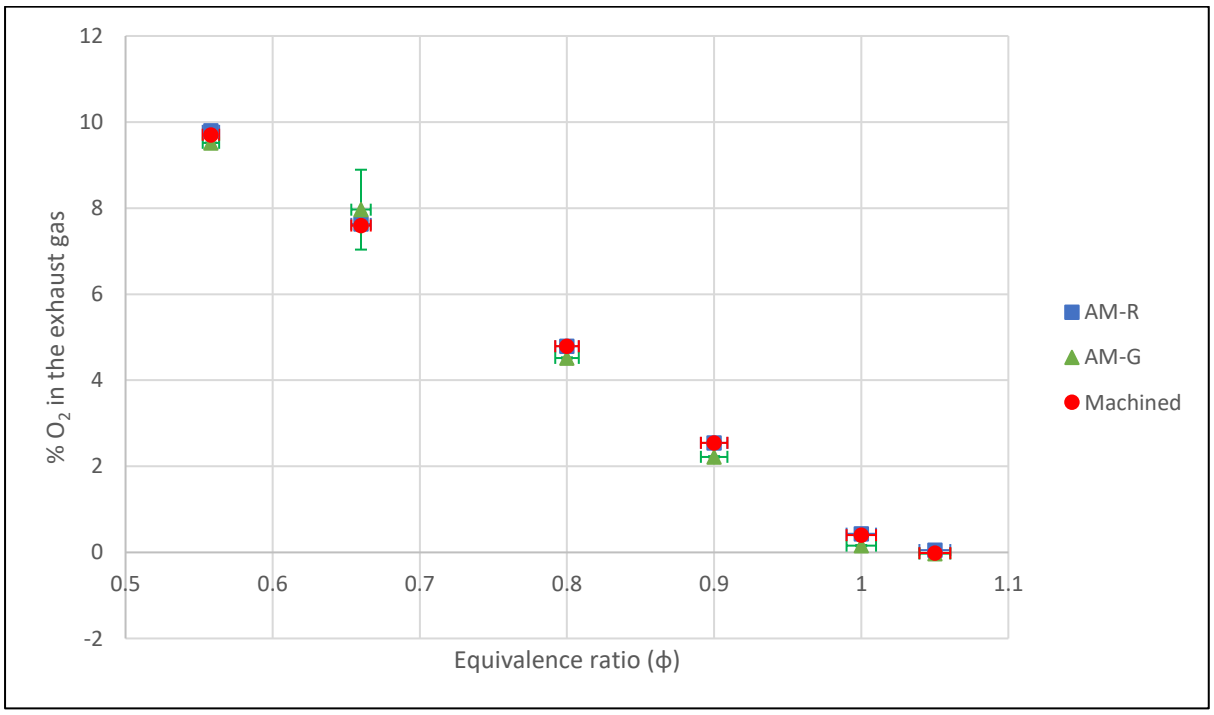

Figure D-1 *Average O_2 concentrations at the exhaust gas indicating the differences between the three swirlers and the level of repeatability for CH_4/air mixtures.*

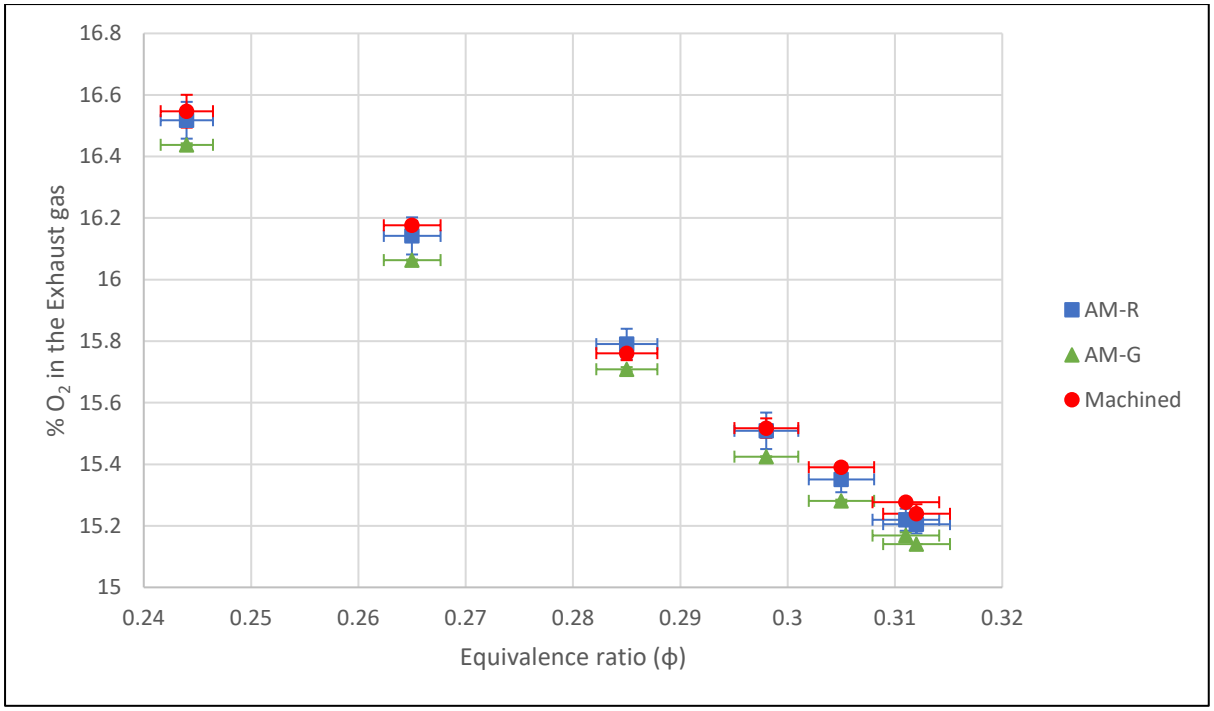

Figure D-2 *Average O_2 concentrations at the exhaust gas indicating the differences between the three swirlers and the level of repeatability for H_2/air mixtures.*

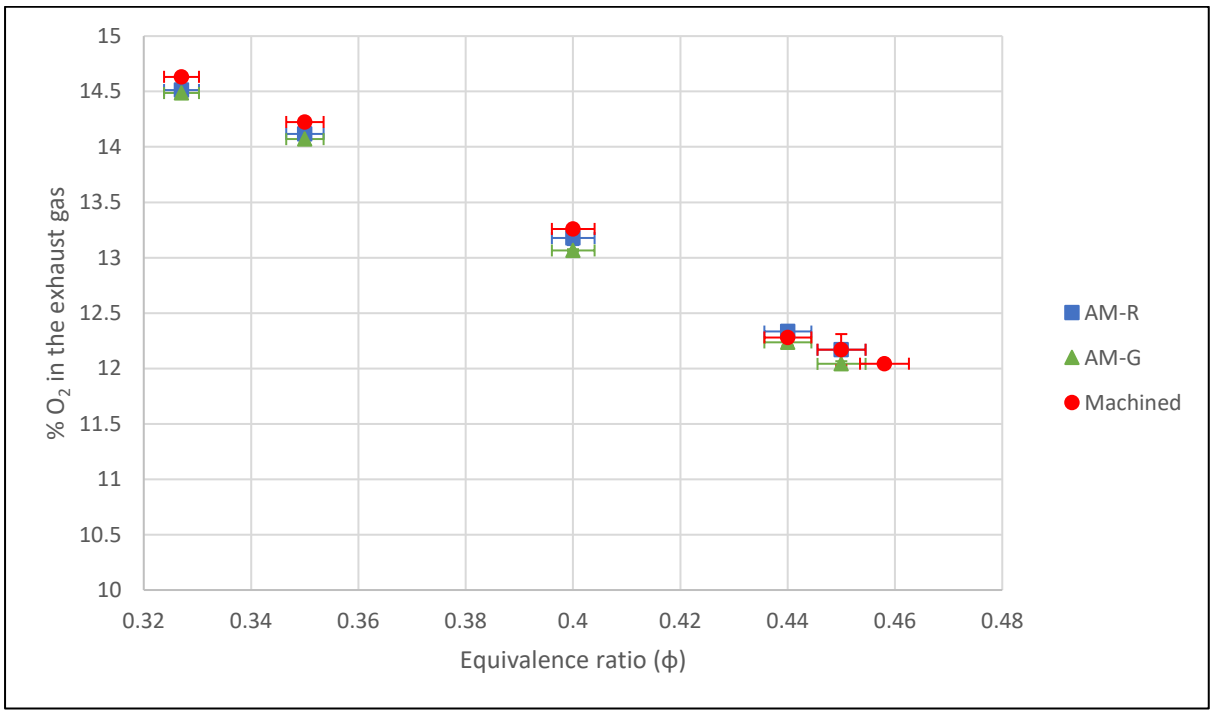

Figure D-3 *Average O_2 concentrations at the exhaust gas indicating the differences between the three swirlers and the level of repeatability for CH_4/H_2 fuel mixtures.*